THE UNIVERSITY *of* EDINBURGH

Photophysical Studies of 2-Aminopurine in DNA

Grant McKenzie

Submitted in total fulfilment of the requirements of the degree of Doctor of Philosophy under a jointly-awarded PhD programme

The University of Edinburgh

●

The University of Melbourne

May 2017

I dedicate this thesis to my father, Peter McKenzie.
Although you are no longer with us, you are with me every day.

Abstract

Deoxyribonucleic acid (DNA) forms the basis of all known living organisms. Despite the essential role played by DNA, its dynamic system and functional behaviour are still not completely understood. The work presented in this thesis aims to explore the structural dynamics of DNA systems, using fluorescence-based approaches, and to attempt to develop a technique for the measurement of fluorescence decays of biological molecules on the ultrafast (femtosecond) timescale.

Absorption of UV radiation by DNA is known to lead to mutations and damage to DNA structure and functionality. For the majority of absorbed photons, the excitation energy dissipates harmlessly as heat, but in some instances this energy transfers to regions of DNA that are more susceptible to damage. 2-Aminopurine (2AP), a fluorescent analogue of the native DNA base adenine, can be incorporated into DNA with minimal perturbation to the DNA structure, and can be used to investigate inter-base electronic energy transfer. By selectively exciting the native DNA base in 2AP-containing dinucleotides and utilising 2AP fluorescence as an energy acceptor, the mechanism of electronic energy transfer has been investigated. Analysis of the resulting fluorescence lifetimes of 2AP has revealed that energy transfer preferentially excites conformations in which the bases are highly stacked, and the fluorescence of 2AP is highly quenched. This has led to a re-evaluation of energy transfer efficiencies between the natural bases and 2AP, and has shown that transfer efficiencies cannot be determined correctly from steady-state fluorescence measurements.

To investigate the influence of base dynamics on the quenching of 2AP fluorescence in DNA, time-resolved fluorescence measurements were carried out on 2AP-containing systems in frozen solution at 77 K. These studies included dinucleotides, single–strand oligonucleotides and their corresponding duplexes. In all cases, comparison of the fluorescence decay parameters measured at room temperature with those measured at 77 K showed that elimination of base dynamics prevented rapid quenching, on the 10s of ps timescale or faster, although quenching on the 100s of ps timescale persisted for 2AP in single strands and duplexes.

The multi-exponential fluorescence decay of 2AP in DNA and its high sensitivity to local environment is commonly exploited to investigate DNA-enzyme interactions.

Transposases are enzymes involved in the movement of sections of DNA (transposons) within the genome. The Mos1 transposase catalyses the movement of a transposon via a cut-and-paste mechanism involving several intermediate complexes. Understanding the complex mechanism by which the transposase can remove and insert a section of DNA would allow these enzymes to be used as biomolecular tools. The structure of the intermediate Mos1 strand-transfer complex (STC) has been investigated by incorporating 2AP into several regions of the transposon and analysing the fluorescence decay. The involvement of a base-flipping-like mechanism has been identified in the mechanism of strand transfer for the Mos1 transposon.

The time-resolved fluorescence measurements performed in this thesis are limited to time resolution of ~20 ps and longer using TSCPC. However, an abundance of photophysical events in DNA occur on the femtosecond timescale. Development of a methodology utilising fluorescence gating techniques (such as sum-frequency generation or diffraction from a transient grating) have been attempted, in order to construct an experimental system that enables the broadband detection of ultrafast fluorescence decays. Despite the lack of immediate success in recording the fluorescence decay from a sample, due to technical issues and time-constraints, initial characterisation of the set-up was performed and the prospect of broadband detection was demonstrated. Overall, this thesis gives insight into some of the dynamic processes taking place in DNA and presents work performed to develop a system that would allow the extension of these studies to processes occurring on the fs timescale.

Lay Summary

Deoxyribonucleic acid, commonly known as DNA, forms the basis of all known lifeforms. Despite the importance of DNA to life, much of how DNA functions and the processes that occur within DNA are still a mystery. DNA is made up of components known as nucleotides that link up to form the DNA strand. Each nucleotide is composed of a sugar group, a phosphate group and one of four types of bases. While the sugar and phosphate groups link together to form the DNA backbone, the sequence of the bases encodes genetic information (the information of life). Although commonly thought of as a motionless molecule, due to the popularity of images of the DNA double helix, the structure of DNA is actually highly energetic and constantly in motion (dynamic), meaning that it is far more complicated than initially thought. The complex dynamics involved in the DNA structure play a vital role in how the molecule functions and so have important consequences for our understanding of DNA processes.

The majority of the experimental work in this thesis has been performed using fluorescence-based techniques. Initially, a molecule absorbs light, giving the molecule extra energy and allowing it to exist in a higher energy (excited) state. Some molecules get rid of this extra energy by releasing the extra energy as light (known as fluorescence), returning the molecule to the lowest energy (ground) state. The time taken for the light to be released, as well as the colour (frequency) and brightness (intensity) of the light can reveal information about the molecule and its environment. Unfortunately, the bases in DNA are not fluorescent and so cannot be studied in this way. 2-aminopurine (2AP) is a fluorescent molecule that closely resembles one of the DNA bases and is able to replace this base without altering the structure or functionality of the DNA molecule. When 2AP is part of the DNA base sequence, its fluorescence is very sensitive to nearby interactions with bases around it or with solvent molecules. Therefore, by using 2AP, fluorescence techniques can be used to study DNA. The usefulness of 2AP as a probe of DNA structure has been demonstrated in this thesis by observing what happens when a strand of DNA interacts with an enzyme, showing the substantially different environment that 2AP exists in (and therefore different level of fluorescence) when the enzyme is present.

Studying DNA is made difficult by the dynamic structure of DNA that is constantly in motion. The flexibility and movements of DNA bases at room temperature may play

an important role in the stability of DNA by allowing bases to interact with each other in specific ways that depend on the localised movement of the bases. A majority of the experimental work in this thesis has been performed on small fragments of DNA that contain only two nucleotides (dinucleotides), where one of the bases present is 2AP. These dinucleotides provide a simplified model of DNA where interactions specific to a base can be clearly identified. Freezing dinucleotides at very low temperatures prevents the bases from moving, allowing the important role played by these movements to be determined.

Even before the discovery of DNA itself, UV light was known to have harmful effects on organisms. It is now known that the bases in DNA absorb UV light, introducing extra energy into the molecule. Most often, when DNA bases are excited via absorption, the extra energy is released harmlessly as heat. However, in a small number of cases, the energy absorbed is able to move and collect in regions of the DNA where damage or mutations to the DNA structure can occur, leading to the loss of genetic information and the eventual formation of melanoma (skin cancer). Figuring out how energy moves between bases in DNA will help to better our understanding of the initial steps that eventually lead to the formation of skin cancer. After providing energy exclusively to the native DNA base in a 2AP-containing dinucleotide, some of the energy moves to 2AP, which then fluoresces. The resulting 2AP fluorescence has revealed information on the type of bases and the arrangement of the bases that encourage the transfer of energy to 2AP from a DNA base.

The last part of this thesis is concerned with the development of an experimental set-up that will enable the measurement of fluorescence that occurs on an extremely fast timescale, too fast to be measured by common fluorescence techniques. Although the progress was limited by time constraints, the capabilities of the set-up were demonstrated and showed promise for further work in the future.

The research conducted in this thesis has provided valuable insights into the processes going on in DNA and the effectiveness of 2AP as a probe of DNA systems.

Declaration

This thesis has been submitted for fulfilment of the requirements of a Universitas 21 Joint PhD, which was hosted by the University of Edinburgh, United Kingdom (lead institution) and the University of Melbourne, Australia (partner institution).

This declaration is to certify that the work contained within has been composed by myself and is entirely my own work, except where otherwise stated. I confirm that appropriate credit has been given within this thesis where reference to the work of others has been made.

Chapter 6 of this thesis has been based on work from the published paper entitled "A bend, flip and trap mechanism for transposon integration" (E. R. Morris, H. Grey, G. McKenzie, A. C. Jones and J. M. Richardson, *Elife*, 2016, **5**, 1–23, DOI: 10.7554/eLife.15537). Notice of the use of this work will be presented appropriately within the relevant chapter.

No part of this thesis has been submitted for any other degree or professional qualification as specified.

Signed:

_____

Date:

_____

Acknowledgements

The completion of this thesis would not have been made possible without the support and guidance of several people, and it is to them that I wish to express my appreciation to here.

First and foremost, I wish to express my deepest gratitude to my supervisors, Prof. Anita C. Jones and A/Prof. Trevor A Smith for their guidance and expert advice, and for giving me the opportunity to undertake and be part of this fascinating research. I have thoroughly enjoyed my time spent involved in this work and have never regretted for a moment in becoming a part of it.

Secondly, my thanks go to Dr Julia Richardson for allowing me to collaborate on and contribute to the Mos1 transposase project.

Thirdly, my gratefulness goes to Dr Jöchen Arlt for his endless support with the laser system in COSMIC (through its good days and its bad days) and for allowing me to be able to begin to take responsibility in the set-up, beginning me on my journey into the world of optics and laser spectroscopy.

Next, my heartfelt appreciation goes to the following people. To the members of the Jones group, past and present, and most especially to Hannah, who has been there with me from day one. Thank you all for your support and true friendship during my time spent at the University of Edinburgh. To the members of the Smith-Ghiggino group in Melbourne, for making me feel welcome in a foreign land and for providing endless support with the more-advanced laser systems in the labs at the University of Melbourne. To the exceptional friends I made during my year spent in Melbourne, without whom I would not have felt quite as at home on the other side of the world as I did. Lastly, to those unseen who have provided my funding and contributed via bursaries and stipends, I will forever be thankful for your support.

My greatest appreciation of all goes to my friends and family who have supported me throughout my academic studies, ultimately leading me to produce this thesis, and who have been there for me when I have needed them. I am eternally indebted to my mother, May, and stepfather, Richard, who have always encouraged me to follow my dreams and to strive for excellence in whatever I do. To my brother, Gregor, for already

setting the bar high and giving me something to strive for, which is a trait inherent to the rivalry between siblings.

And finally, most of all, to the ever-logical advice of my best friend, Lindsey. It has always been a great anchor in my life. Your wisdom and friendship will always be a welcome addition to any time or place in my life, throughout the easy and the tough times and always will be.

List of Abbreviations

2AP	2-aminopurine
2APr	2-aminopurine riboside
3WJ	three-way junction
A	adenine/adenosine
A-factor	lifetime fractional amplitude
BBO	β-barium borate
bp	base pair
C	cytosine/cytidine
CFD	constant fraction discriminator
CI	conical intersection
CT	charge transfer
d	deoxy-
DFG	difference-frequency generation
DNA	Deoxyribonucleic acid
dp	diphosphate
ds-DNA	double-stranded DNA
ET	energy transfer
eT	electron transfer
FQY	fluorescence quantum yield
FRET	Förster resonance energy transfer
fs	femtosecond
FWHM	full width at half-maximum intensity
G	guanine/guanidine
GV	group velocity
HT	hole transfer
HWHM	half width at half-maximum intensity
Hz	Hertz
I	hypoxanthine/inosine
mp	monophosphate
ms	millisecond
η	transfer efficiency
nm	nanometre
ns	nanosecond
nt	nucleotide
NTS	non-transferred strand
OK	optical Kerr
OPA	optical parametric amplifier
PEC	pair-end complex
PMT	photomultiplier tube
ps	picosecond
QY/ϕ	quantum yield
r	riboxy-
RNA	ribonucleic acid
RT	room temperature
S	second
SFG	sum-frequency generation
SS	steady-state
ss-DNA	single-stranded DNA
STC	strand transfer complex
T	thymine/thymidine
τ	lifetime
TA	transient absorption
TAC	time-to-amplitude converter
TCC	target capture complex
TCSPC	time-correlated single photon counting
TG	transient grating
tp	triphosphate

IC	internal conversion
IR	infrared
IRF	instrument response function
ISC	intersystem crossing
λ_{em}	emission wavelength
λ_{exc}	excitation wavelength
LiCl	lithium chloride
M	Molar
MCP	microchannel plate
TRF	time-resolved fluorescence
TS	transferred strand
TTS	time transit spread
µs	microsecond
UV	ultraviolet
V	Volt
vis	visible
WT	wild-type

Contents

Chapter 1: Introduction

1.1. Purpose and Context of Thesis

Despite the fundamental importance of deoxyribonucleic acid (DNA) to our existence, our knowledge of DNA and its functional behaviour remains limited. Images of the famous double helix model of DNA, described by Crick and Watson, mislead the onlooker into believing that the duplex is merely a static, simple, ordered structure. However, the structure of DNA is highly dynamic, with base pairs typically persisting for only milliseconds, and an abundance of processes occur within DNA that are mediated by such fluctuations. The dynamics associated with DNA bases play a crucial role in the stability of DNA and govern how DNA interacts with enzymes. The work presented in this thesis aims to improve our current understanding of the roles played by base dynamics in the integral photophysical processes within DNA molecules, such as interbase charge transfer or electronic energy transfer, which are processes that can alter the electronic structure and affect the stability of DNA molecules.

Fluorescence techniques are ideally suited for probing the conformational dynamics within DNA, due to their inherent sensitivity and selectivity, and the non-invasiveness of optical excitation. Both steady-state and time-resolved fluorescence have been utilised in this thesis. Unfortunately, the native DNA bases are essentially non-fluorescent and their minimal inherent fluorescence cannot be detected by conventional fluorescence spectroscopic methods. Therefore, it is necessary to use an extrinsic fluorescent probe to enable the study of DNA using fluorescence techniques. The fluorescent nucleic acid base analogue 2-aminopurine (2AP) has been widely employed as a fluorescent probe of DNA systems and, as an analogue of the native DNA base adenine (6-aminopurine), can be substituted into the DNA sequence with minimal perturbation to the DNA structure. The photophysical and biochemical properties of 2AP, alongside the high sensitivity of its quantum yield and time-resolved fluorescence decay to changes in its local environment (especially base-stacking interactions), make it an ideal probe in the study of DNA molecules.

The study of DNA is made difficult by the overlapping spectral properties of its constituent bases and by the dynamics inherent to its structure and function. To permit the study of and to identify specific processes in DNA, a single 2AP base has been incorporated into DNA single strands, duplexes and into DNA dinucleotides. The DNA dinucleotides consist of two nucleic acid bases covalently linked through the DNA backbone. In this case, one of the bases present is 2AP and therefore these dinucleotides provide a simple system of 2AP in DNA, in which base-specific interactions can be identified and studied.

This thesis also utilises a technique that allows for the elimination of conformational motions of bases, such as low-temperature measurements, and allow distinct conformations of the DNA structure to be resolved using time-resolved fluorescence measurements of 2AP in DNA. As many important processes in DNA occur on timescales that are too short to be observed by common time-resolved fluorescence measurements, there is a necessity for the development of ultrafast fluorescence spectroscopic techniques that are suited to the study of biological molecules in the ultraviolet (UV) spectral region.

1.2. Structure of Thesis

This section outlines the structure of the thesis, presenting a summary of the content of each chapter.

Chapter 2 presents the fundamental background knowledge and theoretical considerations underlying electronic spectroscopy (absorption and fluorescence), DNA structure and the fluorescent nucleic acid base analogue 2-aminopurine. Further theoretical considerations and a review of the literature specific to each individual study can be found in the Introduction of the relevant chapter devoted to that study.

The experimental techniques that are commonly used throughout this thesis are described in Chapter 3, while specific experimental details relating to a particular study are given in the Methods section of the relevant chapter.

Chapter 4 describes low-temperature fluorescence measurements of 2AP in both DNA oligonucleotides and DNA dinucleotides. A comparison is made between fluorescence decay parameters measured in conformationally static systems in a frozen glassy matrix at 77 K, with those measured at room temperature in fluid solution, in order to examine the effect of base dynamics on interbase quenching of 2AP fluorescence. For 2AP-containing oligonucleotides, the role played by interbase

interactions between 2AP and all nearby bases is explored, while 2AP-containing dinucleotides allow a clear identification of base-specific interactions.

Following this, in Chapter 5 the phenomenon of electronic energy transfer between bases in DNA is explored, using 2AP-containing dinucleotides in which a clear identification of the energy donor (native DNA base) and the energy acceptor (2AP) can be made. By monitoring the fluorescence signal of 2AP while selectively exciting the native DNA base present, steady-state fluorescence measurements have been used to determine the efficiency of energy transfer from each native DNA base to 2AP. It is then shown that time-resolved fluorescence measurements provide new insights into the conformational selectivity of the energy transfer process. In light of the time-resolved fluorescence results, a re-evaluation of the energy transfer efficiencies determined from steady-state fluorescence measurements is presented and discussed. Low-temperature measurements, in the context of energy transfer, are also reported to gain an insight into the role played by base-dynamics in the transfer of electronic energy between bases.

Chapter 6 exemplifies the use of 2AP as a probe of DNA-enzyme interactions, revealing the importance of structural dynamics in the functionality of DNA. Time-resolved fluorescence measurements of 2AP in DNA have been used to study the mechanism of transposition by the Mos1 transposase enzyme, particularly to investigate the hypothesis, based on X-ray crystallography, that specific adenine residues are flipped out of the duplex in the Mos1-DNA strand-transfer complex.

Chapter 7 differs in theme from the previous chapters, in that it describes work towards the development of an ultrafast fluorescence spectroscopic technique, carried out by the author during the period of his PhD spent at The University of Melbourne. Unfortunately, due to technical issues and time-constraints, development of the system was not completed. Despite this, the progress made during the time available is presented and the subsequent development is reported on, with great promise shown for future development of the system.

Finally, Chapter 8 presents an overview of the conclusions drawn from earlier chapters, with suggestions for the future directions of this work.

Chapter 2: Background and Theory

This chapter outlines some of the common principles that underlie the experimental techniques and interpretation of the results presented throughout this thesis. Basic concepts related to fluorescence spectroscopy will be introduced as well as some background knowledge concerning the general structural features of DNA. Following this will be a brief introduction to fluorescent nucleic acid base analogues, with special consideration given to 2-aminopurine. The content presented here is mainly based on the books of Hollas[1], Atkins and de Paula,[2] Turro,[3] Gilbert and Baggott,[4] and Lakowicz.[5]

2.1. Electronic Spectroscopy

Through the monitoring of a molecule's interaction with light, it is possible to gain an insight into the atomic scale behaviour of the molecule. A molecule's ability to absorb and emit radiation is closely related to both its electronic composition and nuclear framework, which are, in principle, sensitive to the immediate environment of the molecule.

2.1.1. Absorption/Excitation

Excitation of a molecule, M, occurs via the absorption of radiation, leading to the production of excited species, M*.

$$M + h\nu \rightarrow M^* \qquad \textbf{2.1}$$

Absorption of radiation (in the form of a photon of light), with energy E (=hν), by a molecule can promote an electron from the ground electronic state (i) to some an excited state (j) (Figure 2.1). The excitation of an electron to a higher electronic state is accompanied by vibrational excitation of the nuclei, resulting in a vibronically (electronically and vibrationally) excited state. Absorption of radiation by a molecule is made possible due to the coupling of the oscillating electrical field of the incident radiation with motion of the electrons in the molecule.

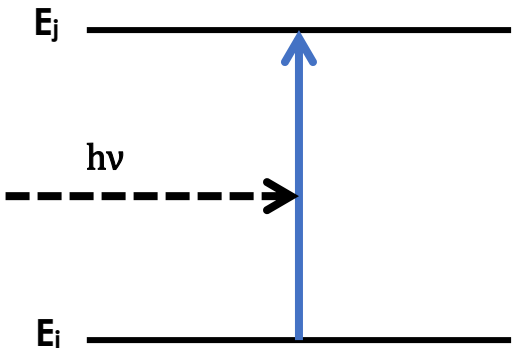

Figure 2.1: Absorption of radiation with energy, *E*, resulting in the excitation of a molecule from ground state (E_i) to an excited state (E_j). The energy difference between the two energy levels is $E_i - E_j = E = h\nu$ (where h = Planck's constant and ν = frequency).

2.1.2. Transition Dipole Moment

The transition dipole moment (TDM), μ_{ij}, is a vector quantity that describes the charge separation effected by the oscillation imposed on the electrons by the electrical field of the absorbed radiation. The probability of an electronic transition occurring between two electronic states is dependent on the TDM and is related to the overlap of the wavefunctions of the two states involved: the initial ground state (ψ_i) and the final excited state (ψ_j). Using the electric dipole moment operator, $\hat{\mu}$, μ_{ij} can be calculated as follows:

$$\mu_{ij} = \int \psi_i^* \cdot \hat{\mu} \cdot \psi_j d\tau \qquad \textbf{2.2}$$

The probability of a given electronic transition occurring can be determined from the square of the TDM. As a result, if the TDM is zero then the probability of the transition occurring is also zero and the transition is forbidden. However, if the TDM is non-zero then the transition is allowed.

The full quantum mechanical state of the system can be described by the wavefunction and, in principle, this can be used to calculate any property of a system. Yet, apart from in very simple cases, it is not possible to obtain an analytical representation that can completely and accurately and describe the system. This problem can, however, be somewhat overcome by focussing on parts of the overall wavefunction that can be defined by independent variables. For example, the Born-Oppenheimer approximation can be applied, allowing electronic and nuclear components of the wavefunction to be considered independently. This approximation

assumes that electrons instantaneously adapt to changes in nuclear position (caused by translational, vibrational, or rotational motion), due to the very large difference in mass between nuclei and electrons.

2.1.3. Absorption Measurements

The rate of change of population *N* of the excited state j due to absorption is given by

$$\frac{dN}{dt} = N_i B_{ij} \rho(\tilde{\nu}) \qquad \textbf{2.3}$$

where B_{ij} is the Einstein *B* coefficient for absorption, N_i is the population of (ground) state i and $\rho(\tilde{\nu})$ is the energy density of the incident radiation. The transition probability (given as the square of the transition dipole moment, $\boldsymbol{\mu}_{ij}$) is related to B_{ij} as follows:

$$B_{ij} = \frac{3\pi^3}{4\pi\varepsilon_0 h^2} \left|\boldsymbol{\mu}_{ij}\right|^2 \qquad \textbf{2.4}$$

where the constant ε_0 is the vacuum permittivity and h is Planck's constant.

The parameters defined above can be related to experimentally observed quantities. The basic concept of absorption experiments is shown in Figure 2.2, where incident radiation, I_0, falls upon a cell of length l containing an absorbing material of concentration c in the liquid phase. By measuring I_0/I while scanning through a range of wavenumbers (or wavelengths), an absorption spectrum can be measured.

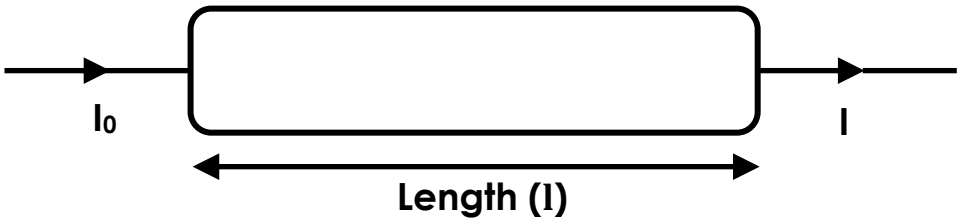

Figure 2.2: Simplified schematic of an absorption experiment. Radiation of intensity I_0 is incident on an absorption cell containing absorbing material of concentration c in the liquid phase. The emerging radiation of intensity I is then detected by the spectrometer.

The absorbance, A, is defined as $\log_{10}(I_0/I)$ of light is proportional to *c* and *l* according to the Beer-Lambert law (Equation 2.5)

$$A = \log_{10}\left(\frac{I_0}{I}\right) = \varepsilon(\tilde{\nu}) c l \qquad \textbf{2.5}$$

where the molar absorption coefficient (also known as the molar absorptivity), ε, is a function of $\tilde{\nu}$ with units of (concentration x length)$^{-1}$, making values of A dimensionless. Since ε (and hence A) varies with wavenumber, it is more sensible to determine the transition strength for absorption by integrating ε over the whole absorption band, giving the integrated absorption coefficient, A_i as shown in Equation 2.6,

$$A_i = \int_{\tilde{\nu}_1}^{\tilde{\nu}_2} \varepsilon\,(\tilde{\nu}) d\tilde{\nu} \qquad \textbf{2.6}$$

where $\tilde{\nu}_1$- $\tilde{\nu}_2$ is the range of wavenumbers over which the absorption band occurs. The transition dipole moment can be related to A_i by a dimensionless quantity that is the ratio of the strength of the transition to that of the dipole transition between two states of an electron oscillating in three dimensions in a simple harmonic way. This is commonly known as the oscillator strength, f. The oscillator strength of the electronic transition from i to j, f_{ij}, is given as

$$f_{ij} = \left[\frac{4\varepsilon_0 m_e c^2 \ln 10}{N_A e^2}\right] A_i \qquad \textbf{2.7}$$

where N_A is the Avogadro constant, m_e is the rest mass of an electron, c is the speed of light and e is the charge on a proton. As the oscillator strength is a ratio, its maximum is at unity (1) and values such as these are observed for electronic dipole-allowed transitions. Conversely, an oscillator strength close to zero typically relates to forbidden transitions. Equation 2.8 shows the relationship between the oscillator strength and the transition dipole moment.

$$f_{ij} = \left[\frac{8\pi^2 m_e c}{3e^2 h}\right] \tilde{\nu}_{ij} \left|\boldsymbol{\mu}_{ij}\right|^2 \qquad \textbf{2.8}$$

where $\tilde{\nu}$ is the wavenumber for the transition (commonly determined by $\tilde{\nu}_{max}$ for a given absorption spectrum).

2.1.4. Relaxation Processes

Following the excitation of a species via absorption of a photon, relaxation of the excited species can occur through a variety of decay processes, which can be categorised into two groups: radiative decay processes and non-radiative decay processes. These processes are defined such that radiative decay processes (or luminescence) involve the emission of light (e.g. fluorescence or phosphorescence) and non-radiative decay processes (e.g. emission of heat or creation of a chemical bond) do not.

The intramolecular photophysical processes that create and subsequently lead to the decay of an excited state singlet state, S_n, are illustrated in Figure 2.3, in the form of a simplified Jablonski diagram.

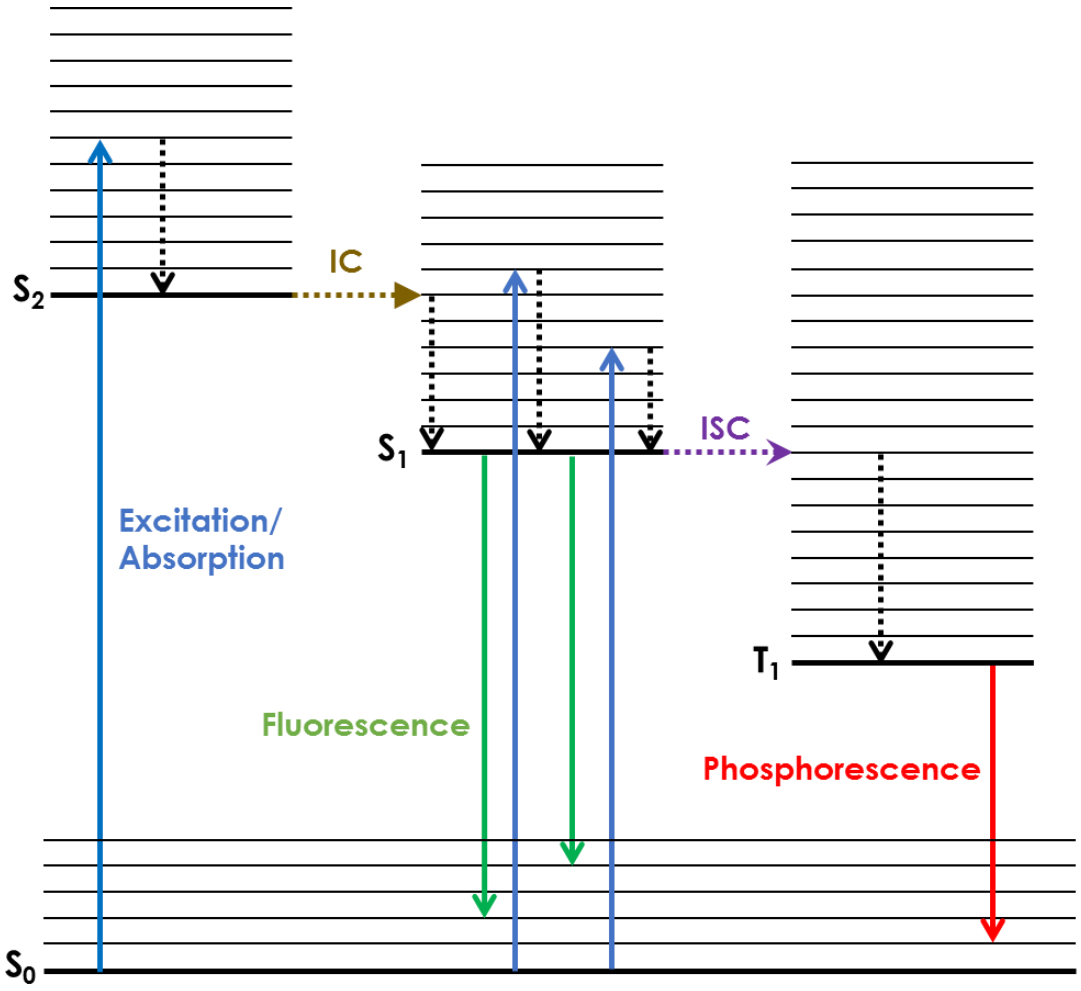

Figure 2.3: A Jablonski diagram showing excitation and excited-state decay processes for a molecule. The transitions shown are excitation (blue), fluorescence (green), phosphorescence (red), vibrational relaxation (dotted black), internal conversion (IC) (dotted brown) and intersystem crossing (ISC) (dotted purple).

When a molecule absorbs energy in the form of a photon of light, it is excited from the ground state to some vibronically excited state (excitation/absorption). Relaxation of the excited state initially occurs via a combination of vibrational relaxation (shown as dotted vertical lines in Figure 2.3) and internal conversion (IC) to the lowest vibrational state of the S_1. Following this, return of the molecule to the electronic ground state occurs via the emission of a photon (fluorescence). Vibrational relaxation and IC, from higher electronic states to S_1, occur on a significantly faster timescale than fluorescence and, for

this reason, the emission of a photon *via* fluorescence will always occur from the lowest vibrational level of S_1 (Kasha's rule). An alternative radiative relaxation process to fluorescence is phosphorescence, in which a molecules in the S_1 state can undergo spin conversion to the first triplet state (T_1), known as intersystem crossing (ISC). Transition from T_1 to S_0 (phosphorescence) is forbidden and thus the rate constants for phosphorescence are orders of magnitudes smaller than for fluorescence (an allowed transition). Further details of each of the decay processes are discussed in the following sections.

2.1.4.1. Radiative Decay Processes

Fluorescence and Phosphorescence

Following the absorption of a photon, the excited molecule may relax to the ground state by emitting a photon. This is generally termed as luminescence. Luminescence can be further characterised as either fluorescence or phosphorescence, depending on the electron spin properties of the transition involved. For a transition to be allowed, the relative orientation of electron spin, characterised by the spin multiplicity, must be maintained. The spin multiplicity, calculated as 2S+1, of an electronic state is described by the total spin quantum number S of the state, where S =$\sum m_s$ and m_s is the spin quantum number. Electrons are fermions (particles with half-integral spin) with $m_s = \pm ½$. Thus, when all electrons are paired (S = 0), the spin multiplicity has a value of 1 and the state is referred to as a singlet state. The Pauli Exclusion Principle states that no two fermions can share an identical set of quantum numbers and, as such, the nature of the ground state of a molecule is typically a singlet state, in order to maximise occupancy of the lowest energy orbitals available. Under certain circumstances (such as following the promotion of an electron to a higher energy orbital), two unpaired electrons may be present (S = 1), resulting in a spin multiplicity of 3 and the state is referred to as a triplet state.

Fluorescence is defined as a radiative transition between electronic states of the same spin multiplicity, such that radiative decay occurs from an electronically excited singlet state (S_1) to its singlet ground state (S_0) and is an allowed transition.

Phosphorescence occurs from the triplet state (T_1), which has been populated by ISC from S_1, to the electronic ground state S_0. In the triplet state, the electrons exist as unpaired electrons and are lower in energy than the paired electrons (as dictated by

Hund's Rule) in the corresponding singlet state. Thus, phosphorescence emission occurs at longer wavelengths than fluorescence emission and is a forbidden transition.

The rate of transition between two states is related to the square of the TDM (Equation 2.2), resulting in allowed transitions occurring more frequently than forbidden transitions. Typically, the lifetime (inverse of the transition rate) of fluorescence is on the nanosecond (10^{-9} s) to picosecond (10^{-12} s) timescale. However, due to phosphorescence being a forbidden transition, the excited triplet state persists for a relatively long timescale (millisecond (10^{-3} s) to seconds (s)) and thus the triplet state is often depopulated by intermolecular quenching processes (such as collisional deactivation) before phosphorescence can occur (see Section 2.1.4.2). As such, in terms of radiative decay of the excited state, phosphorescence is a relatively uncommon event when compared to fluorescence. However, non-radiative decay pathways, such as intersystem crossing, can be promoted such that the probability of phosphorescence relative to fluorescence is increased (through spin-orbit coupling (see Section 2.1.4.2).

2.1.4.2. Non-radiative Decay Processes

Vibrational Relaxation

In the presence of collisions, initial relaxation of the excited vibronic state occurs *via* transfer of vibrational energy to the immediate environment, known as vibrational relaxation (shown as dotted vertical lines in Figure 2.3). This relaxation occurs on a very fast timescale compared to fluorescence (on the scale of 10^{-14} to 10^{-11} seconds) and thus, fluorescence always occurs from the ground vibrational level of the excited electronic state (Kasha's Rule).

Internal Conversion and Intersystem Crossing

Internal conversion (IC) and intersystem crossing (ISC) are both intramolecular non-radiative decay processes. IC is a transition between electronic states of the same multiplicity whereas ISC is the transition between states with different multiplicities. For non-radiative intramolecular transitions to occur, an overlap of the vibrational wavefunctions of the two vibronic states involved in the (horizontal) transition (see Figure 2.3) is required. This overlap is known as the Franck-Condon factor. The probability of a transition occurring decreases as the energy gap separating the initial and final electronic states increases (i.e. as the change in vibrational energy during the transition increases). For ISC (which is formally a forbidden transition) to occur, an interaction between the spin angular momentum and orbit angular momentum of the

transitional states is required. This magnetic interaction between electrons and the nuclei is known as spin-orbit coupling and is capable of allowing transitions to occur between states with a different multiplicity (singlet-triplet or triplet-singlet). The likelihood of such transitions is increased in the presence of heavy-atoms (such as halogens or transition metals) which are capable of inducing a larger spin-orbit coupling because of their larger nuclear charge.

Electronic Energy Transfer

A complete overview of the theory behind the non-radiative transfer of electronic energy from an excited donor molecule to a ground-state is beyond the scope of this thesis. A more detailed account of the theory is given by Turro,[3] while an overview of Förster theory is given by Lakowicz,[5] while only a brief overview will be presented here.

The migration of an excited state (electronic energy) from a donor molecule to an acceptor molecule is described generally as

$$D^* + A \rightarrow A^* + D \qquad \textbf{2.9}$$

Concerning the non-radiative transfer of energy from a donor (D) to an acceptor (A), the electronic states of D and A may be coupled through an electrostatic interaction that can be separated into two parts: electron-exchange and coulombic. Figure 2.4 shows an energy surface description of two possible mechanisms of energy transfer that can

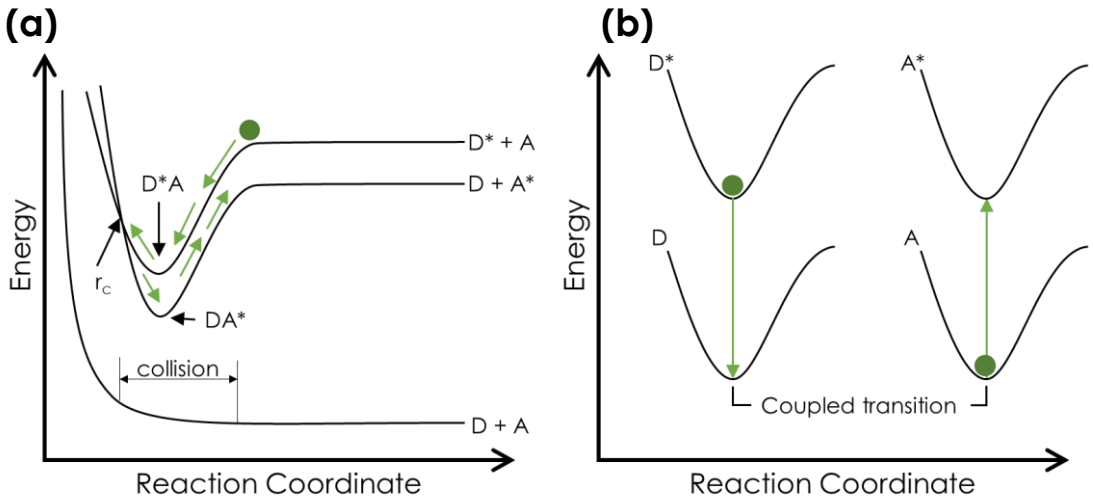

Figure 2.4: Schematic surface representations of (a) collisional energy transfer and (b) energy transfer via coulombic interactions of a donor molecule (D) and acceptor molecule (A). Green arrows show the movement of electronic energy along the potential energy surfaces.

occur: (a) electron exchange through a collisional interaction and (b) via coulombic coupling.

In the collisional energy transfer mechanism, which its name suggests is a short-range interaction, the ground state energy of D + A increases due to repulsive interactions as D and A approach each other in space. However, if D (or A) is excited as they approach, the energy of D*A (or DA*) will generally be lower than that of the separated pairs (D* + A and D + A*). At some geometry, r_c, the potential energy surfaces intersect and internal conversion (or intersystem crossing) to the lower energy state may occur. The crossing point, r_c, is typically situated in a region where some interaction between D^* and A occurs, allowing for the transfer of electronic energy. Following this transfer, thermal energy must be provided in order to allow the DA^* collisional pair to return to the upper surface, returning them to separate monomers (D + A*). If the minima associated with D*A or DA* are sufficiently deep, formation of an exciplex (excited complex) may occur and exciplex emission or absorption may be observed. The rate of electron-exchange energy transfer is typically dependent on the overlap of the emission spectrum of D and the absorption spectrum of A and a parameter Z, which is given as

$$Z^2 \propto e^{-2r/l} \qquad \textbf{2.10}$$

where r is the distance between D and A, and l is the van der Waals radius of the donor-acceptor pair (given as the sum of the van der Waals radii of donor and acceptor molecules). Thus, the rate of energy transfer is larger as the D and A approach and drops off rapidly as D and A separate past the sum of their van der Waals radii. As electron-exchange energy transfer often involves the physical exchange of electrons between D and A, the rules for "allowed" and "forbidden" transitions may not apply.

Another mechanism of energy transfer from D to A is via coulombic interactions. In this model, surface crossing (on the potential energy landscape) does not occur and the surfaces for the corresponding ground state and excited state molecules are considered separate and distinct (as shown in Figure 2.4 (b)). Despite this separation, some interaction (such as dipole-dipole interactions) can cause the simultaneous occurrence of the vertical transition D* → D and A → A*, thus a transfer of energy has occurred and is typically a long-range interaction. In some cases it is the transition moment of D* → D that can trigger A → A* in a mechanism analogous to radiative excitation of A to A* via interaction with the electric vector of a light wave. The transfer of energy via coulombic interactions does not involve a physical interaction between D and A, and thus the electron spin restrictions that apply for individual molecules (for

spin-allowed or spin-forbidden transitions) apply here. The rate of energy transfer due to coulombic interactions is dependent on the oscillator strength of the transition that is accepting the energy (i.e. A→A*) and on the spectral overlap integral, J, which can be evaluated by the region of overlap between the emission spectrum of D* with the absorption spectrum of A.

In most cases, the transfer of electronic energy is classified by the nature of the electronic states involved. Singlet-singlet energy transfer is a "spin-allowed" transfer in which an electronically excited donor in its singlet state produces an electronically excited acceptor in its singlet state. As a result of being a spin-allowed transition, transfer of electronic energy for a donor (singlet) to acceptor (singlet) may occur via long-range coulombic (dipole-dipole) interactions or by a short-range electron exchange (collisional or through orbital overlap) mechanism.

Triplet-triplet energy transfer is "forbidden" by the dipole-dipole mechanism, due to the typically low absorption events resulting in the formation of triplet states. However, triplet-triplet energy transfer via electron-exchange is a spin-allowed transition. Due to this, triplet-triplet energy transfer will generally only occur via the exchange mechanism and over shorter distances (10 – 15 Å). Since triplet states are long lived relative to singlet states, they are a more likely candidate to participate in the transfer of electronic energy than singlet states, given the right circumstances.

As a result of the forbidden nature of singlet-triplet and triplet-singlet energy transfer for both coulombic and exchange mechanisms, occurrence of these are uncommon and will not be covered in the context of this thesis.

A quantitative description of energy transfer between two fluorophores via the long-range dipole-dipole mechanism was developed by Förster, and is known as Förster resonance energy transfer (FRET). In FRET, the energy transfer rate constant is given by

$$k_{ET}(r) = \frac{1}{\tau_D}\left(\frac{R_0}{r}\right)^6 \qquad \textbf{2.11}$$

where τ_D is the decay time of the donor in the absence of the acceptor, R_0 is the Förster distance (defined as the distance at which the transfer efficiency is 50%), and r is the distance between D and A. In FRET, k_{ET} is strongly dependent on the distance r, and is characterised by its r^{-6} dependence. This is often exploited in studies of biological molecules, where FRET is used as a "molecular ruler" to monitor the distance between donor and acceptor fluorophores.

It should be noted here that interbase electronic energy transfer in DNA, discussed later in this thesis, does not follow the FRET mechanism and further discussion on this topic can be found in the Introduction to Chapter 5.

Intermolecular Quenching

Quenching is the broad term used to describe intermolecular non-radiative decay processes. These intermolecular quenching processes include electronic energy transfer and charge transfer, which are particularly relevant to the work presented in this thesis. Intermolecular interactions that lead to quenching include H-bonding, π-stacking or other aggregation or complex formation mechanisms. Intermolecular quenching processes relevant to DNA will be discussed in more detail in Section 2.2.

2.1.4.3. Quantum Yield

The efficiency of the fluorescence process is characterized quantitatively by the absolute fluorescence quantum yield, Φ_{abs}. Φ_{abs} is defined as the ratio of the number of photons emitted to the total number of photons absorbed. This ratio is also equivalent to the ratio of the rate constant of the radiative process to the sum of the rate constants of all processes (radiative and non-radiative), as shown in Equation 2.12.

$$\Phi_{abs} = \frac{k_R}{k_R + k_{NR}} \qquad \textbf{2.12}$$

In some cases, it is more convenient to consider the quantum yield of a fluorophore (ϕ_f) in comparison to the quantum yield of a reference fluorophore (ϕ_{ref}). This value is known as the relative quantum yield, Φ_{rel}, and is calculated as

$$\Phi_{rel} = \frac{\Phi_F}{\Phi_{ref}} \qquad \textbf{2.13}$$

2.1.4.4. Excited State Decay Kinetics

The overall rate of decay of an excited-state population can be defined by considering the radiative and non-radiative processes involved. The rate equation for the decay of a population of excited state fluorophores, [M*] is as follows:

$$-\frac{d[M^*]}{dt} = (k_R + k_{NR})[M^*] \qquad \textbf{2.14}$$

where k_R is the rate constant of the radiative process and k_{NR} is sum of the the rate constants of all non-radiative processes. During measurements, it is not possible to

distinguish k_R and k_{NR} and thus it is more convenient to consider the sum of all rates constants k (=k_R + k_{NR}). Through integration of Equation 2.14, an expression for the decay of the excited state population as a function of time can be obtained.

$$[M^*](t) = [M^*]_0 e^{-(kt)} \quad \textbf{2.15}$$

where $[M^*]_0$ is the concentration of [M*] at t = 0 (commonly defined as the arrival time of the excitation pulse). The observable property in fluorescence measurements is the fluorescence intensity, I, which is directly proportional to the excited state population. This allows the decay dynamics to be described by

$$I(t) = I_0 e^{-\frac{t}{\tau}} \quad \textbf{2.16}$$

where I_0 is the intensity of fluorescence at t=0 (=$k_R[M^*]_0$) and τ is the fluorescence lifetime (= 1/k). Equation 2.16 relates the observable property of fluorescence intensity to the fluorescence lifetime, τ, (the lifetime of the excited state population) and allows τ to be determined experimentally. Thus, by measuring the time taken for the fluorescence intensity to decrease to 1/e of the initial intensity, I_0, immediately following excitation by an infinitesimally short laser pulse, the fluorescence lifetime can be determined. So far, the case in which there is only one fluorescence lifetime (or excited state lifetime) has been considered. However, in cases where the recorded fluorescence decay arises from a heterogeneous sample, such as a mixture of fluorophores or one in which a single fluorophore exists in several different intermolecular quenching environments; the fluorescence decay must be described by a multi-exponential model,

$$\frac{I(t)}{I_0} = \sum_i A_i \, e^{-\frac{t}{\tau_i}} \quad \textbf{2.17}$$

where

$$\sum_i A_i = 1 \quad \textbf{2.18}$$

This model allows the relative population, A_i, of the i-th component of a sample to be quantitatively assigned to its fluorescence lifetime, τ_i. One common experimental method used for determining the lifetime, τ, is the time-resolved fluorescence technique time-correlated single photon counting (TCSPC) which will be discussed in detail in Section 2.1.5.1.

From the calculated values of τ_i and A_i, it is possible to calculate the average lifetime, <τ>, (also called the amplitude-weighted lifetime) using Equation 2.19,

$$\langle \tau \rangle = \frac{\sum_i A_i \tau_i}{\sum_i A_i} \qquad \textbf{2.19}$$

The average lifetime of an emitting species is proportional to the quantum yield (see Section 2.1.4.3) and is a useful experimental measure of relative quantum yield. However, in heterogeneous systems, the relative quantum yield predicted from the average lifetime is sometimes found to be greater than that measured from steady-state intensity and this is an indication of the presence of so-called "dark states" (non-emitting species).

2.1.5. Time-resolved Fluorescence Measurements

Time-resolved fluorescence measurements are widely used in the study of fluorescence and photophysics, containing more information than can be obtained from steady-state fluorescence measurements. They are especially useful in the study of biological molecules where identical fluorophores in different environments may have overlapping absorption and emission spectra, but different fluorescence lifetimes. In cases such as these, the fluorescence emission may be resolved through measurement of the lifetime of the fluorescence emission.

Throughout the work presented in this thesis, time-resolved fluorescence measurements were carried out using the technique of time-correlated single photon counting (TCSPC). For this reason, the technique of TCSPC will be presented here and discussion of other more advanced time-resolved fluorescence techniques will be presented in Chapter 7.

2.1.5.1. Time-Correlated Single Photon Counting

The intricate details of this technique are extensively covered in the works of O'Connor and Phillips,[6] Lakowicz,[5] and Becker[7] and thus only a general overview of the technique will be presented here.

Put simply, the technique of TCSCP works like a stopwatch, with the timer started at the arrival of an excitation pulse and stopped when a photon emitted from the sample first reaches the detector. The time difference between the arrival of an excitation pulse and an emitted photon at the detector is representative of the fluorescence decay of the sample under study and through repeated measurements of this event, a distribution of arrival times for individual photons can be recorded. From this, the fluorescence

lifetime(s) of the sample can be determined. The excitation pulse used for excitation of the sample is required to be significantly shorter (on the picosecond to femtosecond timescale) than the fluorescence lifetime to be measured (~10 picosecond to nanosecond). Typically, conditions are used such that a photon is detected for only approximately 1 in every 100 excitation pulses, to avoid a bias towards photons emitted at short times (so-called pulse pile-up) that would occur if more than one photon arrived at the detector per excitation pulse.

Detection of an excitation pulse is typically achieved through use of a photodiode, which converts the pulse of light to an electrical "start" signal. This electrical signal is passed through a constant fraction discriminator (CFD), which accurately measures the arrival time of the pulse independent of its amplitude, and is then sent on to a time-to-amplitude converter (TAC). The TAC is a component that acts analogous to a stopwatch and converts the time between start and stop pulses into an electrical signal. Upon detection of a fluorescence photon by the detector, the electrical signal is sent through a CFD (to determine accurately the arrival time of the photon) before being relayed to the TAC. When this second electrical signal (the stop pulse) arrives at the TAC, the built up voltage (proportional to the time between pulses) is discharged and an output signal generated. Following discharge of the TAC, a finite amount of time is required for the TAC to reset and be ready to receive another start pulse.

It is important to realise that the measured fluorescence decay will be a convolution integral of the instrument response function (IRF) and the sample decay function due to the shape and transient spread of the pulse used for excitation and, most significantly, the limited time-response of the detector. For these reasons, the early part of the decay will be distorted by the IRF. As such, it is vital to measure the IRF of the experimental set-up associated with each measured sample decay curve to be able to extract any short decay times from this part of the decay curve.

The measurement and analysis of fluorescence decay data are described in Chapter 3.

2.2. DNA

2.2.1. Composition and Structure

Deoxyribonucleic acid (DNA) is one of the major macromolecules that are essential for all known living organisms. DNA is a polymeric molecule whose linear structure is composed of one of four native DNA nucleobases (bases) attached to a repeating phosphate-sugar backbone. The four native bases in DNA are classified into two types according to their ring-structure: purines (adenine (A) and guanine (G)) and pyrimidines (cytosine (C) and thymine (T)). The structures of the native DNA bases, which are essentially flat, are shown in Figure 2.5, alongside the conventional numbering of their cyclic ring structures.

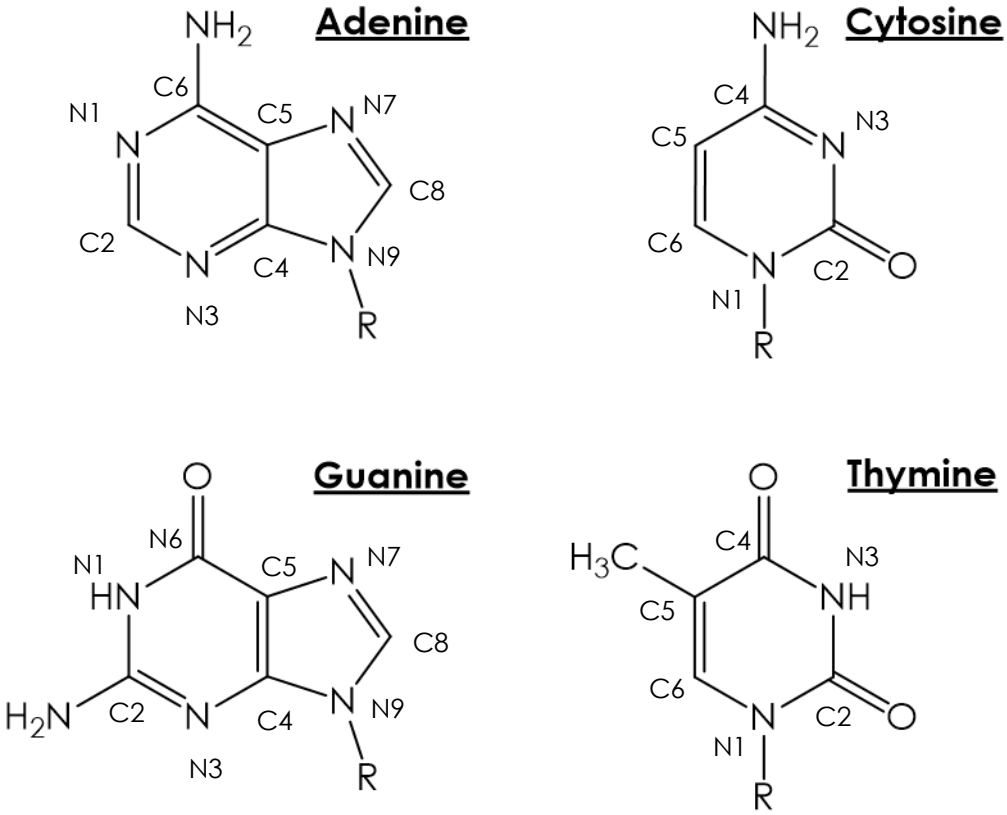

Figure 2.5: Molecular structures and atomic numbering of the native nucleic acid bases, adenine, guanine, cytosine and thymine. Purine bases are shown on the left and pyrimidine bases are shown on the right. "R" denotes the position that links the bases to the DNA backbone (at the C1' position). Alternatively, for isolated bases, R is replaced by a hydrogen atom.

The structure of the backbone of DNA, formed from repeating sugar-phosphate units linked through a 3'-5' phosphodiester bond, is shown in Figure 2.6.

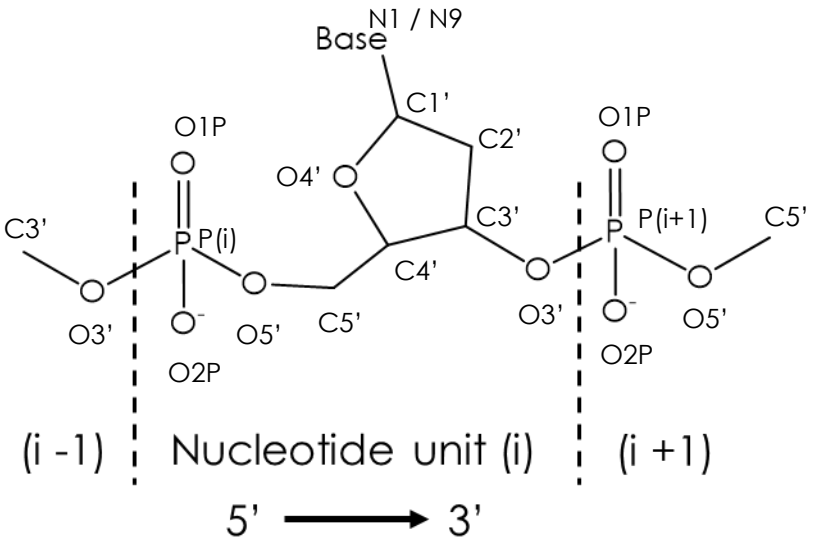

Figure 2.6: Polynucleotide structure with conventional atomic numbering. Each nucleotide unit is composed of a phosphate group and a sugar group connected to a nucleobase (base). The base is attached to the sugar moiety through an N-glycosidic linkage. The conventional 5' to 3' directionality of DNA is shown with the primes on the atomic numbering representing atoms that are components of the DNA backbone, as opposed to components of the base.

The three components of DNA, the nucleobase, ribose sugar and phosphate group, join together to form one monomer and these monomers link together to form polynucleotide strands of DNA (as shown in Figure 2.7). As the nucleotide units of DNA are asymmetrical, DNA strands are directional in nature, and the sequence of bases in DNA is conventionally presented in the 5' to 3' direction, where the prime denotes atoms that are part of the DNA backbone (rather than relating to an atom associated with the base) and the numbers relate to the conventional numbering of the backbone atoms (shown in Figure 2.6).

The most common form in which DNA exists is as a double–stranded helix (shown in Figure 2.7), consisting of two single-strands that have complementary sequences, which coordinate anti-parallel to each other. The helical shape of DNA results from interactions that drive to bury the hydrophobic bases and to expose the hydrophilic DNA backbone (under aqueous conditions). These interactions consist of stacking interactions between neighbouring bases in the same strand of DNA (base-stacking) and H-bonding between the nucleobases on opposite strands (base-pairing). The most stable base pairs are Watson-Crick base pairs, which involve a purine base pairing up with a pyrimidine: A to T and G to C (as shown in Figure 2.7). It should be noted that there are

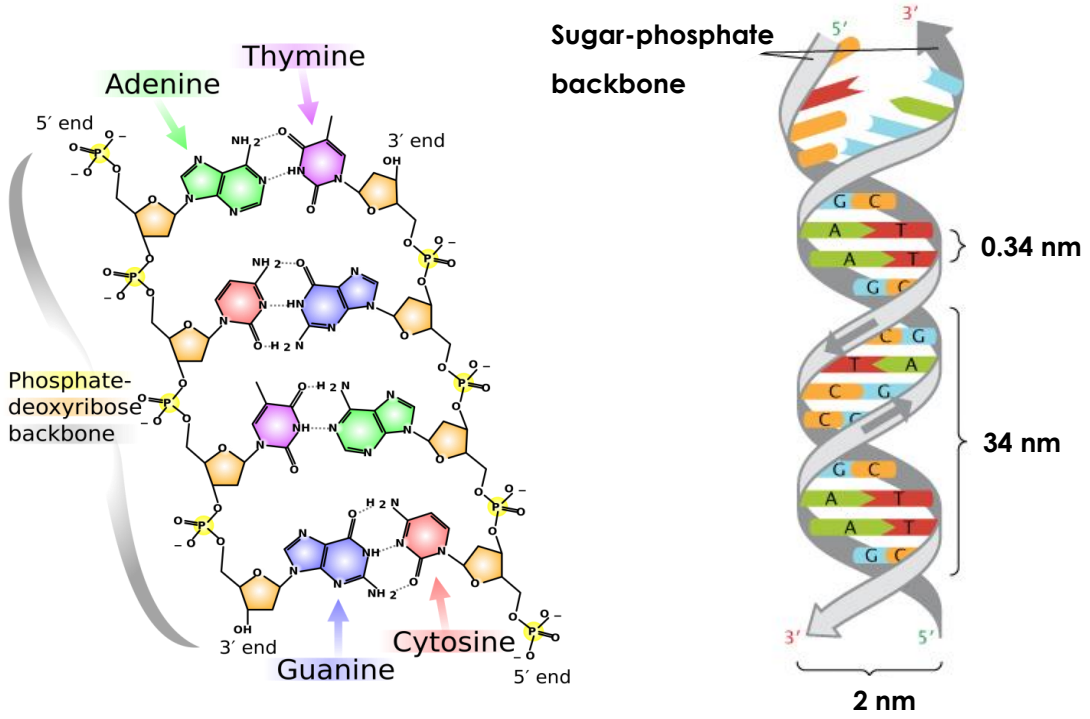

Figure 2.7: (Left) A flattened view of the structure of DNA the four native nucleobases of DNA as well as the structure of the DNA molecule including the sugar-phosphate backbone. Watson-Crick base pairing between A and T and between G and C is shown with hydrogen bonding (H-bonding) shown as dotted lines.) (Right) Cartoon of the double-stranded DNA helix structure showing dimensions of DNA.

3 hydrogen bonds between base pairs of C and G and thus these base-pairs are stronger than those composed of A and T (which only have 2). There are other types of base pairs that occur, such as Hoogsteen base pairs (possessing different geometry that allows the formation of a triple-helix) or wobble base pairs (which are found in RNA), but base pairs other than Watson-Crick base pairs are not important in the context of this thesis and will not be discussed further.

In the DNA double strand, base pairs typically align perpendicular to the phosphate-sugar backbone, with adjacent bases separated by 0.34 nm along the DNA strand. The DNA helix completes a full turn every 10 bases (3.4 nm) and therefore every base pair is rotated 36° relative to the neighbouring base pair. The DNA helix is 2 nm in diameter and can be up to centimetres in length depending on the organism from which it originates. The dimensions associated with DNA are illustrated in Figure 2.7.

The DNA helix can exist in many different conformations depending on a range of conditions, such as the hydration level, base sequence, the level of supercoiling present or presence of metal ions, to name a few. The different conformations of the DNA double helix can be characterised by the number of bases per turn of the helix. Thus far, B form DNA has been described (10 bases per turn) and best describes the conformation of DNA found in most living cells. Alternatively, A form DNA has 11 bases per turn and Z form contains 12. While the spiral of the helix in A and B forms of DNA is to the right, Z form DNA spirals to the left and is thought to be a key feature in the recognition of heavily methylated DNA by certain proteins. The crystal structures of A, B and Z forms of DNA are shown in Figure 2.8. It should be noted that the discussion presented in this thesis relates to B form DNA, unless explicitly stated otherwise.

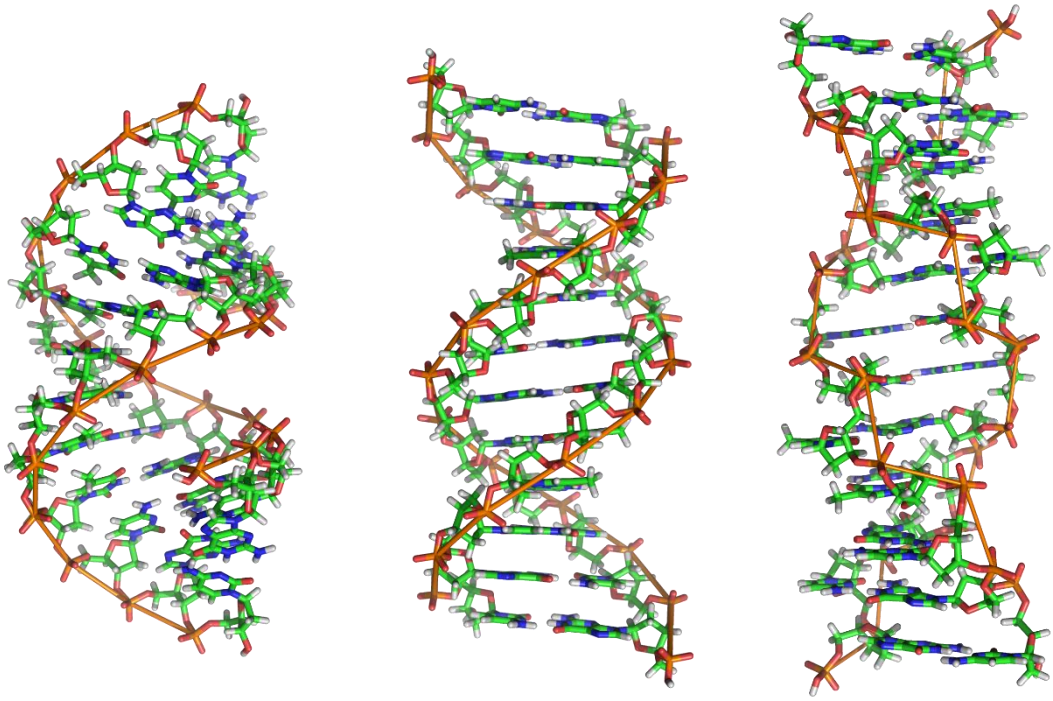

Figure 2.8: A, B and Z forms of the DNA double helix (left to right respectively) Reproduced from http://en.wikipedia.org/ and originally uploaded by Richard Wheeler.

The popular image of the double helix structure of DNA has resulted in the misconception that DNA structure is rigid and fixed. However, DNA is a dynamic molecule and undergoes a variety of structural fluctuations away from the average structure represented in Figure 2.8. The structure of the sugar-phosphate backbone in DNA is constant throughout the molecule and is independent of the DNA base sequence. This means that the DNA base sequence is the controlling factor that is responsible for determining the 3D structure and biochemical properties of DNA. The breaking and

reforming of base pairs in the DNA helix is part of the normal functionality of DNA and is one of many thermal fluctuations that occur. The rate at which this occurs can be strongly dependent on factors such as the solvent conditions and the type of bases involved in the base pair. Relative to a neighbouring base in the same strand, a base can undergo six motions: slide, twist, roll, shift, rise and tilt. These parameters are used to describe the base-step in DNA and are illustrated in Figure 2.9.[8]

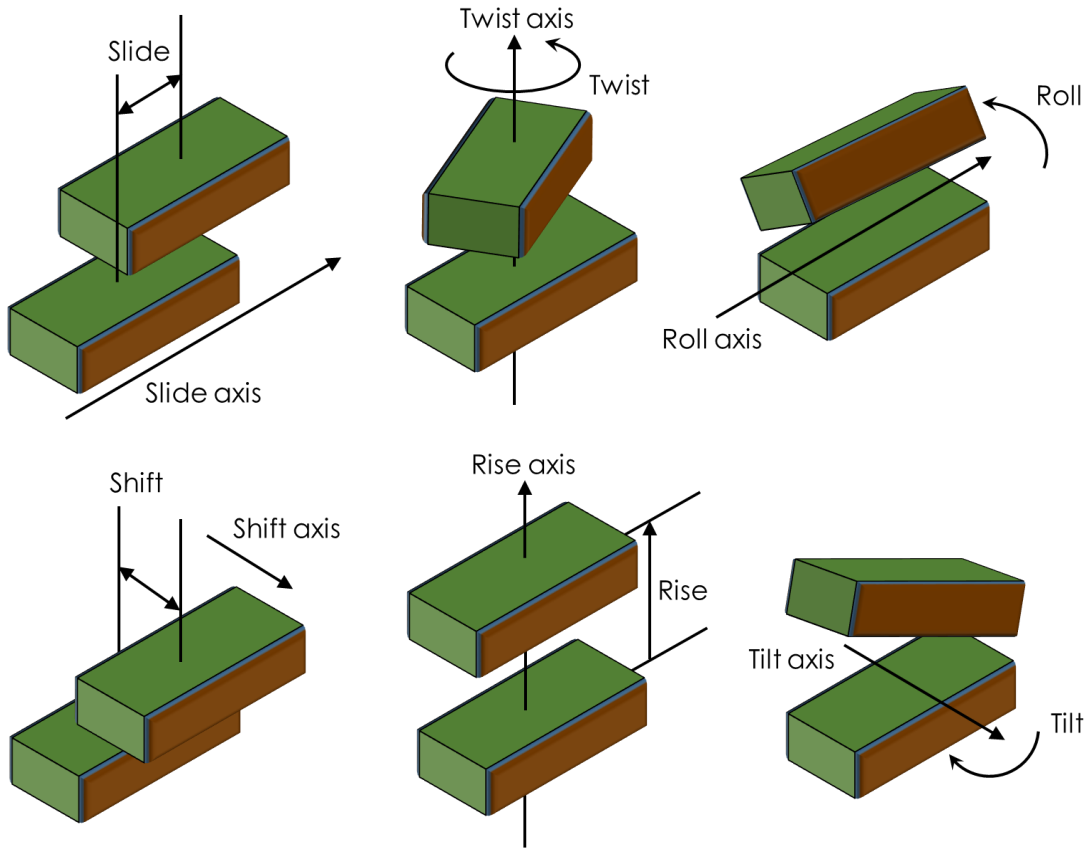

Figure 2.9: Relative motions (slide, twist, roll, shift, rise and tilt) (left to right, top to bottom respectively)) occurring between neighbouring bases in DNA.

Slide and roll are the translation or rotation, respectively, of neighbouring bases along the long axis in the plane of the base, while twist and rise describes the rotation or translation, respectively, of any two bases around an axis perpendicular to the plane of the bases. Shift and tilt describe the translation or rotation of neighbouring bases about the short axis in the plane of the bases. Typically, the motions of bases, relative to a neighbouring base, are described through a combination of these parameters.

In DNA, stacking interactions occur between neighbouring bases in the same strand. These are non-covalent, π-stacking interactions arising mainly from van der

Waals and electrostatic energies.[8] The van der Waals energy is composed of dispersion and repulsion energies. The dispersion energy is an induced dipole-induced dipole interaction, relating to the intermolecular surface contacting area, and is a relatively large attractive force that is insensitive to the precise geometry of the stacking interaction. The repulsion energy is minimal but becomes significant when the atoms are forced closer than their van der Waals contact distance, applying a restriction on the volume occupied by the bases. The non-uniform distribution of electron density across the aromatic bases defines the electrostatic energy. For this reason, the absence or presence of functional groups at different positions on the cyclic structure of DNA bases has a substantial effect on the properties of the base. While the σ-framework of the aromatic base will mostly have a positive character, this will be sandwiched between two out-of-plane π-electron densities that also contributes to the electrostatic energy. Compared to the van der Waals energy, the electrostatic energy is generally weak but is more sensitive to the specific geometry of the stacking interaction and thus are important in determining the conformational preferences of the bases.

In the context of the work presented in this thesis, the non-native DNA bases 2-aminopurine (2AP) and inosine (I) are also of great interest. 2AP is a fluorescent analogue of adenine and will be discussed in detail in Section 2.2.2, while inosine is an

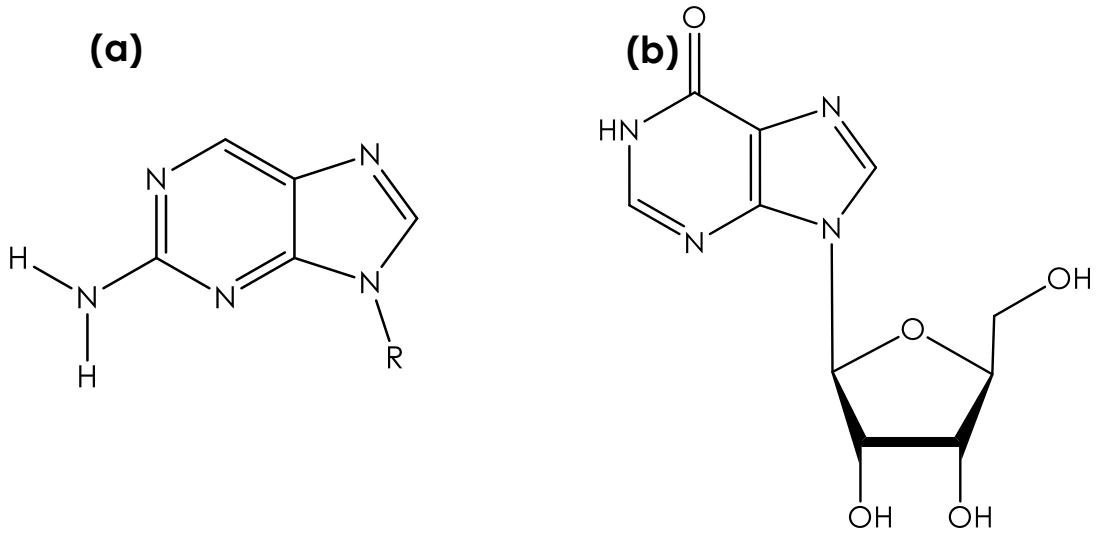

Figure 2.10: Structures of (a) 2-aminopurine, 2AP, and (b) the nucleoside inosine, I, which consists of hypoxanthine attached to a ribose molecule via a N-glycosidic bond

analogue of the native DNA base guanine and is most commonly found in RNA.[9] Inosine is a nucleoside composed of a hypoxanthine molecule attached to a ribosyl group via an

N-glycosidic bond. The structure of 2AP and inosine are shown in Figure 2.10 and the properties of I, relative to that of the native DNA bases and to 2AP, will be discussed in detail in Chapter 4.

Within this thesis, the shorthand notation for the nucleobases (i.e. A, C, G, T, I or 2AP) will also be used to represent the nucleoside or nucleotide structures at times. For clarification, and to dispel any confusion between similarly named molecules, Table 2.1 presents the possible meaning for the shorthand used. It is worth noting that the non-native base hypoxanthine is commonly described using the symbol I, due to the name of its nucleoside, inosine (Figure 2.10).

Code	Nucleobase	Nucleoside	Nucleotide	
A	Adenine	Adenosine	Adenosine monophosphate	Adenosine triphosphate
C	Cytosine	Cytidine	Cytidine monophosphate	Cytidine triphosphate
G	Guanine	Guanosine	Guanosine monophosphate	Guanosine triphosphate
T	Thymine	Thymidine	Thymidine monophosphate	Thymidine triphosphate
I	Hypoxanthine	Inosine	Inosine monophosphate	Inosine triphosphate
2AP	2-aminopurine	2-aminopurine nucleoside	2-aminopurine nucleoside monophosphate	2-aminopurine nucleoside triphosphate

Table 2.1: Terminology associated with the structural components of nucleic acid constituents. Adenine, cytosine, guanine and thymine are the four main bases that are native to DNA while hypoxanthine and 2-aminopurine are relevant in the context of this thesis but are non-native bases in the case of DNA.

For further clarification, the structural difference between nucleobases, nucleosides and nucleotides are shown in Figure 2.11 (using adenine as an example). For discussions involving nucleotides, the prefix “deoxy” or “ribo” will be shortened to d or r, respectively and, in most cases, “monophosphate” and “triphosphate” are shortened to MP or TP, respectively (e.g. ribo-adenosine monophosphate is shortened to “rAMP”).

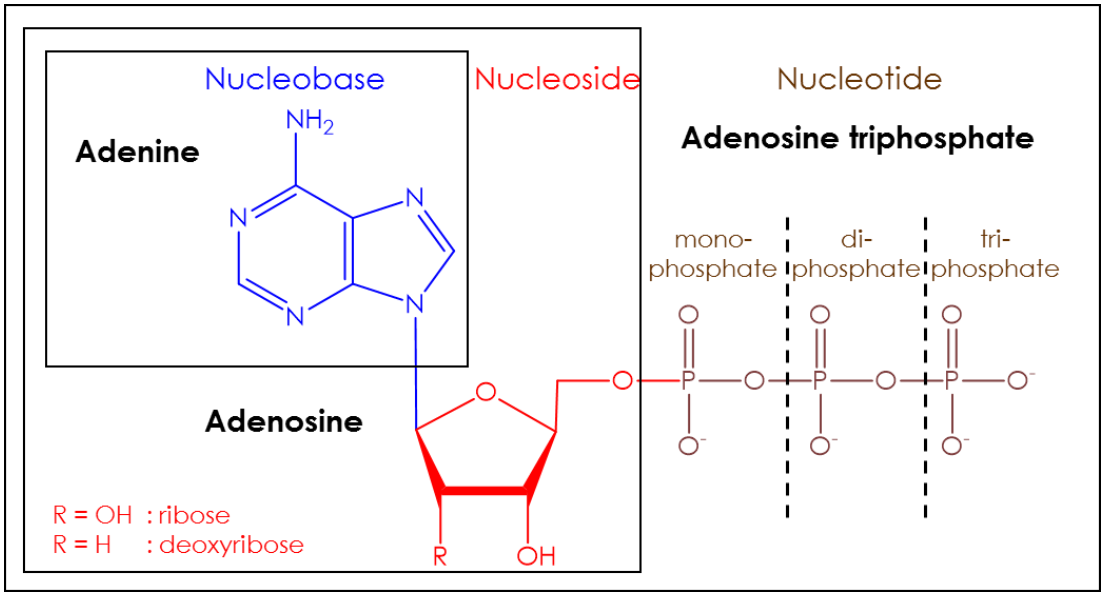

Figure 2.11: Structural components of nucleic acid constituents, with adenine used as an example. Distinct structural sections are represented by colour: blue for the nucleobase, blue and red for the nucleotide, and red, blue and brown for the nucleotide. Labels in black relate to the specific molecule shown in each boxed area.

2.2.2. 2-Aminopurine as a Fluorescent Probe of DNA

Due to the presence of processes that facilitate ultrafast non-radiative decay from the excited state, the native bases of DNA are essentially non-fluorescent, having fluorescence quantum yields on the order of 10^{-4}.[10] A discussion of the ultrafast decay processes of native DNA bases can be found in the Introduction to Chapter 5. Although a number of studies have been performed using the intrinsic fluorescence of DNA bases to study DNA systems using more advanced fluorescence techniques (e.g. ultrafast fluorescence upconversion),[11–15] their extremely low quantum yield makes this a near-impossible task using conventional fluorescence techniques (such as steady-state fluorescence spectroscopy or TCSPC). Furthermore, the significantly overlapping excitation and emisson bands of the native DNA bases,[11,16] makes a clear identification of the excited or emitting species unachievable, especially in DNA molecules with very long sequences.

In order for DNA dynamics and structure to be effectively studied using conventional fluorescence techniques, one must use a fluorescent probe. This section will provide a brief description of fluorescent probes of DNA before presenting a discussion of the most extensively used fluorescent nucleic acid base analogue, 2-

aminopurine (2AP). A more comprehensive discussion of fluorescent nucleic acid base analogues can be found in the review article by Wilhelmsson.[17]

Fluorescent probes are typically characterised as internal or external modifiers depending on the way the fluorescent probe binds to DNA. Probes covalently bound to DNA, replacing a base within the base stack are referred to as internal modifiers, while those that attach (covalently or non-covalently) outside of the DNA base stack are known as external modifiers. To date, a range of external modifiers is commercially available and these are currently the most common way of labelling DNA for study. Examples of the most popular probes are fluorescein, rhodamine derivatives, Alexa dyes and Cy dyes (the details and specifications of which can be found by referring to commercial sources). These probes typically have very high quantum yields and high photostability, but due to the typical method in which these molecules bind to DNA, through covalently bonding with the DNA backbone or through a long linker-molecule, the probe is usually located far from the site of interest. This in turn limits the sensitivity of these external probes to any changes in the regions under study (typically within the DNA base stack). Alternatively, some external probes can non-covalently bind with DNA via intercalation, in which the fluorophore inserts between the planar DNA bases in the DNA helix.

Of more use in the study of DNA are internal modifiers, with the major member of this family of fluorescent probes being fluorescent nucleic acid base analogues. These molecules are typically planar aromatic compounds that closely resemble the native DNA bases but possess minor differences in the covalent structure or composition of the molecule such that the electronic properties of the base have been altered to give much higher fluorescence quantum yields. Unfortunately, these bases are normally significantly different in size or shape from the native bases of DNA and may be unable to H-bond with the base on the opposite strand. Consequently, their incorporation can perturb the local structure of DNA, causing the system of interest to be no longer representative of the unlabelled DNA.

However, the highly fluorescent base analogue 2AP does not suffer from this problem of majorly perturbing DNA, since it closely resembles the shape and size of adenine and can base pair with thymine (and cytosine). The ability of 2AP to be incorporated into a DNA duplex with minimal perturbation of the structure is enabled by its ability to mimic the base-pairing interactions of the native bases. In a similar way to adenine, 2AP is capable forming a Watson-Crick base pair with thymine in the duplex, as shown in Figure 2.12.

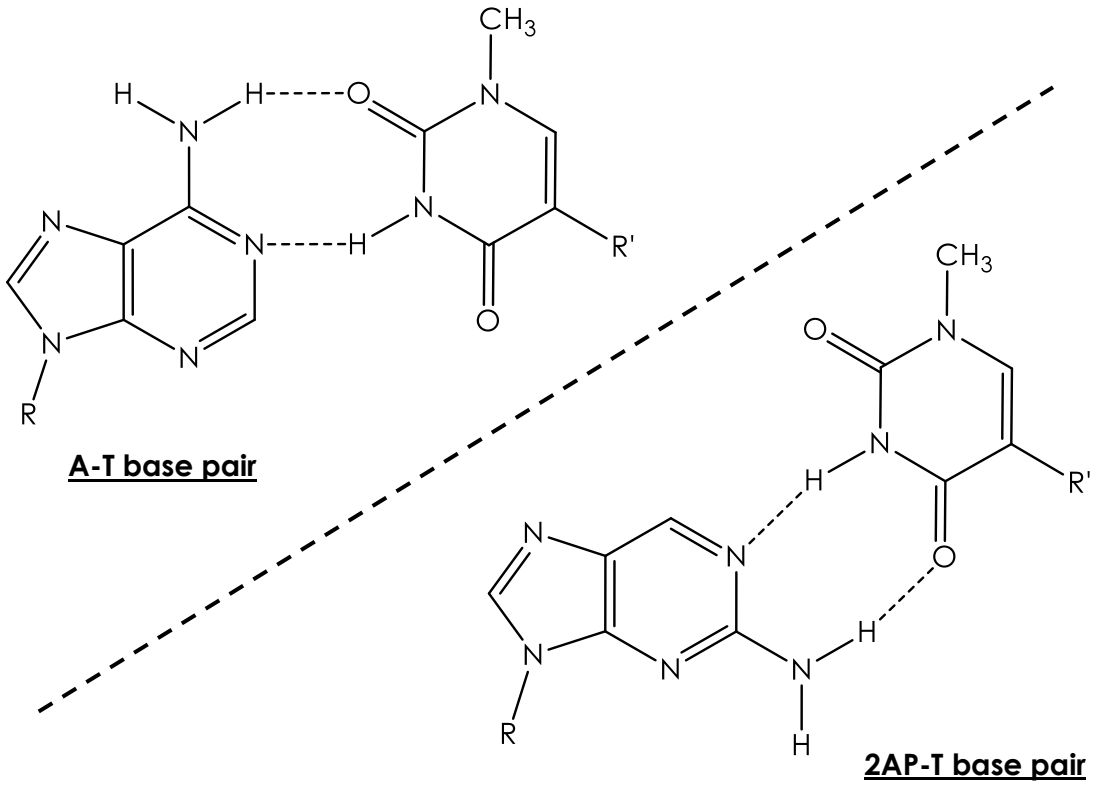

Figure 2.12: Comparison of the Watson-Crick base-pairing interactions of 2AP and thymine (right) compared to that of adenine and thymine (left). Dotted lines between atoms represent hydrogen bonding while R and R' denote the positions that the bases join to their respective DNA backbones.

2AP is also capable of forming a wobble base pair with cytosine (not shown) and is often also considered an analogue of guanine, instead of adenine, for this reason (and due to its closer structural resemblance to guanine).

An in-depth review of 2AP and 2AP photophysics has recently been published by Jones and Neely,[18] providing an extensive view of the suitability of 2AP in the study of DNA systems. However, a summary of the pertinent fluorescence properties of 2AP will be presented here.

It was almost 50 years ago that Ward et al.[19] discovered the fluorescence properties of 2-aminopurine (2AP) and, to date, it is one of the most well-known and commonly used fluorescent base analogues. 2AP is a fluorescent analogue of the native

DNA base adenine (6-aminopurine), with a quantum yield of 0.68. The structure of 2AP is shown in Figure 2.13.

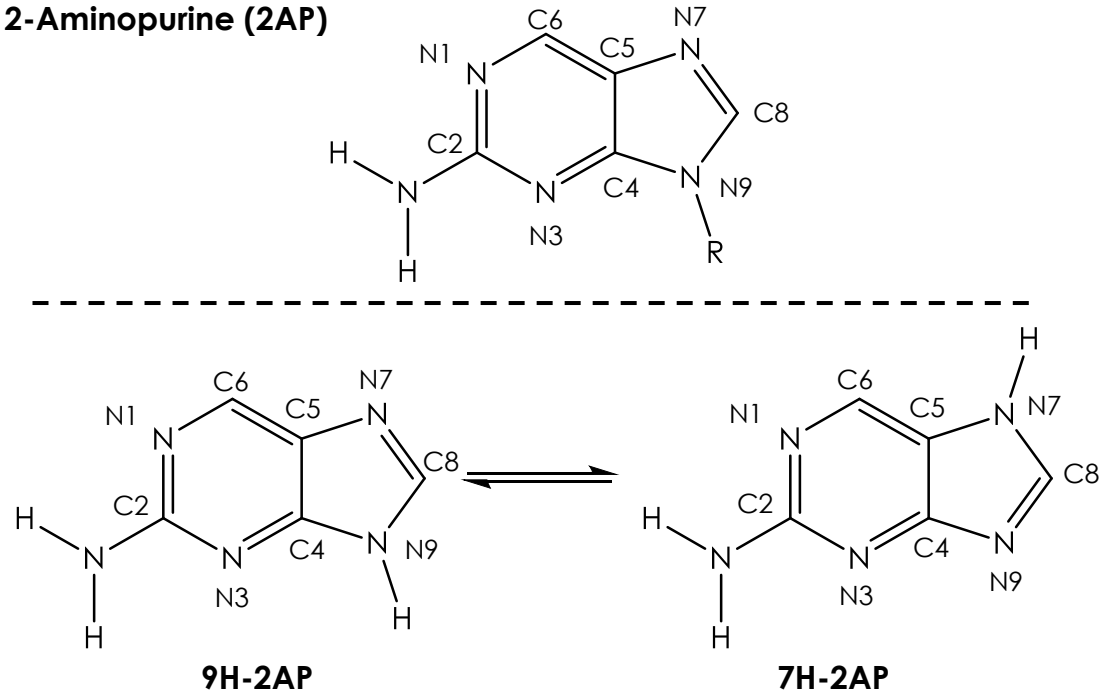

Figure 2.13: Molecular structure of 2-aminopurine (top) and the 9H- and 7H- tautomers of 2AP (bottom), showing the conventional numbering of atoms in the aromatic structure. R denotes the position that 2AP links to the C1' position on the ribose group of the DNA backbone. Alternatively, for the free base, R = H or for 2AP-riboside (2APr), R = ribosyl group.

When free in solution, 2AP exists as a mixture of two tautomers (as shown in Figure 2.13). [20,21] However, when incorporated into DNA, formation of the 7H-tautomer is inhibited due to the presence of the ribose group of the DNA backbone at position N9. Formation of the 7H-tautomer can also be hindered through the presence of a ribosyl group at position N9, to produce 2AP-riboside (2APr), which will be discussed below.

The fluorescence decay of the 2AP base free in aqueous solution is typically reported as mono-exponential (with a lifetime, τ, of ~11.5 ns), which is orders of magnitude greater than the sub-ps fluorescence lifetimes of the natural bases.[10] However due to the presence of two tautomeric forms of 2AP (9H- and 7H-), the fluorescence decay of the 2AP base in aqueous solution is actually bi-exponential with a slightly different lifetime associated with each tautomer (~11 ns and ~13.5 ns, respectively).[21–23] For simplicity, the averaged mono-exponential lifetime of free 2AP in aqueous solution will be used in discussions of 2AP unless otherwise explicitly stated.

The fluorescence decay of 2APr, is, in fact, mono-exponential (τ = ~10.5 ns), due the presence of the ribosyl group at position N9 (in place of the hydrogen atom) that prevents tautomerism. Reichardt *et al.*[24] studied 2AP-deoxyriboside (2APdr) in a variety of solvents via steady-state absorption and emission spectroscopy and using broadband transient absorption (TA) spectroscopy. TA is a pump-probe technique that allows changes in the absorption profile during relaxation after pulsed excitation to be followed. In doing so, dark (non-emissive) states can be identified and directly measured. They were able to use global analysis, using a broadband detection that allowed simultaneous measurement of the full spectral response (rather than the less robust single-wavelength analysis). However, signals recorded via TA measurements are known to be complex and can consist of contributions from multiple sources such as ground-state bleaching (GSB), excited-state absorption (ESA), stimulated emission and absorption from potential photoproducts.[25] Contributions from such a diverse range of processes causes data interpretation to be ambiguous and permits different models to fit the data with similar quality of fit. In some cases the fate of the excited state can only be fully determined by coupling TA measurements with ultrafast fluorescence measurements (upconversion or downconversion), as TA does not necessarily report on the initially populated emitting states (especially if decay rapidly occurs to dark states). Work performed by Reichardt et al. on excited-state decay of 2AP-deoxyriboside (2AP-dr) provides the current interpretation of solvent effects on 2AP photophysics. It was found that up to 40% of the initially populated 2AP-dr* decays through a triplet state ($3\pi\pi^*$) that is formed via internal conversion (IC) to the $1n\pi^*$ state followed by intersystem crossing ($3\pi\pi^* \leftarrow 1n\pi^* \leftarrow 1\pi\pi^*$). The triplet yield was found to be sensitive to the H-bonding ability and polarity of the solvent, with a value of 0.4 in acetonitrile, decreasing to 0.2 in ethanol and 0.08 in aqueous buffer. This correlates with the increasing trend in fluorescence quantum yield: 0.26 in acetonitrile, 0.47 in ethanol and 0.68 in aqueous buffer. It was also inferred from the fluorescence and triplet quantum yields that there is a second solvent-independent non-radiative channel, with a yield of about 0.3, which is most likely internal conversion from the $1\pi\pi^*$ state to the ground state.

The fluorescence character of 2AP sets it apart from the non-fluorescent native DNA bases. The characteristic fluorescence of free 2AP in aqueous solution is a fluorescence emission band of 360-410 nm, with an emission maximum at ~370 nm, and an excitation band at 300-320 nm, with a maximum at ~303 nm. Importantly, the excitation band of 2AP lies to the red of the absorption band of the native DNA bases

(~260 nm), enabling 2AP to be excited selectively when in the presence of native DNA bases.

Solvent polarity has a large effect on the fluorescence quantum yield of 2AP, which significantly decreases with decreasing polarity, alongside a shift in the emission spectra to shorter wavelengths.[19,26,27] The mechanism of this effect has been discussed above.

The crucial role played by solvation in the fluorescence character of 2AP became evident only recently when gas-phase 2AP was found to have a very short fluorescence lifetime (156 ps) and to be essentially non-fluorescent.[28] Through selective microhydration of 2AP at specific sites on the molecule (in gas-phase molecular beam experiments), it has been shown that 2AP fluorescence can be effectively switched on by the presence of H_2O molecules at specific H bonding sites. Despite these findings, a full understanding of the photophysical properties of 2AP has still not been achieved.

An important aspect of 2AP fluorescence is the way in which it is heavily quenched (up to ~ 100-fold decrease in quantum yield) by interaction with the native DNA bases when incorporated into the DNA duplex. This has led to 2AP being widely used as a pseudo-intrinsic and highly responsive fluorescent probe of DNA systems.[18,23,27,29–37]

Upon incorporation of a 2AP base into the DNA sequence, the fluorescence decay of 2AP is not only greatly shortened, but becomes complex (multi-exponential). This complex decay behaviour is indicative of a heterogeneous environment experienced by 2AP in DNA, despite the apparent homogeneity of the systems under study (solutions of identical oligonucleotides with a single 2AP in the identical sequence context). The complex decay of 2AP in DNA reflects the conformational heterogeneity of DNA that results from thermal motion of the bases (DNA breathing).[38] As a result, the population of excited state 2AP is divided into a range of distinct sets of conformational environments that differ in the efficiency of interbase quenching interactions, resulting in a number of different fluorescence lifetimes.

A comparison of the typical decay parameters obtained for 2AP in variety of nucleic acid systems is shown in Table 2.2, including 2AP-containing dinucleotides (composed of two nucleobases (one of which is 2AP) linked through a sugar-phosphate backbone). Dinucleotides are a recurring “simple” DNA system used throughout this work and a full introduction to them is given in Chapter 4.

2AP System	Lifetime /ns				Fractional Population			
	τ_1	τ_2	τ_3	τ_4	A_1	A_2	A_3	A_4
Aqueous solution	-	-	-	11.5	-	-	-	1.00
Dinucleotide	<0.1	0.2 - 0.6	2.0 - 4.0	7.0 - 9.0	0.40	0.15	0.40	0.05
ss-DNA					0.50	0.20	0.15	0.15
ds-DNA					0.80	0.10	0.05	0.05

Table 2.2: Comparison of typical fluorescence lifetimes (τ_i) and related fractional populations (A_i) obtained for 2AP in aqueous solution and as part of the DNA sequence in a dinucleotide, single-stranded DNA (ss-DNA) and double-stranded DNA (ds-DNA) using TCSPC. The values shown in this table are compiled from the work of Neely *et al.*,[20,21,39,40] **Somsen *et al.*,**[37] **and Wu.**[41]

Neglecting the effect of tautomerism, free 2AP in aqueous solution has a fluorescence lifetime of ~11.5 ns. However, due to interbase quenching interactions, when 2AP is present in DNA, the fluorescence decay of 2AP becomes complex and typically four lifetimes are required to provide an adequate description. The commonly accepted interpretation of the complex decay behaviour of excited state 2AP is that each lifetime relates to a distinct set of conformational states, which have a different set of intermolecular interactions associated with each of them. Despite the difference in the complexity of the 2AP-DNA systems presented in Table 2.2, the lifetime values show little variation between these systems, while the relative populations differ significantly depending on the system. The shortest lifetime component, τ_1, is commonly found to be less than 100 ps and is attributed to highly stacked conformations, in which excited state 2AP is rapidly quenched by interbase interactions, typically through processes such as charge transfer from nearby G bases.[18,35,42–44] In single-stranded (ss) and double-stranded (ds) oligonucleotides this is typically found to be the dominant component. The longest lifetime component, τ_4, typically around 9 ns, is thought to be due to extra-helical 2AP, which is completely unstacked from neighbouring bases in the DNA sequence. In this conformation, 2AP is isolated from other DNA bases, experiencing only a solvated environment and minimal interbase quenching interactions. The lifetime value of this decay component is comparable with that of free 2APr in solution. Typically, under normal conditions, the population of this conformation is minor and generally accounts for $\lesssim$5% of the emitting population. However, in some scenarios, such as in the presence of certain enzymes or in certain solvents, the DNA structure is distorted such that a base can become extrahelical or heavily exposed to solvent molecules, resulting in a higher population of τ_4. Due to the difference in magnitude between the lifetime values of τ_1 and

τ_4, even a small shift in population between these conformations has a significant effect on the fluorescence quantum yield. Often, this is used as a clear identifier of the presence of base-flipping mechanisms in DNA-enzyme complexes.[33,34,39,40,45–47] The intermediate lifetimes, τ_2 and τ_3, ~0.3 ns and ~3 ns, respectively, are more difficult to attribute to a specific conformational state. These lifetimes are more commonly thought of as relating to ranges of states in which 2AP is still partially stacked within the hydrophobic intra-helical environment experienced by the DNA bases but is no longer subject to the fast decay processes (such as charge transfer) responsible for τ_1. Figure 2.14 illustrates a simplified representation of potential geometries of 2AP and a DNA base that results in the complex decay of 2AP in DNA. It must be emphasised however that the conformations shown in Figure 2.14 are only a very simplified representation and are not representative of the conformation flexibility of bases in DNA revealed by computational studies.[48]

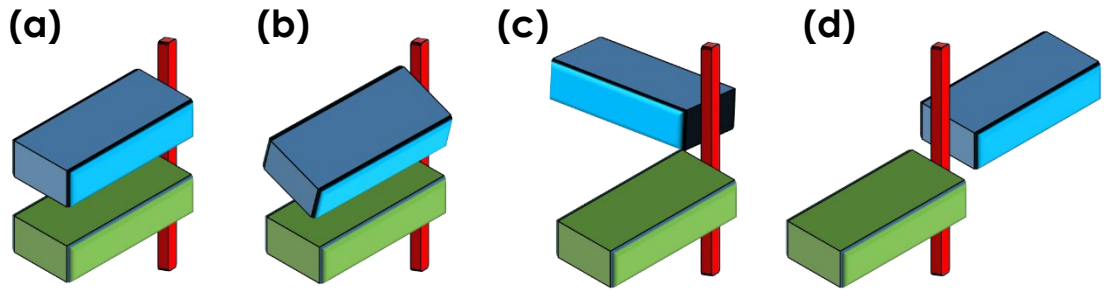

Figure 2.14: Simplified schematic of the varying degrees of base stacking interactions experienced between adjacent bases from highly stacked (a) (relating to τ_1), through imperfectly stacked (b) and (c) (relating to τ_2 and τ_3), to completely unstacked (extra-helical) (d) (relating to τ_4). The DNA backbone is represented in red, while 2AP in blue and the partner base in green. For simplicity, the twisted orientation of adjacent bases in the DNA helix has been omitted.

In an attempt to understand the excited-state properties of 2AP that are behind the spectral features of 2AP in DNA, Jean and Hall[30,49] performed computational studies of gas-phase 2AP-containing dimers (and trimers), in which 2AP is stacked with neighbouring bases in a B-form structure but without being covalently linked through a sugar-phosphate backbone. These studies used time-dependent density functional theory (TDDFT) and identified two or three charge-transfer states (lower-energy excited states) for the DNA trimers that could be accessed by internal conversion that could be responsible for, or aid in, non-radiative transitions from the excited state of 2AP. It was shown that in these systems, 2AP demonstrates a diminished radiative rate, caused by a

reduction in the oscillator strength of the low-lying π-π* 2AP-like allowed transitions. However, it is now known that TDDFT methods are incapable of accurately computing charge-transfer states. Later, studies using configuration interaction singles (CIS) predicted that these charge transfer states are actually higher in energy than the locally excited 2AP ππ* state.[36,50] More recently, computational studies performed (using CIS with second-order perturbation theory) by Liang *et al.*[51] and Liang and Matsika,[23] on 2AP-purine dimers and 2AP-pyrimidine dimers, respectively, provided a much clearer insight into the fate of the excited state population following absorption. By examining relaxation along the S_1 surface, following calculation of the excited state for a typical B form DNA conformation, different quenching paths were identified, which were dependent on whether 2AP was located on the 5' or 3' position, and on the identity of the partner base. While some pathways involved charge transfer, other pathways involving dark states localized on 2AP or involving conical intersection were also identified. These studies highlighted that, even in the simplified model used (DNA dimers where no DNA backbone is present), the findings are far from simple, and different initially excited conformations could lead to alternative quenching mechanisms that may or may not involve charge transfer. The pathways not involving charge transfer were identified as being favoured by interbase H-bonding interactions involving the NH_2 group of 2AP, which stabilise the nπ* state. However, under experimental conditions where the DNA backbone and solvent molecules are present, the scenario will become even more complex. In order to provide a complete picture explaining the photophysical mechanisms of interbase quenching of 2AP in DNA, further development of computational methods that can simultaneously account for the complex influence of solvation and conformational dynamics, in both ground state and excited states, are required. As of yet this has not been achieved.

2.2.3. Electron Transfer in DNA

The ability of DNA to transport charge over long distances (>20 Å) through the π-stacking interactions is a controversial matter. However, the transport of a charged species over relatively short distances (<20 Å) has been established as an important process in DNA duplexes. Unlike energy transfer, charge transfer is the migration of a mass with charge (such as an electron) from one species to another, rather than the migration of an excited state. The complete theory underlying electron transfer is beyond the scope of this thesis. However, in light of the role of interbase electron transfer in quenching of 2AP fluorescence and the consequent use of 2AP in the investigations of

charge transfer in the DNA duplex, a brief overview of the principles of electron transfer (eT) will be covered here in the context of the DNA duplex.[52]

Figure 2.15 shows a schematic representation of the energetic steps required for electron transfer to occur in the DNA duplex, in which the donor (D) and acceptor (A) bases are separated by one or more "bridging" bases that must undergo reduction for electron transfer to occur efficiently.[52]

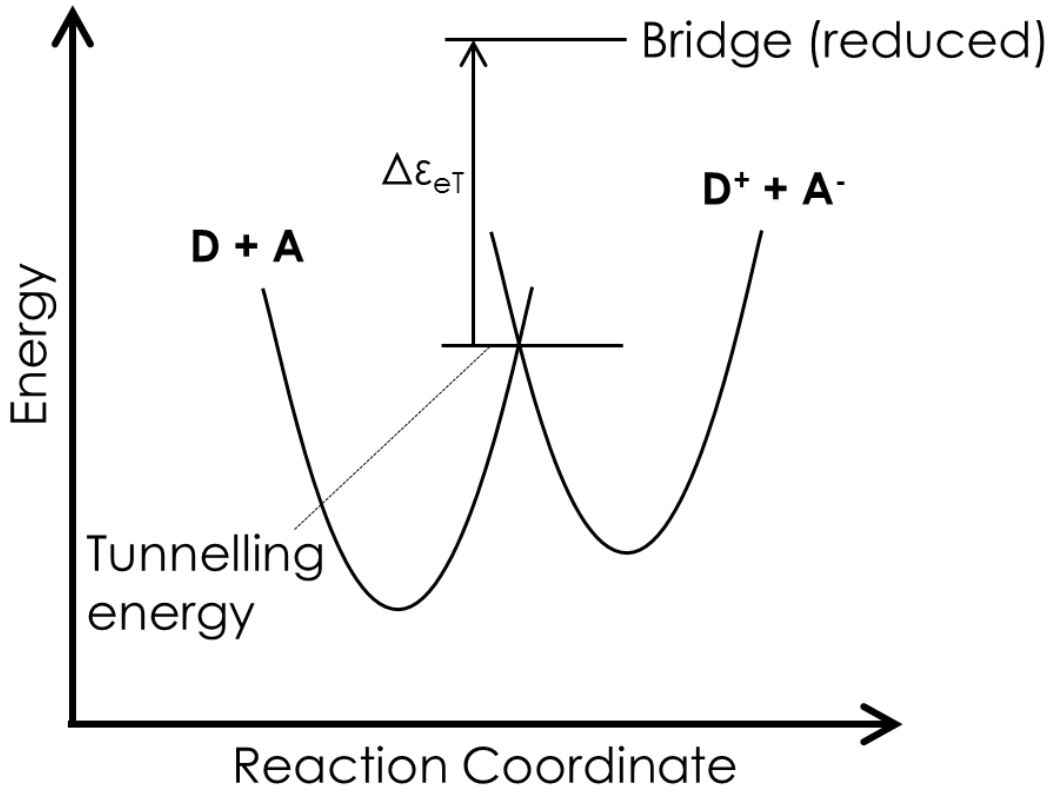

Figure 2.15: Schematic representation of the energetic levels involved in electron transfer (eT) between a donor (D) and acceptor (A), via a bridging molecule that undergoes reduction during the electron transfer process. Figure reproduced from the review on electron transfer in DNA by Treadway *et al.*[52].

The rate of electron transfer between D and A molecules along the duplex, k_{eT} is defined as

$$\mathrm{k}_{eT} = \nu\kappa_E\kappa_N \qquad \textbf{2.20}$$

Where ν is the frequency of the nuclear motion along the transition state, κ_E is the probability of the reactants crossing the transition state to the products and κ_N is the nuclear reorganisation factor, which is defined as shown in Equation 2.21

$$\kappa_N = e^{-\left(\frac{(\Delta G^\circ + \lambda)^2}{4\lambda k_B T}\right)} \quad \textbf{2.21}$$

where ΔG° is the thermodynamic free energy of the system, λ is a parameter used to describe the extent of the nuclear motion required to reach the transition state, k_B is the Boltzmann constant and T is the temperature. In the DNA duplex, where the interaction between the donor and acceptor molecules is weak, k_{eT} is determined by the rate of surface crossing at the transition state. The rate of electron transfer under these conditions, k°_{eT}, is given as

$$\mathrm{k}^\circ_{eT} = \sqrt{\frac{4\pi^3}{h^2 \lambda k_B T}} H_{AB}^2 \quad \textbf{2.22}$$

where H_{AB} describes the matrix element that defines the interaction between the reactants (D + A) and products (D^+ + A^-) at the transition state. For the case shown in Figure 2.15, where n bridging bases are involved in the transfer, H_{AB} is described by Equation 2.23

$$H_{AB} = \frac{h_{Db} h_{bA}}{\Delta \varepsilon_{eT}} \left(\frac{h_b}{\Delta \varepsilon_{eT}}\right)^{n-1} \quad \textbf{2.23}$$

where h_{Db} and h_{bA} are descriptions of the coupling between the donor and bridge and bridge and acceptor, respectively. In cases where more than one bridging base is present between the donor and acceptor molecules, the coupling between adjacent bases is described by h_b. The energy difference between the reduced state of the bridging base and the transition state between donor and acceptor bases, $\Delta \varepsilon_{eT}$, is defined in Figure 2.15.

Further discussion of charge transfer in DNA, in the context of the mechanism of interbase quenching of 2AP fluorescence, will be presented in Chapter 4.

2.3. References

1 J. M. Hollas, *Modern spectroscopy*, John Wiley & Sons, Fourth Edi., 2004.

2 P. Atkin and J. Paula, *Physical chemistry*, New York, 8th Edi., 2006.

3 N. J. Turro, *Modern molecular photochemistry*, University Science Books, 1991.

4 A. Gilbert and J. Baggott, *Essentials of Molecular Photochemistry*, Blackwell Science, 1991.

5 J. R. Lakowicz, *Principles of Fluorescence Spectroscopy*, Springer US, Boston, MA, 3rd Edi., 2006, vol. 3.

6 D. V. O'Connor and D. Phillips, *Time-Correlated Single Photon Counting*, Academic Press, 1984.

7 W. Becker, *Advanced Time-Correlated Single Photon Counting Techniques*, Springer Berlin Heidelberg, Berlin, Heidelberg, 2005, vol. 81.

8 C. A. Hunter, *BioEssays*, 1996, **18**, 157–162.

9 I. Alseth, B. Dalhus and M. Bjørås, *Curr. Opin. Genet. Dev.*, 2014, **26**, 116–123.

10 J. Peon and A. H. Zewail, *Chem. Phys. Lett.*, 2001, **348**, 255–262.

11 M. Barbatti, *Photoinduced Phenomena in Nucleic Acids I*, Springer International Publishing, Cham, 2015, vol. 355.

12 M. Barbatti, *Photoinduced Phenomena in Nucleic Acids II*, Springer International Publishing, Cham, 2015, vol. 356.

13 A. Banyasz, T. Gustavsson, D. Onidas, P. Changenet-Barret, D. Markovitsi and R. Improta, *Chem. - A Eur. J.*, 2013, **19**, 3762–3774.

14 D. Markovitsi, T. Gustavsson and F. Talbot, *Photochem. Photobiol. Sci.*, 2007, **6**, 717–724.

15 I. Vayá, T. Gustavsson, F.-A. Miannay, T. Douki and D. Markovitsi, *J. Am. Chem. Soc.*, 2010, **132**, 1–4.

16 D. E. Metzler, *Biochemistry, Second Edition: The Chemical Reactions of Living Cells*, Academic Press, 1977.

17 L. M. Wilhelmsson, *Q. Rev. Biophys.*, 2010, **43**, 159–183.

18 A. C. Jones and R. K. Neely, *Q. Rev. Biophys.*, 2015, **48**, 244–279.

19 D. C. Ward, E. Reich and L. Stryer, *J. Biol. Chem.*, 1969, **244**, 1228–1237.

20 R. K. Neely, PhD Thesis, University of Edinburgh, 2005.

21 R. K. Neely, S. W. Magennis, D. T. F. Dryden and A. C. Jones, *J. Phys. Chem. B*, 2004, **108**, 17606–17610.

22 R.-X. He, X.-H. Duan and X.-Y. Li, *Phys. Chem. Chem. Phys.*, 2006, **8**, 587–591.

23 J. Liang and S. Matsika, *J. Am. Chem. Soc.*, 2011, **133**, 6799–808.

24 C. Reichardt, C. Wen, R. A. Vogt and C. E. Crespo-Hernández, *Photochem. Photobiol. Sci.*, 2013, **12**, 1341–1350.

25 R. Berera, R. van Grondelle and J. T. M. Kennis, *Photosynth. Res.*, 2009, **101**, 105–118.

26 K. O. Evans, D. Xu, Y. Kim and T. M. Nordlund, *J. Fluoresc.*, 1992, **2**, 209–216.

27 E. L. Rachofsky, R. Osman and J. B. Ross, *Biochemistry*, 2001, **40**, 946–956.

28 S. Lobsiger, S. Blaser, R. K. Sinha, H. Frey and S. Leutwyler, *Nat. Chem.*, 2014, **6**, 989–993.

29 N. P. Johnson, W. A. Baase and P. H. Von Hippel, *Proc. Natl. Acad. Sci. U. S. A.*, 2004, **101**, 3426–3431.

30 J. M. Jean and K. B. Hall, *Proc. Natl. Acad. Sci. U. S. A.*, 2001, **98**, 37–41.

31 S. P. Davis, M. Matsumura, A. Williams and T. M. Nordlund, *J. Fluoresc.*, 2003, **13**, 249–259.

32 Q. Wang, M. Raytchev and T. Fiebig, *Photochem. Photobiol.*, 2007, **83**, 637–641.

33 T. Lenz, E. Y. M. Bonnist, G. Pljevaljcić, R. K. Neely, D. T. F. Dryden, A. J. Scheidig, A. C. Jones and E. Weinhold, *J. Am. Chem. Soc.*, 2007, **129**, 6240–6248.

34 E. Y. M. Bonnist, K. Liebert, D. T. F. Dryden, A. Jeltsch and A. C. Jones, *Biophys. Chem.*, 2012, **160**, 28–34.

35 P. Manoj, C. K. Min, C. T. Aravindakumar and T. Joo, *Chem. Phys.*, 2008, **352**, 333–338.

36 S. J. O. Hardman and K. C. Thompson, *Int. J. Quantum Chem.*, 2007, **107**, 2092–2099.

37 O. J. G. Somsen, A. Van Hoek and H. Van Amerongen, *Chem. Phys. Lett.*, 2005, **402**, 61–65.

38 D. Jose, S. E. Weitzel and P. H. von Hippel, *Proc. Natl. Acad. Sci.*, 2012, **109**, 14428–14433.

39 R. K. Neely, *Nucleic Acids Res.*, 2005, **33**, 6953–6960.

40 R. K. Neely, G. Tamulaitis, K. Chen, M. Kubala, V. Siksnys and A. C. Jones, *Nucleic Acids Res.*, 2009, **37**, 6859–6870.

41 X. Wu, PhD Thesis, University of Edinburgh, 2012.

42 C. Wan, T. Fiebig, O. Schiemann, J. K. Barton and A. H. Zewail, *Proc. Natl. Acad. Sci.*, 2000, **97**, 14052–14055.

43 J. M. Jean and K. B. Hall, *Biochemistry*, 2004, **43**, 10277–10284.

44 M. A. O'Neill and J. K. Barton, *J. Am. Chem. Soc.*, 2004, **126**, 13234–13235.

45 B. Holz, S. Klimasauskas, S. Serva and E. Weinhold, *Nucleic Acids Res.*, 1998, **26**, 1076–1083.

46 E. R. Morris, H. Grey, G. McKenzie, A. C. Jones and J. M. Richardson, *Elife*, 2016, **5**, 1–23.

47 L. Ma, X. Wu, G. G. Wilson, A. C. Jones and D. T. F. Dryden, *Biochem. Biophys. Res. Commun.*, 2014, **449**, 120–125.

48 D. A. Smith, L. F. Holroyd, T. van Mourik and A. C. Jones, *Phys. Chem. Chem. Phys.*, 2016, **18**, 14691–14700.

49 J. M. Jean and K. B. Hall, *Biochemistry*, 2002, **41**, 13152–13161.

50 S. J. O. Hardman and K. C. Thompson, *Biochemistry*, 2006, **45**, 9145–9155.

51 J. Liang, Q. L. Nguyen and S. Matsika, *Photochem. Photobiol. Sci.*, 2013, **12**, 1387–1400.

52 C. R. Treadway, M. G. Hill and J. K. Barton, *Chem. Phys.*, 2002, **281**, 409–428.

Chapter 3: Experimental Methods

In this Chapter can be found the generic descriptions of the methods commonly used throughout the work presented in this thesis, while specific details, including sample preparation, are included in the Materials and Methods sections of each of the chapters that follow.

3.1. UV-vis Absorption Measurements

UV-visible absorption spectra were measured using a Varian Cary 300 UV-Vis spectrophotometer. The spectrophotometer was used in dual-beam mode and samples were contained in a matched pair of fused silica, 1-cm path length cuvettes (Starna Scientific Ltd). All absorption measurements were performed at room temperature and using a baseline/zero correction.

3.2. Steady-state Fluorescence Measurements

Steady-state fluorescence measurements were performed using a Fluoromax 3P Spectrofluorometer (Horiba Jobin Yvon) under the full control of either Datamax spectroscopy software (for initially performed measurements) or FluorEsscence software (following an upgrade of the software).

In the Fluoromax 3P, an ozone-free xenon lamp is used as the excitation source and delivers light in the range of 200 to 700 nm. The Fluoromax is equipped with monochromators in both excitation and emission arms, which employ modified Czerny-Turner mounted gratings (groove density 1200 gr/mm), allowing light to be dispersed from 200 to 900 nm. Adjustments of slit widths in each monochromator allows the intensity and bandpass of the light to be controlled. Throughout this work, the slit widths were optimised for each set of experiments, in order to keep the intensity below the saturation limit of detector for the fluorescence signal (S), but were kept constant within each set of experiments in order to ensure the results were quantitatively comparable. A beam splitter directs a small portion (~5%) of the excitation light to a reference photodiode to monitor the excitation light and record a lamp reference signal (R). To correct S for wavelength-dependence and temporal fluctuations of the lamp intensity, the ratio S/R is used. The reported spectra in this work are the corrected spectra (S/R).

Samples were held in a fused-silica cuvette (with 10 mm path length), which was optically transparent between 170 nm and 2700 nm. Fluorescence emission from the sample is collected orthogonal to the excitation beam and dispersed via the emission monochromator. Signal detection is by a red-sensitive, photon-counting photomultiplier tube (PMT) allowing detection of wavelengths up to 850 nm. The saturation limit of the PMT was 4 x10^6 counts per second. The bandpass of the excitation light was controlled using the slit widths of the monochromators, ensuring that the maximum fluorescence emission intensity was below this saturation limit, thus maintaining a linear response of the PMT.

3.3. Time-Correlated Single Photon Counting

Fluorescence lifetime decays were recorded using the TCSPC set-up housed in COSMIC (Collaborative Optical Spectroscopy, Micromanipulation and Imaging Centre) at The University of Edinburgh. Figure 3.1 shows a schematic of the equipment used. Only a brief description of the TCSPC set-up will be given here, while an in depth discussion of the components involved in the system can be found in the works of Lakowicz,[1] O'Connor and Phillips,[2] and Becker.[3]

The excitation source was a tuneable, mode-locked Ti-Sapphire laser system (Coherent Mira 900-F) pumped by a Coherent Verdi V-10 continuous wave solid state laser (532 nm, 10 W). The Ti-Sapphire laser produces a tuneable, pulsed fundamental beam (700-1000 nm). The width of the passively mode-locked pulses is ~200 fs and the pulses are produced at a rate of 76 MHz. Using a pulse picker (Coherent 9200), the repetition rate is reduced to 4.75 MHz (one pulse every 210 ns). The output of the pulse picker is then guided into a harmonic generator (Coherent 5-050) and is either frequency doubled or tripled. Residual fundamental/second harmonic from frequency doubling/tripling respectively is diverted to a fast photodiode that converts the laser pulse to an electronic trigger ("start") pulse. The amplitude of the "start" pulse (altered by adjusting the intensity of the incident light on the photodiode) was set to approximately 1 V for all experiments. A photon-counting card (Edinburgh Instruments TCC900) was used, containing the discriminators and a time-to-amplitude converter

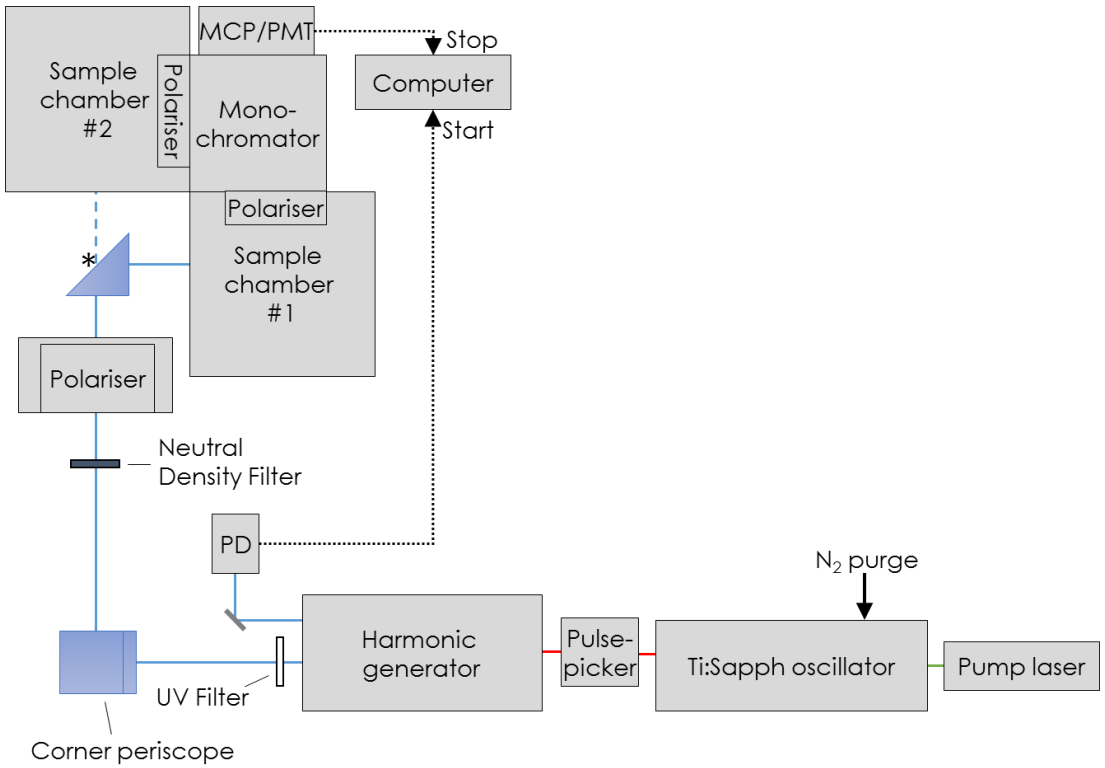

Figure 3.1: Schematic of the experimental set-up used for TCSPC measurements. The corner periscope is composed of two UV enhanced right angle prism mirrors arranged in a corner-periscope formation (used to simultaneously raise the height of the beam and redirect the beam by 90°). Sample chamber #1 was used for measurements performed at room temperature with the sample contained in a cuvette. Sample chamber #2 was used for measurements performed at 77 K, with the dashed blue line showing the beam path taken when using this chamber, following removal of the UV-enhanced right angle prism mirror (labelled with an asterisk and located immediately before the sample chambers). Further details of low temperature measurements can be found in Section 3.4.

(TAC). The discriminator for the start pulse was set to use leading-edge discrimination with a threshold set at -300 mV to ensure that only pulses with a magnitude greater than 300 mV trigger the TAC. The discriminator for the stop pulse (corresponding to detection of a fluorescence photon) was set to use constant fraction discrimination with a threshold of -30 mV and a zero-crossing level of -8 mV. The photon counting card was controlled using Edinburgh Instruments F900 software and allows decays with a time resolution as high as 610 fs per channel and allows for a maximum count rate of up to 6.6 MHz.

The remainder of the excitation pulse is directed to one of two spectrometer sample chambers, after passing through a Soleil-Babinet compensator. The compensator

allows for control of the orientation of the plane of the polarised excitation pulse and consists of a pair of quartz wedges that are aligned 45° to the incoming laser light. Varying the total thickness of the quartz that the beam passes through allows the vertical or horizontal components of the incident beam to be optically retarded, controlling the plane of polarisation of the emerging light. The ability of the Soleil-Babinet compensator to rotate the plane of polarisation of light is dependent upon the wavelength of the light incident upon it. Using the Edinburgh Instruments F900 software, the resolution of the Soleil-Babinet compensator is set for the wavelength of the incident light using Equation 3.1.

$$Resolution = \frac{41.62}{\lambda} \qquad \textbf{3.1}$$

Using Equation 3.1, the polarisation of the excitation pulse is controlled such that it is aligned vertically. After passing through the Soleil-Babinet compensator, the excitation pulses pass through a focusing lens and arrive at the sample. Fluorescence emission from the sample is detected through a polariser set at the magic angle (54.7°) relative to the vertically polarised excitation pulse, in order to exclude any anisotropic effects from the recorded decay data.

Dispersion of emitted light from the sample is controlled *via* an aperture in the sample chamber before reaching the monochromator. The diameter of the aperture can be altered (between 2 mm to 37 mm) and has the effect of adjusting the width of the instrument response function (IRF) since this controls the volume of sample from which fluorescence emission is detected. Narrowing the aperture decreases the area that photons are incident on the detector, which, in turn, decreases the transit-time spread (TTS) through the microchannel plate. After the aperture, the emission then passes through a lens, an emission polariser and then arrives at the detector via a monochromator. A set of slits at the entrance and exit of the monochromator are used to set to allow a 10 nm bandpass for all experiments unless otherwise stated.

The detector is a microchannel plate (MCP) (Hamamatsu R3809-50 series) for TCSPC or red-sensitive-sensitive photomultiplier tube (PMT) (Edinburgh instruments) for steady-state fluorescence measurements (which are also possible to perform in this set-up and are routinely used to check excitation and emission wavelengths). The MCP has a transit-time spread of 25 ps and a dark count rate of ~50 Hz. The TAC used in the current set up has a dead time of <150 ns.

It is commonplace to record fluorescence decay curves on a timescale of approximately 4-5 times longer than the duration of the longest expected lifetime. Thus, for example, when measuring 2AP fluorescence decay curves (~11.5 ns), a timescale of 50 ns was used. In the current set up, this time scale was spread over 4096 channels, resulting in ~12 ps per channel. Decay curves were recorded to a value of 10,000 counts in the peak channel and all measurements were recorded at room temperature, with samples contained in a fused silica micro-volume cuvette (10 mm path length), unless otherwise stated (see Section 3.4 for a description of low temperature measurements). The emission wavelength used in each experiment varies slightly and are stated in the relevant sections of the thesis.

The IRF of the TCSPC set-up was routinely recorded by scattering the excitation pulses using a weak solution of colloidal silica (Ludox, Sigma-Aldrich). This enabled an intensity profile of the excitation pulse to be obtained without a fluorescent sample present in the chamber (using only scattered light). Figure 3.2 shows a typical IRF obtained from the set-up with the full width half-maximum (FWHM) measured to be ~85 ps.

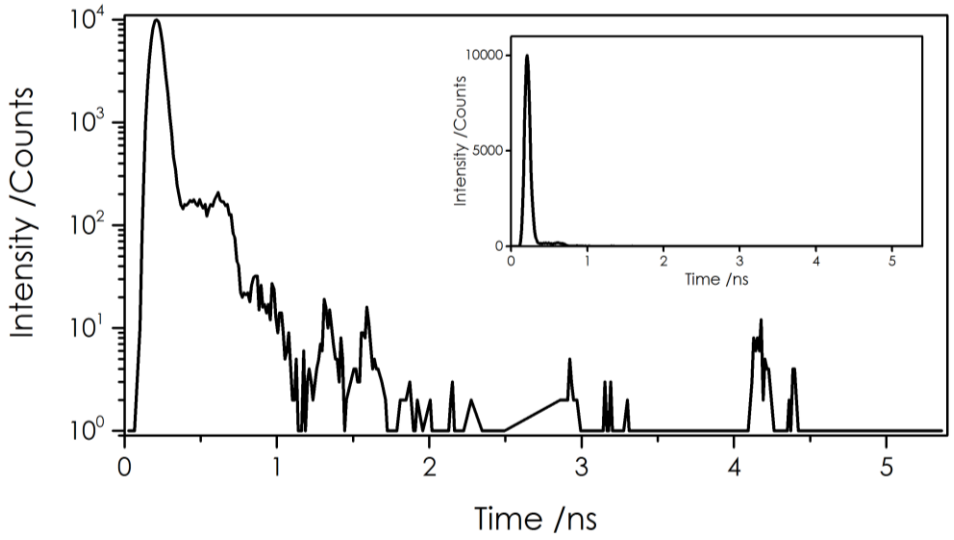

Figure 3.2: A typical instrument response function (IRF) measured for the TCSPC set-up used for the work in this thesis. The main graph shows the IRF data on a logarithmic intensity scale while the inset shows the same data presented on a linear intensity scale, highlighting the intensity of the main peak compared to the "afterpulse". The FWHM of the IRF was measured to be ~85 ps.

A range of factors will affect the measured width of the IRF, such as the wavelength of light or the settings of the discriminators, but the main contributor to IRF broadening is the transit time spread (TTS) of electrons passing through the MCP. TTS is the variation

in the time taken for electrons to pass through the MCP, from the photocathode to the anode, as they are being amplified.

Analysis of the recorded decay curves was performed using an iterative reconvolution method in the F900 software (Edinburgh Instruments) for individual fits or in the FAST software package (Edinburgh Instruments) for global fits. Global analysis was typically performed using three sets of data, recorded at different emission wavelengths, with common parameters linked between the different data sets, during the fitting process. In the present experiments, the same lifetime components were present at all emission wavelengths, but with differing relative populations. Initially, a single exponential fit was used (as described by Equation 2.16) and the quality of the fit was assessed based on the calculation of the reduced chi-squared (χ^2) (Equation 3.2) and the randomness of the plotted residuals (as calculated using Equation 3.3 and described below). The values of χ^2 are calculated as follows,

$$\chi^2 = \sum_k w_k^2 \frac{[F_k - S_k]^2}{n} \qquad \textbf{3.2}$$

where w_k is the weighting factor, F_k is the measured values and S_k is the data points of the fitted curve at time k and n is the number of free parameters)approximately the number of fitted data points subtracted by the number of lifetime parameters used in the fit). Equation 3.2 allows the goodness-of-fit to be determined independently of the number of data points used and allows different fits to be quantitatively compared. Typically, if the model fits the data perfectly then χ^2 will be close to unity (1.0), while values much larger than 1.0 are deemed poor fits of the data (as illustrated below). In the work presented in this thesis, a χ^2 value of <1.2 was deemed a good fit. In cases where the fit was not good (χ^2>1.2), a multi-exponential fit was attempted (as described by Equation 2.17). The software used for data analysis allows for fits of up to four exponentials to be attempted.

Also taken into consideration to determine the goodness-of-fit are the weighted residuals, X, calculated as follows,

$$X_k = w_k(F_k - S_k) \qquad \textbf{3.3}$$

For a good fit, the residuals show only random noise distributed around zero. A significant shape or deviation from a random distribution in a plot of the weighted residuals is indicative of a poor fit of the data.

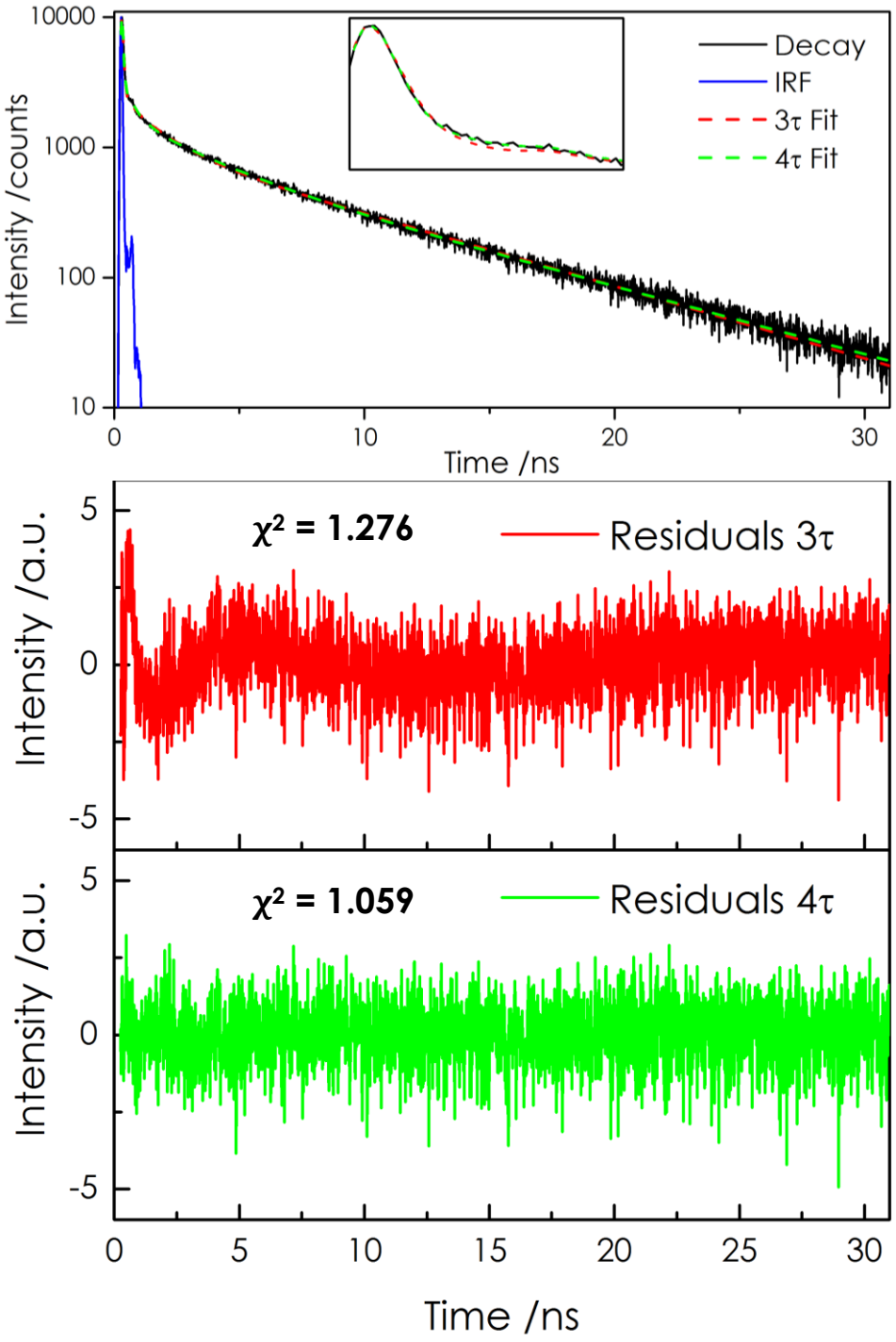

Figure 3.3: An example of an inadequate fit (red) using 3 lifetime components (χ^2 = 1.276) and of a good fit (green) using 4 lifetime components (χ^2 = 1.059) of fluorescence decay data. The fluorescence decay of sample ds6 at an emission wavelength of 380 nm (from Chapter 4) has been used as an example. The IRF is shown in blue while the fluorescence decay is shown in black. The only difference between the two data fits is the number of lifetime components. The inset shows a close-up of the decay and fits between 0 and 1 ns in which differences between the fits can be more readily seen.

Figure 3.3 shows an example of a case of data fitting when the use of three lifetime components was inadequate to fit the data and produced a χ^2 greater than 1.2. Alongside a high χ^2 value, the residuals show a non-random distribution (most apparent in the region of 0-10 ns). This indicates that this is a poor fit. As such, four lifetime components were required to fir the decay data, resulting in a random distribution of the residuals centred around zero and a χ^2 value lower than 1.2.

3.4. Low-temperature Measurements

For studies conducted at 77 K, samples were dissolved in 6 M aqueous LiCl. This was found to be the lowest concentration of LiCl that would form a stable and reproducible clear glass when frozen, and was sufficiently low to prevent significant perturbation to dinucleotide decay parameters. The concentrations of the samples were kept the same as for room temperature measurements. Samples in LiCl solution were placed in NMR-style fused silica tubes (diameter 5 mm) (made in-house by the glassblowing workshop). The tubes containing the samples were inserted into liquid nitrogen that was contained within a fused silica Dewar flask (Horiba Jobin Yvon), as illustrated in Figure 3.4.

The arrangement shown in Figure 3.4 allowed measurements of both steady-state fluorescence and time-resolved fluorescence to be performed at 77 K. Together with the Dewar flask, a light-tight stovepipe lid (not shown) was used with spectrometers to enable easy access to the sample tube and replenishment of the liquid N_2 in the flask when required. During experiments, the level of liquid N_2 was maintained above the level of the sample solution to ensure uniform cooling of the entire sample. Condensation of water on the outside of the Dewar flask and formation of ice crystals during measurements were problematic. In order to mitigate these problems and obtain good quality data, a beaker of liquid N_2 was placed in the chamber during measurements to condense out water vapour.

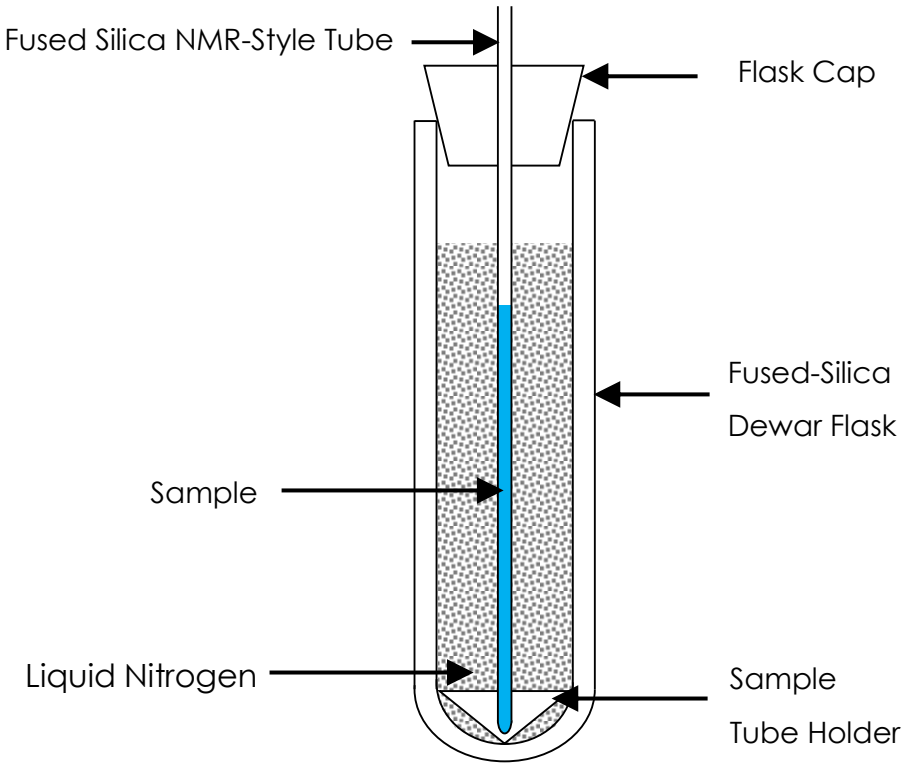

Figure 3.4: Schematic of the low temperature set-up used for steady-state and time-resolved fluorescence measurements at 77 K consisting of a fused-silica Dewar flask with sample tube holder, a cap and a removable fused silica NMR style tube containing the sample. For measurements at 77 K, the Dewar flask, filled with liquid N_2, was mounted in a custom holder in the sample compartment of the spectrometer (not shown). For simplicity, the mirrored surface of the top 2/3rds of the outside of the Dewar flask is not shown while the bottom third of the flask was transparent to allow a window to excite the sample and to collect fluorescence emission.

Steady-state fluorescence excitation and emission spectra were recorded as described in Section 3.2, but with the adaptation of the low temperature set-up.

For time-resolved fluorescence measurements performed at 77 K, the low temperature set-up was installed in chamber #2 of the set-up shown in Figure 3.1 and an IRF was recorded for the set-up using a Ludox scattering solution contained in an NMR-style fused silica tube at room temperature (similar to those used to contain samples) without the presence of liquid N_2.

3.5. References

1 J. R. Lakowicz, *Principles of Fluorescence Spectroscopy*, Springer US, Boston, MA, 3rd Edi., 2006, vol. 3.

2 D. V. O'Connor and D. Phillips, *Time-Correlated Single Photon Counting*, Academic Press, 1984.

3 W. Becker, *Advanced Time-Correlated Single Photon Counting Techniques*, Springer Berlin Heidelberg, Berlin, Heidelberg, 2005, vol. 81.

Chapter 4: Use of 2-Aminopurine as a Fluorescent Probe in DNA: Low Temperature Photophysics

4.1. Introduction

For many decades now, 2-aminopurine (2AP) has been widely used as a fluorescent probe to study the conformational changes and base interactions in DNA systems. While the DNA double helix has been the focus of a majority of the studies performed,[1–5] more recent studies have expanded to include study of DNA single strands[3,5–9] and other DNA constructs, such as the DNA 3-way junction (3WJ)[6,10] or DNA hairpins.[11–13] Conformational motion and base dynamics are thought to mediate processes within DNA strands that contribute to the stability and function of DNA and are known to play a major role in mechanisms that lead to quenching of 2AP fluorescence in DNA.[14–17] As discussed previously, in Chapter 2, the fluorescence properties of 2AP make it an ideal candidate as a fluorescent probe of DNA systems. When incorporated into oligonucleotides, the time-resolved fluorescence decay profile of 2AP becomes complex (multi-exponential), rather than the mono-exponential decay observed for the isolated base in solution, and a complete explanation of this behaviour has not yet been achieved. To date, no definitive physical model has been presented that can fully explain the multi-exponential fluorescence decay profile of 2AP in DNA. While the fluorescence decay of 2AP free in solution can be adequately described by a mono-exponential function, 2AP incorporated into oligonucleotides typically requires four exponentials to describe its fluorescence decay and calls for measurements on the picosecond-nanosecond timescale. Of the four fluorescence lifetimes that are typically used to describe the fluorescence decay of 2AP in DNA, the shortest lifetime (τ_1, <100 ps) is attributed to those conformations of 2AP which are highly quenched through interactions with neighbouring bases, such as charge transfer. At the other extreme, the longest lifetime, τ_4, (~9 ns) is comparable to the lifetime of free 2AP in solution and is therefore accredited to the conformations of 2AP that are the least quenched and do not

experience significant intramolecular interactions. Likely conformations of 2AP that this describes are extra-helical or base-flipped 2AP (Figure 2.14). In the current model, the two intermediate lifetimes (τ_2 and τ_3, ~0.3 ns and ~3 ns respectively) have no definitive assignment that can relate to physical states of 2AP in DNA. These lifetimes are most likely distributions of conformational states that experience similar levels of quenching from local interactions with nearby bases that may not necessarily all exist in identical conformational states. Due to insufficient knowledge on the origin of these intermediate lifetimes, they are generally regarded as intermediate conformations of the local duplex structure that lie somewhere between the tightly stacked and fully unstacked. Alternative explanations of the source of these lifetimes have also been proposed, such as the involvement of dark states or mechanisms relating to specific transitional conformations of base-dynamics from τ_1 to τ_4 in excited state 2AP (transient unstacking).[18]

The work presented here aims to investigate the role played by base dynamics that leads to the population of heterogeneous conformational states of 2AP in DNA and to investigate the nature of the conformational states that give rise to the multi-exponential decay of excited-state 2AP in these systems. By performing fluorescence studies of 2AP in DNA in frozen solution at 77 K, in which conformational motions have been restricted, the steady state and time-resolved fluorescence properties can be compared with those determined for conformationally mobile systems at room temperature. Initial studies on solutions of 2AP-labelled oligonucleotides were performed to complement the previous study of Neely and Jones.[14] Later studies focussed on 2AP-containing DNA dinucleotides in which only one DNA base and one 2AP base are present in each molecule. By limiting the complexity of the DNA systems to only two bases, base-specific interactions can be identified and ambiguity in the collected data is reduced.

Larsen *et al.*[19,20] performed ultrafast TA and steady-state fluorescence measurements to study the excited-state properties of free 2AP and 2AP-containing oligonucleotides and dinucleotides. However, limitations of the TA measurements presented as an inability to determine the long lifetime states of 2AP accurately. The time-range used for TA measurements (1 ns for the dinucleotide samples and 5 ns for the oligonucleotides) was only a fraction of the longest lifetime for 2AP (~11.5 ns). Lifetime components determined previously for 2AP by Larsen *et al.*[20] for free 2AP in aqueous buffer solution were 1.3 ps, 3.5 ns and ~14 ns. Similar to the findings of Reichardt *et al.*,[21] the shortest lifetime can be attributed to solvation dynamics, while the two longer lifetimes are likely to be an artefact of data fitting, in which the characteristic

2AP lifetime has split into two components. Larsen at al. comment that the precision of the long 2AP lifetimes is limited due to the short time range used for TA measurements. The decay components determined for 2AP in dinucleotides and oligonucleotides were found to both be heterogeneous, implying that the decay of excited 2AP (2AP*) is more complex in these systems than for free 2AP but, in light of the short-timescales used for TA measurements, the full extent of results will not be fully discussed here. The steady-state fluorescence measurements performed by Larsen *et al*. on 2AP-containing oligonucleotides and dinucleotides showed that 2AP fluorescence was heavily quenched in all samples studied; demonstrating that guanine is not the only DNA base capable of quenching 2AP fluorescence. Table 4.1 shows a comparison of the reduction potentials for excited 2AP and nucleosides G, A, I, C and T. The reduction potentials relative to 2AP* are also given and the lifetime values for the fast decay component of 2AP in aqueous solutions containing mononucleotides (dGTP, dATP, dITP, dCTP or dITP), which are not covalently bound to 2AP (but merely present in solution), determined from ultrafast TA measurements are also shown.[22]

Nucleoside	Reduction Potential / V (versus NHE)	Reduction Potential / V (vs 2AP*)	Lifetime / ps
Guanosine (G)	+1.29	-0.21	19
Adenosine (A)	+1.42	-0.08	350
2AP*	+1.50	0.00	-
Inosine (I)	+1.50	0.00	120
Cytidine (C)	+1.60	+0.10	47
Thymidine (T)	+1.70	+0.20	20

Table 4.1: Reduction potentials for nucleosides in water and the reduction potential relative to 2AP*. Lifetimes shown are for the fast decay component of 2AP in aqueous solutions containing mononucleotides measured via TA measurements conducted by Fiebig *et al*.[22] Reduction potentials for the natural DNA bases are from Steenken and Jovanovic[23] and 2AP* and inosine are from Kelley and Barton.[24]

Based on the difference in reduction potentials (vs 2AP*) shown in Table 4.1, there is a high drive for oxidation of G by 2AP* (Equation 4.1) while oxidation of T by 2AP* is the least favourable. However, reduction of T by 2AP* could alternatively occur (Equation 4.2).

$$2AP^* + G \rightleftarrows 2AP^{\bullet-} + G^{\bullet+} \qquad \textbf{4.1}$$

$$2AP^* + T \rightleftarrows 2AP^{\bullet+} + T^{\bullet-} \qquad \textbf{4.2}$$

While oxidation potentials would be more useful in determining the drive for electron transfer (eT) in these systems, there unfortunately is a lack of data available for those in aqueous solution at this current time and so cannot be directly compared at present.

Although charge transfer processes play a major role in the quenching of 2AP*, the minimal difference in reduction potential between 2AP* and I would suggest that there is no drive for charge transfer to occur between the two bases and that quenching would be minimal. However, the steady-state fluorescence has shown that 2AP is still heavily quenched in the 2AP-I dinucleotide suggesting that other quenching processes are also present in these systems. It is however important to note that the activation energies for these charge transfer (CT) reactions are yet unknown and, along with the reduction potentials, may differ when incorporated into DNA.

Fiebig *et al.* investigated the CT dynamics of 2AP and deoxynucleotide triphosphates (dNTPs) via TA and fluorescence upconversion spectroscopy.[22] Although not covalently bound to 2AP, the presence of dNTPs in solution quenched 2AP fluorescence and allowed CT to be identified as the origin of quenching of 2AP fluorescence by dNTPs. Both the oxidation of 2AP* (electron transfer (eT)) and the reduction of 2AP* (hole transfer (HT)), were implicated as effective quenching processes and it was concluded that the direction of the redox process is heavily dependent on the DNA base(s) present. These trends predicted that, based on free energy estimates derived from measured decay rates, HT occurs from 2AP* to G and A and eT occurs from 2AP* to T and C with the redox process being more favourable for the former base in each case. Due to the minimal differences in reduction potentials for A and I, it was concluded that reduction or oxidation of these bases could potentially occur from 2AP*. These results are consistent with the determined relative propensity for the natural DNA bases to be oxidised (G > A > C > T) or reduced (T > C > A > G) but it should be noted that these trends were not obtained under aqueous conditions but in acetonitrile (ACN) and dimethylformamide (DMF), respectively. [22,25]

More recently, Narayanan *et al*.[26] measured the oxidation potential of 2AP* as -2.02 V in ACN and the reduction potential to be +1.44 V in DMF. The results of free energy calculations of CT with nucleotides suggested that, in water, 2AP* can act as an electron donor (acting to reduce dTMP) or as an electron acceptor (to oxidise rGMP and rAMP). In the case of rCMP, it was inconclusive as to whether CT from 2AP* occurs via oxidation or reduction but potentially both are possible. The predictions of charge transfer character by Narayanan *et al*. are based on a number of assumptions that should

be evaluated before considering the conclusions of the work performed. Both theoretical calculations (performed by Crespo-Hernandez *et al.*[27]) and experimental values (determined by Seidel *et al.*[25]) form the basis of their conclusions, while an estimate of the free energy decrease, arising from effects resulting from a difference in solvents used (aprotic organic (ACN or DMF) to aqueous (water)), was also required. Typically, absolute values from calculations can only be compared with other values that have used a similar level of theory to produce them. Combining these calculated values with experimental values is therefore debatable as to their validity.

Overall, however, it is clear that the intrinsic redox potentials of the neighbouring bases of 2AP in the DNA sequence have a significant effect on the characteristics of 2AP fluorescence in DNA.

4.1.1. 2AP-containing Dinucleotides

In order to simplify the systems under study and to reduce the number of interactions experienced by 2AP with other bases when incorporated into DNA, studies of 2AP-containing dinucleotides have been conducted (where only one 2AP base and one DNA base are present and are linked through a sugar-phosphate backbone). The structure of the 2AP-containing dinucleotides studied in the present work are shown in Figure 4.1; the backbone joining the two bases is composed of two ribose groups and one phosphate group.

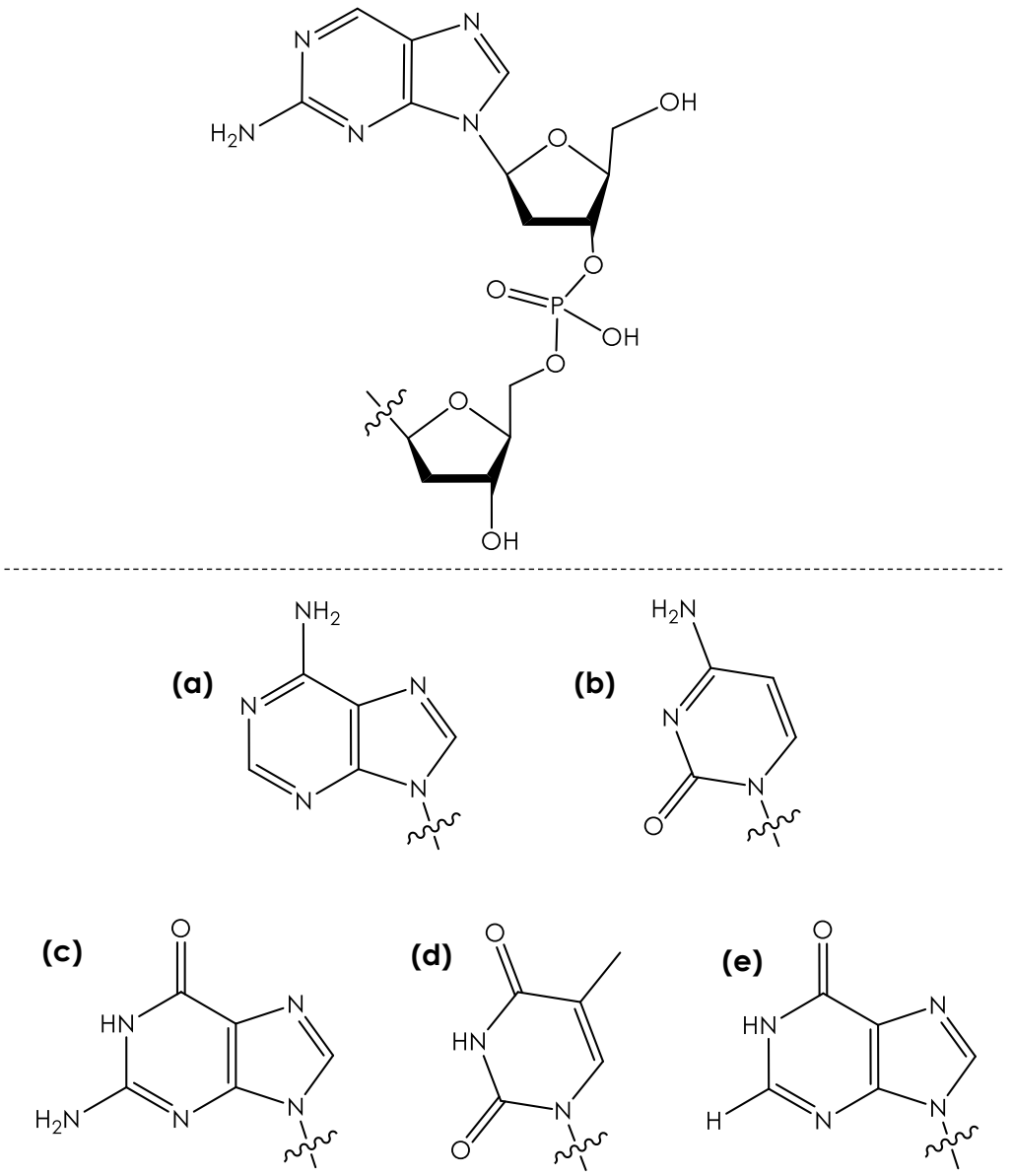

Figure 4.1: Molecular structure of 2AP-containing dinucleotides, 2AP-X, where X = (a) adenine (A), (b) cytosine (C), (c) guanine (G), (d) thymine (T) or (e) hypoxanthine (I). The wavy line denotes where the A, C, G, T or I is bonded to the sugar-phosphate backbone.

Somsen *et al*. investigated the temperature-dependence of the fluorescence decay of 2AP-containing dinucleotides, making measurements at three different temperatures (20°C, 40°C and 60°C).[18] A four-exponential model was used to fit all of the decay curves, which is consistent with the typically observed heterogeneity of 2AP fluorescence in DNA. Table 4.2 (top row for each dinucleotide) shows a summary of the lifetimes parameters obtained by Somsen *et al*. at 20°C. In order to explain the temperature dependence of A_1 and A_3 (the sum of which does not change), Somsen *et al*. proposed a model to explain the four-component fit of the decay curves that resembles gating

mechanisms previously used to describe CT dynamics in DNA.[15,16] In this model (shown in Figure 4.2), there are three distinct ground states and four excited-states where one of the ground states is associated with two of the excited-state that exist in equilibrium

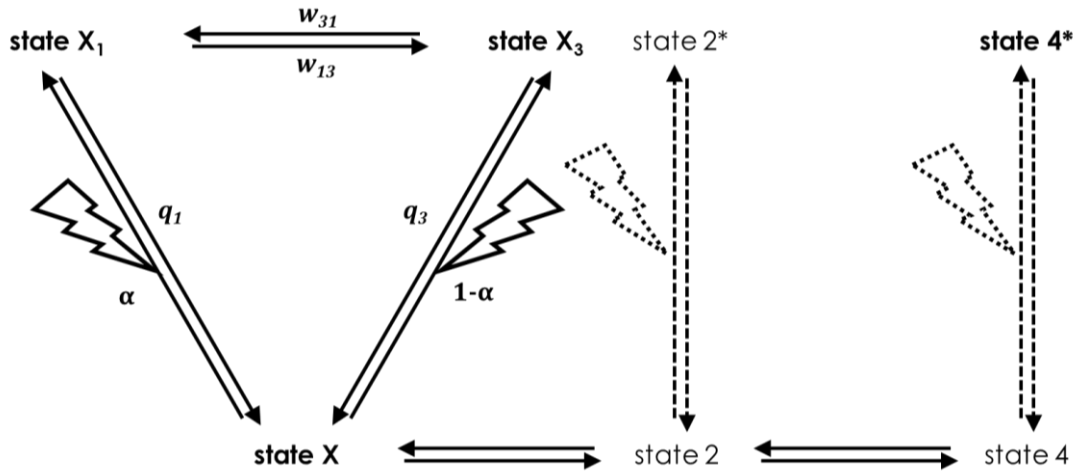

Figure 4.2: The three-state model invoked by Somsen *et al.*[18] to describe the fluorescence decay parameters determined for 2AP-dinucleotides. Where states X, 2 and 4 are the ground states with associated excited states (X_1 and X_3), 2* and 4* respectively. α and 1-α indicate the relative excitation of excited-states X_1 and X_3, q_1 and q_3 are the quenching rates of these states and w_{13} and w_{31} are the transition rates between these two excited-states of X.

with each other.

To justify this model, Somsen *et al*. proposed that transient unstacking of the DNA bases occurs in the excited state and does not occur in the ground state. However, reasons why this phenomenon would not also occur in the ground state is unclear.

There have been two subsequent studies of fluorescence lifetime parameters of 2AP-dinucleotides in aqueous solution, reported in the PhD theses of Wu[3] and Smith[28]. These studies of aqueous 2AP-dinucleotides also investigated the removal of conformational motions by freezing the sample at 77 K, and the influence of solvent composition using alcohol-water mixtures, respectively. Table 4.2 presents a summary of the fluorescence decay parameters for 2AP-X dinucleotides determined by Somsen *et al*. (top row), Wu (middle row) and Smith (bottom row).

X	τ_i /ns				A_i				<τ>
	τ_1	τ_2	τ_3	τ_4	A_1	A_2	A_3	A_4	/ ns
G	0.03	0.33	1.80	8.80	0.78	0.07	0.12	0.02	0.44
	0.06	0.63	1.80	10.30	0.47	0.14	0.33	0.06	1.33
	0.04	0.51	1.70	8.98	0.66	0.09	0.22	0.03	0.69
T	0.03	0.38	2.40	8.20	0.60	0.10	0.29	0.01	0.84
	0.07	0.65	2.30	10.20	0.27	0.11	0.59	0.03	1.75
	0.05	0.66	2.45	9.36	0.55	0.09	0.34	0.01	1.07
C	0.04	0.45	2.50	8.00	0.48	0.14	0.36	0.02	1.14
	0.16	0.78	2.40	9.20	0.17	0.14	0.68	0.01	1.86
	0.06	0.58	2.45	8.96	0.40	0.13	0.44	0.04	1.49
A	0.03	0.59	2.10	8.30	0.33	0.41	0.23	0.03	0.98
	-	0.61	2.00	9.60	-	0.64	0.33	0.03	1.34
	0.08	0.65	2.13	8.97	0.27	0.45	0.22	0.06	1.29
I	0.02	0.80	3.10	8.40	0.35	0.20	0.39	0.06	1.87
	-	0.83	3.10	8.50	-	0.33	0.61	0.06	2.67
	0.06	0.85	2.69	9.20	0.35	0.20	0.36	0.09	1.95

Table 4.2: Summary and comparison of previously determined lifetime parameters for 2AP-containing dinucleotides, 2AP-X (where X = A, C, G, T or I), in aqueous solution at room temperature. Decay parameters have been compiled from publications of Somsen *et al.*[18] (top row), Wu[3] (middle row) and Smith[28] (bottom row).

A comparison of the three sets of fluorescence decay parameters for the 2AP-containing dinucleotides reveals that the values obtained by all investigators fit fairly well into the four distinct ranges of 2AP lifetimes that are typical of the multi-exponential decay of 2AP-containing DNA. It should be noted that while aqueous conditions were used by all, Somsen *et al*. and Wu studied 2AP-dinucleotides in phosphate-buffered solution (at pH 7.0 and pH 7.4, respectively), while no buffer was present in measurements performed by Smith (100% H_2O solvent). Table 4.2 demonstrates how lifetime parameters obtained from the same fluorophore, under marginally different conditions, can vary and that this, alongside differences in data-fitting methods, can account for variation in the decay parameters determined. Concerning the models used to describe the decays of 2AP-A and 2AP-I by Wu, the obvious difference from others data sets is the use of only three exponentials while Somsen *et al*. and Smith both used four exponentials (similar to the models used to describe the dinucleotides involving the other DNA bases). In Wu's three component fits, it is the shortest component, τ_1 that is not present. As previously stated, the relative CT efficiencies of A and I is low when compared to that of other DNA bases. Fiebig, Wan and Zewail found the shortest decay components of 2AP in the presence of dATP and dITP (determined from TA measurements) to be 350 ps and 120 ps while for 2AP in the presence of other DNA bases

typically ranged from 2.7 ps to 47 ps. Thus, as the lifetimes are an order of magnitude greater, they more closely resemble the second decay component, τ_2. It is possible that in fitting the data, these components have been grouped together and represented by an averaged lifetime value, despite the presence of two different relaxation pathways. A limited experimental resolution can lead to this sort of anomaly in the data fitting procedure. Arguments can be made in favour of fitting these decay curves with either four exponentials or three exponentials; using four exponentials provides a further layer of complexity to the systems by introducing another variable into the system but allows for a common model to be used to describe all of the 2AP-dinucleotides (arguably more favourable). The use of three exponentials reduces the complexity of the model used to describe the system but still requires an explanation of why this lifetime is not present. It seems unlikely that the shortest component (those relating to highly stacked conformations of 2AP in DNA) does not exist and it is highly possible that experiments with higher resolution to those performed in these studies will be able to resolve such lifetimes.

Smith *et al*. performed DFT calculations of dinucleotides of 2AP with natural DNA bases (A, C, G or T) to investigate the conformational structures adopted.[29] The calculations performed included full optimisation of the sugar-phosphate backbone, a component that previous studies had omitted.[30–32] Smith *et al*. used the M06-2X functional to allow for reliable treatment of dispersion interactions and included implicit aqueous solvation in the calculations. Interestingly, a comparison of 2AP-containing dinucleotides was made with the corresponding adenine-containing dinucleotides and it was found that the computed structures showed a close resemblance, confirming the suitability of 2AP as a fluorescent analogue of adenine in DNA. It was found that the 2AP-containing dinucleotides adopt conformational structures that bear a striking resemblance to B-DNA and the base-step parameters (and backbone torsion angles and sugar pucker) derived from crystallographic data of B-DNA were consistent with those obtained from calculated structures. Concerning the calculated minimum energy structures, three structures were identified and characterised, which is indicative of the heterogeneity that presents as multi-exponential fluorescence decay of 2AP-containing dinucleotides. Structures closely resembling B-DNA (as shown in Figure 4.3) are proposed to be responsible for the shortest fluorescence decay components of 2AP while twisted structures and the diverse range of them could be responsible for the intermediate lifetimes observed in the 2AP fluorescence decay parameters.

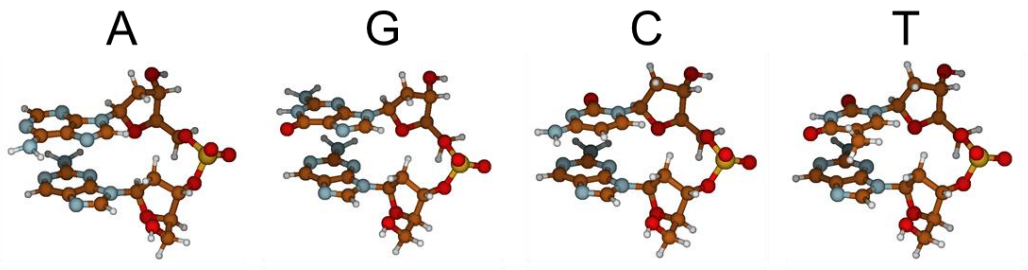

Figure 4.3: DFT-calculated B-form structures of dinucleotides of 2AP with each of the native DNA bases (A, G, C, or T).

While the minimum energy structures indicate the possible heterogeneity of base conformations, they are not to be taken as being exclusive and thus far, global minimum energy structures have not been confirmed. It is clear from the findings of Smith *et al*. that even DNA dinucleotides, where only two DNA bases are present, are far from simple, but that limitations to the possible conformations can be predicted by considering base-stacking interactions and constraints of the DNA backbone structure (a potentially important component omitted from previous studies).

4.1.2. 2AP-containing Oligonucleotides

As part of an investigation of local DNA structure in DNA 3-way junctions (3WJs), Sabir *et al*. performed time-resolved fluorescence measurements on a set of single-stranded and corresponding double-stranded 2AP-labelled oligonucleotides.[10] This work demonstrated the diverse range of base-stacking interactions that can occur in DNA systems as well as the suitability of 2AP as a probe of DNA systems. It was shown that, in some regions, the 3WJ resembles well-stacked DNA duplexes while elsewhere in the same structure the DNA local structure resembled the more flexible and more imperfectly stacked nature of single-stranded DNA. A full discussion of the fluorescence decay parameters of these 2AP-containing ss- and ds- oligonucleotides (of length 50 nucleotides), and their relation to the sequence context of 2AP can be found in the thesis of Ma;[6] these results are reproduced in Table 4.7 in Section 4.3.2.1 of this thesis. The work presented later in this chapter investigates the effect of low temperature on the fluorescence properties of 2AP-containing oligonucleotides with identical sequences to those studied by Ma; the results of Ma will be considered in detail at that point.

It is commonly found that a higher degree of structural stability and order is present in DNA duplexes compared to ss-DNA and the results presented by Ma confirm this, as a higher population of the fluorescence lifetimes are attributed to the more highly

stacked conformations. Charge transfer from neighbouring bases has previously been identified as one of the major quenching processes of 2AP in DNA,[1,22] with the rate of charge transfer following the trend of G>T>A>C, similar to the magnitude of the redox potentials presented in Table 4.1.[23] The decay parameters presented by Ma showed a good correlation with the number of Gs present in close proximity to the 2AP (either in the same strand or in the opposite strand), with G exhibiting the strongest drive for charge transfer (Table 4.1).

4.1.3. Low-Temperature Fluorescence Measurements of 2AP in DNA

Previous low-temperature fluorescence measurements of 2AP in DNA were performed using 10M LiCl as solvent, in order to form an optically transparent glass at 77K.[14,16] Fluorescence decays of three 2AP-labelled DNA duplexes in LiCl at 77 K were reported by Neely and Jones.[14] The high concentration of LiCl appeared to cause only a minor perturbation to the DNA structure, presented as a minor disruption to base-stacking interactions, resulting in minor differences to the amplitude and magnitude of the shortest decay components while the longest lifetimes became shorter (due to differences in interactions between extra-helical 2AP and the solvent). Table 4.3 shows the DNA base sequence of the duplexes studied by Neely and Jones, while the fluorescence decay parameters and relative quantum yields for the duplexes can be found in Table 4.4.

Duplex	Sequence
GPG	5' ACTGGTACAGTATCAGG**P**GCTGACCCACAACATCCG 3' 3' TGACCATGTCATAGTCCGCGACTGGGTGTTGTAGGC 5'
CPC	5' CACGGGCCTAACGATATCGTGCGTACGAGC 3' 3' GTGCCCGGATTGCTATAGC**P**CGCATGCTCG 5'
TPA	5' CACGGGCCT**P**ACGATATCGTGCGTACGAGC 3' 3' GTGCCCGGATTGCTATAGCACGCATGCTCG 5'

Table 4.3: DNA base sequences of 2AP-labelled duplexes studied by Neely and Jones in time-resolve fluorescence measurements of 2AP in DNA at low temperatures. "P" denotes the position of 2AP in the sequence. The sample names of the duplexes reflect the sequence context of 2AP within the duplexes. Reproduced from the work of Neely and Jones.[14]

Sample		τ_i /ns				A_i				$\langle \Phi_{rel} \rangle$ /ns
		τ_1	τ_2	τ_3	τ_4	A_1	A_2	A_3	A_4	
GPG	293K	0.17	0.97	3.9	8.5	0.56	0.23	0.13	0.08	0.19
GPG	77K	-	0.76	3.6	10.1	-	0.33	0.51	0.16	0.40
CPC	293K	0.06	0.34	2.0	7.9	0.67	0.16	0.07	0.10	0.10
CPC	77K	-	0.79	3.7	9.9	-	0.40	0.34	0.26	0.51
TPA	293K	0.22	0.94	2.0	7.9	0.67	0.15	0.09	0.07	0.15
TPA	77K	-	-	2.9	11.3	-	-	0.14	0.86	1.21

Table 4.4: Fluorescence decay parameters and relative quantum yields of 2AP-containing DNA duplexes studied by Neely and Jones at low temperatures.[14]

It was found that the heterogeneous nature of 2AP fluorescence lifetimes in DNA remains at 77 K but the number of components required to describe the fluorescence decay curve reduces from four components at 293 K to three (or two) at 77 K. The loss of the shortest lifetime, τ_1, at 77 K suggests that base dynamics (which are not present when the duplexes are frozen at 77 K) are highly influential in allowing the bases to access the highly quenched states (responsible for the short lifetime of τ_1) that are found at 293 K. It was highlighted by Neely and Jones that fluorescence decay of 2AP is highly sensitive to the local environment and also to the sequence context in which 2AP is present. Duplexes GPG and CPC, with sequences where G is in close proximity to 2AP, show much shorter lifetimes for the highly quenched states of 2AP, τ_1, at 293 K. The absence of this shortest decay component in these duplexes in the frozen matrix at 77 K demonstrates that rapid charge transfer quenching is the consequence of base dynamics and is eliminated when the bases are static, even when 2AP is stacked and paired with G (as in GPG). However, the heterogeneity of the 2AP decay function persists at 77 K, and the observation of three decay components indicates the existence of a number of discrete, static conformational states that can be characterized by three distinguishable intrinsic decay times. In these two duplexes, quenching on the sub-nanosecond timescale (τ_2) persists at 77 K. In contrast, for duplex TPA, both sub-nanosecond decay components, τ_1 and τ_2, are eliminated at 77K and the predominant decay time of 11.3 ns (τ_4) is characteristic of unquenched 2AP. It was inferred that, in this duplex, base motion is required to access any conformation in which 2AP is subject to rapid non-radiative decay, suggesting that, in the absence of neighbouring Gs, greater conformational motion would be required to facilitate charge transfer from G to 2AP through intervening bases.

Although the decay parameters of TPA at 77 K are markedly different from those of GPG and CPC, Neely and Jones argued that this does not mean that the conformational structures adopted by the TPA duplex are significantly different from those of the other

two. In fact, the similarity of the decay parameters of all three duplexes at 293 K suggest that their conformational behaviour is similar. Their interpretation was that the decay time of 2AP in frozen duplexes of similar conformational structure could be quite different, depending on the relative location of 2AP and G. Thus, the absence of τ_2 in TPA at 77 K does not indicate the absence of conformations of similar geometry to those that display lifetimes τ_2 in GPG and CPC, but that 2AP in these frozen conformations of TPA is inaccessible to electron transfer from G and exhibits a longer lifetime. Applying a similar argument, the large amplitude of the 11.3-ns component in APA does not indicate a large population of a conformation with 2AP extrahelical, but shows that in ~80% of the multiplicity of structures represented by τ_2 and τ_3 in GPG and CPC, 2AP in TPA is free from quenching in the rigid duplex.

Although no major perturbation to the DNA structure was observed when 10 M LiCl was used as solvent for 2AP in larger DNA system (those of 10 or more bases or more), Wu[3] found that for 2AP-containing dinucleotides dissolved in 10M LiCl there was a noticeable perturbation to the dinucleotide conformation, manifested by changes in the 2AP decay parameters. In all dinucleotides, the population of the shortest lifetime component increased significantly and, with the exception of 2AP-G, the value of τ_1 decreased substantially, adopting a value of around 60 ps in all cases. It appears that the presence of a high concentration of LiCl greatly enhances interbase quenching in all of the dinucleotides. It was inferred that the highly concentrated LiCl dehydrates the dissolved dinucleotides, so that they exist in a locally hydrophobic environment that promotes interbase stacking and hydrogen-bonding interactions. (This effect is not seen for 2AP in DNA, where the bases within the hydrophobic core of the duplex are shielded from the external solvent environment.)

In the present work, it was found that it was possible to avoid the perturbing effect caused by dissolving samples in 10 M LiCl by using a lower concentration of LiCl that still produced a reproducible transparent glass when frozen. Thus, measurements of 2AP in DNA at low temperatures has highlighted the crucial role played by base dynamics in accessing conformations required for the fast decay processes of 2AP. The work presented in the remainder of this chapter aims to compare the effect of freezing on the time-resolved fluorescence decay of 2AP-labelled single stranded oligonucleotides and their corresponding duplexes, and to re-examine the effect of freezing on 2AP-dinucleotides in the absence of the perturbation caused by 10 M LiCl in previous studies.

4.2. Materials and Methods

4.2.1. Sample Preparation

HPLC-purified 2AP-containing DNA oligonucleotides (ss1-4) and DNA oligonucleotides with complementary sequences (used to anneal ds1-4) were purchased from ATDBio (Southampton, UK). The sequences of the oligomers used for the fluorescence measurements can be found in Table 4.5 where the position of 2AP (**P**) in each oligonucleotide is shown.

Sample	Sequence
ss1	5' GTCGGATCCTCT**P**GATATCTCCATGCTCACTGGTTATAGGAGAATCCGGG 3'
ss2	5' AATCTCACAGCTGATC**P**CATTGCTACATGGAGATATCTAGAGGATCCGAC 3'
ss3	5' CCCGGATTCTCCT**P**TAACCAGTGAGTAGCAATGTGATCAGCTGTGAGATT 3'
ss4	5' CCCGGATTCTCCTATAACCAGTG**P**GTAGCAATGTGATCAGCTGTGAGATT 3'
ds1	5' GTCGGATCCTCT**P**GATATCTCCATGCTCACTGGTTATAGGAGAATCCGGG 3' 3' CAGCCTAGGAGA**T**CTATAGAGGTACGAGTGACCAATATCCTCTTAGGCCC 5'
ds2	5' AATCTCACAGCTGATC**P**CATTGCTACATGGAGATATCTAGAGGATCCGAC 3' 3' TTAGAGTGTCGACTAG**T**GTAACGATGTACCTCTATAGATCTCCTAGGCTG 5'
ds3	5' CCCGGATTCTCCT**P**TAACCAGTGAGTAGCAATGTGATCAGCTGTGAGATT 3' 3' GGGCCTAAGAGGA**T**ATTGGTCACTCATCGTTACACTAGTCGACACTCTAA 5'
ds4	5' CCCGGATTCTCCTATAACCAGTG**P**GTAGCAATGTGATCAGCTGTGAGATT 3' 3' GGGCCTAAGAGGATATTGGTCAC**T**CATCGTTACACTAGTCGACACTCTAA 5'

Table 4.5: Sequences of the 2AP-containing DNA oligomers used in the fluorescence experiments where "P" represents the position where an adenine base has been replaced by 2AP in the sequence. Sequences for 2AP-containing DNA oligomers are shown in 5' to 3' order while the complementary strands of the duplexes (ds1-4) are shown in 3' to 5' order, as labelled.

2AP-containing oligonucleotides were stored as concentrated solutions (~50 μM) in tris buffer (containing 0.02 M Tris-HCl pH 7.5 and 0.1 M NaCl) and diluted for use in experiments using tris buffer.

Studies conducted at room temperature were performed at a 2AP concentration of ~10 μM for samples of single-stranded DNA and ~3.3 μM for duplex samples. Duplexes were annealed by mixing solutions of 2AP-containing oligonucleotides (ss1-4) with the appropriate complementary DNA strand for each in the molar ratio 1:2 and heating to 95°C for 5 minutes before leaving to cool slowly to room temperature overnight.

2AP-containing dinucleotides (2AP-X, where X = adenine (A), cytosine (C), guanine (G), thymine (T) or inosine (I)) were purchased from ATDBio (Southampton, UK). For storage, dinucleotide solutions were kept as concentrated solutions (~500 -1000 μM) in tris buffer (containing 0.02 M Tris-HCl pH 7.5 and 0.1 M NaCl) and diluted for use in UV-

vis absorption measurements (~50 µM) and fluorescence measurements (~10 µM) with tris buffer solution. The structure of the 2AP-dinucleotides can be found previously in Figure 4.1.

4.3. Results and Discussion

4.3.1. Monomeric 2AP and 2AP-riboside

4.3.1.1. Steady-state Fluorescence

A comparison of the normalised excitation spectra for 2AP and 2APr in 6 M LiCl solution, recorded at room temperature and at 77 K is shown in Figure 4.4.

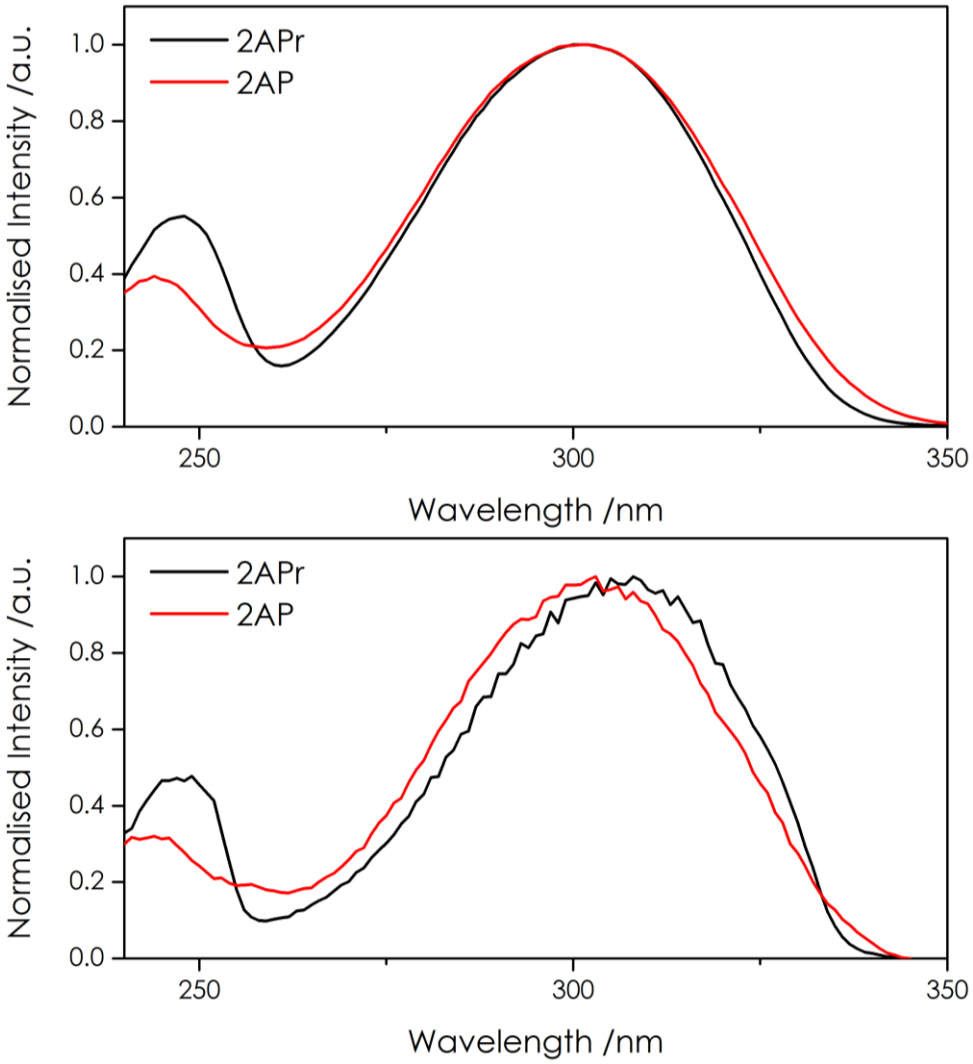

Figure 4.4: Normalised excitation spectra of 2AP and 2APr in aqueous LiCl solution at room temperature monitoring an emission wavelength of 370 nm (top) and at 77 K monitoring an emission wavelength of 355 nm (bottom).

At room temperature, the excitation maximum of both monomeric 2AP and 2APr is located at 302 nm. However, at 77 K, the position of the excitation maximum of 2APr is red-shifted by ~5 nm while no shift is observed for the excitation maximum of 2AP. The positions of the shorter-wavelength excitation peaks (at ~245 nm) of 2AP and 2APr are unaffected by the change in temperature. The typical shift in excitation maxima for solutions of 2AP-DNA is ~20 nm to the red for DNA duplexes when frozen at 77 K,[3,16,17] while a red-shift of ~15 nm is observed for the 2AP-containing dinucleotide samples presented later in this chapter.

The recorded fluorescence emission spectra for 2AP and 2APr in LiCl solution at room temperature and at 77K, excited at 305 nm, are shown in Figure 4.5.

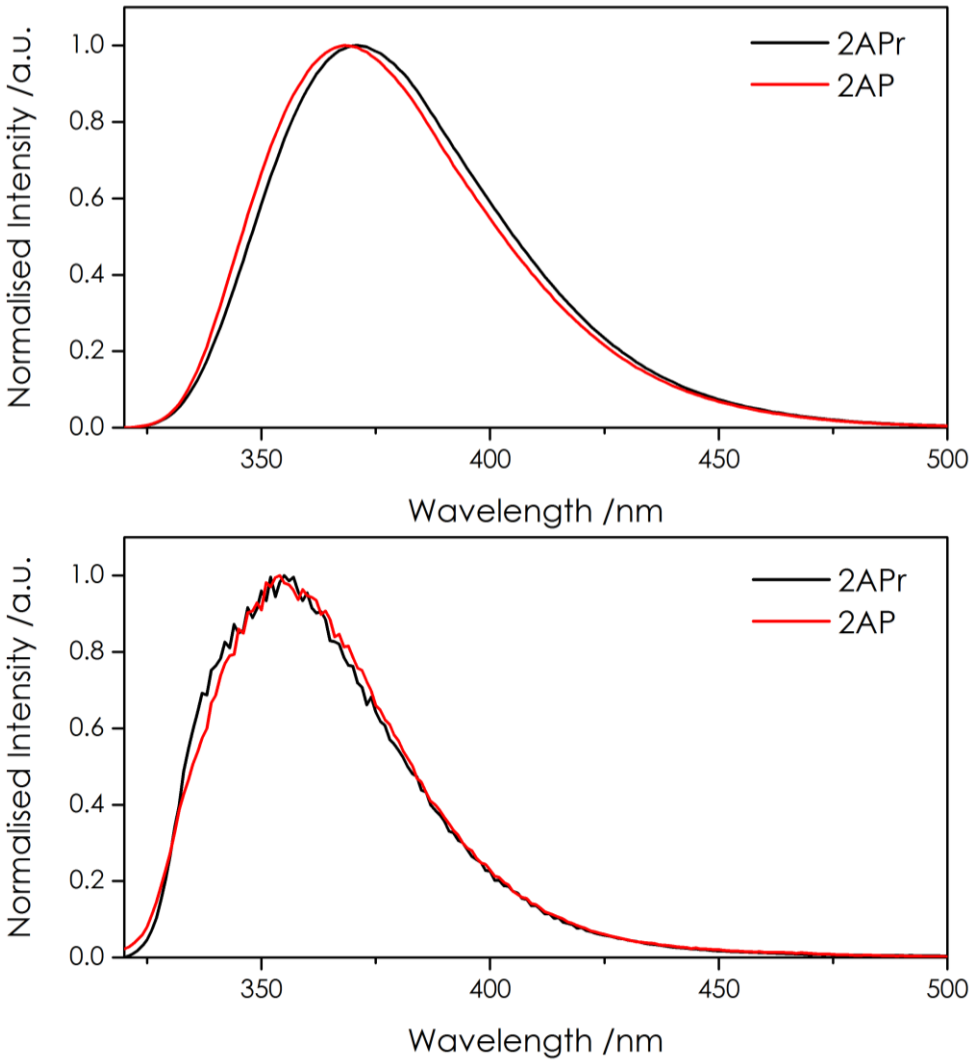

Figure 4.5: Normalised emission spectra of 2AP and 2APr in aqueous LiCl solution at room temperature (top) and at 77 K (bottom) recorded using an excitation wavelength of 305 nm for all measurements shown.

At room temperature, the emission maximum of 2APr is located ~3 nm to the red of that or 2AP while at 77 K, no differences were found between the emission spectra of 2AP and 2APr. Comparing the emission spectra obtained at room temperature to that obtained for 2AP and 2APr at 77 K, at 77 K the emission peaks are blue-shifted by ~15 nm and the maximum of the emission band of each is now located at ~355 nm. A blue-shift in emission maxima is a typical observation for frozen measurements due to the removal of dynamic solvent-interactions and discussed further in the context of the 2AP-containing dinucleotides in Section 4.3.3.2.

4.3.1.2. Time-resolved Fluorescence

Figure 4.6 shows the fluorescence decay curves for 2AP and 2APr at room temperature, in tris buffer and aqueous 6 M LiCl solution, and at 77K in frozen aqueous LiCl glass. The corresponding decay parameters are shown in Table 4.6.

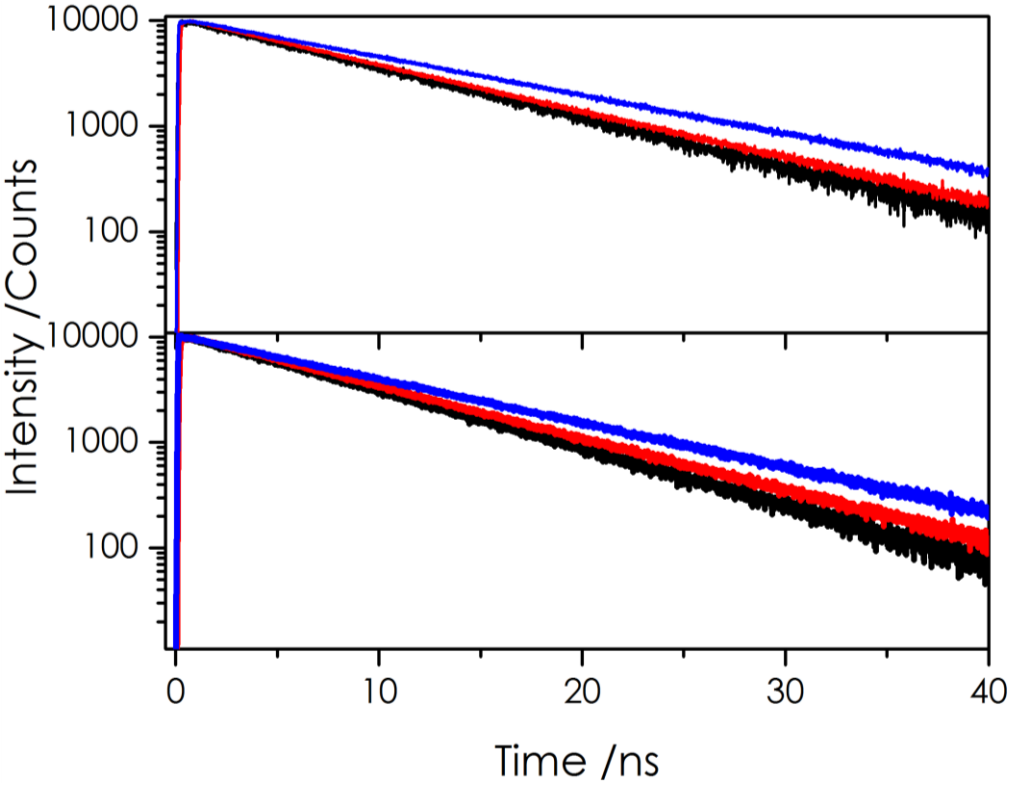

Figure 4.6: Fluorescence decay curves for 2AP (top) and 2APr (bottom) at room temperature in tris buffer (blue) and 6M LiCl solution (black), and at 77K in frozen 6M LiCl glass (red).

For 2AP and 2APr, the presence of LiCl causes a noticeable reduction (~25%) in the fluorescence lifetime at room temperature. This is consistent with the findings of Wu,[3] and Jones and Neely,[14] indicating that 2AP experiences a less protic environment in

the presence of a high concentration of LiCl. When frozen at 77 K, the average fluorescence lifetimes of 2AP and 2APr increase by ~5% and ~9% respectively. In the case of monomeric 2AP at 77 K, the lifetimes associated with the two tautomers (9H and 7H) can be resolved (8.6 ns and 11.8 ns respectively). The fluorescence decay of 2APr at 77 K is shown to be mono-exponential. This is due to the presence of only the 9H-tautomer of 2AP, as formation of the 7H tautomer is prevented by bonding of the ribosyl group at position N7 (Figure 2.13). It is evident that 2APr is more appropriate to use than 2AP as a reference when examining the effects of interbase interaction on the photophysics of 2AP, since its steady-state and time-resolved fluorescence properties more closely mimic those of 2AP in an oligonucleotide.

Sample		τ_i /ns		A_i		$<\tau>$ (ns)
		τ_1	τ_2	A_1	A_2	
2AP	Tris, RT	-	11.9	-	1.00	11.9
	LiCl, RT	-	9.2	-	1.00	9.2
	LiCl, 77 K	8.6	11.8	0.68	0.32	9.6
2APr	Tris, RT	-	10.4	-	1.00	10.4
	LiCl, RT	-	8.0	-	1.00	8.0
	LiCl, 77 K	8.7	-	1.00	-	8.7

Table 4.6: Fluorescence decay parameters for 2AP and 2APr in aqueous tris buffer or 6M aqueous LiCl at room temperature (RT) and in 6M LiCl at 77 K. An excitation wavelength of 310 nm was used for all measurements. The decay parameters were determined from individual fits of fluorescence decays and were recorded using an emission wavelength of 380 nm. Experimental uncertainties (estimated by dividing the standard deviation of values by the corresponding values): $\tau_1 \leq 1\%$, $\tau_2 \leq 1\%$, $A_1 \leq 2\%$, $A_2 \leq 2\%$.

4.3.2. 2AP-containing Oligonucleotides

4.3.2.1. Fluorescence Decay Parameters at Room Temperature

Initial studies were performed for 2AP-oligonucleotides in aqueous 6M LiCl at room temperature in order to compare the fluorescence decay parameters with those measured previously by Ma in aqueous buffer,[6] and to confirm that no major perturbation to the DNA structure was caused by the presence of LiCl at this concentration. The decay parameters reported previously by Ma are shown in Table 4.7.

As described previously in Chapter 2, the formation of DNA duplex structure from component single-stranded DNA, reduces the average observed lifetime of 2AP in DNA. This reduction in average lifetime results from a shift in populations of 2AP that are in unstacked (or imperfectly stacked) conformations to those that are better stacked in the

DNA helix. A higher degree of base stacking results in greater interaction of 2AP with neighbouring bases and leads to quenching of the fluorescence and results in shorter fluorescence lifetimes. Characteristic of single-stranded DNA is the observation of a lower population of 2AP in well-stacked conformations than for 2AP in double-stranded DNA. An associated increase in the population of weakly stacked or extra-helical 2AP results from the increased degree of flexibility of the bases in single-stranded DNA compared to double-stranded DNA.[33]

Sample	2AP Sequence Context	τ_l /ns				A_i				$<\tau>$ /ns
		τ_1	τ_2	τ_3	τ_4	A_1	A_2	A_3	A_4	
ss1	T**P**G	0.07	0.66	2.5	7.4	0.69	0.13	0.13	0.05	0.83
ds1	(ATC)	0.08	0.50	2.9	10.2	0.70	0.18	0.09	0.04	0.82
ss2	C**P**C	0.10	0.63	2.5	7.4	0.57	0.20	0.17	0.06	1.05
ds2	(GTG)	0.04	0.38	2.8	10.5	0.76	0.18	0.04	0.02	0.42
ss3	T**P**T	0.06	0.53	2.1	5.4	0.64	0.13	0.18	0.05	0.75
ds3	(ATA)	0.08	0.35	2.5	9.1	0.53	0.41	0.04	0.01	0.38
ss4	G**P**G	0.07	0.69	2.9	7.6	0.64	0.14	0.15	0.07	1.11
ds4	(CTC)	0.07	0.45	2.6	8.8	0.65	0.20	0.11	0.04	0.77

Table 4.7: 2AP sequence context and fluorescence decay parameters for 2AP-labelled ss and ds oligomers in aqueous buffer solution at room temperature. The sequence context of the 2AP base (P) in each single strand (ss1 – ss4) is shown and the complementary sequence in the double strand (ds1-ds4) is given in brackets. The full sequence of the 50 bases in each oligonucleotide can be found in Table 4.5. The reported A factors are the average of the global fitting results from emission at 370, 380 and 390 nm (which showed minimal wavelength-dependence). The values for the τ and A have been taken from the thesis of Ma,[6] while the sample names have been changed to match the nomenclature used in the present studies.

The decay parameters for ds1 and ds4 show little difference in the A factors compared to their single-stranded counterparts (ss1 and ss4, respectively). The sequences of ss1 and ss4 (shown in Table 4.5) show that a G base is already within close proximity to 2AP and thus are already heavily quenched by a nearby G base before the formation of the duplex. No G base is present in the immediate environment of 2AP in the sequence of ss2 but once annealed to form the ds2 duplex, the complementary strand introduces two G bases into close proximity of 2AP. On the other hand, the sequences of ss3 and ds3 show no G bases in close proximity to 2AP and thus the decay parameters do not possess a high population of the highly quenched conformations of 2AP, as was found for the other strands and duplexes containing G in proximity to 2AP. The decay

parameters for ds3, however, show an unusual population distribution for τ_1 and τ_2 (0.53 and 0.41 respectively) which is atypical of 2AP in DNA duplexes where the local conformation of 2AP is expected to be highly stacked and the 2AP fluorescence well quenched (with $A_1 \gtrsim 60\%$ and $A_2 \lesssim 20\%$). Despite this, these findings are consistent with previous studies of DNA duplexes containing ATAT/TATA sequences involving 2AP (where one A base has been substituted for 2AP). In regions containing the 2AP-containing ATAT motif, unusual conformations have been reported in which 2AP is found to be highly constrained and a red-shift in its fluorescence excitation maxima was indicative of reduced solvent exposure.[34]

The recorded decay curves for all 2AP-containing oligomers were similar and those for ss1 and ds1 in 6 M LiCl are shown in Figure 4.7, while the decay curves for the remainder of the oligonucleotides and duplexes can be found in Appendix I (Figures I.1 and I.2).

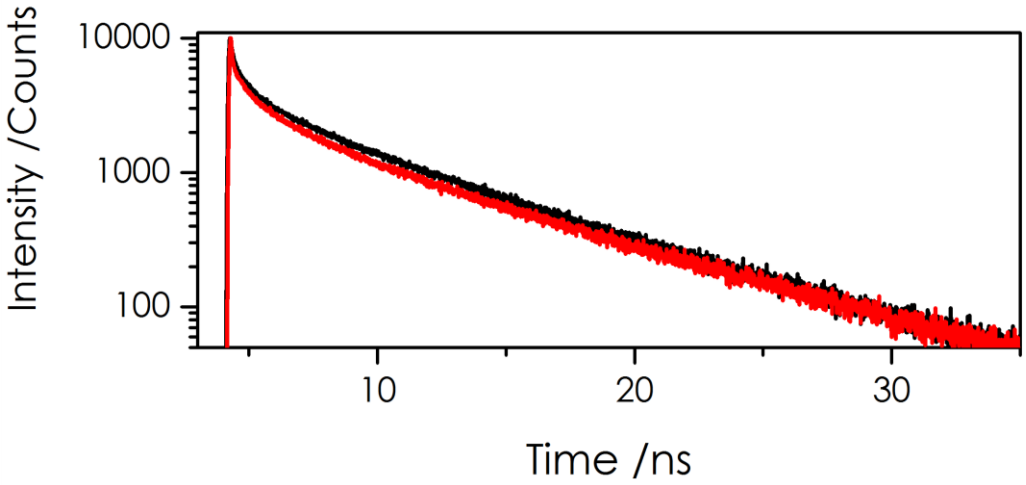

Figure 4.7: Fluorescence decay curves for ss1 (black) and ds1 (red) in aqueous LiCl at room temperature, for excitation at 310 nm and emission at 380 nm.

The fluorescence decay parameters of the four ss oligonucleotides and their corresponding duplexes are shown in Table 4.8.

Sample	2AP Sequence Context	τ_i /ns				A_i				< τ > /ns
		τ_1	τ_2	τ_3	τ_4	A_1	A_2	A_3	A_4	
ss1	T**P**G	0.09	0.59	3.1	7.9	0.53	0.21	0.12	0.14	1.65
ds1	(ATC)	0.04	0.55	2.9	8.4	0.70	0.13	0.09	0.08	1.03
ss2	C**P**C	0.09	0.65	3.3	7.9	0.47	0.19	0.13	0.21	2.25
ds2	(GTG)	0.04	0.48	2.7	8.3	0.90	0.04	0.03	0.03	0.39
ss3	T**P**T	0.10	0.60	2.8	7.3	0.52	0.24	0.13	0.11	1.36
ds3	(ATA)	0.18	0.58	1.9	7.7	0.33	0.62	0.03	0.02	0.63
ss4	G**P**G	0.07	0.57	3.2	7.7	0.56	0.14	0.11	0.19	1.93
ds4	(CTC)	0.06	0.71	3.5	8.6	0.61	0.16	0.12	0.11	1.51

Table 4.8: Fluorescence decay parameters for 2AP-labelled oligomers in 6M LiCl at room temperature. The sequence context of the 2AP base (P) in each single strand (ss1 – ss4) is shown and the complementary sequence in the double strand (ds1-ds4) is given in brackets. The full sequence of the 50 bases in each oligonucleotide can be found in Table 4.5. Experimental uncertainties (estimated by dividing the standard deviation of values by the corresponding values): $\tau_1 \leq 20\%$, $\tau_2 \leq 6\%$, $\tau_3 \leq 1\%$, $\tau_4 \leq 1\%$, $A_1 \leq 2\%$, $A_2 \leq 1\%$, $A_3 \leq 1\%$, $A_4 \leq 1\%$.

Overall, only a minimal perturbation of the DNA structure (and hence on the fluorescence decay parameters of 2AP in these oligonucleotides) is caused by dissolving the samples in 6 M LiCl. In LiCl, there is an increase of a factor of approximately 1.5-2 in the average fluorescence lifetime for 2AP in the ss and ds oligomers alike. This arises mainly from an increase in the population of longest lifetime component (A_4). ds2 is unique in retaining a very low value of A_4 in LiCl, and hence a negligible increase in average lifetime, <τ>, is observed. Relative to unquenched 2APr, the increase in <τ> amounts only to ~8-16% for single stranded DNA samples and approximately 4-10% double-stranded samples. For ds-DNA samples, the lifetime of extra-helical 2AP, τ_4, typically shortens from ~9-10 ns (in buffer) to ~7-8 ns (in LiCl). The shortening of τ_4 reflects the difference in the solution-phase environment experienced by extra-helical 2AP in the two solvents. In ss-DNA samples, the presence of LiCl has minimal effect on τ_4, which, in buffer, is already shorter than in the ds-DNA because the 2AP base does not fully escape from stacking-interactions with other bases in the ss oligonucleotides (evident from the values of τ_4 in Table 4.7 and Table 4.8).[10] Base-pairing of one DNA strand with another, to create a DNA duplex, and intra-strand stacking interactions between bases, causes the DNA bases involved to be more ordered and less conformationally flexible. This consequently results in a lower population of 2AP conformations that are extra-helical but those that do adopt this conformation will be

free from stacking interactions (since neighbouring bases will be held in place due to their own base-pairing and stacking interactions) and thus display longer fluorescence lifetimes. In general, the presence of LiCl has little effect on the conformational populations (A factors), as expected based on the minimal influence caused by previous studies' use of 10 M LiCl. However, in the case of ds2, there is a considerable transfer of population from τ_2 to τ_1 (approximately 14%).

4.3.2.2. Fluorescence Decay Parameters at 77 K

A comparison of the fluorescence decay curves at room temperature and 77 K for ss1 and ds1 is shown in Figure 4.8, while Figures I.3 and I.4 (in Appendix I) show the effect of freezing on the fluorescence decay curves of the other 2AP-oligonucleotides. The corresponding fluorescence decay parameters can be found in in Table 4.9 alongside those for the other 2AP-containing oligonucleotides in aqueous 6 M LiCl and frozen at 77 K.

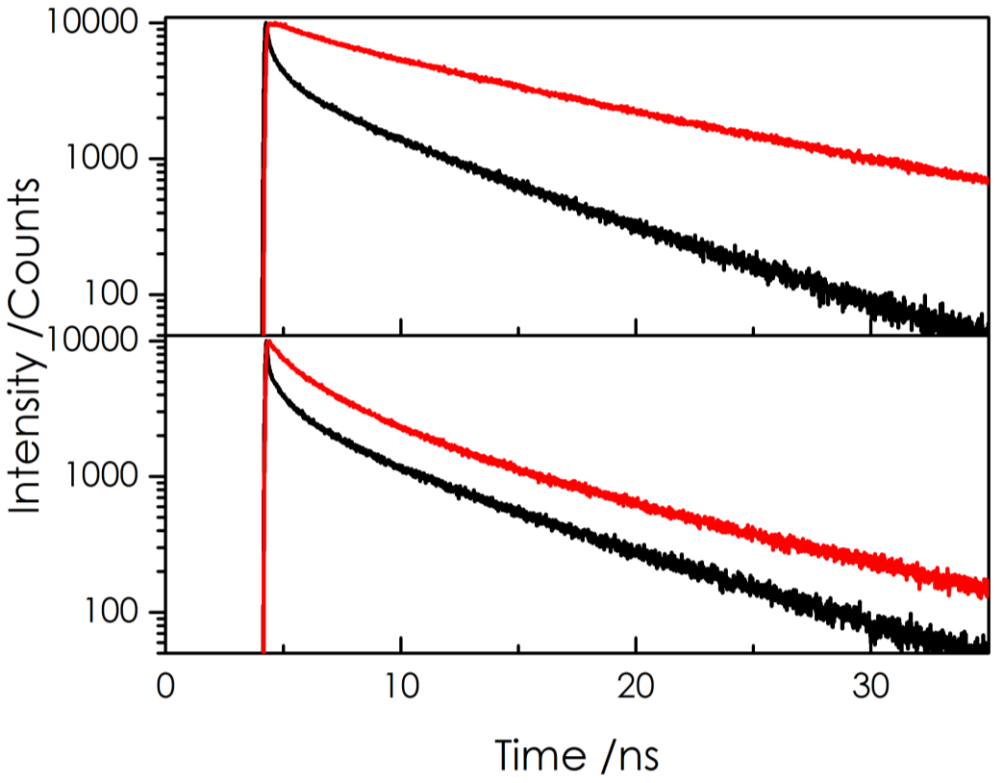

Figure 4.8: Fluorescence decay curves recorded at room temperature (black) and at 77 K (red) for ss1 (top) and ds1 (bottom) in aqueous 6 M LiCl. Excitation and emission wavelength were 310 nm and 380 nm respectively.

Sample	2AP Sequence Context	τ_i /ns				A_i				< τ > /ns
		τ_1	τ_2	τ_3	τ_4	A_1	A_2	A_3	A_4	
ss1	T**P**G	-	0.51	4.7	13.1	-	0.13	0.25	0.62	9.36
ds1	(ATC)	-	0.54	3.1	10.5	-	0.31	0.49	0.20	3.79
ss2	C**P**C	-	0.56	4.8	11.1	-	0.14	0.33	0.53	7.55
ds2	(GTG)	-	0.47	3.1	10.2	-	0.40	0.37	0.23	3.68
ss3	T**P**T	-	-	3.8	11.7	-	-	0.24	0.76	8.76
ds3	(ATA)	-	-	2.9	10.6	-	-	0.16	0.84	9.37
ss4	G**P**G	-	0.72	4.9	14.8	-	0.20	0.31	0.49	8.92
ds4	(CTC)	-	0.43	3.0	10.4	-	0.46	0.41	0.13	2.78

Table 4.9: Fluorescence decay parameters for 2AP-oligonucleotides in aqueous 6 M LiCl solution frozen at 77 K. Decay parameters were determined from global fits of the decay curves recorded at three emission wavelengths (360 nm, 380 nm, and 400 nm) and the reported A factors are those resulting from the 380 nm emission. Little wavelength-dependence in the A factors was observed. Experimental uncertainties (estimated by dividing the standard deviation of values by the corresponding values): $\tau_2 \leq 4$ %, $\tau_3 \leq 2$%, $\tau_4 \leq 1$%, $A_2 \leq 1$%, $A_3 \leq 1$%, $A_4 \leq 1$%.

Consistent with the findings of Neely and Jones,[14] when 2AP-containing oligonucleotides are frozen in LiCl at 77 K, the heterogeneity of 2AP fluorescence decay persists but the shortest lifetime, τ_1, vanishes. As the measured fluorescence decays typically require three components for an adequate fit, it shows that, when incorporated into DNA, 2AP has a number of distinct sets of distributions of conformations that can be characterised by three distinct fluorescence lifetimes. For ss3 and ds3, where no G is present in close proximity to 2AP, the shortest lifetimes (τ_3 in these samples) presents as more than an order of magnitude longer than for oligomers where there is a G in close proximity to 2AP. This is consistent with the room temperature results (where a nearby G allows for very fast quenching of the excited-state) and with the findings of Neely and Jones (in which the duplex with a similar 2AP sequence context, "TPT", only required two components for an adequate fit). The observation, at 77 K, of τ_4 values that are greater than the lifetime of unquenched 2APr will be discussed below, in the context of similar behaviour observed for 2AP-containing dinucleotides.

4.3.2.3. The Effect of Freezing

It is clear from the fluorescence decay curves shown in Figure 4.8 that there is a pronounced effect caused by freezing to the fluorescence decay of the 2AP-oligonucleotides.

When comparing the lifetimes of τ_2 and τ_3 at room temperature with those determined at 77 K, the values determined are nearly identical for individual samples. This indicates that these intermediate lifetimes result from the presence of the same conformations of bases at 77 K as at room temperature and thus accessing these conformations does not rely on conformational motions. Because of the consistency in lifetimes despite of the removal of conformational motions, it is implied that these intermediate decay parameters relate to intrinsic conformations of 2AP whose populations are constant on the time scale of the excited-state decay.

The elimination of τ_1 for oligonucleotides in which 2AP is in close proximity to G at 77 K confirms that base dynamics are a requirement for rapid quenching of 2AP fluorescence in DNA via charge-transfer. The removal of conformational motions inhibits the access of the bases to the required conformations for fast decay of the excited-state of 2AP and shows that these conformations are not present in the absence of thermal fluctuations. These findings support the suggestion by O'Neill *et al.*[15] that charge transfer in DNA is conformationally gated and that the fastest quenching rates do not correspond with the lowest energy conformations. For ss3 and ds3, where only A and T bases are in proximity to 2AP, the additional elimination of τ_2 at 77 K demonstrates that in the absence of G, conformational motions are essential for efficient sub-nanosecond quenching of 2AP. The persistence of τ_3 for all oligonucleotides at 77 K demonstrates that nonradiative decay of 2AP can still occur despite the absence of G. Further discussion on the possible origin of τ_3 will feature in the following section on 2AP-dinucleotides. The findings here for the time-resolved fluorescence of 2AP-oligonucleotides at 77 K are consistent with the time-resolved fluorescence studies of 2AP-duplexes at 77 K conducted by Neely and Jones and those conducted by O'Neill and Barton.[14–16]

4.3.3. 2AP-containing Dinucleotides

4.3.3.1. Steady-State Fluorescence at Room Temperature

The steady-state fluorescence properties of the 2AP-containing dinucleotides were investigated and compared to those of 2APr. The excitation and emission spectra for the dinucleotides in aqueous buffered solution are shown in Figure 4.9 and the corresponding normalised excitation and emission spectra can be found in Figure I.5 in Appendix I.

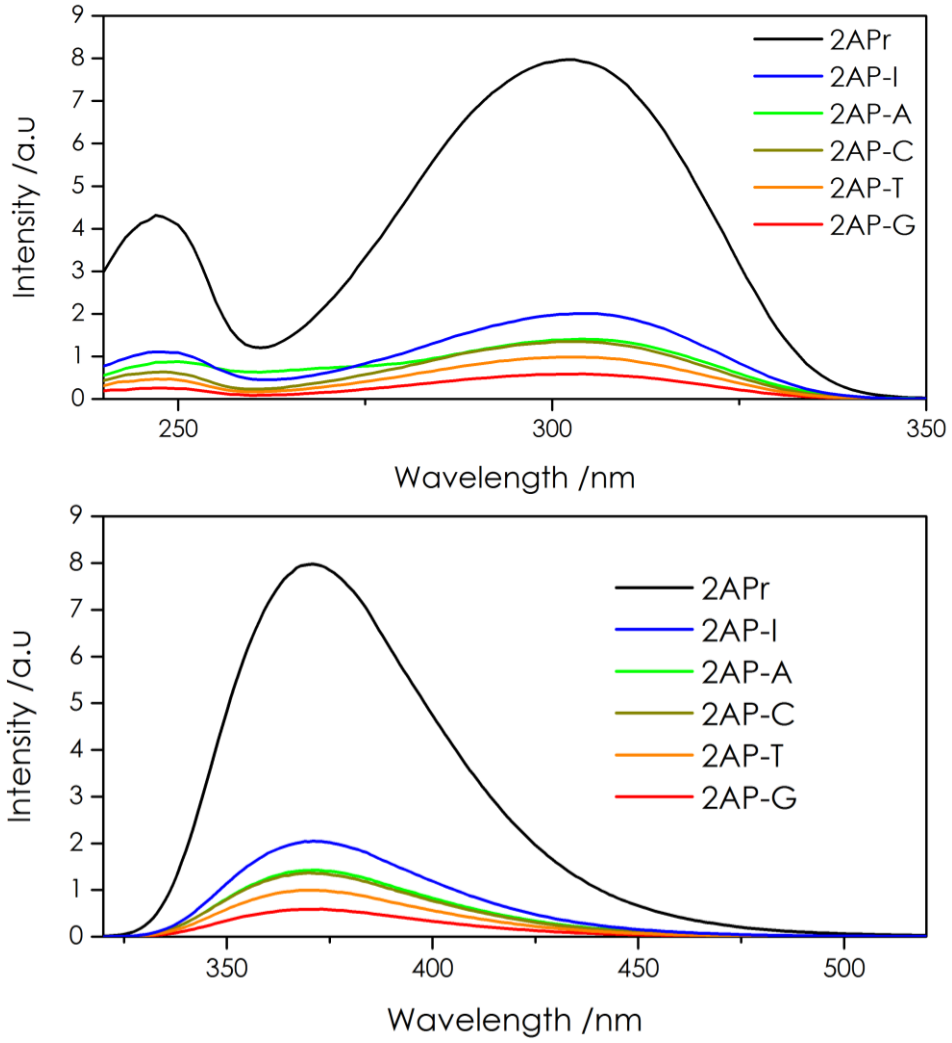

Figure 4.9: Top: Excitation spectra of 2APr and dinucleotides 2AP-X in aqueous tris buffer at room temperature with an emission wavelength of 370 nm. Bottom: Emission spectra of 2APr and dinucleotides 2AP-X in aqueous tris buffer at room temperature with an excitation wavelength of 305 nm. The orders of the samples in the legends reflect the orders of the intensities at the maximum wavelength in each set of spectra.

The spectra presented are characteristic of 2AP excitation and emission spectra,[1] with excitation maxima at ~305 nm and emission maxima at ~ 370 nm. The level of quenching

of 2AP by the accompanying base in the dinucleotides is in alignment with the trend of redox potentials presented in Table 4.1, where G is the most quenching and I is the least (G>T>C>A>I). The small peak in the excitation spectra of 2AP-A at ~260 nm is related to energy transfer and thus will be discussed in Chapter 5.

To determine any major differences in the spectral profiles caused by the presence of LiCl (in preparation for low temperature measurements), fluorescence excitation and emission spectra for 2APr and the dinucleotides in aqueous LiCl solution were recorded and are shown in Figure 4.10 while the corresponding normalised spectra can be found in Figure I.6 in Appendix I.

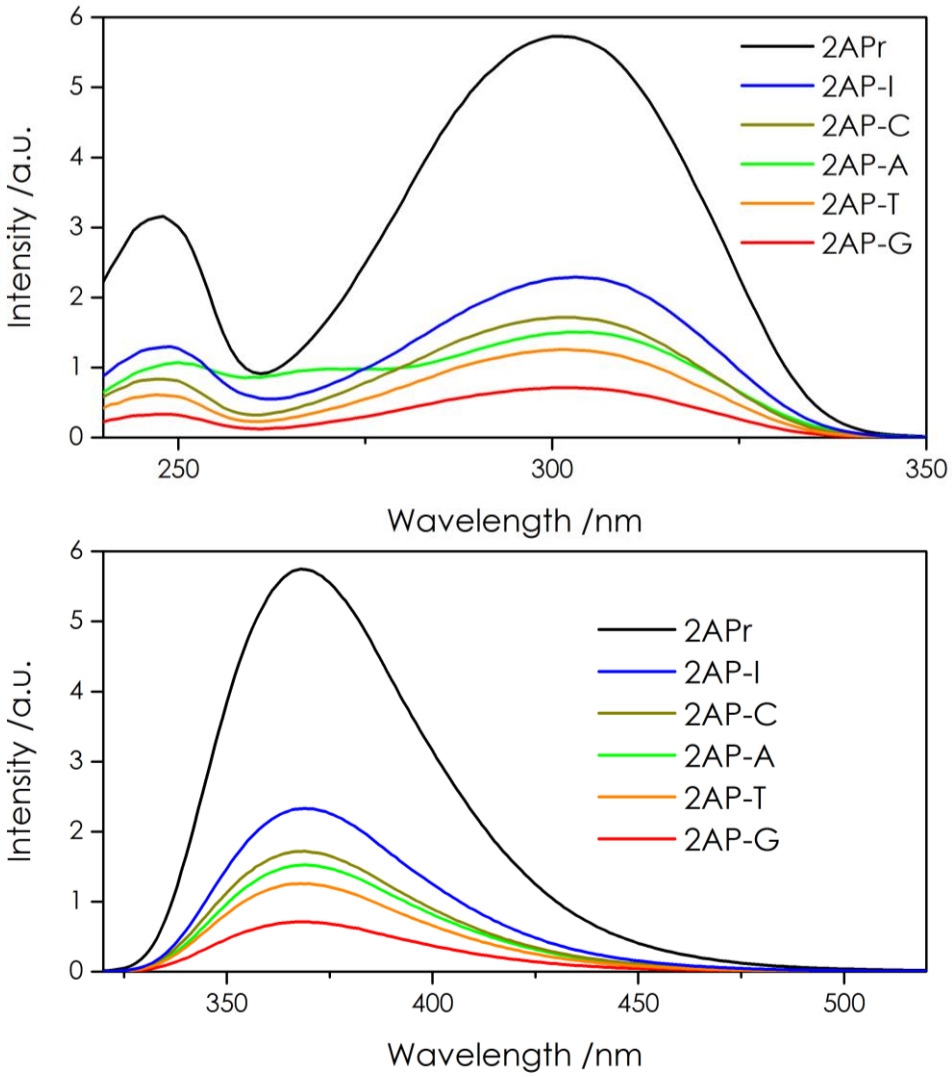

Figure 4.10: Top: Excitation spectra of 2APr and dinucleotides 2AP-X in aqueous LiCl solution at room temperature with an emission wavelength of 370 nm. Bottom: Emission spectra of 2APr and dinucleotides 2AP-X in aqueous LiCl solution at room temperature with an excitation wavelength of 305 nm. The orders of the legends reflects the orders of the intensities at the maximum wavelength in each set of spectra.

The spectral profiles of the dinucleotides in LiCl are consistent with those measured in tris buffer and differences in fluorescence intensities can be attributed to the presence of LiCl solvent. Key differences are that the fluorescence quantum yield (FQY) of all of the dinucleotides increases slightly (by ~10-20%) while the FQY of 2APr is decreased slightly (by ~30%) (similar to the shortening of the fluorescence lifetime of 2APr by the presence of LiCl shown in Table 4.6). The reasons behind this have been covered in Section 4.3.2.1 where the effect of LiCl on the fluorescence lifetimes of 2AP in DNA has been discussed. A comparison of the fluorescence quantum yields for the dinucleotides in tris buffer with those in LiCl solution (relative to 2APr) is shown in Table 4.10.

Sample	In Tris Buffer		In LiCl	
	Φ_{rel} (to 2APr)	Φ_{rel} (to 2AP-I)	Φ_{rel} (to 2APr)	Φ_{rel} (to 2AP-I)
2AP-G	0.07	0.29	0.12	0.31
2AP-T	0.12	0.49	0.22	0.54
2AP-C	0.17	0.67	0.30	0.74
2AP-A	0.18	0.70	0.27	0.65
2AP-I	0.26	1.00	0.41	1.00
2APr	1.00	3.89	1.00	2.47

Table 4.10: Quantum yield ratios of fluorescence intensities of dinucleotides relative to 2APr and 2AP-I in aqueous buffer and LiCl solution.

For most of the dinucleotides, there is an almost 2-fold increase in the intensity ratios relative to the respective solutions of 2APr (in buffered solution or in LiCl solution). This can be explained as a cumulative effect of a slight increase in the FQY of the 2AP dinucleotides accompanied with a slight decrease in the FQY of 2APr (caused by the LiCl solvent). Also shown in Table 4.10 are ratios of the fluorescence intensities relative to that of 2AP-I. A comparison of the emission intensities relative to that of 2AP-I reveals that the presence of LiCl has little effect on the relative quenching efficiencies of the different partner bases, implying that the charge-transfer quenching mechanism is unperturbed by the LiCl.

4.3.3.2. Steady-State Fluorescence at 77 K

Figure 4.11 shows the excitation and emission spectra for the dinucleotides in aqueous LiCl solution recorded at 77 K (the associated room temperature measurements can be found in Figure 4.10). The steady-state excitation and emission spectra for the dinucleotides frozen at 77 K normalised to the characteristic 2AP fluorescence peaks can

be found in Figure I.7 in Appendix I. The steady-state fluorescence excitation and emission spectra for LiCl solvent at room temperature and at 77 K can be found in Figure

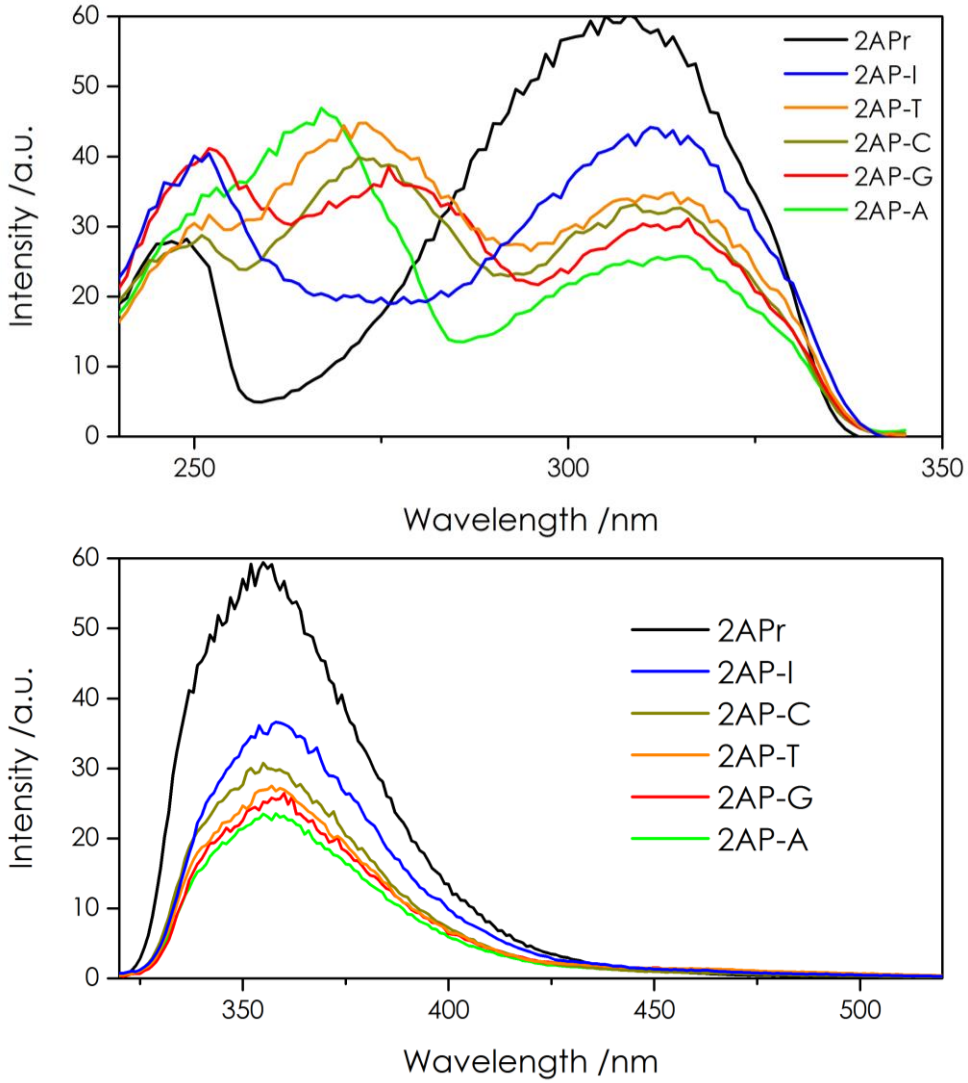

Figure 4.11: Top: Excitation spectra of 2APr and dinucleotides 2AP-X in aqueous LiCl solution buffer at 77 K recorded observing an emission wavelength of 355 nm. Bottom: Emission spectra of 2APr and dinucleotides 2AP-X in aqueous LiCl at 77 K with an excitation wavelength of 305 nm. The orders of the legends reflects the orders of the intensities at the maximum wavelength in each set of spectra.

I.8 in Appendix I and show minimal contribution to the spectra shown here.

It is evident from the low-temperature excitation spectra, in Figure 4.11, that the spectral properties of the dinucleotides become much more complex at 77 K and that excitation of species other than the 2AP moiety can lead to fluorescence emission from 2AP. The mechanism of electronic energy transfer from DNA bases to 2AP within the dinucleotides will be discussed in further detail in Chapter 5. The excitation peaks of all

the dinucleotides are red-shifted by ~10 nm on freezing, whereas the excitation band of 2APr is shifted by ~5 nm, relative to the corresponding bands at room temperature. The emission bands of the dinucleotides and 2APr are all blue-shifted by ~15 nm, relative to emission bands at room temperature. This is characteristically observed when samples are frozen and solvent relaxation is removed.[14,16,35] Table 4.11 shows the ratios of the peak emission intensities relative to 2APr and 2AP-I at 77 K.

Sample	Φ_{rel} (to 2APr)	Φ_{rel} (to 2AP-I)
2AP-G	0.4	0.7
2AP-T	0.5	0.8
2AP-C	0.5	0.8
2AP-A	0.4	0.6
2AP-I	0.6	1.0
2APr	1.0	1.6

Table 4.11: Quantum yield ratios of dinucleotides 2AP-X in aqueous LiCl solution frozen at 77 K relative to 2APr, relative to 2AP-I at 77K and relative to fluorescence emission intensity at room temperature. Uncertainty in these values are estimated to be ~30% due to issues inherent to the low-temperature set-up.

At 77 K, where conformational motions are removed, emission from 2AP in the dinucleotides is still quenched by the neighbouring base by ~50%. However, this is an increase from those determined at room temperature, suggesting that conformational motions are required to achieve efficient quenching of 2AP by the neighbouring base. It should be noted that a high degree of uncertainty is present in the values presented in Table 4.11, stemming from issues inherent to low temperature measurements (mentioned in Chapter 3). Despite this, it is clear that there is distinct increase compared to the QY ratios determined at room temperature with QY ratios.

4.3.3.3. Time-resolved Fluorescence at Room Temperature

The fluorescence decay parameters of the 2AP-containing dinucleotides in aqueous buffer at room temperature are shown in Table 4.12.

X	τ_i /ns				A_i				<τ> / ns
	τ_1	τ_2	τ_3	τ_4	A_1	A_2	A_3	A_4	
G	0.05	0.29	1.7	9.3	0.64	0.12	0.20	0.04	0.77
T	0.07	0.37	2.3	9.2	0.53	0.10	0.34	0.03	1.13
C	0.09	0.47	2.4	9.0	0.46	0.10	0.41	0.03	1.34
A	0.12	0.67	2.2	9.3	0.38	0.35	0.18	0.09	1.51
I	0.12	0.85	3.0	8.7	0.31	0.20	0.42	0.07	2.08

Table 4.12: Fluorescence lifetimes, τ_i, and corresponding fractional amplitudes, A_i, of dinucleotides 2AP-X in aqueous buffer solution at room temperature using an excitation wavelength of 310 nm. Decay parameters were determined from globally fitting the decays collected at 360 nm, 380 nm and 400 nm; the A factors (which showed little wavelength-dependence) are quoted for 380-nm emission. Experimental uncertainties (estimated by dividing the standard deviation of values by the corresponding values): $\tau_1 \leq 20\%$, $\tau_2 \leq 10\%$, $\tau_3 \leq 1\%$, $\tau_4 \leq 1\%$, $A_1 \leq 2\%$, $A_2 \leq 2\%$, $A_3 \leq 3\%$, $A_4 \leq 1\%$.

The fluorescence decay parameters determined in this work for 2AP-containing dinucleotides are generally in good agreement with those determined by Somsen *et al.*,[18] Wu,[3] and Smith,[28] and minor differences can be accounted for by taking into account the slight differences in experimental conditions (pH or the presence of buffer). The lifetime values of the four-component fits fall in the range of the typical values found for 2AP in DNA. Four-component fits were clearly required to adequately describe the decay functions for the dinucleotides where X = C, G or T. However, for the dinucleotides where X = A or I, the situation was less clear-cut and a three-component fit could be considered to give an adequate description of the fluorescence decay (with χ^2 values of 1.056 and 1.164 for 2AP-A and 2AP-I respectively). However, for consistency and ease of comparison between the different dinucleotides under different experimental conditions, four component fits were adopted for all dinucleotides studied. (The three-component fits for 2AP-A and 2AP-I can be found in Tables I.1 and I.2 in Appendix I.) It is noted that, as previously shown in Table 4.2, Wu reported three-component decays for 2AP-A and 2AP-I, whereas both Somsen and Smith reported four-component decays.

The quantum yields of the dinucleotides, relative to that of 2APr are shown in Table 4.13. The relative quantum yields were determined by two alternative methods: the value obtained from the average lifetimes is denoted ϕ_{fit} and the value obtained from steady-state intensities is denoted ϕ_{rel}. It can be seen that there is good agreement

between the two values for each of the dinucleotides, indicating the absence of any shorter lifetime components that might be beyond the resolution of the TCSPC system used here.

Sample	ϕ_{fit}	ϕ_{rel}
2AP-G	0.07	0.07
2AP-T	0.11	0.12
2AP-C	0.13	0.17
2AP-A	0.15	0.18
2AP-I	0.20	0.26
2APr	1.0	1.0

Table 4.13: Quantum yields of 2AP-X relative to 2APr, for buffer solutions at room temperature. ϕ_{fit} was determined from average lifetimes and ϕ_{rel} was determined from steady-state intensities.

For 2AP-A and 2AP-I, the lifetimes associated with highly stacked conformations τ_1, are significantly longer than those determined for the other dinucleotides. In this respect, the present results differ from those of Somsen *et al*.[18] (shown in Table 4.2) who reported very short values of τ_1 (20-30 ps) for all the dinucleotides, although the values of A_1 reported by Somsen *et al*. are consistent with those presented here. The present results are in line with those of Smith[28] who also found τ_1 for 2AP-A to be significantly longer than that for 2AP-G. All of these studies are consistent in showing that the specific conformations required for the very fast decay of the excited states of 2AP-A and 2AP-I constitute a smaller fraction of the total conformational population than in the other dinucleotides. This is consistent with a low driving force for charge transfer in 2AP-A and 2AP-I. Conversely, in 2AP-G where the driving force for charge transfer is greatest, a wider range of conformations are associated with the fast decay component, since charge transfer can occur without the need for such a high degree of base-stacking to be present.

In preparation for low temperature measurements, fluorescence decay curves for 2AP-dinucleotides in aqueous LiCl were recorded and Table 4.14 shows the resulting decay parameters.

X	τ_i /ns				A_i				<τ> / ns
	τ_1	τ_2	τ_3	τ_4	A_1	A_2	A_3	A_4	
G	0.07	0.67	3.1	7.7	0.53	0.11	0.23	0.13	1.82
T	0.06	0.68	3.6	6.4	0.43	0.10	0.38	0.09	2.04
C	0.12	0.82	3.8	7.5	0.27	0.14	0.50	0.09	2.72
A	0.08	0.76	3.0	7.7	0.14	0.50	0.20	0.16	2.22
I	0.03	0.90	3.1	6.0	0.15	0.28	0.35	0.22	2.66

Table 4.14: Fluorescence lifetimes, τ_i, and corresponding fractional amplitudes, A_i, of dinucleotides 2AP-X in aqueous LiCl solution at room temperature using an excitation wavelength of 310 nm. Decay parameters were determined from globally fitting the decays collected at 360 nm, 380 nm and 400 nm; the A factors showed minimal wavelength-dependence, and A factors are quoted for 380-nm emission. Experimental uncertainties (estimated by dividing the standard deviation of values by the corresponding values): $\tau_1 \leq 10\%$, $\tau_2 \leq 5\%$, $\tau_3 \leq 1\%$, $\tau_4 \leq 1\%$, $A_1 \leq 1\%$, $A_2 \leq 2\%$, $A_3 \leq 3\%$, $A_4 \leq 2\%$.

The fluorescence decay parameters shown in Table 4.14 are in generally good agreement with those determined in tris buffer (Table 4.12), demonstrating that LiCl at a concentration of 6 M does not substantially alter the decay characteristics. However, some changes in lifetimes and conformational populations are observed. The presence of LiCl has the effect of shortening τ_4, as observed for oligonucleotides, due to the change in solvent environment of unstacked 2AP. There is also an increase in the fractional population of τ_4. For 2AP-G, 2AP-T and 2AP-C, there are significant increases in τ_2 and τ_3 and a transfer of population from well-stacked conformations (τ_1) to poorly stacked or destacked states (τ_3 and τ_4). For 2AP-A and 2AP-I, τ_1 becomes much shorter, particularly so for 2AP-I, and the population of this component is considerably reduced. In LiCl, 2AP-A and 2AP-I continue to possess relatively large populations of τ_2 in comparison with the other dinucleotides.

The quantum yields of the dinucleotides in LiCl, relative to that of 2APr, for both ϕ_{fit} and ϕ_{rel}, are shown in Table 4.15. It can be seen that, with the exception of 2AP-G, there is good agreement between the two values for each of the dinucleotides. However, for 2AP-G ϕ_{fit} is significantly greater than ϕ_{rel} (by about a factor of 2) implying the presence of effectively non-fluorescent species, with lifetimes too short to be resolved by the TCSPC measurements. Therefore, although τ_1 of 2AP-G appears to increase from 50 ps to 70 ps on going from buffer to LiCl solution, it appears that there is an additional ultrashort decay component present when in LiCl solution that is not directly observed here.

Sample	ϕ_{fit}	ϕ_{rel}
2AP-G	0.23	0.12
2AP-T	0.25	0.22
2AP-C	0.34	0.30
2AP-A	0.28	0.27
2AP-I	0.33	0.41
2APr	1.0	1.0

Table 4.15: Quantum yields of 2AP-X relative to 2APr, for solutions in 6 M LiCl at room temperature. ϕ_{fit} was determined from average lifetimes and ϕ_{rel} was determined from steady-state intensities.

4.3.3.4. Time-resolved Fluorescence at 77 K

The fluorescence decay parameters of the dinucleotides in 6 M LiCl at 77 K are presented in Table 4.16.

X	τ_i /ns				A_i				<τ> / ns
	τ_1	τ_2	τ_3	τ_4	A_1	A_2	A_3	A_4	
G	-	-	3.1	10.2	-	-	0.11	0.89	9.42
T	-	-	3.9	9.8	-	-	0.08	0.92	9.33
C	-	-	5.6	10.3	-	-	0.16	0.84	9.55
A	-	-	8.4	12.2	-	-	0.54	0.46	10.15
I	-	-	8.5	11.6	-	-	0.45	0.55	10.21

Table 4.16: Fluorescence lifetimes, τ_i, and corresponding fractional amplitudes, A_i, of dinucleotides 2AP-X in aqueous LiCl solution at 77 K using an excitation wavelength of 310 nm. Decay parameters were determined from globally fitting the decays collected at 360 nm, 380 nm and 400 nm. A factors (which show little wavelength-dependence) are quoted for 380 nm emission. Experimental uncertainties (estimated by dividing the standard deviation of values by the corresponding values): τ_3 ≤1%, τ_4 ≤1%, A_3 ≤ 1%, A_4 ≤ 1%.

It can be seen that freezing the dinucleotides had a dramatic effect on their decay parameters. In all cases, only two components were required for an adequate description of the fluorescence decay whereas, at room temperature, four components had been necessary. The elimination of the two shorter lifetimes is a common theme in measurements of the fluorescence decay of 2AP in DNA at 77 K.[3,14] For dinucleotides 2AP-G, 2AP-T and 2AP-C, the trend in the values of the shorter remaining lifetime (τ_3) which constitutes about 10% of the emitting population can be correlated with the redox potentials of the bases (shown in Table 4.1), i.e. the propensity for charge-transfer quenching. For 2AP-A and 2AP-I, the value of τ_3 is very close to the 8.7-ns lifetime of unquenched 2APr at 77 K.

Remarkably, the second, longer decay time (τ_4) around 10-12 ns, that is displayed by all of the frozen dinucleotides, is longer than that of unquenched 2APr. This implies that the long lifetime is not simply the result of an absence of quenching, but is due to a species in which 2AP is perturbed electronically by stacking with its partner base in the dinucleotide. The observed red-shift (~10 nm) in the fluorescence excitation spectrum of the dinucleotides at 77 K (Figure 4.11) is also evidence of such an electronic interaction in the ground state. This long-lived excited state is by far the dominant emitting species in 2AP-G, 2AP-C and 2AP-T. Similar long-lived emission was also evident in 2AP-containing duplexes and single strands at 77 K presented in this work (Table 4.9) and also in other decay parameters reported for 2AP in DNA at 77 K, notably in the works of Neely and Jones[14] (presented in Table 4.4) and Wu,[3] and can be attributed to analogous interaction of 2AP with its stacking partners in the oligonucleotide. The presence of a lifetime longer than that of 2APr frozen in an aqueous LiCl matrix (8 ns), suggests that 2AP in DNA (in the dinucleotides or in the oligonucleotides) is undergoing some interaction that is not present for 2APr alone and does not result in quenching of the 2AP fluorescence. The existence of such an interaction is highly speculative and further investigations are required to identify such an interaction.

The elimination of the shorter decay components in both 2AP-oligonucleotides and 2AP-dinucleotides systems is indicative that base dynamics play a large role in the quenching of 2AP in DNA. The effect of freezing on the decay kinetics in the dinucleotides is similar to that seen previously for 2AP-containing duplexes, but is more extreme in the case of the dinucleotides. Where 2AP was in close proximity to G in the duplex, only the sub-100 ps component was lost and quenching on the sub-ns timescale persisted. Conformational fluctuations seem to be even more crucial to quenching in the dinucleotides. In the frozen matrix, the conformations that display lifetimes τ_1 and τ_2 at room temperature cannot be accessed on the ground state potential energy surface and/or are unable to undergo the geometric relaxation (from the Franck-Condon state) on the excited state surface that may be necessary for fast non-radiative decay. Under these conditions, a large proportion of emitting population exists in a stacked, interacting structure characterised by a lifetime that is considerably longer than that of unquenched, locally excited 2AP.

The quantum yields of the dinucleotides in LiCl, relative to that of 2APr, are shown in Table 4.17.

Sample	ϕ_{fit}	ϕ_{rel}
2AP-G	1.1	0.4
2AP-T	1.2	0.5
2AP-C	1.1	0.5
2AP-A	1.1	0.4
2AP-I	1.1	0.6
2APr	1.0	1.0

Table 4.17: Quantum yields of 2AP-X relative to 2APr, for frozen solutions at 77 K. ϕ_{fit} was determined from average lifetimes and ϕ_{rel} was determined from steady-state intensities.

In contrast to the results at room temperature, it can be seen that there is a large discrepancy, of about a factor of 2, between the values of ϕ_{fit} and ϕ_{rel} for all of the dinucleotides at 77 K. This indicates that ultrafast decay processes, resulting in unresolved ultrashort decay components, are at play in all of the dinucleotides at 77 K. The similarity in behaviour across all the dinucleotides suggests that the ultrafast decay is due, at least in part, to processes that do not involve charge transfer.[36] A possible non-CT decay channel was identified in a computational study 2AP-pyrimidine dimers, by Liang and Matsika, and was found to be facilitated by interbase hydrogen bonding.

While it is not surprising that ultrafast decay processes do not involve structural motion on the excited state potential energy surface, it is interesting that the conformations subject to ultrafast quenching are equilibrium structures on the ground-state surface, rather than being populated by thermal fluctuations. This contrasts with the situation for quenching on the 10s to 100s of picosecond timescale (relating to τ_1 and τ_2) which is eliminated in the absence of thermal motion of the bases.

4.4. Conclusions

The results presented here for the 2AP-containing oligonucleotides are in good agreement with the findings of Neely and Jones, who demonstrated that the fluorescence decay of 2AP in DNA at 77 K remained heterogeneous while the shortest lifetime, τ_1, is eliminated by the removal of conformational motions. The disappearance of τ_1, even in the presence of G confirms that base dynamics are required for rapid interbase quenching of 2AP fluorescence via charge transfer. The further elimination of τ_2 for ss3 and ds3, where no G is present in close proximity to 2AP, is consistent with these findings. The persistence of τ_3 in all the frozen oligonucleotides demonstrates that nonradiative decay of 2AP can still occur even in the absence of G and base dynamics.

Room temperature measurements of 2AP-containing dinucleotides in aqueous buffer showed results consistent with those found in the literature for both steady-state fluorescence and time-resolved fluorescence decay parameters. As it was previously found that the dinucleotides were more susceptible to the high concentration of LiCl used in previous studies (10 M), this work successfully used a reduced concentration of LiCl (6 M) and found that there was less of a perturbing effect on the fluorescence properties caused by LiCl solvent while still maintaining the favourable formation of a reproducible clear glass at 77 K. The discrepancies between the QY ratios (relative to 2APr) determined from the decay parameters, ϕ_{fit}, and those determined from steady-state fluorescence intensities ϕ_{rel}, found for dinucleotides dissolved in LiCl, demonstrates the existence of ultrafast decay processes beyond the scope of the observable timescale of the present experiments. This supports previous observations of ultrafast fluorescence decays of <200 fs for 2AP-G and 2AP-T that were attributed to barrierless charge transfer.[37]

Through the study of the fluorescence properties of 2AP-containing dinucleotides frozen at 77 K in a LiCl matrix, insights into the nature of the decay processes of 2AP in DNA have been obtained. The almost 2x difference observed between ϕ_{fit} and ϕ_{rel} for the frozen dinucleotides implies that ultrafast decay to dark states persists in the frozen dinucleotides and are thus associated with excitation of equilibrium ground state conformations. Thus, a substantial fraction (~50 %) of the conformational population is not observed via fluorescence detection.

The persistence of τ_3 in the frozen dinucleotides shows that it is a result of the excitation of a ground state equilibrium conformation that decays without structural relaxation. This contradicts the three-state model presented by Somsen *et al.*[18] (Figure 4.2) in which τ_3 was attributed to a thermally activated conformational change. The loss of the two shortest decay components, τ_1 and τ_2, indicate that conformational dynamics play a role in the population and/or excited state decay of this species. There are two possible scenarios that could explain the loss of a decay component upon freezing. The first is that the decay component in question relates to a thermally excited (non-equilibrium) ground-state conformation that is not populated at 77 K. The second explanation is that if the decay component corresponds to the excitation of an equilibrium ground-state conformation but that the decay process involves geometric relaxation (from the Franck-Condon state) on the excited state surface. Due to the implication of conformationally distinct dark states (specifically in LiCl solvent) and the

high population of τ_1 at room temperature, it is most likely that τ_1, at least partially, relates to excitation of equilibrium ground-state conformations.

For the mechanism of interbase quenching of 2AP in DNA, it seems likely that the dominant decay time of ≤100 ps, attributed to highly-stacked conformations, is mainly due to quenching via charge transfer interactions with G and T. The drive for charge transfer from A and C is somewhat less, resulting in a slower rate of quenching via charge transfer, but could be greater in DNA if the conformational landscape is more favourable (such as a higher degree of base stacking interactions or a reduction in thermal motion of the bases).

It is clearly evident that ultrafast fluorescence measurements are necessary in order to understand the complete picture of the fate of the excited state and the mechanisms involved in the interbase quenching of 2AP in DNA.

4.5. References

1 A. C. Jones and R. K. Neely, *Q. Rev. Biophys.*, 2015, **48**, 244–279.

2 L. Ma, X. Wu, G. G. Wilson, A. C. Jones and D. T. F. Dryden, *Biochem. Biophys. Res. Commun.*, 2014, **449**, 120–125.

3 X. Wu, PhD Thesis, University of Edinburgh, 2012.

4 E. Y. M. Bonnist, K. Liebert, D. T. F. Dryden, A. Jeltsch and A. C. Jones, *Biophys. Chem.*, 2012, **160**, 28–34.

5 H. Lee, C. M. Ol and L. A. Marky, *Acta Chim Slov.*, 2012, **59**, 443–453.

6 L. Ma, PhD Thesis, University of Edinburgh, 2012.

7 M. Kawai, M. J. Lee, K. O. Evans and T. M. Nordlund, *J. Fluoresc.*, 2001, **11**, 23–32.

8 H.-N. Nguyen, L. Zhao, C. W. Gray, D. M. Gray and T. Xia, *Biochemistry*, 2011, **50**, 8989–9001.

9 S. J. O. Hardman and K. C. Thompson, *Int. J. Quantum Chem.*, 2007, **107**, 2092–2099.

10 T. Sabir, A. Toulmin, L. Ma, A. C. Jones, P. McGlynn, G. F. Schröder and S. W. Magennis, *J. Am. Chem. Soc.*, 2012, **134**, 6280–6285.

11 A. F. El-Yazbi and G. R. Loppnow, *Anal. Chim. Acta*, 2012, **726**, 44–49.

12 T. Gelot, P. Tourón-Touceda, O. Crégut, J. Léonard and S. Haacke, *J. Phys. Chem. A*, 2012, **116**, 2819–2825.

13 P. T. Touceda, T. Gelot, O. Crégut, J. Léonard and S. Haacke, *Tech. Dig. OSA 2012*, 2012, 6–7.

14 R. K. Neely and A. C. Jones, *J. Am. Chem. Soc.*, 2006, **128**, 15952–15953.

15 M. A. O'Neill, H.-C. Becker, C. Wan, J. K. Barton and A. H. Zewail, *Angew. Chemie*, 2003, **115**, 6076–6080.

16 M. A. O'Neill and J. K. Barton, *J. Am. Chem. Soc.*, 2004, **126**, 13234–13235.

17 E. Y. M. Bonnist and A. C. Jones, *Chemphyschem*, 2008, **9**, 1121–1129.

18 O. J. G. Somsen, L. B. Keukens, M. N. De Keijzer, A. van Hoek and H. van Amerongen, *Chemphyschem*, 2005, **6**, 1622–16227.

19 O. F. A. Larsen, I. H. M. van Stokkum, F. L. de Weerd, M. Vengris, C. T. Aravindakumar, R. van Grondelle, N. E. Geacintov and H. van Amerongen, *Phys. Chem. Chem. Phys.*, 2004, **6**, 154–160.

20 O. F. A. Larsen, I. H. M. van Stokkum, M.-L. Groot, J. T. M. Kennis, R. van Grondelle and H. van Amerongen, *Chem. Phys. Lett.*, 2003, **371**, 157–163.

21 C. Reichardt, C. Wen, R. A. Vogt and C. E. Crespo-Hernández, *Photochem. Photobiol. Sci.*, 2013, **12**, 1341–1350.

22 T. Fiebig, C. Wan and A. H. Zewail, *Chemphyschem*, 2002, **3**, 781–788.

23 S. Steenken and S. Jovanovic, *J. Am. Chem. Soc.*, 1997, **7863**, 617–618.

24 S. O. Kelley and J. K. Barton, *Science*, 1999, **283**, 5400, 375-381.

25 C. A. M. Seidel, A. Schulz and M. H. M. Sauer, *J. Phys. Chem.*, 1996, **100**, 5541–5553.

26 M. Narayanan, G. Kodali, Y. Xing and R. J. Stanley, *J. Phys. Chem. B*, 2010, **114**, 10573–10580.

27 C. E. Crespo-Hernández, D. M. Close, L. Gorb and J. Leszczynski, *J. Phys. Chem. B*, 2007, **111**, 5386–5395.

28 D. A. Smith, PhD Thesis, University of Edinburgh, University of Melbourne, 2014.

29 D. A. Smith, L. F. Holroyd, T. van Mourik and A. C. Jones, *Phys. Chem. Chem. Phys.*, 2016, **18**, 14691–14700.

30 J. M. Jean and K. B. Hall, *Proc. Natl. Acad. Sci. U. S. A.*, 2001, **98**, 37–41.

31 J. M. Jean and K. B. Hall, *Biochemistry*, 2002, **41**, 13152–61.

32 J. Liang and S. Matsika, *J. Am. Chem. Soc.*, 2011, **133**, 6799–808.

33 A. A. Travers, *Philos. Trans. R. Soc. A Math. Phys. Eng. Sci.*, 2004, **362**, 1423–1438.

34 P. Rai, T. D. Cole, E. Thompson, D. P. Millar and S. Linn, *Nucleic Acids Res.*, 2003, **31**, 2323–2332.

35 J. W. Longworth, *J. Chem. Phys.*, 1966, **45**, 2930–2939.

36 J. Liang, Q. L. Nguyen and S. Matsika, *Photochem. Photobiol. Sci.*, 2013, **12**, 1387–1400.

37 C. Wan, T. Xia, H.-C. Becker and A. H. Zewail, *Chem. Phys. Lett.*, 2005, **412**, 158–163.

Chapter 5: Electronic Energy Transfer in 2AP-Containing Dinucleotides

5.1. Introduction

As early as 1896 it was proposed that exposure to UV radiation causes skin cancer.[1] Since then, much research has been devoted to understanding the processes that underlie photoinduced damage of DNA and the formation of melanoma, ranging from acute to chronic effects of UV radiation exposure.[2] It has long been hypothesised that transfer of electronic energy between bases in DNA and the preferential transfer of energy to certain regions of DNA has led these regions to be more susceptible to mutations and damage.[3–8] However, the mechanism of interbase electronic energy transfer in DNA is not well understood and previously suggested mechanisms cannot explain completely the observed distribution of DNA damage.[9]

Initially, this introduction will present a brief overview of photoinduced damage of DNA before introducing the reader to some common UV-induced photoproducts. The transfer of electronic energy between nucleic acid bases in DNA is only one of the many competing decay processes that are accessible by electronically-excited DNA bases. A discussion of the important aspects of excited-state decay processes of natural DNA bases will next be presented from a bottom-up perspective, with each step building upon the complexity of the DNA systems, from monomeric DNA bases in the gas-phase to DNA *in vivo*. The concept of electronic energy transfer between DNA bases will then be focussed on before explaining how this phenomenon is quantified and studied in DNA systems. The remainder of this chapter focusses on work performed by this author with the aim to better our understanding of the mechanism of electronic energy transfer from DNA bases to 2AP in 2AP-containing dinucleotides. By studying DNA systems consisting of only one DNA base and one 2AP base, the relative complexity of the DNA system is reduced, allowing for a clear identification of the energy donor and energy acceptor in these systems. Dinucleotides consisting of 2AP and one of the four canonical DNA bases, as well as the non-native DNA base inosine, have been investigated. The relevance of inosine to this study stems from its redox potential being similar to that of excited 2AP

and thus there is no drive for quenching of 2AP fluorescence *via* electron transfer by inosine.[10] Both steady-state and time-resolved fluorescence spectroscopy has been utilised to provide an insight into the mechanism of energy transfer at room temperature and at 77 K, where conformational motions and base dynamics have been removed.

5.1.1. Photoinduced Damage of DNA

Even before the discovery that DNA encodes genetic information in 1944,[11,12] the detrimental effects of sunlight, or more specifically UV radiation, were observed and studied as early as 1877.[13] This would later lead to investigations into the role played by UV radiation in the formation of mutations in fruit flies (in 1928)[14] alongside the bactericidal action of UV radiation.[13,15] This field of research is largely driven by the desire to understand the role of UV radiation in causing sunburn, skin cancer, skin aging and corneal damage in humans, while also being the cause of cell death and mutations in microorganisms.[16,17] Despite the fact that prebiotic Earth experienced much higher levels of UV radiation than modern day Earth,[18] DNA molecules (mainly the component DNA bases) were able to effectively quench excess absorbed energy on a fast enough timescale to compete with other processes that could be damaging to DNA. Thus, DNA was able to form the basis for life on Earth.[19–21]

As mentioned in Chapter 2, the broad absorption band of DNA in the UV region is caused by the widely overlapping absorption spectra of the four native DNA bases (A, C, G, and T) that, along with the sugar-phosphate backbone, make up the DNA strand. The non-native base inosine also shows a similar absorption band. The main absorption bands of the bases peak around 260 nm with extinction coefficients ranging from ~7 $x10^3$ to ~15 $x10^3$ cm^{-1}/M (in the order of C<T<G<A).[21,22] The fluorescence quantum yields of the native DNA bases are extremely low (on the order of 10^{-4}) because excited DNA bases relax back to the ground state primarily via very rapid non-radiative processes. These ultrafast non-radiative decay processes will be discussed in more detail later in this section.

The harmful effects to organisms caused by UV radiation stems from the introduction of energy into the vibronic (vibrational and electronic) structure of DNA molecules via the absorption of photons by its component nucleic acid bases. The formation of vibronically excited-states and the way in which these excited-states relax determines the extent of the photodamage caused to DNA. Figure 5.1 gives an indication of the many different possible relaxation pathways resulting from excitation of nucleic acid bases in DNA systems.[20]

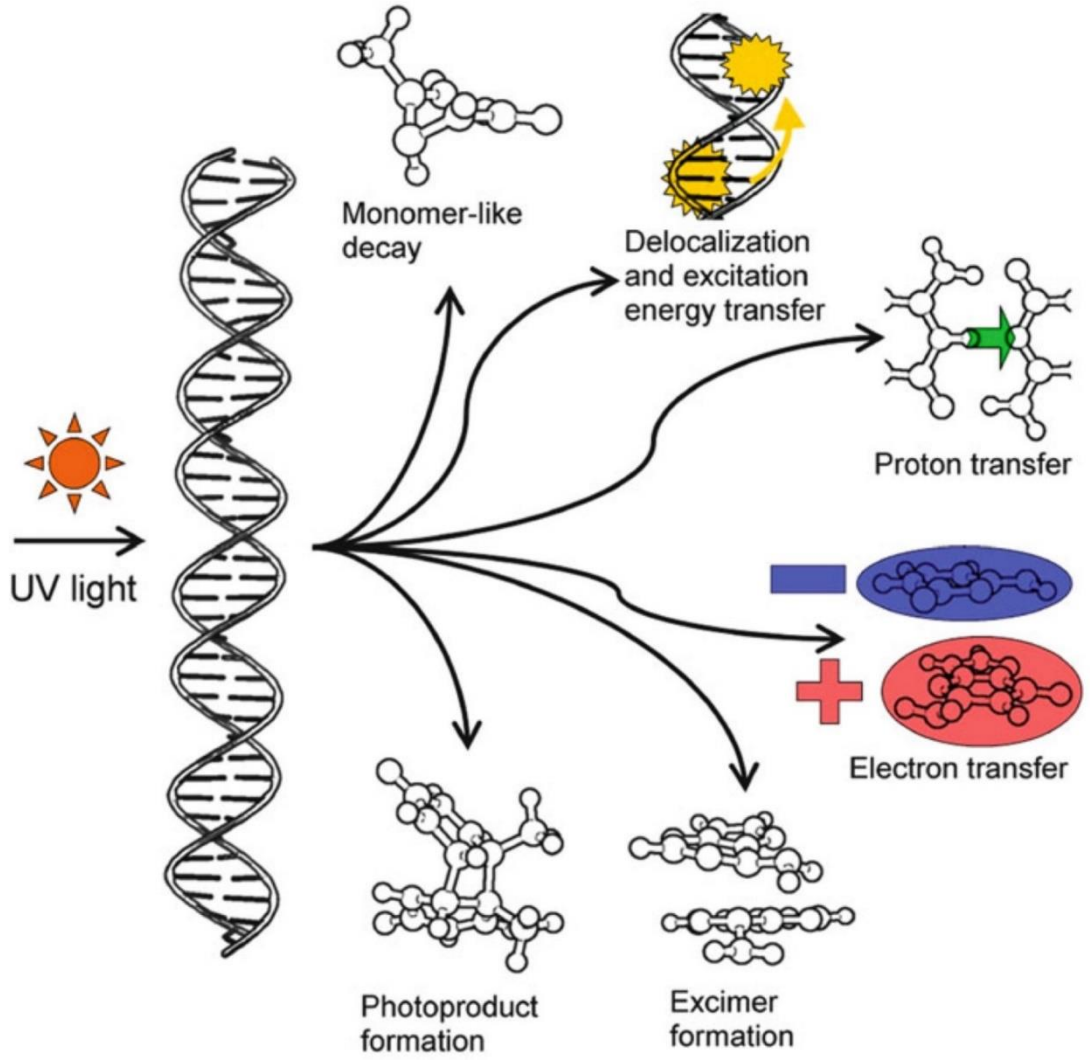

Figure 5.1: Possible relaxation pathways following the absorption of UV light by DNA bases. Reproduced from reference 20.

Native DNA bases possess many competing relaxation pathways and which route is taken depends on the photodynamics and photochemistry accessible to the molecule in the excited-state.[20,21] Possible excited-state relaxation pathways for DNA bases include spontaneous decay analogous to that of an excited-state monomer; the transfer of electronic energy (as discussed in this chapter) or transfer of a species (such as a proton or electron and in (which has been discussed previously in Chapters 2 and 4) ; or via a biochemical reaction pathway. Biochemical relaxation pathways result in the formation of photoproducts that can alter the chemistry and shape of the DNA molecule itself, thus inhibiting any biological activity involving these now-modified regions of the duplex. For example, this can result in the inhibition of DNA replication and repair enzymes that utilise the specific chemistry related to the shape of the DNA strand for the

recognition of target sites on which to act.[23,24] Interestingly, specific repair enzymes (photolyases) are often required to fix such photoinduced damage in DNA, which specifically target these photo-damaged sites.[25]

It is important to note that "DNA mutation" is not necessarily synonymous with "DNA damage". A mutation is the result of a damaged base that, upon replication (or transcription) of DNA, results in the preservation of the mutation such that the replicated DNA (or RNA) contains a base in the sequence that is non-identical to the initial sequence before DNA damage had occurred. On the other hand, "DNA damage" refers to damage to a nucleic acid base in the sequence of the initial DNA and may or may not cause a mutation.

5.1.2. Common UV-induced Photoproducts in DNA

The most prevalent DNA modification caused by the absorption of UV radiation is the formation of pyrimidine dimers (illustrated in Figure 5.2) which cause a distortion to the DNA structure that inhibits the regular function of the DNA molecule.

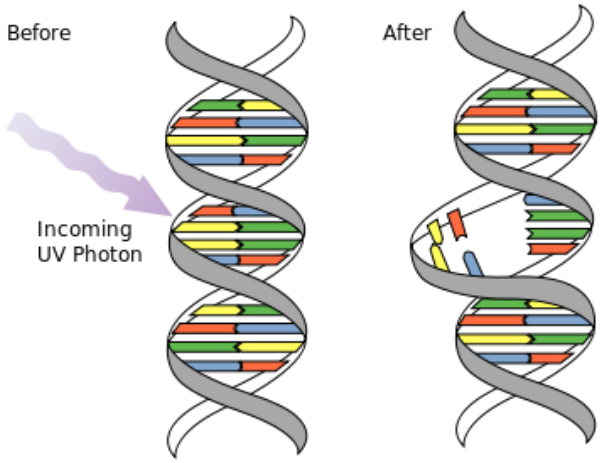

Figure 5.2: Cartoon depicting the effect of the formation of pyrimidine dimers in DNA duplexes. The absorption of a UV photon by the DNA bases results in the distortion of the DNA molecule via inter-strand covalent bonding of adjacent bases rather than intra-strand H-bonding.

The two most common pyrimidine dimers are cyclobutane pyrimidine dimers and (6-4) pyrimidine-pyrimidone dimers,[26–28] the structures of which are shown in Figure 5.3, using thymine dimers as an example.

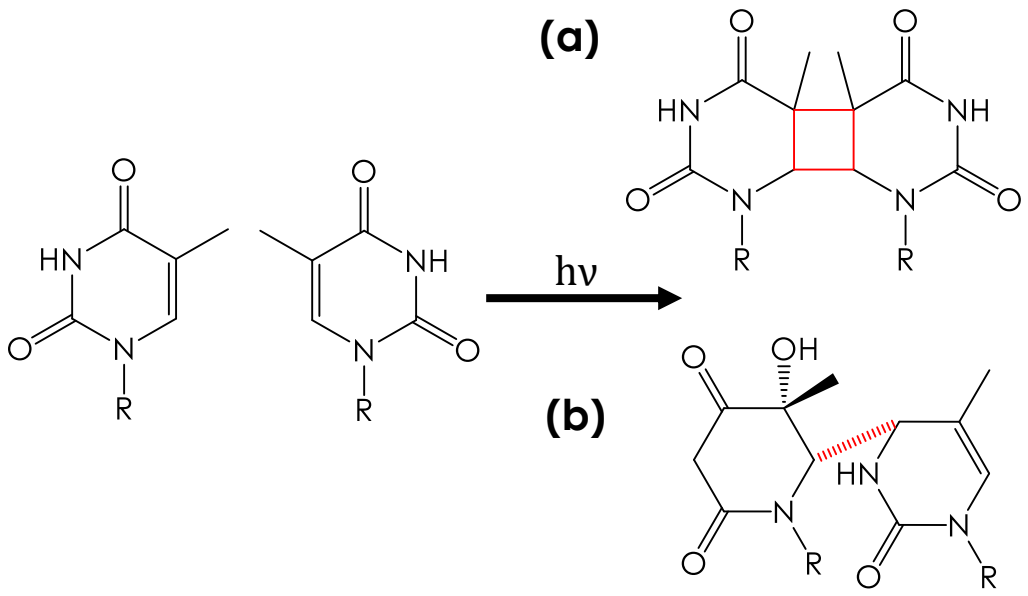

Figure 5.3: Formation of two possible pyrimidine dimers resulting from thymine bases, for example, that are located sequentially in the DNA sequence. "R" denotes the bond to the rest of the DNA molecule via a glycosidic bond with C1' of the riboside (as labelled in Figure 2.6). The two photoproducts shown are (a) cyclobutane pyrimidine dimers and (b) (6-4) pyrimidine-pyrimidone dimer.

In 1971, Lamola demonstrated the ability of pyrimidine bases in DNA *in vitro* to form homodimers under dark conditions (in the absence of UV-radiation).[26] In these studies, thermal decomposition of an appropriate sensitizer (trimethyl-1, 2-dioxethane) caused the formation of pyrimidine dimers *in vitro* via triplet-energy transfer. This opened up the idea that pyrimidine dimers do not only form as the result of direct absorption of UV radiation, but can also occur through the transfer of electronic energy from other molecules.

When DNA polymerases encounter UV-induced pyrimidine dimers that they are not able to recognise, the default result is to insert an adenine into the sequence.[29,30] Consequently, during subsequent semiconservative replication of DNA, TT sequences are preserved but cytosine bases in damaged sequences are mutated to thymine (leading CC pyrimidine dimers to become TT dimers).[30]

In 2013, Douki presented a review article emphasising the suitability of chromatographic techniques for enhancing our understanding of basic DNA photochemistry while allowing the extent of photoinduced damage present in DNA to be quantified. A number of assays have been developed based on using the known chemical structure of pyrimidine dimers to produce suitable chemical and biochemical tools for

their detection. These assays fall into three main categories: antibody-based, electrophoresis-based and chromatography-based assays. The decision to use one technique over another is largely influenced by the samples available and the specific scientific topic under investigation. As these assay-based chromatographic techniques are not widely used in the work presented in this thesis, this introduction will not focus on the specifics of these techniques but further details can be found in the review article by Douki.[27] Of note, the review emphasises the usefulness of recent developments of HPLC-MS/MS to offer a further level of understanding of DNA photoreactivity for DNA in solution and in cells. The sensitivity offered by these chromatographic techniques and the technological developments being made in this field will fast enable smaller sample sizes to be used to qualitatively and quantitatively study DNA photodamage.

Previously, in 2012, El-Yazbi & Loppnow demonstrated the suitability of the modified-DNA base 2AP as a simple, fast and sensitive probe for the detection of UV-induced damage in DNA.[31] Due to the favourable properties of 2AP (as described previously in Chapters 2 and 4), it was shown that the fluorescence signal of 2AP incorporated into a DNA hairpin structure was directly proportional to the amount of DNA damage present. More so, the incorporation of multiple 2AP bases into the DNA hairpin structure allowed for greater sensitivity and selectivity of the probe-construct. These 2AP hairpin probes also have the advantage of being cheaper and easier to synthesise than other currently available *in vitro* probes that are used for the detection and quantification of DNA damage.

Another important UV-induced photoproduct in the context of this work are those formed from the photohydration of a pyrimidine base, as shown in Figure 5.4 for cytidine.

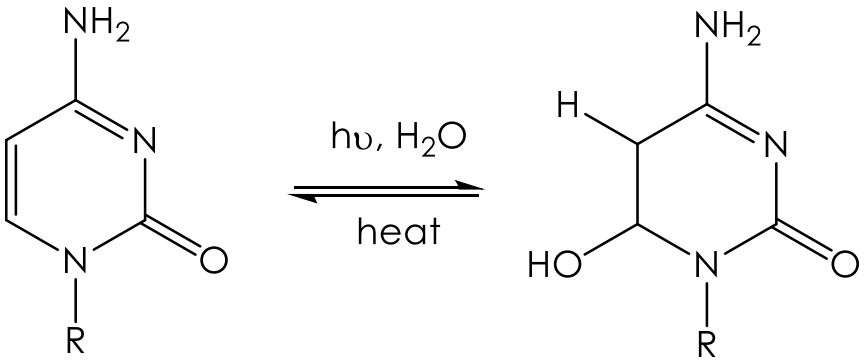

Figure 5.4: Reaction scheme for the photohydration of cytidine (where R denoted the position of the DNA backbone via a glycosidic link to C1' of the riboside group). The forward reaction is driven by the absorption of a photon while the reverse reaction is thermal in nature.

As early as 1949, a photoreaction of uracil (a pyrimidine base found in RNA) was observed that was reversible under thermal or acidic conditions.[32] The key photoproduct responsible for this observation was later indirectly identified, in studies performed by other subsequent researchers as the addition of water across the C5-C6 double bond.[33,34] Equivalent photoproducts were identified in similar pyrimidine molecules (thymidine and cytidine) as well as in the nucleoside and nucleotide derivatives. Identification of the photohydrated-product was performed via a reduction of cytidine photohydrate with sodium borodeuteride to obtain a derivative rearranged alkylated glycosylurea with deuterium located at a position consistent with a hydroxyl located originally at position C6 on cytidine (as labelled in Figure 2.5).[35] The formation of photohydrated pyrimidines is known to be thermally reversible under ambient conditions and is an area that has been well studied and characterised. [33,34,36–38]

In 1978, Liu and Yang utilised H-NMR spectroscopy to characterise photohydrates of cytidine and cytidilic acids which were identified definitively as isomeric 6-hydroxy-5, 6-dihydrocytosine.[34] This work presented a study of the photohydration and dehydration mechanisms, characterising the stereochemistry of photohydration as random while identifying the dehydration mechanism as a trans-elimination reaction.

5.1.3. Excited State Decay Processes of DNA Bases

In order to build up a picture that explains the fate of the excited-states of DNA bases, a range of studies have been performed on a variety of systems that mimic the structural components of DNA. These systems range from simple systems, such as monomeric bases in the gas phase,[39–43] increasing in complexity to the most complex cases, such as DNA *in vivo*.[2,20,21] Studies included investigations of the effects of interactions between bases, such as base pairing (intrastrand) or base-stacking (inter-strand), interactions of DNA bases with solvent molecules, and interactions of DNA with other molecules/enzymes that are relevant to DNA *in vivo* and will be discussed below.

A common photophysical feature associated with DNA bases is the ultrafast (picosecond to femtosecond) relaxation of the excited-state. Gas-phase DNA base monomers have been widely studied, due to their relative simplicity compared to solution-phase DNA, and provide a foundation for more complex systems to build upon.[44] In the gas-phase, ultrafast de-excitation of excited-state monomeric bases has been found to involve accessing conical intersections (CI) either by deformation of the cyclic rings of the molecule or by dissociation of hydrogen.[45] CIs are sets of points where multiple adiabatic potential energy surfaces intersect (become degenerate), allowing efficient and rapid relaxation of a species *via* internal conversion. An illustration of potential CIs accessible by excited-state adenine is shown in Figure 5.5.[21]

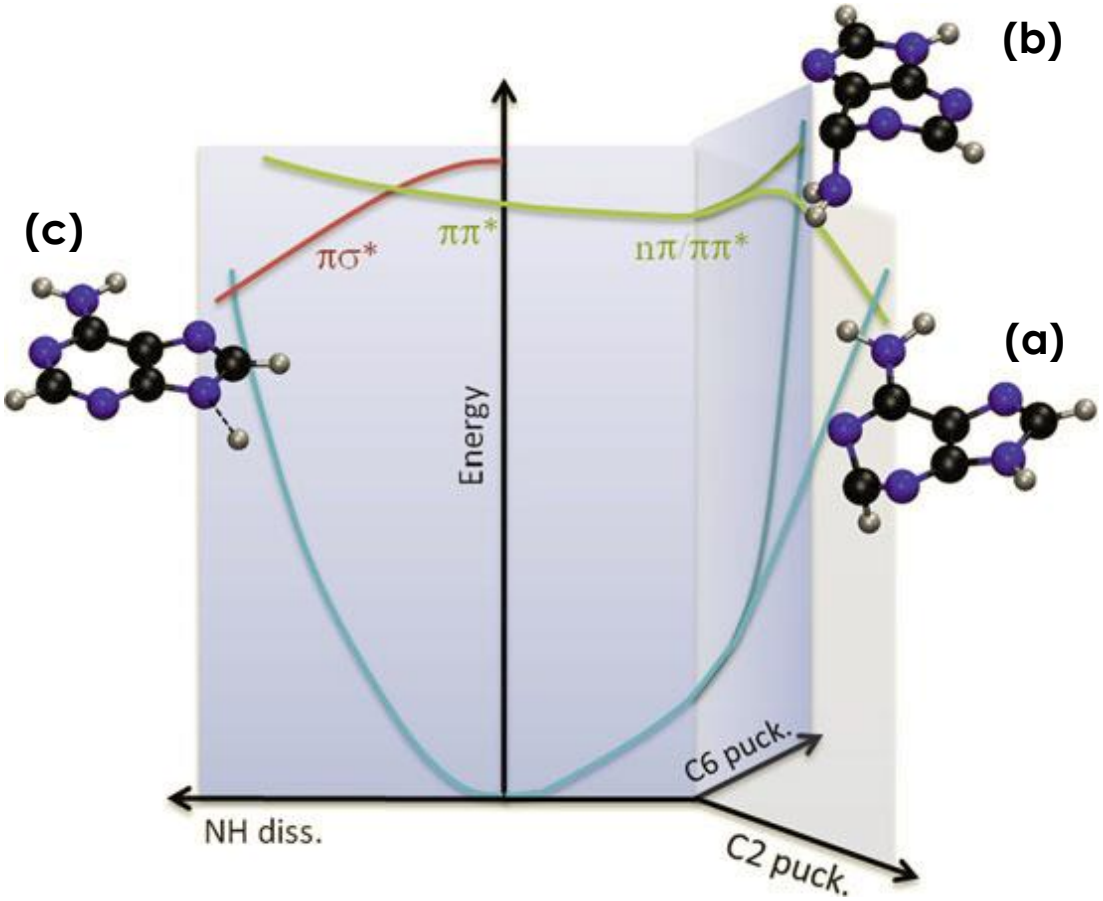

Figure 5.5: Cartoon of a 3D reaction landscapes proposed for deactivation pathways in adenine via CIs. From the Franck-Condon region, adenine relaxes to a mixed nπ*/ππ* S_1 minimum. From this minimum, puckering at positions C2 (a) or C6 (b) can allow the molecule to access CIs in the ps timescale. Alternatively, for higher excitation energies, CIs formed from NH dissociation may also be accessed (c). Figure reproduced from reference 21.

By accessing a CI, DNA bases in electronically excited states can rapidly relax back to the electronic ground state via non-radiative transitions. The photostability of DNA and its component bases is thought to be due to the presence of conical intersections in their associated energy landscapes.[21,46,47] Because ultrafast non-radiative de-excitation pathways occur on a fast enough timescale, they are able to compete with other processes such as fluorescence emission, or biochemical processes. Being in competition with biochemical processes allows for protection against the formation of photoproducts that could result in irreversible damage to DNA or that could cause mutations in DNA structure and sequence.

So far, in this short review, only the simple case of isolated monomeric DNA bases in the gas-phase have been discussed. These systems are devoid of interactions with

solvent and the other components of DNA, making them ideal in the study of the underlying photophysical processes inherent to DNA alone. However, in DNA, the bases are merely one part of a much larger structure and are present in the form of nucleosides (each DNA base is attached to a riboside group). Recent studies performed by Camillis *et al*. demonstrated the role played by the riboside group in the excited-state relaxation of gas-phase nucleosides.[43] Utilising a 'soft' laser desorption method, time-resolved ion yield measurements in the gas-phase were performed on DNA base nucleosides and it was found that, following excitation, the lifetime for internal conversion to the ground state was reduced by a factor of two for adenosine, cytidine and thymidine when compared to the isolated bases (without the riboside group present). This reduction of the lifetime was not found for guanosine, and was potentially due to a mixture of conformers/tautomers being present under the experimental conditions.

For DNA bases in solution, the excited-state lifetimes for isolated bases are known to be shorter than for those in the gas-phase.[21] This suggests that DNA bases interact with solvent molecules resulting in the dissipation of electronic energy vibrationally and may play an important role in the photostability of DNA in solution.

Similar short lifetimes were found for bases involved in H-bonding with other DNA bases. In ds-DNA (duplexes), two DNA strands are held together via intra-strand H-bonding between the DNA bases of each strand (base-pairing) as well as *via* electrostatic interactions (base-stacking) (as described in Chapter 2). An example of H-bonded DNA base-pairs has been shown previously Figure 2.7.

When base-pairing interactions are present, the relaxation of excited-state bases via internal conversion pathways (similar to that of isolated DNA bases) remains present but is also accompanied by intermolecular proton-transfer processes associated with charge transfer, which occur on the sub-picosecond timescales.[20]

The next step up in the complexity of DNA to be considered is the role played by the base-stacking interactions in DNA. Base-stacking interactions are an important feature in DNA strands with lengths of two or more bases and have been described in Chapter 2. Base-stacking occurs in ss-DNA to a degree but is more prevalent in ds-DNA and strongly contributes to its stability. Stacking interactions are hydrophobic and electrostatic in nature and thus the relaxation processes of base-stacked ds-DNA or ss-DNA rely strongly on the sequence of DNA bases. Due to the complexity of the systems involved, the complete picture of the effect of base-stacking in native DNA is still unclear. However, initial studies have been performed on simpler systems (e.g. homopolymers or short sequences of ss-DNA or ds-DNA) and the decay processes of excited-state bases are

thought to supersede those caused by base-pairing.[48] In the presence of base-stacking, the de-excitation pathways of monomeric and base-paired DNA bases may still be present, but the fate of the excited state is thought to be governed by excimer/exciplex states.[20,48] A major issue in the study of DNA base-stacking is that incorporation of a fluorophore or fluorescent label will typically perturb the stacking interactions and thus affect the system under study. Later in this chapter (and previously in Chapter 4), the use of 2AP (which has minimal effect on the DNA structure) to study base-stacking and other interactions in DNA will be discussed.

Excimers can form due to base-stacking interactions and the electronic coupling between adjacent bases, allowing for electronic energy to be delocalised across more than one base.[49] Thus, in regions of DNA where bases are poorly stacked, excited-state bases exhibit monomer-like relaxation while those that are highly stacked exhibit relaxation characteristic of excimers/exciplexes.[50] Crespo-Hernandez *et al*. studied single-stranded DNA homopolymers (for example poly(dA)) by way of fs-TA to determine the effect that different degrees of base stacking have on the lifetimes of excited-states.[48] Overall, it was found that base-stacking and the electronic coupling between adjacent bases played a major role in the fate of the excited-state of bases in oligo- and polynucleotides and also highlighted the importance of base-sequence in DNA. ss-Homopolymers of thymine ($(dT)_{18}$) showed no evidence of the formation of excimers, demonstrating only monomer-like decay (ps decay) and suggesting the presence of poorly stacked bases, while ss-homopolymers of adenine ($(dA)_{18}$) exhibited evidence of different degrees of base-stacking interactions in the form of both short and long lifetimes.

The DNA system with the greatest complexity, and thus the most difficult to study, is DNA *in vivo.* Under typical biological conditions, all of the aforementioned de-excitation pathways are thought to be present as well as a diverse range of possible biochemical mechanisms involving an assortment of enzymes and other molecules. Markovitsi *et al*. postulated that the molecularly crowded conditions in cells enhances the collective character of the electronic excitations due to a decrease in conformational motions.[51] This effect caused by molecular-crowding is lost for samples in solution at μM concentrations when at ambient temperatures and may be an important factor missing from current studies.

5.1.4. Electronic Energy Transfer

The remainder of this section will focus on the transfer of electronic energy between nucleic acid bases within DNA. Energy transfer is thought to be one of the major decay processes that contributes towards the formation of mutations and damage to DNA in some regions while effectively protecting others from which the energy migrates. If the factors affecting the transfer of electronic energy to the regions of DNA susceptible to mutation can be understood then we will be closer to understanding the complex system of native DNA *in vivo* and its susceptibility to damage from UV radiation.

5.1.4.1. Electronic Energy Transfer between Native DNA Bases

Early studies to investigate the transfer of electronic energy transfer in DNA molecules focussed on the systematic characterisation of the steady-state fluorescence spectra of DNA bases in DNA in order to understand the mechanism of energy transfer in DNA.[8,52–54] In recent decades, the advances in ultrafast pump-probe spectroscopy and computational methods have been utilised.[55–60] As will become evident, the majority of these studies have focussed on DNA containing only adenine and thymine bases in order to simplify the otherwise complex systems under study.[44,61,62]

In 2004, Crespo-Hernández *et al*. published a review on the ultrafast excited-state dynamics in nucleic acids that highlighted that the decay of electronic energy in single bases is mediated differently than in double-helix DNA.[63] Base-stacking and base-pairing dynamics control the decay of excess electronic energy in the double helix structure of DNA while in single bases, sub-picosecond non-radiative decay occurs to eliminate excess electronic energy. Later, in 2005, a study was published by the same group that showed that base-stacking (and not base-pairing) is more important in determining the fate of the excited-state in ss-DNA and ds-DNA composed of adenine and thymine bases.[48] By recording fs-TA signals for DNA oligomers containing defined sequences with varying levels of base-stacking and base-pairing interactions, this study detected intra-strand excimer states with lifetimes ranging from 50-150 ps, which formed in high yields for oligomers where adenine was stacked with another adenine or with a thymine base in the DNA strand. This study also suggested that by maintaining the intra-strand nature of the excited state, the DNA strand could be preserved and that the undamaged DNA strand could be used as a template for replication.

Studies performed by Markovitsi *et al*. in 2007 related time-resolved fluorescence measurements to steady-state fluorescence measurements of poly(dA).poly(dT) (polymers of DNA consisting of about 2000 A-T base pairs) in order to suggest a model

for energy transfer in DNA.[57] A well-known issue in the study of DNA systems is the complexity of native DNA (non-synthetic) due to the complexity of DNA base sequence. Markovitsi *et al*. overcame this issue by using only A-T base pairs in the ds-DNA. It was found that the excited states that are populated from excitation at 267 nm are delocalised over a few bases. Through initial ultrafast internal conversion (taking place in less than 100 fs), the excited state population is directed to the lower part of the exciton band which then results in fluorescence emission from the native DNA bases (as shown in Figure 5.6).

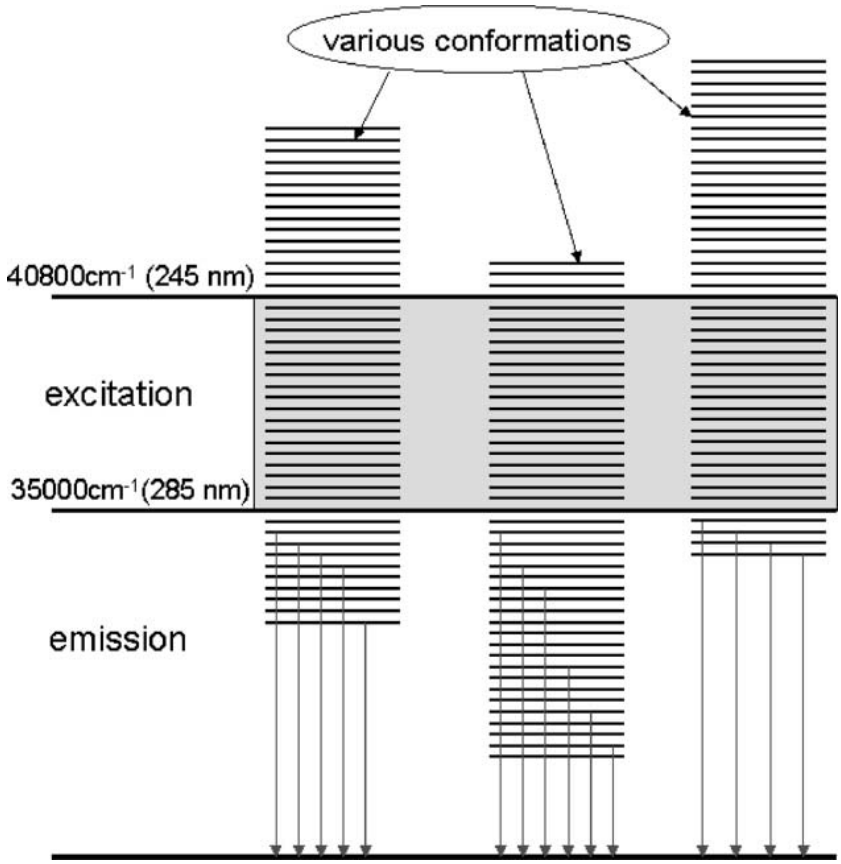

Figure 5.6: Proposed schematic representation describing energy transfer in poly(dA).poly(dT) in the sub-picosecond timescale. Excitation at 267 nm (within the 245 - 285 nm band (grey band) results in the population of a large number of excited states that are delocalised over a few bases and are commonly accessible in a range of conformations. In less than 100 fs, internal conversion among these states takes place to bring the system to the lower part of the exciton band from which emission takes place. Figure reproduced from the publication of Markovitsi.[57]

This model presented by Markovitsi *et al*.[57] provides a possible explanation for the ultrafast energy transfer mechanism while still allowing for the occurrence of further

energy transfer on longer timescales, that may be assisted by conformational motions of the DNA double helix structure and base-dynamics. DNA is a highly dynamic molecule and such base-dynamics allow bases to fluctuate from the average structure of DNA. Fluctuations between DNA bases have been found to lead to the modification of the electronic coupling between bases involved in delocalised excited states spanning more than one base. This is a known driving force for the transfer of electronic energy between DNA bases.[64] Previously, local structural fluctuations of DNA bases have also been suggested to play a role in the mechanism of excitation energy transfer from adenine to 2AP in ss-DNA oligomers, although over a different timescale involved in the mechanism of charge transfer.[65] Further discussion on energy transfer from A to 2AP will be covered in Section 5.1.4.2.

Without a fluorescent modified DNA base present, excited states dynamics of DNA dinucleotides have mainly been studied via ultrafast-pump-probe techniques such as femtosecond-transient absorption (fs-TA) spectroscopy[48,49,66] or femtosecond-time-resolved infrared (fs-TRIR) spectroscopy.[67–70] These ultrafast techniques are necessary to probe the sub-ps excited-state lifetimes of the native DNA bases, which is not accessible using standard TCSPC. While fs-TA experiments allow electronic transitions to be probed, fs-TRIR experiments enable the study of time-dependent vibrational resonances of both the ground state and the excited state.

5.1.4.2. Electronic Energy Transfer from DNA Bases to 2AP

This work utilises the modified DNA base 2AP to probe photophysical processes on DNA on the ps to ns timescale. 2AP has many favourable properties that make it ideal to use as a probe of DNA systems. These properties have been introduced and discussed thoroughly in previous chapters, but the particular properties that make 2AP favourable for energy transfer studies will be discussed here. The FQY of 2AP is far greater than that of the native DNA bases, enabling the use of fluorescence spectroscopy in investigations involving energy transfer from the natural bases to 2AP. The significant spectral overlap of the UV-absorption bands of the canonical DNA bases makes selective excitation of a specific base, and its identification as the excitation energy donor, not possible in unlabelled DNA.[21,22] The red-shifted excitation wavelength of 2AP, compared to that of the native DNA bases, overcomes this problem and enables selective excitation of native DNA bases as energy donor(s), with 2AP is acting as the acceptor (detectable by its fluorescence emission). As the excitation energy of 2AP is lower than that of the native

DNA bases, 2AP* cannot be quenched by electronic energy transfer to the native bases and instead acts as an acceptor of electronic energy from excited-state native DNA bases.

Nordlund, Xu and Evans are the main contributors of studies of energy transfer from DNA bases to 2AP in DNA and it is these studies that form the foundation for the work presented in this thesis.[9,53,71] In 1993, Nordlund *et al.* first showed the occurrence of singlet-singlet energy transfer from native DNA bases to 2AP in DNA oligonucleotides. It was shown that excitation of the native DNA bases (at 260 nm – 270 nm) in DNA decamers, containing a single 2AP base in each DNA strand (resulting in two 2AP bases per DNA duplex) (d(CTGA[2AP]TTCAG)$_2$), results in a fluorescence emission profile that is identical to that of 2AP excited directly, at 300 nm - 315 nm.[71] Nordlund *et al*. demonstrated the presence of energy transfer by observing additional peaks in the excitation spectrum of 2AP fluorescence in the region where the native DNA bases absorb. Energy transfer efficiency is defined as the ratio of the number of excited donors that result in excitation of the acceptor compared to the total number of excited donors. The overall energy transfer efficiency, η(t), (defined as the average transfer efficiency per donor) from DNA bases to 2AP was determined by measuring the fluorescence intensity from the sample excited in the region where only donor DNA bases absorb and normalising the recorded intensity relative to that of the sample excited in a region where only 2AP absorbs. It is then necessary for the normalised fluorescence intensity to be corrected for differences in the absorbance of the donor(s) and acceptor(s) in the sample, as shown in Equation 5.1,

$$\eta(t) = I(\lambda_d)\left\{\frac{\left[1-10^{-A(\lambda_a)}\right]}{\left[1-10^{-A(\lambda_d)}\right]}\right\} \qquad \textbf{5.1}$$

where, λ_d and λ_a are the wavelengths at which only the energy donor or the energy acceptor absorb, respectively, and $A(\lambda_a)$ and $A(\lambda_d)$ are the absorbance values of the sample at wavelengths λ_a and λ_d, respectively. $I(\lambda_d)$ is the fluorescence intensity when excited at wavelength λ_d, normalised such that the fluorescence intensity excited at λ_a is equal to 1. Normalisation of $I(\lambda_d)$ is required to provide a direct comparison of the energy transfer efficiency while the latter ratio, involving the absorbance values of the donor and acceptor, corrects for differences in absorption at the different wavelengths used. Nordlund et al. used wavelengths of 260 nm and 307 nm for λ_d and λ_a, respectively, to achieve selective excitation of the acceptors (2AP bases) or the donors (DNA bases). Use of Equation 5.1 is only appropriate in cases where there is no spectral overlap between the energy acceptor and energy donor, such that two distinct wavelengths can be identified for λ_a and λ_d. Improper use of Equation 5.1, using wavelengths where both the

donor and acceptor absorb, will result in a measure of the excitation dependence of the quantum yield of the acceptor. For the ds-DNA decamers studied by Nordlund *et al*., absorption by 2AP at 260 nm was negligible, relative to that of the native DNA bases, and could be ignored. As such, use of Equation 5.1, using measurements recorded at 260 nm and 307 nm, was justified. However, this factor cannot be ignored for shorter DNA sequences where the relative absorbance of 2AP at 260 nm, compared to the native DNA bases, will be greater (as discussed below).

By performing steady-state fluorescence measurements over a range of temperatures, and correcting for differences in absorption coefficients of the natural bases compared to 2AP, the efficiency of transfer between DNA bases and 2AP was shown to be temperature-dependent. Nordlund *et al*. measured the efficiency of energy transfer from the native DNA bases to 2AP in the decamers over a temperature range of 4°C to 50°C and found the efficiency to be 4-5% at 4°C, falling rapidly to 0% at 30°C, but then rising again to 1% at 48°C. The discovered temperature-dependence of energy transfer found in this study highlights the potential importance of populating DNA base conformations in which energy transfer will be more favourable. An increase in the temperature of the system promotes base-mobility and results in an increase in distribution of conformations accessed by the DNA bases and in the presence of conformations that deviate from those that are favourable for energy transfer. Nordlund *et al.* proposed that the duplex structure merely aids energy transfer but it is not a requirement for energy transfer to occur, as energy transfer efficiency was shown to increase again at temperatures above the duplex melting temperature, where only ss-DNA is present. The temperature dependence of energy transfer revealed that base-mobility is a more important factor than the duplex/single-strand ratio and that the orientation of the 2AP base in relation to the other DNA bases is a key factor. The temperature-dependence of energy transfer in 2AP-containing oligomers has also shown that, while energy transfer does occur minimally at biologically-relevant temperatures in synthesised 2AP-containing DNA oligomers(<5%), the efficiency of energy transfer is greater at lower temperatures (and greatly increases below 0°C), where base-dynamics of DNA are greatly reduced.[72] As mentioned previously, molecular-crowding is a common feature of DNA *in vivo* and could contribute to the further reduction of base-mobility in DNA and, in theory, could increase the efficiency of energy transfer. So far, no such studies have been performed mimicking this factor.

In 2000, Xu and Nordlund further explored the temperature dependence as well as the sequence-, concentration- and solvent-dependences of energy transfer from DNA

bases to 2AP in an assortment of 2AP-containing DNA oligonucleotides, ranging in length from three bases to ten bases. A majority of the work was performed on single-stranded DNA oligomers but the effects of base-pairing and DNA melting were also investigated by a comparison with the corresponding double-stranded DNA oligomers.[9] These studies calculated the energy transfer efficiencies using a different method to that used previously, which could account for any spectral overlap of the acceptor and donor bases. Xu and Nordlund compared the fluorescence emission from a single 2AP base contained in the sequence of a DNA oligomer, excited at 300-315 nm, with that of 2AP excited indirectly via energy transfer from native DNA bases, using an excitation wavelength in the region of 250-280 nm. As native DNA bases show no absorbance bands in the former region and 2AP absorbance is present but minimal in the latter region (compared to that of the DNA bases), an estimate of the energy transfer efficiency can be determined, as follows. As mentioned previously, the absorption band of 2AP in the 300-315 nm region is distinct from the absorption spectra of the natural DNA bases. At approximately 260 nm, where the native DNA bases absorb strongly, absorption by 2AP still occurs but is minimal (as demonstrated later in Figure 5.10). Equation 5.2 can be used to calculate the transfer efficiency, η(t), from donor to acceptor, following excitation at wavelength λ_{ex}, and accounts for any absorption by the acceptor itself,

$$\eta(t) = \frac{A_a(\lambda_{ex})}{A_d(\lambda_{ex})} \times \left(\left(\frac{F(\lambda_{ex})}{F_a(\lambda_{ex}) * Q} \right) - 1 \right) \qquad \textbf{5.2}$$

where $A_a(\lambda_{ex})$ and $A_d(\lambda_{ex})$ are the absorbance values of the energy acceptor (2APr) and energy donor(s) (normal DNA base(s)) respectively, at excitation wavelength, λ_{ex}. The latter can be calculated by subtracting the absorbance of 2APr from that of the oligonucleotide sample ($A_d(\lambda_{ex}) = A_{oligonucleotide} - A_{2APr}$). $F_a(\lambda_{ex})$ and $F(\lambda_{ex})$ are the fluorescence intensity of directly excited energy acceptor or the 2AP-containing oligonucleotide, respectively, at λ_{ex}. Q is the ratio of the quantum yield of 2APr and that for 2AP in the oligonucleotides, and is used to account for the reduction in the fluorescence quantum yield of 2AP caused by quenching interactions with neighbouring bases when 2AP is incorporated into the DNA strand. As $A_d(\lambda_{ex})$ is the total absorbance of all donors, calculation of η(t) using Equation 5.2 yields the energy transfer efficiency averaged over all bases that absorb at λ_{ex} (which may differ depending on the bases present in the DNA sequence).

The variation in energy transfer efficiencies found for different sequences of DNA bases in ss-DNA oligomers is exemplified in Table 5.1.

Oligomer length /bases	Oligonucleotide Sequence	η(t) /%	η(-1) /%
10	AAAA[2AP]AAAAA	46 ± 5	-
	GGGG[2AP]GGGGG	5.1 ± 1.2	23 ± 3
	CCCC[2AP]CCCCC	5.3 ± 0.9	24 ± 3
	TTTT[2AP]TTTTT	3.5 ± 0.5	16 ± 2
6	CCA[2AP]CC	22 ± 2.5	57 ± 7
	CCG[2AP]CC	7.3 ± 0.9	19 ± 3
	CCC[2AP]CC	4.4 ± 0.7	12 ± 2.5
	CCT[2AP]CC	4.6 ± 0.8	10 ± 3

Table 5.1: Selection of calculated efficiencies for the transfer of electronic energy from DNA bases to 2AP in 2AP-containing single stranded DNA decamers and hexamers, showing the measured overall transfer efficiency from all bases present, η(t), and the calculated energy transfer efficiency from the DNA base 5'-adjacent to 2AP in the DNA sequence, η(-1). Energy transfer efficiencies in the DNA decamers were determined at 4°C at a DNA concentration of 6 μM, while those in the DNA hexamers were determined at 5°C using a DNA concentration of 2.7 μM for "CCA[2AP]CC" or 50 μM for the other DNA hexamers. Transfer efficiencies have been reproduced from the publication of Xu and Nordlund.[9]

The overall energy transfer efficiencies, η(t), shown in Table 5.1, reflect the averaged efficiency of energy transfer from all donor bases (per donor) to the acceptor 2AP base. Energy transfer efficiencies from a single DNA base to 2AP, η(n), were determined systematically by Nordlund *et al.* from a series of measurements of η(t) for ss-DNA oligomers of increasing length. In this nomenclature, 2AP is located at position 0 and n is an integer relating to the location of the DNA base relative to 2AP. Negative integers indicate bases on the 5' side of 2AP while positive integers indicate those on the 3' side of 2AP (e.g. η(-1) is the energy transfer efficiency from the DNA base located immediately adjacent to 2AP in the 5'-direction along the DNA strand sequence). Details of the model used to calculate the transfer efficiencies for particular bases can be found in the appendices of the publication by Xu and Nordlund.[9] However, determination of η(n) relies on the assumption that the energy transfer efficiency from a base adjacent to 2AP is independent of the number of other bases in the DNA oligomer sequence and without this assumption this model would not be viable. While this assumption may hold true for the local environment of sections of DNA duplexes and for DNA oligomers with large sequences, the inherent flexibility of DNA bases in single stranded DNA, and specifically those with a length of only two or three bases (dinucleotides or

trinucleotides), when compared to DNA duplexes, must be considered. It is conceivable that the same base-conformations are populated in short DNA oligomers as for longer DNA oligomers and time-resolved fluorescence studies on 2AP-containing dinucleotides have revealed that the conformations present in samples very closely resemble those found in single-stranded DNA oligomers of longer lengths (also demonstrated previously in Chapter 4).[73,74]

The variety of 2AP-containing oligomers studied by Xu and Nordlund revealed that efficiency of energy transfer from adenine to 2AP was an order of magnitude higher than that from other canonical DNA bases. This can be seen in the values of η(t) and η(-1) of the decamers and hexamers shown in Table 5.1. In the DNA decamers, where only one type of base is present other than 2AP, the overall energy transfer efficiency for those composed of adenines is approximately 40% higher than for those composed of the other DNA bases (C, G or T). Likewise, in the DNA hexamers, the energy transfer efficiency increases by an order of magnitude when A is present in the DNA sequence and is minimal for the other DNA bases.

Xu and Nordlund showed that energy transfer efficiency is only mildly dependent on the direction along the DNA strand (5' to 3' vs 3' to 5') by determining values for η(t) of CCA[2AP]CC and CCA[2AP]ACC (at 5°C, λ_{ex} = 260 nm) and calculating the values for η(-1) and η(+1) in each oligomer. The resulting energy transfer efficiencies are shown in Table 5.2 and clearly show a similar calculated result for η(-1) and η(+1) when the identity of both bases is adenine.

Oligonucleotide Sequence	**η(t) /%**	**η(-1) /%**	**η(+1) /%**
CCA[2AP]CC	22 ± 2.5	57 ± 5	12 ± 2.5
CCA[2AP]ACC	29 ± 3	57 ± 5	58 ± 6

Table 5.2: Overall energy transfer efficiencies, η(t) and calculated base-specific energy transfer efficiencies from donor bases left-adjacent and right-adjacent to 2AP, η(-1) and η(+1) respectively in 2AP-containing DNA oligomers recorded at 5°C using an excitation wavelength of 260 nm. The values shown here have been reproduced from the publication by Xu and Nordlund.[9]

It is clear from a comparison of the values for η(t) and η(-1) in Table 5.1 and Table 5.2 that the energy transfer from the base immediately adjacent to 2AP has a higher efficiency than the overall energy transfer efficiency per donor. This can be attributed to the drop-off in energy transfer efficiency of a base with distance from the acceptor base. However, in comparison with calculated Förster transfer efficiencies (shown in Table

5.3), Nordlund found that the rate of the energy transfer efficiencies from DNA bases to 2AP in adenine tracks did not decrease at as fast a rate as the $1/r^6$ dependence typical to Förster transfer efficiencies. Therefore, standard Förster theory cannot explain the mechanism of energy transfer to 2AP present in DNA oligomers.

	η(-1) /%	**η(-2) /%**	**η(-3) /%**	**η(-4) /%**	**η(-5) /%**
Experimental	57	16.4	4.0	15.1	15.3
Theoretical	83	7.0	0.66	0.12	0.03

Table 5.3: Comparison of the experimentally determined energy transfer efficiencies from specific bases in a ss-DNA oligomer, CCAAAAA[2AP]CC, (51μM, at 5°C, λ_{ex}= 260 nm) with the theoretical Förster energy transfer efficiencies calculated as described in the review by Nordlund.[53]

As energy transfer to 2AP along tracks of adenine bases has been shown to be efficient, these systems have been the focus of a majority of investigations. By determining the energy transfer efficiency of a set of ss-DNA pentamers composed of four adenine bases and one 2AP base (e.g. AA[2AP]AA), in which the position of 2AP was altered such that it occupied positions 1 through 5 in the DNA base sequences (where the left-most base is position 1 and the right-most is position 5), two main observations concerning energy transfer to 2AP in DNA oligomers were revealed.[75] Firstly, energy transfer to 2AP is greater when adenine is located on both sides of 2AP in the sequence rather than for 2AP at the end of the oligomer (5' end or 3' end). Secondly, the transfer efficiency contribution is greatly reduced past the second-nearest base from 2AP and thus the main contribution via energy transfer comes from the nearest and the next nearest neighbouring base to 2AP. Nordlund and Xu found that incorporating a cytosine, guanine or thymine base in-between adenine and 2AP was enough to block the efficient energy transfer from adenine to 2AP, and this was attributed to the substantially lower efficiency of energy transfer to 2AP.[53]

Typically, for 2AP-containing oligomers, the transfer efficiency for energy transfer to 2AP was found to be greater when DNA bases were located on either side of 2AP (as opposed to at the end of the DNA strand). However, in 2AP-containing guanine pentamers, Nordlund *et al.* measured the energy transfer efficiency to be greater when 2AP is positioned at the 3' end of the oligomer (GGGG[2AP]) than at other locations in the pentamer. To explain this discrepancy, Evans performed energy-minimisation calculations, showing that the 2AP base could move in such a way to adopt a

conformation that allows the NH_2-group of 2AP to be brought close enough for intra-strand H-bonding with O6 group of G to occur (as shown in Figure 5.7).[53,76]

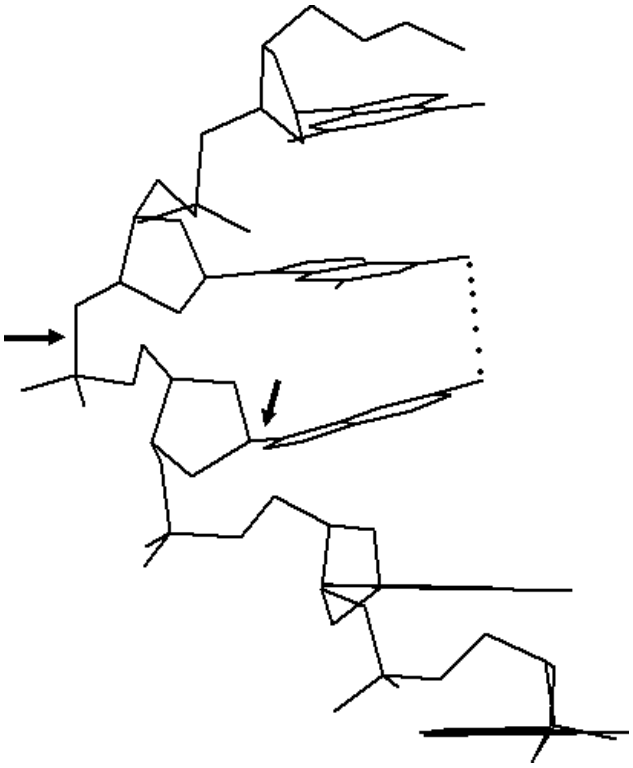

Figure 5.7: Possible conformation of 2AP-containing guanine pentamers (GG[2AP]GG) showing that intra-strand H-bonding between 2AP and adjacent guanine can occur. Reproduced from the review article by Nordlund.[53]

If intra-strand H-bonding can occur then base mobility will be further reduced. These findings suggested that when 2AP is located at the 3' end of the DNA oligomer, conformational freedom of the base is greater than when located with a base on either side. In this case, intra-strand H-bonding could more readily occur, resulting in a decrease in base mobility and an increase in energy transfer. This further highlights the importance of base-dynamics and the necessity to understand the conformations accessible by DNA bases to understand such a mechanism as electronic energy transfer in DNA.

Typically, the formation of DNA duplexes has been found to have minimal effect on the energy transfer efficiency between DNA bases and 2AP.[9] However, this is not the case in one scenario: that of 2AP located within ATAT and TATA sequences in DNA oligomers. 2AP has been known to adopt unusual conformations when located within these sequences, which results in changes to the spectral properties of 2AP, such as red-shifted excitation maxima or the appearance of extra excitation bands around 275 nm, indicating

reduced 2AP-solvent exposure and the presence of energy transfer to 2AP.[53,61] 2AP is highly constrained within these sequences and the formation of DNA duplexes containing these sequences results in an unusually large increase in the cross-strand transfer efficiency (to a value of 38%). Such high cross-strand transfer efficiencies have not been observed in the context of any other sequences. Cross-strand energy transfer has typically been negligible and not significantly observed in the studies by performed by Xu and Nordlund.[9]

Within the intermediate temperature range studied (-5°C to 25°C), the energy transfer efficiencies from DNA bases to 2AP determined by Xu and Nordlund were shown to be only moderately dependent on DNA concentration and salt concentration and could only account for ±1% out of the total 2-5% transfer efficiency. On the other hand, energy transfer was found to be highly dependent on the solvent used, which could be explained by the stabilisation of stacking interactions between DNA bases caused by hydrophobic forces.

While Nordlund, Xu and Evans have been the main contributors to the studies of energy transfer from DNA bases to 2AP, a number of studies have also been performed by other authors. Jean and Krueger investigated the viscosity- and temperature-dependences for energy transfer in 2AP-containing DNA trinucleotides,[65] (with sequences of T[2AP]T and A[2AP]A), and determined that the viscosity- and temperature-dependences of energy transfer efficiency differed qualitatively from those determined for charge transfer in DNA. Using time-resolved anisotropy measurements and molecular dynamics simulations, Jean and Krueger investigated the structural dynamics of these systems and investigated how local fluctuations away from the average DNA structure (such as the stacking and unstacking of DNA bases) modulate the electronic interactions between 2AP and neighbouring bases. It was found that the energy transfer rate was greatly overestimated using a standard transition dipole-dipole approximation for the Coulombic coupling and that energy transfer to 2AP from a neighbouring adenine base occurs on a much faster timescale than charge transfer occurs. Ultimately, the findings suggested that although charge transfer is largely controlled by conformational gating, these large amplitude fluctuations are not relevant on the faster timescales involved in the transfer of electronic energy between DNA bases and 2AP.

The remainder of this chapter presents the results of work performed that utilised the favourable properties of 2AP that make it an ideal fluorescent probe of DNA structure, in order to better understand electronic energy transfer in DNA. Initially, energy transfer efficiencies are reported for 2AP-containing dinucleotide samples at room temperature determined using steady-state fluorescence spectroscopy. The time-resolved fluorescence properties of 2AP-containing dinucleotides at room temperature excited at 260 nm are also presented and the energy transfer efficiencies determined from the lifetime parameters are discussed. Finally, an estimate of the energy transfer efficiency for 2AP-dinucleotides at 77 K, determined from steady-state fluorescence measurements, will be presented before being compared with the time-resolved fluorescence decay parameters under these conditions.

5.2. Materials and Methods

Samples of 2AP-containing dinucleotides, 2AP-X (where X = A, T, C, G or I), were prepared as described in Section 4.2 and studies were performed in aqueous tris buffer for room temperature measurements, or in aqueous 6M LiCl for 77 K measurements.

Absorption spectra were recorded as described in Section 3.1. The absorbance values for 2APr and 2AP-containing dinucleotides, at the 2AP absorption maximum (~305 nm) were used to apply a concentration correction to the absorption and steady-state fluorescence intensities, under the assumption that 2AP is the only absorbing species at this wavelength.

Energy transfer efficiencies were calculated from steady-state fluorescence and absorbance data following the method of Nordlund *et al*., using Equation 5.2. The absorbance values used for $A_a(\lambda_{ex})$ and $A_d(\lambda_{ex})$ were the absorbance values for 2APr and for the DNA bases, respectively, at λ_{ex} (260 nm) following correction for concentration differences. Note that the absorbance of the DNA base, $A_d(\lambda_{ex})$, is obtained via subtraction of the absorbance of 2APr from the absorbance of the dinucleotide, rather than from a measurement of the absorbance spectra of the DNA bases alone (as described previously in Section 5.1.4.2). Fluorescence intensities, $F(\lambda_{ex})$ and $F_a(\lambda_{ex})$, were determined via integration of the emission spectrum at 20 nm either side of the emission peak following excitation at 305 nm or 260 nm, respectively. Quantum yield ratios, Q, were determined from values obtained via integration of the fluorescence emission spectra at 20 nm either side of the emission peak at ~370 nm when excited at 305 nm.

Time-resolved fluorescence measurements were recorded as described in Section 3.2 for direct excitation of 2AP. Indirect excitation of 2AP, via energy transfer, was achieved using an excitation wavelength of 260 nm to excite the normal DNA bases while monitoring the fluorescence decay of 2AP at 3 emission wavelengths (360, 380 and 400 nm) similar to those for direct excitation of 2AP. Fluorescence decays were fitted as described in Chapter 3.

Steady-state fluorescence and time-resolved fluorescence measurements recorded at 77 K were performed as described in Chapter 3, using an excitation wavelength of 260 nm for the indirect excitation of 2AP via energy transfer.

5.3. Results and Discussion

5.3.1. Steady-state Fluorescence at Room Temperature

The fluorescence emission spectra of 2AP-containing dinucleotides, obtained from indirect excitation of 2AP (*via* energy transfer from the partner DNA base) using an excitation wavelength of 260 nm, are shown in Figure 5.8. For comparison, the fluorescence emission spectra obtained from direct excitation of 2AP in the dinucleotides at 305 nm (reproduced from Figure 4.9) are also shown in Figure 5.8

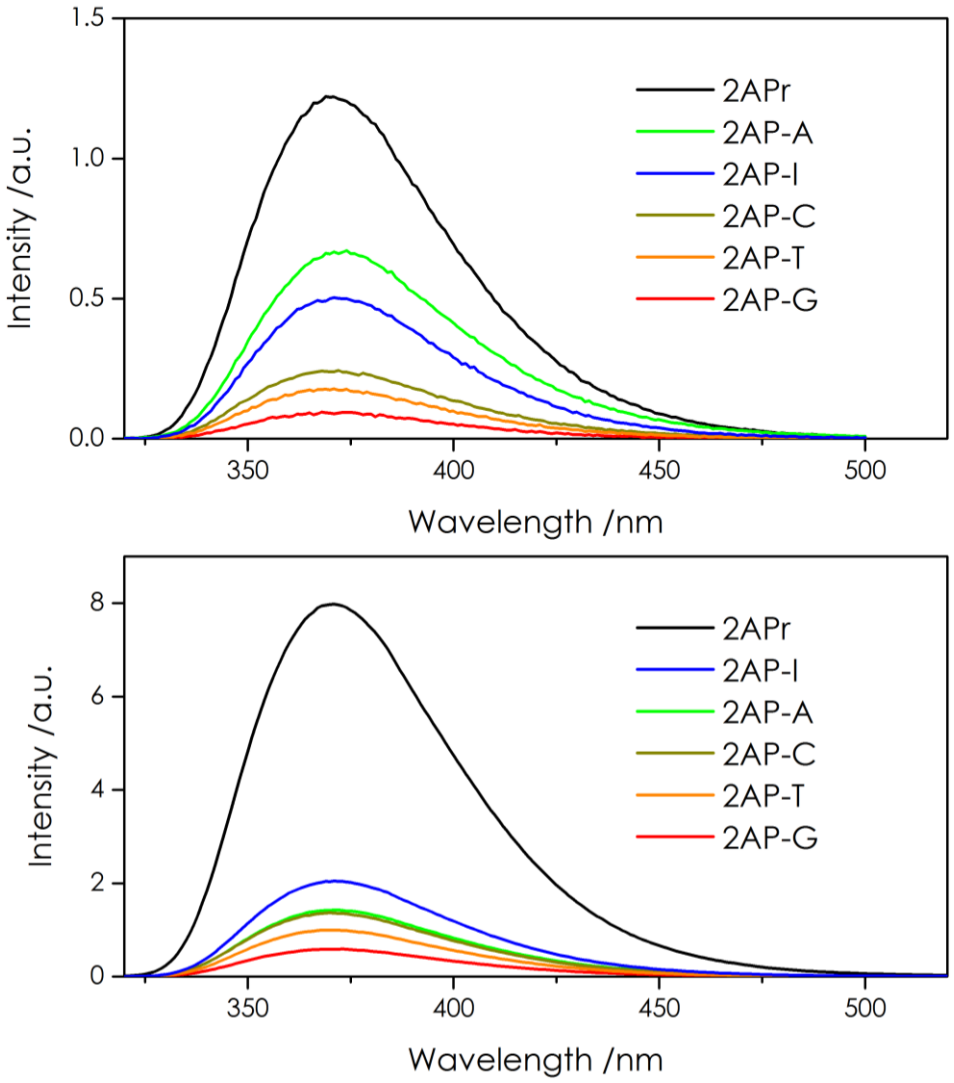

Figure 5.8: Fluorescence emission spectra of dinucleotides 2AP-X in aqueous tris buffer at room temperature, excited at 260 nm (top) and at 305 nm (bottom). The orders of the legends reflects the orders of the intensities at the maximum wavelength (~370 nm) in each set of spectra.

It can be seen that, regardless of the excitation pathway, fluorescence emission results solely from 2AP, evident from its characteristic emission profile and maximum emission wavelength of 370 nm and no shifts in the position of the emission maximum in each spectrum was observed. However, the dependence of the fluorescence intensity on the identity of the partner base differs for the two different wavelengths used for excitation. Fluorescence intensity ratios, relative to 2APr, for direct and indirect excitation are shown in Table 5.4.

Sample	Fluorescence Intensity Ratio (2AP-X/2APr)	
	λ_{exc} = 260 nm	λ_{exc} = 305 nm
2AP-G	0.08	0.07
2AP-T	0.15	0.12
2AP-C	0.20	0.17
2AP-A	0.55	0.18
2AP-I	0.41	0.25
2APr	1.00	1.00

Table 5.4: Fluorescence emission intensities of dinucleotides 2AP-X, relative to 2APr, for excitation at 260 nm and 305 nm observing emission at 370 nm. Intensities were corrected for minor concentration differences based on absorbance measurements.

For direct excitation, at 305 nm, the relative intensities reflect the differing quenching efficiencies of the partner bases. However, for 260 nm excitation, there is an additional influence on the fluorescence intensity that can be attributed to the transfer of energy from the partner base to 2AP following the absorption of a photon by the partner base. An increase in the relative intensity for indirect excitation (at 260 nm) compared with direct excitation (at 305 nm) is indicative of energy transfer, This increase is particularly evident for 2AP-A and 2AP-I, which show the largest differences in the relative fluorescence intensities when direct and indirect excitation are compared.

Further evidence of energy transfer from adenine to 2AP is illustrated when the normalised excitation spectra of 2AP-A and 2AP-I are compared with that of 2APr (Figure 5.9).

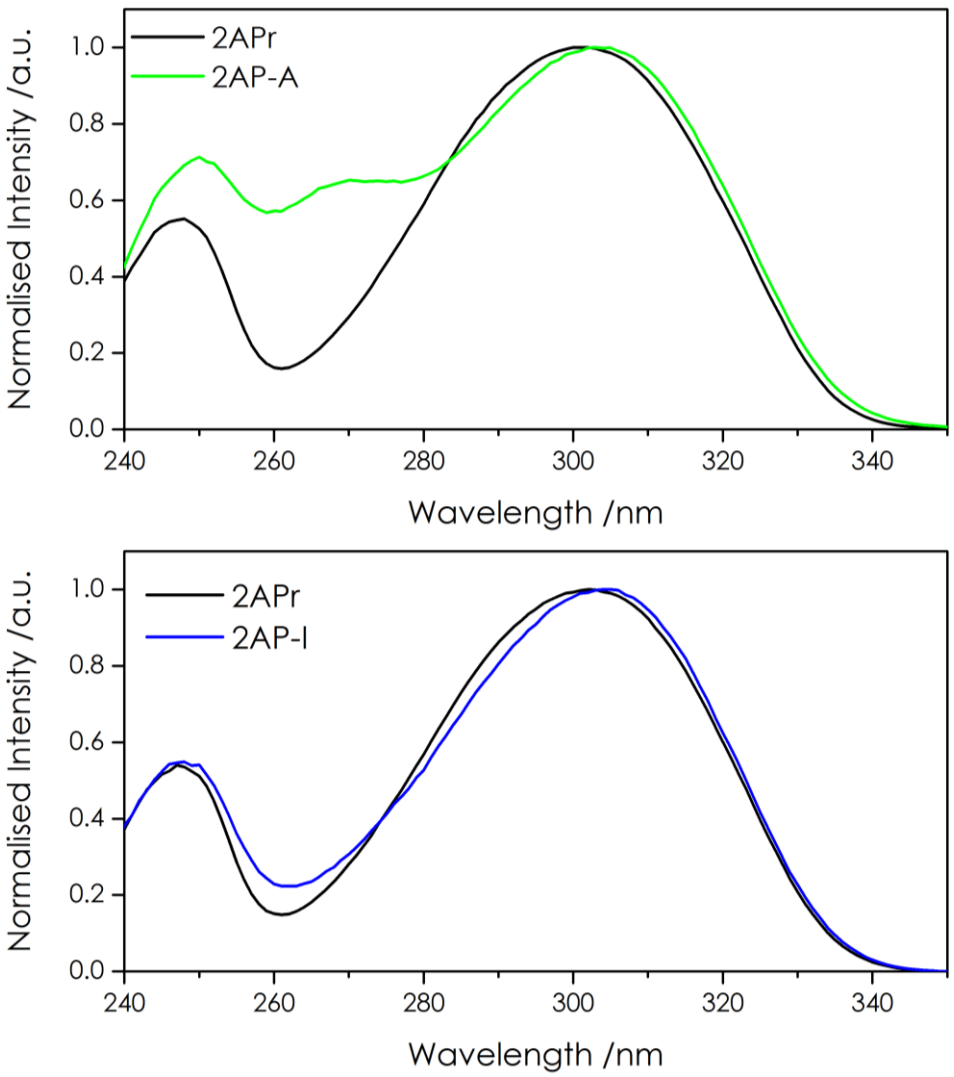

Figure 5.9: Normalised fluorescence excitation spectra of 2AP-A (top) and 2AP-I (bottom) with 2APr. Spectra have been normalised to intensity maximum relating to excitation of 2AP (~305 nm).

The spectra shown in Figure 5.9 are clearly dominated by the 2AP excitation band at ~305 nm (which is red-shifted by a few nm in the case of the dinucleotides, due to reduced interactions of 2AP with solvent molecules). However, there is clearly an additional contribution to the excitation spectrum of 2AP-A at around 260 nm – 280 nm that can be attributed to absorption by adenine (Figure 5.10) (and subsequent energy transfer to 2AP). Additional excitation intensity is also observed for 2AP-I, manifesting as an increase in excitation intensity in the region around 260 nm, where absorption by inosine occurs. To show this absorption by the non-fluorescent DNA bases, the normalised absorption spectra of 2AP-A, 2AP-I and 2APr are presented in Figure 5.10

and the absorption bands associated with adenine and inosine are clearly identified in the region of 250 nm – 280 nm and are not present in the absorption spectrum of 2APr.

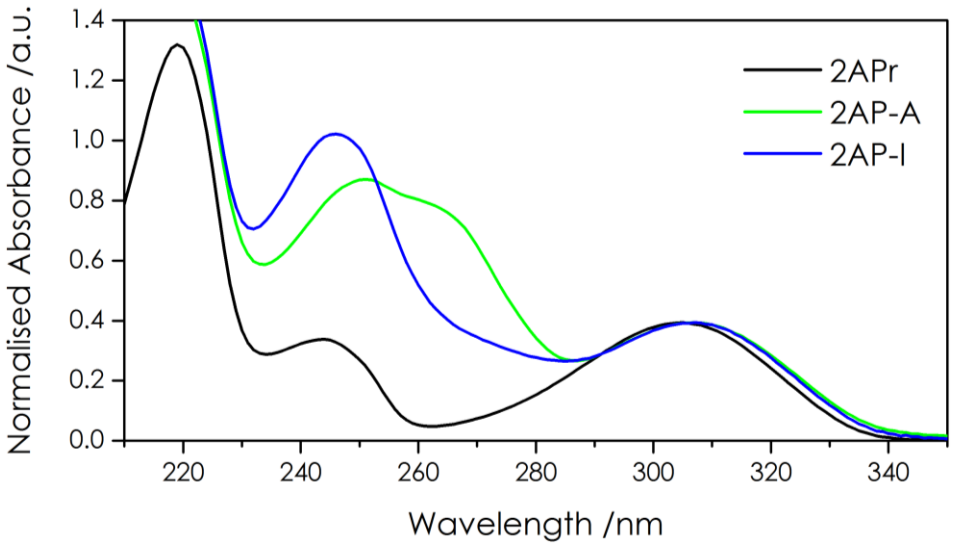

Figure 5.10: Normalised absorption spectra of 2APr (black), 2AP-A (green) and 2AP-I (blue) in aqueous tris buffer solution, normalised to the absorption band of 2AP at ~305 nm

Concerning 2AP-C, 2AP-G and 2AP-T, in which no significant increase is observed in the fluorescence intensity ratio when excited at 260 nm compared to 305 nm, the fluorescence excitation spectra (shown in Figure 5.11) show no discernible evidence of

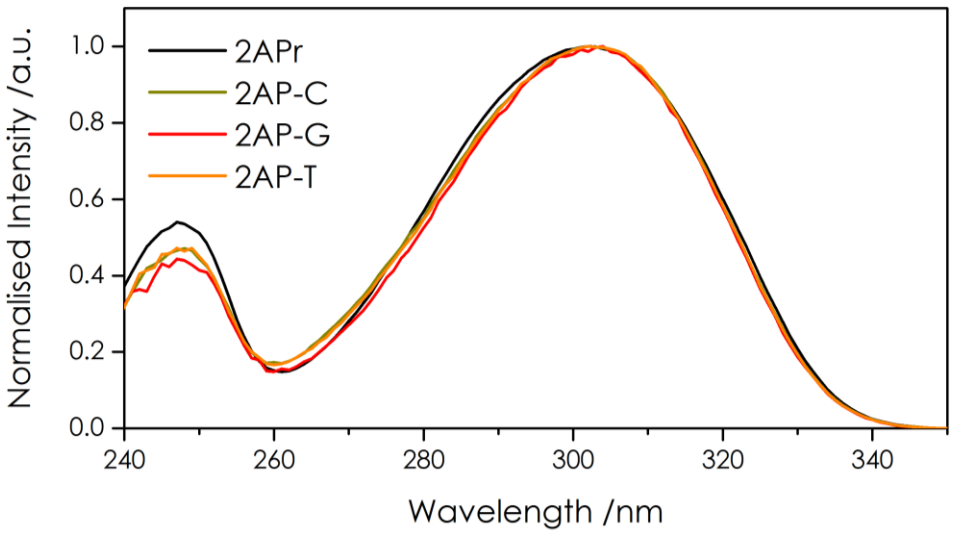

Figure 5.11: Normalised fluorescence excitation spectra for dinucleotides 2AP-X (X = cytosine (dark yellow), guanine (red) or thymine (orange)) and 2APr (black), normalised to excitation peak at ~305 nm.

additional excitation features relating to energy transfer from the DNA bases to 2AP.

The largely overlapping excitation spectra of 2APr with the spectra of 2AP-C, 2AP-G, and 2AP-T, when normalised to excitation peak of 2AP at ~305 nm, implies that the occurrence of energy transfer to 2AP from C, G or T is minimal.

5.3.1.1. Electronic Energy Transfer Efficiencies

The efficiencies of energy transfer from each of the DNA bases to 2AP in 2AP-containing dinucleotides were calculated using Equation 5.2 and the values of the input parameters derived from steady-state fluorescence emission spectra and absorption spectra, used in these calculations, are given in Table II.1 in Appendix II. The nomenclature used in previous studies of energy transfer to 2AP in DNA, in which η was defined terms of the total averaged efficiency per base (η(t)) or as the efficiency from a single DNA base (η(n), where n denotes the position relative to 2AP, as described previously), does not apply in the studies of 2AP-containing dinucleotides. These two terms are essentially equivalent as each 2AP-dinucleotide consists of only one DNA base and one 2AP base. Thus, for simplicity, energy transfer efficiency will be written simply as "η_x", where "x" denotes the method used to calculate the energy transfer efficiency. The subscript "SS" is used to indicate that the efficiencies were calculated from steady-state intensities and "TRF" (used later in this chapter) indicates those calculated from time-resolved fluorescence measurements. The energy transfer efficiencies obtained from steady-state fluorescence measurements, η_{ss}, are shown in Table 5.5

X	η_{ss} /%
G	<1
T	2.2
C	2.3
A	15.0
I	7.4

Table 5.5: Energy transfer efficiencies (from X (3') to 2AP (5')) for dinucleotides 2AP-X in aqueous tris buffer at room temperature.

The energy transfer efficiency from adenine was found to be the highest, at 15%, and is approximately an order of magnitude greater than the values determined for the other natural bases. The transfer efficiency for guanine is lowest, less than 1%, and was barely detectable. The energy transfer efficiencies are consistent with those reported in the review by Nordlund,[53] in which energy transfer from adenine is by far the greatest, as exemplified in Table 5.5. The efficiencies measured here, at room temperature, are much lower than the efficiencies measured by Xu and Nordlund, at 5°C, supporting the finding that transfer efficiency increases significantly with decreasing temperature. No

literature values pertaining to room temperature transfer efficiencies could be found and, as such, no direct comparison with those presented in Table 5.5 can be made. However, the trend in the values presented in Table 5.1 for η(-1) in 2AP-containing hexamers at 5°C is consistent with those measured for 2AP-containing dinucleotides at room temperature (η of A>>C ≈ G ≈ T)

Transfer efficiency from inosine to 2AP, 7.4%, was found to be lower than from A but is significantly greater than from C, G and T.

5.3.2. Time-resolved Fluorescence at Room Temperature

Steady-state measurements have shown the occurrence of electronic energy transfer from the DNA bases to 2AP, resulting in the excitation of 2AP via an indirect route. However, as far as the author is aware, the effect of indirect excitation on the fluorescence decay properties of 2AP in DNA (i.e. the nature of the excited state conformational population) has not been studied previously.

The fluorescence decay parameters measured for the dinucleotides following indirect excitation (at 260 nm) are presented in Table 5.6, in comparison with those for direct excitation (at 310 nm). The results for 2AP-C are omitted from Table 5.6 because, following 260 nm-excitation, anomalous behaviour was observed, due to the formation of photohydrated cytidine.[20,23,33,35,77] The formation of the photohydrate was not significant during the steady-state fluorescence measurements but became evident in the time-resolved measurements due to the longer timescale required for measurements and the increased intensity of the excitation light. The lifetime parameters for 2AP-C excited at 260 nm in aqueous tris buffer or in aqueous LiCl solution are presented in Table II.3 and TableII.4, respectively, in Appendix II. Even though photohydration of 2AP-C was not extensively studied, the effect of excitation at 260 nm (which was not observed during excitation at 310 nm) and the resulting change in the fluorescence quantum yield, along with the thermal reversibility of this effect with time, confirmed that photohydration of cytidine was the cause of this anomaly.

X	Excitation pathway	τ_i /ns				A_i				<τ> / ns
		τ_1	τ_2	τ_3	τ_4	A_1	A_2	A_3	A_4	
G	Indirect	0.04	0.37	1.7	9.1	0.84	0.07	0.08	0.01	0.33
	Direct	0.05	0.29	1.7	9.3	0.64	0.12	0.20	0.04	0.77
T	Indirect	0.06	0.41	2.3	9.2	0.70	0.08	0.20	0.02	0.70
	Direct	0.07	0.37	2.3	9.2	0.53	0.10	0.34	0.03	1.17
A	Indirect	0.14	0.65	2.2	9.8	0.21	0.63	0.13	0.03	1.04
	Direct	0.12	0.67	2.2	9.3	0.38	0.35	0.18	0.09	1.56
I	Indirect	0.07	0.80	2.9	8.3	0.18	0.44	0.34	0.04	1.66
	Direct	0.12	0.85	3.0	8.7	0.31	0.20	0.42	0.07	2.06

Table 5.6: Fluorescence lifetimes, τ_i, and corresponding fractional amplitudes, Ai, for 2AP-X (X= A, G, T or I) in aqueous buffer at room temperature, for indirect excitation (λ_{exc} = 260 nm) or direct excitation (λ_{exc} = 310 nm). Lifetimes were obtained from globally fitting of decays recorded at three emission wavelengths (360nm, 380 nm and 400 nm). The fractional amplitudes show little variation with emission wavelength and those for 380 nm emission are given. The average lifetimes, <τ>, are also given. The fluorescence decay parameters for 2AP-C are not shown in this table but can be found in Table II.3 in Appendix II. Experimental uncertainties (estimated by dividing the standard deviation of values by the corresponding values): $\tau_1 \leq 8\%$, $\tau_2 \leq 5\%$, $\tau_3 \leq 1\%$, $\tau_4 \leq 1\%$, $A_1 \leq 4\%$, $A_2 \leq 3\%$, $A_3 \leq 2\%$, $A_4 \leq 1\%$.

It can be seen that the values of the lifetimes, τ_i, obtained from direct and indirect excitation of 2AP are very similar for all dinucleotides. However, significant differences are observed in the A factors for the two excitation pathways used. For 2AP-G and 2AP-T, the A factor of the well-stacked conformations, A_1, shows an increase of approximately 0.2. A corresponding decrease in the other A factors is observed but is not equally spread, with the greatest decrease (of about 0.12) for A_3. For 2AP-A and 2AP-I, there is an increase in A_2, together with a substantial decrease in A_1. Differences in the A factors lead to a reduction in the average lifetime observed for 2AP in each dinucleotide by approximately 400 ps on indirect excitation, as a result of the preferential population of those conformations with shorter lifetimes.

The near-identical fluorescence lifetimes determined for each dinucleotide, using different excitation pathways, indicate that the interactions of 2AP with the neighbouring base and solvent molecules remain unchanged and it can be assumed that essentially the same conformational states are accessible by 2AP. It must not be forgotten that, the fluorescence decay of 2AP when excited at 260 nm, contains contributions from both the minimal direct excitation of 2AP as well as from 2AP excited indirectly via energy transfer (and will be discussed further in Section 5.3.2.1). As the fluorescence

decay parameters of 2AP describe the conformational states of 2AP in DNA (from well-stacked species to unstacked species), if excitation of 2AP via energy transfer were to excite all conformations of 2AP present equally, then the A factors determined from 260-nm excitation would be equivalent to those resulting from 310-nm excitation. Furthermore, if this were the case, then it would not be possible to identify the presence of energy transfer from the fluorescence decay parameters, as both sets would be identical. However, this is not the case. The significant difference observed in the A factors, while the lifetime values remain consistent, indicates that energy transfer does not result in excitation of all conformations of 2AP equally and some conformations of 2AP are more favourable for energy transfer than others. The increase in A_1 of G and T indicates that energy transfer is more preferential for the most well-stacked states of 2AP. On the other hand, for A and I, the observed increase in A_2 suggests that, although still intra-helical, imperfectly or partially stacked states of 2AP are more favourable for energy transfer from adenine or inosine rather than the most well-stacked conformations.

Previously, Nordlund *et al*. drew a correlation between the highly constrained, well-stacked conformations of 2AP located within TATA and ATAT sequences, and the abnormally high efficiency of energy transfer found in these systems.[61] The high efficiency of energy transfer in these systems, where the bases are known to be highly constrained, support the findings of the work presented here showing that well-stacked conformations are more favourable for energy transfer from DNA bases to 2AP.

The identification of well-stacked states as more favourable for energy transfer is also consistent with the temperature-dependence of energy transfer determined by Xu and Nordlund. The temperature-dependence shows that energy transfer efficiency decreases with increasing temperature due to an increase in base-mobility. This implies that specific conformations of DNA bases are more favourable for energy transfer, while deviation from these conformations lead to a reduction in the transfer efficiency. As such, the fluorescence lifetime parameters shown in Table 5.6 provide an insight into the nature of the DNA base conformations (well stacked-states) in which energy transfer is more efficient and provides direct evidence that energy transfer is not equally favourable for all states of 2AP in DNA.

5.3.2.1. Evaluation of Fractional Populations Excited by Energy Transfer

In order to evaluate more precisely the fractional populations of 2AP indirectly excited via energy transfer, it must be recalled that so-called "indirect" excitation at 260 nm, in fact, also results in some direct excitation, since 2AP has a non-zero absorbance at this wavelength. The observed fluorescence decay excited at 260 nm, $I(t)_{260}$, therefore consists of contributions from both direct ($I(t)_{260\,dir}$) and indirect ($I(t)_{260\,ind}$) excitation, as follows.

$$I(t)_{260} = I(t)_{260,dir} + I(t)_{260,ind} \quad \textbf{5.3}$$

If we assume that the values of the lifetimes of the decay components are independent of the excitation wavelength, and that indirect excitation, by energy transfer, populates only one of the lifetime components, τ_j, we can define the decays measured at the two excitation wavelengths, $I(t)_{310}$ and $I(t)_{260}$, as follows,

$$I(t)_{310} = \sum_i A_{i\,(310)}\, exp\left(-{}^{t}/_{\tau_i}\right) \quad \textbf{5.4}$$

$$I(t)_{260} = \sum_i A_{i\,(260)}\, exp\left(-{}^{t}/_{\tau_i}\right) \quad \textbf{5.5}$$

$$\Rightarrow I(t)_{260} = \left(\frac{1}{1+B_j}\right)\left\{\sum_i A_{i\,(310)}\, exp\left(-{}^{t}/_{\tau_i}\right) + B_j\ exp\left(-{}^{t}/_{\tau_j}\right)\right\} \quad \textbf{5.6}$$

where $\sum_i A_{i\,(310)} = 1$ and $\left(\frac{B_j}{1+B_j}\right)$ is the fractional population of component *j* excited by energy transfer.

The fractional amplitude of component *j* in the decay excited at 260 nm can then be defined as

$$A_{j(260)} = \left(\frac{A_{j(310)} + B_j}{1+B_j}\right) \quad \textbf{5.7}$$

Hence, B_j can be determined from the measured A factors, as follows,

$$B_j = \left(\frac{A_{j(260)} - A_{j(310)}}{1 - A_{j(260)}}\right) \quad \textbf{5.8}$$

The fractional population arising from energy transfer, A_{ET}, can thus be obtained:

$$A_{ET} = \left(\frac{B_j}{1+B_j}\right) \quad \textbf{5.9}$$

For the other three decay components, $i \neq j$, the A factors in the decay excited at 260 nm are given by:

$$A_{i(260)} = \left(\frac{A_{i(310)}}{1 + B_j}\right) \qquad \textbf{5.10}$$

In the case of G and T, energy transfer is assumed to contribute only to the population of component 1, i.e. j=1, and for A and I it is assumed to contribute only to component 2, i.e. j=2. For each of the dinucleotides, the calculated value for the fractional population due to energy transfer, A_{ET}, is presented in Table 5.7.

X	Fractional population excited by energy transfer, A_{ET}
G	0.53
T	0.37
A	0.43
I	0.30

Table 5.7: The fractional population excited by energy transfer, A_{ET}, in each of the dinucleotides 2AP-X (X = G, T, A or I). These values were calculated on the assumption that energy transfer populates only one of the four lifetime components: for X=G and T, this is component 1, and for X=A and I, this is component 2.

The values of the A factors predicted for the 260-nm excitation, based on Equation 5.10, are given in Table 5.8, in comparison with the experimentally measured values (from Table 5.6).

X		A_i				$<\tau>$ /ns
		A_1	A_2	A_3	A_4	
G	Measured	0.84	0.07	0.08	0.01	0.33
	Predicted	0.84	0.05	0.09	0.02	0.37
T	Measured	0.70	0.08	0.20	0.02	0.70
	Predicted	0.70	0.06	0.22	0.02	0.74
A	Measured	0.21	0.63	0.13	0.03	1.04
	Predicted	0.22	0.63	0.10	0.05	1.17
I	Measured	0.18	0.44	0.34	0.04	1.66
	Predicted	0.22	0.44	0.29	0.05	1.63

Table 5.8: Comparison of measured and predicted A factors for fluorescence decays excited at 260 nm. The predicted values are based on the assumption that energy transfer populates only one of the four lifetime components: component 1 for X=G and T, component 2 for X=A and I. The measured values are reproduced from Table 5.6. Average lifetimes, $<\tau>$, for the predicted decay-parameters are calculated using the same τ_i values as the measured decay parameters.

At first glance, the predicted A factors, determined using Equation 5.10, bear a close resemblance to the measured A factors, from 310-nm excitation, and shows that the assumption that energy transfer only populates one of the lifetime components gives a close estimate of those components involved in energy transfer. However, minor differences in the A factors of the other three components (of up to 0.05) that are assumed not to be populated by energy transfer, results in a discrepancy in the average lifetimes calculated using these A factors. The differences in the average lifetimes implies that the previously made assumption is insufficient to describe the lifetime components involved in energy transfer and suggests that more than one component is populated by energy transfer from the DNA base. The involvement of the population of multiple lifetime components via energy transfer will be investigated in Section 5.3.2.3.

Time-resolved fluorescence measurements provide an alternative method to determine the energy transfer efficiency. The efficiency is related to the fraction of the excited state populated by energy transfer as shown in Equation 5.11

$$\eta_{TRF} = \frac{A_a(\lambda_{ex})}{A_d(\lambda_{ex})} \times \left(\frac{A_{ET}}{1 - A_{ET}}\right) \qquad \textbf{5.11}$$

The efficiencies calculated in this way, designated η_{TRF}, are presented in Table 5.9.

X	**η_{TRF} /%**
G	8.2
T	5.6
A	5.1
I	4.5

Table 5.9: Energy transfer efficiencies for dinucleotides 2AP-X in aqueous tris buffer determined from time-resolved fluorescence measurements and absorption measurements.

The energy transfer efficiencies presented in Table 5.9 show a marked discrepancy with those determined from the steady-state fluorescence measurements shown in Table 5.5. From TRF measurements, the transfer efficiency for A (5.1%) is no longer an order of magnitude greater than that of the other DNA base and the greatest transfer efficiency is calculated to be from G (8.2%). These results are inconsistent with the values of η_{SS} determined previously in this work and inconsistent with the trend of transfer efficiencies determined from steady-state intensities by Xu and Nordlund (A>>G>T).

Based upon a comparison of the lifetime parameters determined from direct and indirect excitation of 2AP in the dinucleotides, two issues have been identified that should be addressed to correct the values of η_{SS} and η_{TRF} calculated in this work and provide a better estimate of the energy transfer efficiencies. The first issue is that the calculation of the transfer efficiency from steady-state measurements is based on the assumption that the FQY of 2AP in DNA is independent of the mode of excitation, that is to say that energy transfer is assumed to populate all conformational states of 2AP equally. However, the lifetime parameters following indirect excitation of 2AP demonstrate that energy transfer selectively populates well-stacked, highly quenched conformations; that is, the FQY of 2AP populated by indirect excitation is less than that for direct excitation. This will lead to an underestimation of the transfer efficiencies, as the FQY has been overestimated. The second issue identified here is that the assumption has been made that only one lifetime component is populated via energy transfer, which does not provide a sufficient description of the conformations involved in energy transfer due to the discrepancy between the calculated $\eta_{SS,\,corr}$ and η_{TRF} values. These two issues will now be addressed in the following sections.

5.3.2.2. Re-evaluation of the Energy Transfer Efficiencies Determined from Steady-state Measurements

In the calculation of transfer efficiencies from steady-state fluorescence intensities, it was assumed that the quantum yield for indirect excitation of 2AP, ϕ_{ind} is equivalent to the quantum yield for direct excitation, ϕ_{dir}. However, it has now been shown, from the time-resolved fluorescence measurements, that this is not the case, due to the selective excitation of quenched species by energy transfer. A correction can, however, simply be applied to η_{SS} to account for this difference in quantum yield using Equation 5.12.

$$\eta_{SS,corr} = \eta_{SS} \times \frac{\phi_{dir}}{\phi_{ind}} \qquad \textbf{5.12}$$

The QY ratio can be replaced by the ratio of average lifetimes of the species resulting from direct and indirect excitation, respectively

$$\frac{\phi_{dir}}{\phi_{ind}} = \frac{\langle\tau\rangle_{dir}}{\langle\tau\rangle_{ind}} \qquad \textbf{5.13}$$

The resulting corrected energy transfer efficiencies, $\eta_{SS,\,corr}$, are presented in Table 5.10.

X	$<\tau>_{dir}$ /ns	$<\tau>_{ind}$ /ns	η_{SS} /%	$\eta_{SS,\,corr}$ /%
G	0.77	0.04	<1	<20
T	1.17	0.06	2.2	42.1
A	1.56	0.65	15.0	35.9
I	2.06	0.80	7.4	19.0

Table 5.10: Average lifetimes resulting from direct and indirect excitation used to correct the energy transfer efficiencies measured from steady-state fluorescence, η_{SS}, to give the corrected efficiencies, $\eta_{SS,\,corr}$, according to Equation 5.12 (where it is assumed that only one conformation is selectively excited via energy transfer.

The corrected values of $\eta_{SS,}$ reveal that the uncorrected values significantly underestimated the transfer efficiency, particularly in the case of G and T, where the FQY for indirect excitation is much less than for direct excitation. However, the corrected values, $\eta_{SS,\,corr}$, still do not agree with efficiencies calculated from the decay parameters, η_{TRF}. This suggests that the assumption made in the analysis of the time-resolved fluorescence results (that energy transfer only contributes to the population of one lifetime component of 2AP) is not valid, leading to incorrect estimation of both η_{TRF} and $<\tau>_{ind}$. If more than one component is populated via energy transfer, especially those with longer lifetime values, then the values of $<\tau>_{ind}$ used to correct η_{SS} in Table 5.10 will be too short and will result in an over estimation of the transfer efficiency. In the following section, a re-analysis of the time-resolved fluorescence data is presented, taking into account the population of multiple lifetime components by energy transfer.

5.3.2.3. The Involvement of Multiple Lifetime Components

Rather than assume that only one fluorescence lifetime component is populated by energy transfer, the population of multiple fluorescence lifetimes by energy transfer was investigated. We now define the decay measured at 260-nm excitation as follows.

$$I(t)_{260} = \sum_i A_{i\,(260)}\, exp\left(-{}^{t}/_{\tau_i}\right) \qquad \textbf{5.14}$$

$$= \frac{1}{\sum_i (A_{i(310)} + B_i)} \left\{ \sum_i (A_{i\,(310)} + B_i) exp\left(-{}^{t}/_{\tau_i}\right) \right\} \qquad \textbf{5.15}$$

Hence the A factors measured for 260-nm excitation are given by:

$$A_{i\,(260)} = \frac{(A_{i\,(310)} + B_i)}{\sum_i A_{i\,(310)} + B_i} \quad \text{for i = 1 to 4} \qquad \textbf{5.16}$$

where $\frac{A_{i\,(310)}}{\sum_i (A_{i(310)} + B_i)}$ is the fractional population of component *i* that is excited directly and $\frac{B_i}{\sum_i (A_{i(310)} + B_i)}$ is the fractional population of component *i* that is excited indirectly, by energy transfer, $A_{i(ET)}$.

Using non-linear least squares fitting in Microsoft Excel, Equation 5.16 was solved to give values of B_i and hence $A_{i(ET)}$, as listed in Table 5.11. Using Equation 5.17 (where A_a and A_d are the absorbance values of the acceptor and donor bases, respectively), energy transfer efficiencies are calculated from time-resolved fluorescence measurements, allowing for the involvement of multiple lifetime components, $\eta_{TRF,\,multi}$, and are presented in Table 5.11 alongside the sum of the A factors populated by energy transfer, $\sum A_{ET}$.

$$\eta_{TRF} = \frac{A_a(\lambda_{ex})}{A_d(\lambda_{ex})} \times \left(\frac{\sum A_{ET}}{1 - \sum A_{ET}} \right) \qquad \textbf{5.17}$$

The transfer efficiencies calculated from steady-state measurements and corrected for differences in FQY, due to inhomogeneous population of the lifetime components of 2AP in DNA via energy transfer, this time allowing for the involvement of multiple lifetime components, $\eta_{SS,\,corr,\,multi}$, are also shown in Table 5.11.

X	$A_{i\,(ET)}$				$\sum(A_{i\,(ET)})$	$<\tau>_{ind,\,multi}$ /ns	$\eta_{TRF,\,multi}$ /%	$\eta_{SS,corr,\,multi}$ /%
	A_1	A_2	A_3	A_4				
G	0.59	0.02	0.00	0.00	0.61	0.05	11	<15
T	0.42	0.03	0.02	0.00	0.46	0.23	10	11
A	0.13	0.55	0.09	0.01	0.79	0.86	26	27
I	0.02	0.34	0.12	0.00	0.48	1.36	11	11

Table 5.11: A factors relating to indirect excitation of multiple lifetime components via energy transfer, $A_{i\,(ET)}$ and the corresponding average lifetimes, $<\tau>_{ind,\,multi}$ are shown alongside energy transfer efficiencies, $\eta_{TRF,\,multi}$, calculated from $A_{i\,(ET)}$ (using Equation 5.17). Also shown are $\eta_{SS,corr,\,multi}$ values determined from SS measurements and corrected using $<\tau>_{ind,\,multi}$.

Comparison of the transfer efficiencies calculated from TRF measurements ($\eta_{TRF,\,multi}$) and those from SS measurements ($\eta_{SS,\,corr,\,multi}$) shows that there is now a high level of consistency between the two methods used. The calculated A factors relating to energy transfer, shown in Table 5.11, confirm that the previously made assumption of only one lifetime component being populated by energy transfer was incorrect and that multiple

lifetime components are actually involved. For G, the main component populated by energy transfer remains as component 1, but component 2 is also marginally populated by energy transfer. In the case of T, component 1 is preferentially populated but components 2 and 3 are also populated by a few percent (3% and 2% respectively), while for A the indirectly excited population is spread heterogeneously across all four components, with the most favourable being component 2. In the case of I, energy transfer mainly populates components 2 and 3, with a small percentage of component 1. It is evident that the population of even a small percentage of τ_3 and τ_4 has an enormous effect on the calculated average lifetime, and hence on the correction factor applied to the efficiency determined from steady-state intensity. The results shown in Table 5.11 demonstrate that the heterogeneous excitation of 2AP in different conformational states must be accounted for in order to provide an accurate measure of the energy transfer efficiency in DNA. From the consistency between the values calculated using two different methods, it can be assumed that these are accurate measures of the efficiencies of the transfer of electronic energy from the DNA bases to 2AP.

5.3.3. Steady-state Fluorescence at 77 K resulting from 260-nm Excitation

5.3.3.1. Monomeric 2AP and 2AP-riboside

As mentioned previously, in Chapter 4, the fluorescence excitation spectra of monomeric 2AP and 2APr are not identical, differing at excitation wavelengths below 280 nm. This difference is also clearly apparent in the absorption spectra, at room temperature, as shown in in Figure 5.12.

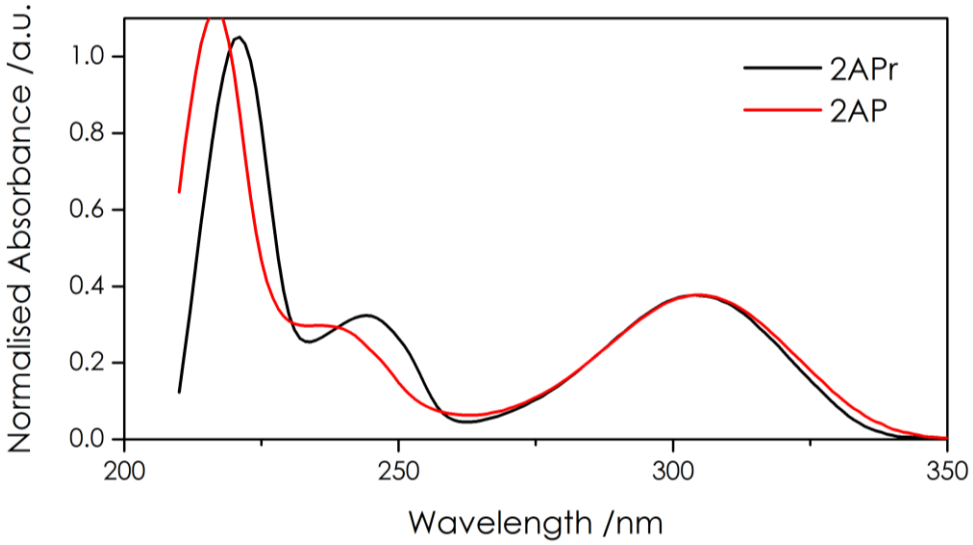

Figure 5.12: Normalised absorption spectra for 2AP monomer (red) and 2APr (black) in aqueous LiCl solution normalised to absorbance peak at ~305 nm.

The 2APr absorption bands are marginally narrower than those for 2AP are and the shorter-wavelength absorption band of 2AP, at ~240 nm, is located approximately 5 nm to the red of the corresponding 2APr band. Absorbance at 260 nm results from overlap of the two main absorption bands (with λ_{max} ~245 nm and ~305 nm). Comparing the absorbance value of 2APr at 260 nm and at room temperature with that of 2AP, the ratio of 0.78 for solutions in LiCl is comparable with a ratio of 0.81 in aqueous tris buffer. At room temperature, the fluorescence excitation spectra of 2APr and 2AP (shown in Figure 4.4 in Chapter 4) give identical intensity ratios at 260 nm to those determined from the absorbance values. However, when frozen at 77 K, the ratio of the fluorescence excitation intensities is only 0.58 at 260 nm, implying that the absorption spectra change on freezing. On the basis of the excitation intensities, the absorbance of 2APr decreases by a factor of about 0.6 on cooling from room temperature to 77 K, whereas for 2AP there is a decrease by a factor of about 0.8. Unfortunately, it was impractical to measure the absorption spectra at 77 K.

In evaluating energy transfer efficiencies at 77 K, the absorbance values were derived from the room temperature absorption spectra. However, as noted above, the excitation spectrum of 2APr indicates that there is a decrease in its absorbance at 260 nm on cooling to 77 K. If there were not a corresponding decrease in the (much greater) absorbance of the natural base in the dinucleotide, this might suggest that use of the room temperature value would result in overestimation of the energy transfer efficiency at 77 K. However, it is possible that there will also be changes in the absorption spectra of the natural bases on cooling. These factors, together with technical difficulties in making quantitative fluorescence intensity measurements at 77 K (discussed later) mean that there is greater uncertainty in efficiency values measured at 77 K than those determined at room temperature. The fact that the excitation spectrum of 2AP is affected differently from that of 2APr on cooling, further emphasises the importance of using 2APr, rather than 2AP, in determining energy transfer efficiencies. In future work, it would be desirable to devise a method of measuring absorption spectra for samples at 77 K.

5.3.3.2. 2AP-containing Dinucleotides

As reported in Chapter 4, when 2AP-dinucleotides are frozen in aqueous LiCl solution at 77 K, a large increase in fluorescence quantum yield is observed for 2AP when directly excited at 305 nm. When 2AP is excited indirectly, via energy transfer from a DNA base, a large increase in fluorescence intensity is also observed. This increase is best illustrated by the appearance in the excitation spectrum of an area of increased intensity in the region of 250 nm to 280 nm where absorption by the natural DNA bases occurs (as seen in Figure 4.11). The observation of additional peaks in the excitation spectra of 2AP-containing dinucleotides, when frozen at 77 K, is consistent for all native DNA bases, and can be attributed to the increased efficiency of energy transfer from the DNA base to 2AP, as exemplified for 2AP-A in Figure 5.13. Relevant excitation spectra for the other dinucleotides, where X = C, G, T or I, can be found in spectra in Figures 4.10 and 4.11 in Chapter 4 and in the normalised spectra in Figures I.6 and I.7 in Appendix I.

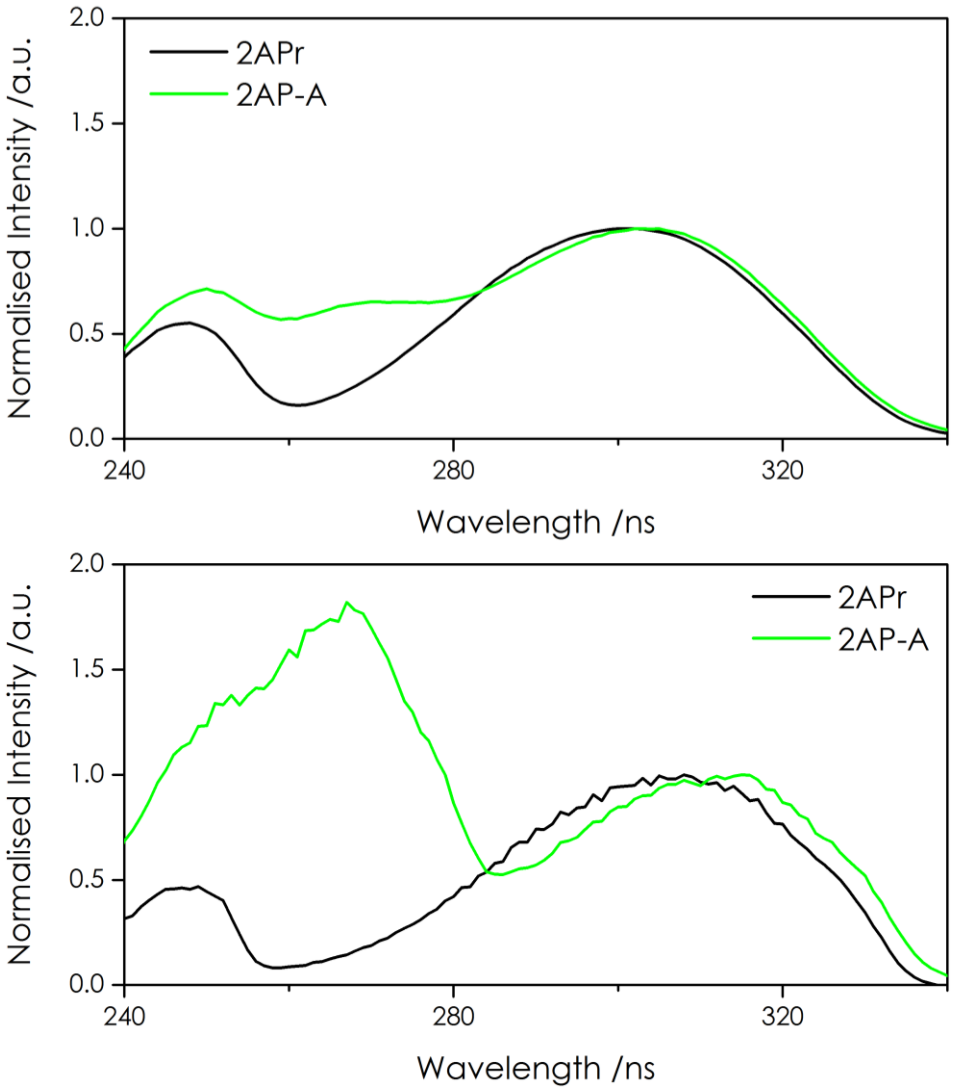

Figure 5.13: Normalised fluorescence excitation spectra of 2APr and 2AP-A dissolved in aqueous LiCl solution recorded at room temperature (top) and at 77 K (bottom). Spectra are normalised relative to the maximum of the excitation band of 2AP at ~305 nm for room temperature measurements and at approximately 305-315 nm for measurements performed at 77K.

A comparison of the spectra presented in Figure 5.13 shows that the readily observable peak at ~250 nm to ~280 nm in the excitation spectra of 2AP-A at room temperature (relating to energy transfer to 2AP following absorption by adenine) greatly increases when the sample is frozen at 77 K. For the other 2AP-dinucleotides, containing DNA bases C, G, T or I, a similar increase in fluorescence intensity is also observed in the region where absorption bands of the DNA bases are present (as shown in Figure 4.11 in Chapter 4). For those in which no excitation peak relating to energy transfer was

identifiable at room temperature, (X = C, G or T) a clearly identifiable peak is present at 77 K (Figure 4.11).

Energy transfer efficiencies, η_{SS}, derived from steady-state measurements at 77 K are reported in Table 5.12. Steady-state efficiences (uncorrected) measured in LiCl solution at room temeprature (given in Table II.2 Appendix II) are very similar to those obtained in aqueous tris buffer at room temperature (Table 5.5), confirming that the presence of LiCl has no significant effect on the energy transfer process. This is consistent with the minimal effect of LiCl on the conformational properties of the dinucleotides that was reported in Chapter 4.

X	η_{SS} /%
	77 K
G	63
T	~100
C	80
A	86
I	54

Table 5.12: Transfer efficiencies calculated from steady-state fluorescence, η_{SS}, for energy transfer from donor DNA bases, X, to acceptor 2AP in 2AP-containing dinucleotides 2AP-X, frozen in aqueous LiCl glass at 77 K.

The results presented in Table 5.12 indicate that, at 77 K, the energy transfer efficiency dramatically increases in all cases. There is a caveat that the uncertainties in the calculated transfer efficiencies at 77 K are greater than for those determined at room temperature because of the greater difficulty in making quantitative fluorescence intensity measurements at 77 K. This was due to the formation of condensation on the outside of the Dewar flask, as well as the formation of ice crystals in the liquid N_2 held within the Dewar flask, which resulted in a decrease in fluorescence intensity observed during measurements, and was attributed to increased light scattering. Nevertheless, the efficiencies presented in Table 5.12 are clearly indicative of a dramatic increase in the energy transfer efficiencies at 77 K for all DNA bases. Further discussion will be reserved until time-resolved fluorescence results have been considered in the next section.

5.3.4. Time-resolved Fluorescence at 77 K resulting from 260-nm Excitation

5.3.4.1. Lithium Chloride and 2-Aminopurine

The time-resolved fluorescence resulting from the indirect excitation of 2AP-containing dinucleotides was investigated at 77 K using aqueous LiCl as a solvent and an excitation wavelength of 260 nm. However, under these conditions, some background emission from the LiCl solvent was evident, giving rise to a spurious, minor, lifetime component in the decay of 2AP, as shown in Table 5.13. Also shown in Table 5.13 are the decay parameters of the frozen LiCl solvent.

Sample	τ_i /ns			A_i			$<\tau>$ / ns
	τ_1	τ_2	τ_3	A_1	A_2	A_3	
LiCl	0.14	1.3	6.2	0.26	0.40	0.34	2.68
2AP	-	2.8	10.6	-	0.10	0.90	9.79

Table 5.13: Fluorescence decay parameters for frozen LiCl glass and 2AP frozen in aqueous LiCl glass excited at 260 nm at 77 K. The decay parameters for LiCl and 2AP were determined by individually fitting the decay curves recorded at 400 nm and 380 nm, respectively. Experimental uncertainties (estimated by dividing the standard deviation of values by the corresponding values): $\tau_1 \leq 10\%$, $\tau_2 \leq 8\%$, $\tau_3 \leq 1\%$, , $A_1 \leq 10\%$, $A_2 \leq 5\%$, $A_3 \leq 3\%$.

When excited at 260 nm, the fluorescence decay of aqueous LiCl solution required three components for a satisfactory fit of the data, suggesting the presence of several emitting impurity species. The average lifetime resulting from these components is 2.68 ns, and accounts for the additional component seen in the 2AP decay. (When exciting at 310 nm, at both room temperatures and 77 K, fluorescence emission from LiCl was negligible, as was it for 260-nm excitation at room temperature.)

5.3.4.2. 2AP-containing Dinucleotides

The decay parameters of the 2AP-dinucleotides frozen at 77 K in aqueous LiCl solution, following excitation at 260 nm (indirect excitation), are shown in Table 5.14, together with those recorded for 310 nm excitation (direct excitation). (As with room temperature measurements, the results for 2AP-C are omitted from Table 5.14, due to the aforementioned formation of photohydrated cytidine when 2AP-C is excited at 260 nm.)

X	Excitation pathway	τ_i /ns				A_i				< τ > /ns
		τ_1	τ_2	τ_3	τ_4	A_1	A_2	A_3	A_4	
G	Indirect	-	-	5.1	10.7	-	-	0.09	0.91	10.20
	Direct	-	-	3.1	10.2	-	-	0.11	0.89	9.42
T	Indirect	-	-	4.6	9.9	-	-	0.08	0.92	9.48
	Direct	-	-	3.9	9.8	-	-	0.08	0.92	9.33
A	Indirect	-	-	6.9	11.1	-	-	0.15	0.85	10.47
	Direct	-	-	8.4	12.2	-	-	0.54	0.46	10.15
I	Indirect	-	-	5.8	11.1	-	-	0.12	0.88	10.45
	Direct	-	-	8.5	11.6	-	-	0.45	0.55	10.21

Table 5.14: Fluorescence decay parameters of dinucleotides 2AP-X in aqueous LiCl frozen at 77 K for direct (excitation 310 nm) and indirect excitation (260 nm). The decay parameters shown for indirect excitation of 2AP-dinucleotides are the result of individual fits of the fluorescence decay collected at 360 nm while those shown for direct excitation are repeated from Table 4.16 in Chapter 4 (global fits). Experimental uncertainties (estimated by dividing the standard deviation of values by the corresponding values): $\tau_3 \leq 5\%$, $\tau_4 \leq 1\%$, $A_3 \leq 8\%$, $A_4 \leq 1\%$.

As discussed previously in Chapter 4, when frozen at 77K, the shorter decay components, characteristic of 2AP in the dinucleotides at room temperature, are no longer present due to the removal of base-dynamics that allow 2AP to access states required for very fast fluorescence quenching at room temperature. This elimination of shorter decay components, which is observed for direct excitation of 2AP, was also found to occur for indirect excitation at 260 nm and, as such, only two components were required for an adequate fit of the fluorescence decays at 77K.

It is important to remember that when using an excitation wavelength of 260 nm, fluorescence emission from LiCl solvent is also observed at an intensity significant enough that it must be taken into consideration. An indication of the difference in the fluorescence intensity resulting from the LiCl can be seen in that excitation spectra recorded for aqueous LiCl solution shown in Figure I.6 in Appendix I. The contamination of the fluorescence emission of the dinucleotides at wavelengths of 380 nm and 400 nm was significant and thus only fits of the fluorescence decays recorded at 360 nm are shown in Table 5.14 to minimise this effect. The values of τ_3 following 260 nm excitation do not appear to be short enough to be explained as originating from LiCl alone. It is likely that the value of τ_3 observed is the result of an averaging of the lifetime associated with LiCl solvent and one due to 2AP in the dinucleotide. Thus the measured values of τ_3, for indirect excitation, may be underestimates of the true value.

For 2AP-G and 2AP-T, the decay parameters for indirect excitation are very similar to those for direct excitation, and are dominated by a long-lifetime component of around 10 ns. The conformational states accessed by energy transfer cannot be distinguished from those accessed by direct excitation on the basis of their lifetimes, since, at 77 K, highly stacked states do not display distinct lifetimes.

For 2AP-A and 2AP-I there is a clear distinction between the decay parameters for indirect and direct excitation, in terms of the values of the A factors. In both cases, energy transfer favours the population of the conformational states characterised by the longer lifetime, ~ 11 ns. This is consistent with the observation at room temperature for these dinucleotides that the conformations most susceptible to charge-transfer quenching do not coincide with those for which energy transfer is most favourable. Due to the potential contribution to component τ_3 from background emission from the LiCl solvent at 77 K, no further analysis of the populations excited by energy transfer has been undertaken.

It is clear from the average lifetimes presented in Table 5.14 that fluorescence quantum yield of 2AP in the dinucleotides does not differ significantly between direct and indirect excitation. The energy transfer efficiencies determined from the steady state intensities at 77 K (Table 5.12) are, therefore, valid without further correction and may now be compared with those measured at room temperature (Table 5.10).

X	η_{SS} /%	
	RT	77 K
G	<15	63
T	11	~100
A	27	86
I	11	54

Table 5.15: Comparison of the transfer efficiencies calculated from steady-state fluorescence, η_{SS}, for energy transfer from donor DNA bases, X, to acceptor 2AP in 2AP-containing dinucleotides 2AP-X, in aqueous LiCl solution at 77 K to those determined at room Temperature (RT) in aqueous buffer. Those shown for RT measurements have been corrected for differences in FQY, due to inhomogeneous population of multiple lifetime components of 2AP in DNA via energy transfer and are the values of $\eta_{SS,\,corr,\,multi}$ shown in Table 5.11.

A comparison of the calculated energy transfer efficiencies shown in Table 5.15 shows that upon removal of conformation motions, the efficiency of energy transfer increases dramatically, with energy transfer from T now being the most efficient. At room temperature, following correction for differences in FQY due to inhomogeneous population of multiple lifetime components of 2AP in DNA via energy transfer, the energy

transfer efficiency from A still remains greater than that from the other bases, as shown by Nordlund *et al.*[53], but is only ~50% of that calculated for η(-1) of an A base in 2AP-containing single stranded oligomers (Table 5.1).[53] However, as the bases in the dinucleotides are more conformationally free, being less hindered due to the absence of any other bases, one cannot directly compare these values. Despite this, the trend of the efficiency from A being far greater than that of the other bases is consistent with Nordlund *et al.* At 77 K, the trend of the transfer efficiencies is now T>A>G (with that from I being comparable to the transfer efficiency from G). A possible contributing factor to the increase in energy transfer efficiency at 77 K could be an increase in the excited state lifetime (quantum yield) of the natural nucleosides at low temperature, which would allow energy transfer to compete more effectively with intramolecular non-radiative decay. Quantum yields of the natural nucleosides at 77 K, in ethanol or ethylene glycol-water glasses, have been reported in several studies as summarised by Görner.[78] While there is some variation from study to study, reported values lie in the range 10^{-3} to 10^{-2} and are significantly greater (an order of magnitude or more) than at room temperature. Interestingly, thymidine has been found consistently to have the highest quantum yield, which might account for it showing the highest energy transfer efficiency at 77 K.

The increase in transfer efficiency upon removal of base dynamics, contrasts greatly with the inhibition of charge-transfer quenching under these conditions. It is clear that the interbase interactions involved in the mechanisms of the two processes are affected quite differently by conformational motion. The observation that, at 77 K, the decay component with the longest lifetime is preferentially populated by energy transfer, confirms that this lifetime is characteristic of highly stacked conformations.

5.4. Conclusions

The work presented in this chapter has shown that, although both steady-state fluorescence and time-resolved fluorescence measurements are capable of providing an estimate of the energy transfer efficiencies from DNA bases to 2AP, in 2AP-containing DNA dinucleotides, a combination of these measurements are required to deliver a true measure of the transfer efficiencies and to provide insight into the mechanism of electronic energy transfer in DNA.

Steady-state excitation spectra of the dinucleotides, recorded at room temperature, show a clear region of increased intensity that can be attributed to excitation of 2AP via energy transfer from the nearby DNA base (at ~260 nm). This is

concordant with the identification of such peaks in fluorescence excitation spectra of oligonucleotides where energy transfer is occurring from a DNA to 2AP.[9,53,61] From a quantitative analysis of the steady-state fluorescence emission spectra, together with corresponding absorption spectra of the 2AP-containing dinucleotides, the transfer efficiency from adenine (15%) to 2AP at room temperature was found to be an order of magnitude greater than that from any of the other native DNA bases (≤2%).

By performing time-resolved fluorescence measurements, the fluorescence decay parameters following excitation of 2AP in the dinucleotides at 260 nm, via energy transfer, were compared to those following direct excitation at 310 nm. The clear difference observed in the decay parameters depending on the excitation wavelength could be explained by heterogeneous population of the decay components of 2AP via energy transfer from the DNA base present. This in turn has repercussions for the transfer efficiencies calculated from steady-state fluorescence measurements, as it was found that energy transfer populates highly stacked conformational states in which 2AP is more highly quenched, rather than all states of 2AP homogeneously. It is therefore clear that the energy transfer efficiencies presented by Nordlund *et al.* determined from steady-state measurements greatly underestimate the efficiency of transfer from G, T and C, since these measurements were based on the (reasonable) assumption that the fluorescence quantum yield of 2AP excited by energy transfer was the same as that for direct excitation. This would be the case if energy transfer homogeneously excited all conformational states but the time-resolved fluorescence measurements presented in this thesis have shown this to be an incorrect assumption.

Analysis of the decay parameters, based on the assumption that energy transfer only populates one of the four decay components of 2AP in DNA, provided a revised estimate of the transfer efficiencies and suggested that the efficiency was of comparable magnitude for all of the bases. The decay parameters also allowed a correction to the transfer efficiencies from steady-state measurements to be made, taking into account the difference in quantum yields for direct and indirect excitation. However, there were discrepancies between the efficiency values obtained from the time-resolved and steady-state methods. This suggested that the assumption of population of only one decay component by energy transfer was not valid.

A re-evaluation of the decay components excited by energy transfer, allowing for the involvement of multiple decay components, showed that, although one component is preferentially excited via energy transfer, other (but not necessarily all) components are also populated. The number of components involved in energy transfer differs

depending on the identity of the donor base, ranging from two (for 2AP-G) to four components (for 2AP-A). The transfer efficiencies determined, on this basis, from TRF measurements and the corrected steady-state values were in good agreement, and showed that energy transfer with the highest efficiency, around 25% occurs from A, with efficiencies of around 10% from the other bases. Thus, the conclusion from Nordlund's work that A is the most efficient donor still holds, but the transfer efficiencies estimated by Nordlund *et al.* for the other bases were greatly underestimated.

The removal of base dynamics, and the effect of this on energy transfer efficiencies in 2AP-containing dinucleotides, was revealed using low-temperature measurements. Energy transfer efficiencies determined from steady-state measurements at 77 K showed a remarkable increase for all DNA bases. Time-resolved fluorescence measurements performed at 77 K using an excitation wavelength of 260 nm, showed a similar result to those excited at 310 nm, with the elimination of the shorter decay components (τ_1 and τ_2). The preferential excitation of the longest lifetime component, τ_4, by energy transfer at 77 K, confirms that this lifetime can be attributed to well-stacked conformations. Comparison of the average lifetimes, $<\tau>$, resulting from direct and indirect excitation of 2AP in the dinucleotides indicated that the fluorescence quantum yield does not differ significantly for the two modes of excitation, and thus the transfer efficiencies determined from steady-state fluorescence measurements at 77 K require no further correction. At 77 K, the native DNA base T was found to have the greatest energy transfer efficiency (~100%), then A (~86%), followed by G (63%) and I (54%). The increase in transfer efficiency at 77 K is consistent with the reported increase in the fluorescence quantum yields of the natural nucleosides in frozen glasses at 77 K. However, the large uncertainties in the quantum yield values, and their apparent solvent-dependence, means that it is not possible to determine the relative contributions of increased donor lifetime and rate of energy transfer to the increased transfer efficiency.

Unlike charge transfer, electronic energy transfer between bases in DNA is not inhibited by the removal of base dynamics. The static conformations in the frozen LiCl glass at 77 K are amenable to efficient energy transfer, but are immune to rapid charge-transfer quenching, pointing to a fundamental difference in the mechanistic influence of conformational fluctuations in the two processes.

5.5. References

1 P. Unna, *The histopathology of the diseases of the skin*, General Books LLC, 1894.

2 V. O. Melnikova and H. N. Ananthaswamy, *Mutat. Res. Mol. Mech. Mutagen.*, 2005, **571**, 91–106.

3 R. B. Setlow and J. K. Setlow, *Proc. Natl. Acad. Sci. U. S. A.*, 1962, **48**, 1250–1257.

4 N. N. Shafranovskaya and E. N. Trifonov, *Nature*, 1973, **241**, 58–60.

5 M. Guéron, J. Eisinger and R. G. Shulman, *J. Chem. Phys.*, 1967, **47**, 4077–4091.

6 J. P. Ballini, P. Vigny, G. Thomas and A. Favre, *Photochem. Photobiol.*, 1976, **24**, 321–329.

7 S. Georghiou, S. Zhu, R. Weidner, C. R. Huang and G. Ge, *J. Biomol. Struct. Dyn.*, 1990, **8**, 657–674.

8 M. Guéron, R. G. Shulman and J. Eisinger, *Proc. Natl. Acad. Sci. U. S. A.*, 1966, **56**, 814–818.

9 D. Xu and T. M. Nordlund, *Biophys. J.*, 2000, **78**, 1042–1058.

10 M. A. O'Neill and J. K. Barton, *J. Am. Chem. Soc.*, 2004, **126**, 13234–13235.

11 R. Dahm, *Dev. Biol.*, 2005, **278**, 274–288.

12 O. T. Avery, C. M. MacLeod and M. McCarty, *J. Exp. Med.*, 1944, **79**, 137–158.

13 A. Downes and T. P. Blunt, *Proc. R. Soc. London*, 1877, **26**, 488–500.

14 E. Altenburg, *Am. Nat.*, 1928, **62**, 540–545.

15 M. Ward, *Proc Roy Soc L.*, 1892, **52**, 393–403.

16 F. L. Gates, *J. Gen. Physiol.*, 1930, **14**, 31–42.

17 D. Markovitsi, E. Sage, F. D. Lewis and J. Davies, *Photochem. Photobiol. Sci.*, 2013, **12**, 1256–1258.

18 C. Sagan, *J. Theor. Biol.*, 1973, **39**, 195–200.

19 L. Serrano-Andrés and M. Merchán, *J. Photochem. Photobiol. C Photochem. Rev.*, 2009, **10**, 21–32.

20 M. Barbatti, *Photoinduced Phenomena in Nucleic Acids II*, Springer International Publishing, Cham, 2015, vol. 356.

21 M. Barbatti, *Photoinduced Phenomena in Nucleic Acids I*, Springer International Publishing, Cham, 2015, vol. 355.

22 D. E. Metzler, *Biochemistry, Second Edition: The Chemical Reactions of Living Cells*, Academic Press, 1977.

23 R. P. Sinha and D.-P. Häder, *Photochem. Photobiol. Sci.*, 2002, **1**, 225–236.

24 T. Lindahl, *Nature*, 1993, **362**, 709–715.

25 T. Todo, H. Takemori, H. Ryo, M. Lhara, T. Matsunaga, O. Nikaido, K. Sato and T. Nomura, *Nature*, 1993, **361**, 371–374.

26 A. A. Lamola, *Biochem. Biophys. Res. Commun.*, 1971, **43**, 893–898.

27 T. Douki, *Photochem. Photobiol. Sci.*, 2013, **12**, 1286–1302.

28 S. E. Freeman, R. W. Gange, J. C. Sutherland and B. M. Sutherland, *Photochem. Photobiol.*, 1987, **46**, 207–212.

29 N. Bastien, J.-P. Therrien and R. Drouin, *Photochem. Photobiol. Sci.*, 2013, **12**, 1544–1554.

30 J.-H. Choi, A. Besaratinia, D.-H. Lee, C.-S. Lee and G. P. Pfeifer, *Mutat. Res. Mol. Mech. Mutagen.*, 2006, **599**, 58–65.

31 A. F. El-Yazbi and G. R. Loppnow, *Anal. Chim. Acta*, 2012, **726**, 44–49.

32 R. L. Sinsheimer and R. Hastings, *Sci.* , 1949, **110**, 525–526.

33 A. M. Michelson, *J. Cell. Physiol. Suppl.*, 1951, **38**, 11–19.

34 F. T. Liu and N. C. Yang, *Biochemistry*, 1978, **17**, 4877–4885.

35 N. Miller and P. Cerutti, *Proc. Natl. Acad. Sci. U. S. A.*, 1968, **59**, 34–38.

36 K. L. Wierzchowski and D. Shugar, *Biochim. Biophys. Acta*, 1957, **25**, 355–364.

37 a J. Lomant and J. R. Fresco, *J. Mol. Biol.*, 1972, **66**, 49–64.

38 S. Franzen, B. Skalski, L. Bartolotti and B. Delley, *Phys. Chem. Chem. Phys.*, 2014, **16**, 20164–20174.

39 H. Kang, K. T. Lee, B. Jung, Y. J. Ko and S. K. Kim, *J. Am. Chem. Soc.*, 2002, **124**, 12958–12959.

40 L. Belau, K. R. Wilson, S. R. Leone and M. Ahmed, *J. Phys. Chem. A*, 2007, **111**, 7562–7568.

41 O. Kostko, K. Bravaya, A. Krylov and M. Ahmed, *Phys. Chem. Chem. Phys.*, 2010, **12**, 2860–2872.

42 K. Khistyaev, K. B. Bravaya, E. Kamarchik, O. Kostko, M. Ahmed and A. I. Krylov, *Faraday Discuss.*, 2011, **150**, 313–330.

43 S. De Camillis, J. Miles, G. Alexander, O. Ghafur, I. D. Williams, D. Townsend and J. B. Greenwood, *Phys. Chem. Chem. Phys.*, 2015, **17**, 23643–23650.

44 C. T. Middleton, K. de La Harpe, C. Su, Y. K. Law, C. E. Crespo-Hernández and B. Kohler, *Annu. Rev. Phys. Chem.*, 2009, **60**, 217–239.

45 S. Yamazaki and W. Domcke, *J. Phys. Chem. A*, 2008, **112**, 7090–7097.

46 J. Liang, Q. L. Nguyen and S. Matsika, *Photochem. Photobiol. Sci.*, 2013, **12**, 1387–1400.

47 T. Schultz, *Science*, 2004, **306**, 1765–1768.

48 C. E. Crespo-Hernández, B. Cohen and B. Kohler, *Nature*, 2005, **436**, 1141–1144.

49 T. Takaya, C. Su, K. de La Harpe, C. E. Crespo-Hernández and B. Kohler, *Proc. Natl. Acad. Sci. U. S. A.*, 2008, **105**, 10285–10290.

50 B. Kohler, *J. Phys. Chem. Lett.*, 2010, **1**, 2047–2053.

51 D. Markovitsi, *Photochem. Photobiol.*, 2016, **92**, 45–51.

52 C. Helene, P. Douzou and A. M. Michelson, *Proc. Natl. Acad. Sci. US*, 1966, **55**, 376–381.

53 T. M. Nordlund, *Photochem. Photobiol.*, 2007, **83**, 625–636.

54 J. Eisinger and R. G. Shulman, *J. Mol. Biol.*, 1967, **28**, 445–449.

55 D. Markovitsi, D. Onidas, T. Gustavsson, F. Talbot and E. Lazzarotto, *J. Am. Chem. Soc.*, 2005, **127**, 17130–17131.

56 E. R. Bittner, *J. Chem. Phys.*, 2006, **125**, 1–12.

57 D. Markovitsi, T. Gustavsson and F. Talbot, *Photochem. Photobiol. Sci.*, 2007, **6**, 717–724.

58 A. Trifonov, M. Raytchev, I. Buchvarov, M. Rist, J. Barbaric, H.-A. Wagenknecht and T. Fiebig, *J. Phys. Chem. B*, 2005, **109**, 19490–19495.

59 C. Curutchet and A. A. Voityuk, *Angew. Chem. Int. Ed. Engl.*, 2011, **50**, 1820–1822.

60 C. Curutchet and A. A. Voityuk, *Chem. Phys. Lett.*, 2011, **512**, 118–122.

61 P. Rai, T. D. Cole, E. Thompson, D. P. Millar and S. Linn, *Nucleic Acids Res.*, 2003, **31**, 2323–2332.

62 G. Ge and S. Georghiou, *Photochem. Photobiol.*, 1991, **54**, 477–480.

63 C. E. Crespo-Hernández, B. Cohen, P. M. Hare and B. Kohler, *Chem. Rev.*, 2004, **104**, 1977–2019.

64 B. Bouvier, J. Dognon, R. Lavery, D. Markovitsi, P. Millié, D. Onidas and K. Zakrzewska, *J. Phys. Chem. B*, 2003, **107**, 13512–13522.

65 J. M. Jean and B. P. Krueger, *J. Phys. Chem. B*, 2006, **110**, 2899–2909.

66 C. Su, C. T. Middleton and B. Kohler, *J. Phys. Chem. B*, 2012, **116**, 10266–10274.

67 G. W. Doorley, M. Wojdyla, G. W. Watson, M. Towrie, A. W. Parker, J. M. Kelly and S. J. Quinn, *J. Phys. Chem. Lett.*, 2013, **4**, 2739–2744.

68 M. Towrie, G. W. Doorley, M. W. George, A. W. Parker, S. J. Quinn and J. M. Kelly, *Analyst*, 2009, **134**, 1265–1273.

69 D. B. Bucher, B. M. Pilles, T. Carell and W. Zinth, *Proc. Natl. Acad. Sci.*, 2014, **111**, 4369–4374.

70 Y. Zhang, J. Dood, A. A. Beckstead, X.-B. Li, K. V Nguyen, C. J. Burrows, R. Improta

and B. Kohler, *Proc. Natl. Acad. Sci.*, 2014, **111**, 11612–11617.

71 T. M. Nordlund, D. Xu and K. O. Evans, *Biochemistry*, 1993, **32**, 12090–12095.

72 M. A. O'Neill, H.-C. Becker, C. Wan, J. K. Barton and A. H. Zewail, *Angew. Chemie*, 2003, **115**, 6076–6080.

73 X. Wu, PhD Thesis, University of Edinburgh, 2012.

74 L. Ma, PhD Thesis, University of Edinburgh, 2012.

75 S. P. Davis, M. Matsumura, A. Williams and T. M. Nordlund, *J. Fluoresc.*, 2003, **13**, 249–259.

76 K. O. Evans, PhD Thesis, University of Alabama at Birmingham, 1998.

77 A. Kumar and M. D. Sevilla, *Radiation Induced Molecular Phenomena in Nucleic Acids*, Springer Netherlands, Dordrecht, 2008, vol. 5.

78 H. Görner, *J. Photochem. Photobiol. B.*, 1990, **5**, 359–377.

Chapter 6: 2-Aminopurine as a Probe of DNA-protein Interactions: Mos1 Transposase Strand Transfer Complex

6.1. Introduction

As mentioned previously, the time resolved fluorescence of 2AP becomes multi-exponential when 2AP is incorporated into DNA and is highly sensitive to changes in its local environment. These characteristics of 2AP in DNA make it ideal for probing for DNA-enzyme interactions despite the highly dynamic structure of DNA making the quantitative interpretation of the fluorescence signal of 2AP in DNA somewhat challenging. However, the success of using 2AP as a sensitive probe of DNA-enzyme interactions has previously been widely demonstrated.[1–8]

The work in this chapter presents a study of the Mos1 strand transfer complex (STC) in which replacement of an adenine base by the fluorescent base analogue 2AP at key locations in the DNA sequence has allowed the local DNA structure in these locations to be investigated via fluorescence spectroscopy. Both steady-state and time-resolved fluorescence measurements have been implemented, showing the effect caused by enzyme-binding to the fluorescence signal of 2AP in DNA and providing an insight into the dynamics that could not be shown in crystal structures previously presented.[9–11]

6.1.1. Transposons and Transposase Enzymes

Transposable elements (or transposons) are a type of mobile genetic element able to change their location within the genome, and as such, are often referred to as "jumping genes". It was in the 1940s that Barbara McClintock, while researching inheritance in maize, discovered that some sequences of DNA within the chromosome were able to change their position and could interchange between chromosomes.[12] As the genes under study by McClintock coded for colour, the repositioning of these genes allowed for the expression of genes for other pigments and resulted in colour changes to occur in the

maize. McClintock hypothesised that this mechanism of "jumping genes" was common in all living things and was later confirmed with the identification of transposons in other organisms.[13] McClintock later won a Nobel Prize in 1983 for her work resulting in the discovery of mobile genetic elements.

Transposons are divided into two classes: retrotransposons (class I)[14] and DNA transposons (class II),[15] depending on the mechanism involved in transposition. Class I transposons transpose *via* RNA intermediates while class II transposons transpose directly without the involvement of an RNA intermediate. Class I transposons propagate via a two-step copy-and-paste amplification mechanism, involving transcription from DNA to RNA followed by reverse transcription from RNA to DNA, which is catalysed by a reverse transcriptase (often encoded by the transposon itself). This copied DNA is then inserted at the new position in the genome. This mechanism allows for the accumulation of repeats in DNA and thus forms the bulk of repeats in eukaryotic genomes. As class II transposons do not involve an RNA-intermediate step, transposition occurs via a cut-and-paste mechanism that is catalysed by one or more transposase enzymes, usually transposon-encoded recombinases. The transposase is the enzyme encoded by the transposon and typically binds to the end(s) of the transposon, facilitating the movement of the transposon to another part of the genome. There are many related transposases that share a conserved RNaseH-like catalytic domain containing a catalytic triad of residues consisting of two aspartic acid (D) residues and either a glutamic acid (E) residue or another aspartic acid residue (DD(E/D)).[16,17] Examples of these are numerous and range from DNA transposases such as Mos1, Tn5 and bacteriophage MuA to retroviral integrases, such as HIV-1 and RAG recombinases. These DD(E/D) enzymes perform similar DNA cleavage and integration reactions by using common active site chemistry to cut out DNA transposons and to ligate the excised DNA into the target site at a new location in the genome.

Due to the ability of transposases to excise and relocate DNA, transposases are capable of creating or reversing mutations and of altering the size of a cell's genome. Thus, transposases have found great use as tools in the field of genomic engineering.

6.1.2. *Mariner*/Tc1 Transposons

The *mariner*/Tc1 transposon superfamily is one of the many transposon families that are widespread in animals. Its members are most prevalent in invertebrates compared to other transposon families, both in number of copies and in number of different transposons within the same organism.[18,19] This superfamily of transposons has

been named for its most well studied members, the Tc1 and *mariner* transposable elements, but also includes other elements such as the *pogo* family.[19,20] *Mariner*/Tc1 transposons are described as class II transposons, encoding a single protein (the transposase) that performs the entire transposition reaction *in vitro*. The ends of the transposon are delimited by a pair of repeated sequences of DNA in which one repeat is the inverse of the other, known as inverted repeats (IRs). It is these IRs that contain the binding site for the transposase.[19] Common to all *mariner*/Tc1 transposons, the encoded transposase contains three domains. Two of these domains coordinate to form a bipartite DNA-binding domain that recognises the target binding site of the IRs *via* the N-terminal region,[21] enabling the third domain (the catalytic domain) to be in a position that allows it to cleave the transposon at the junction of each IR with flanking DNA.[18,22] The catalytic domain contains a DD(E/D)-motif that is similarly found in many Mg^{2+}-dependent catalytic enzymes. Another feature common to DD(E/D) recombinases is the formation of an extreme bend (~140°) in the target DNA during the transposition mechanism. It has been proposed that it is this bend that drives the isoenergetic strand transfer reaction in the transposition mechanism forward.[23] The *mariner*/Tc1 family of transposases stand apart from other transposase families in that they integrate their transposons strictly at a TA target sequence and with a 2 base-pair stagger.[24,25] Transposases such as these are commonly found in nature and are widely used as genetic tools and for therapeutic applications.

6.1.2.1. Mariner/Tc1 Transposases as Tools for Genomic Engineering

The cut-and-paste mechanism of the *mariner*/Tc1 transposase has been vital for their use as genetic tools in the analysis of gene and protein function. The ability to harness transposases as carriers of genetic material to and from genomes and to introduce gain-of-function mutations (which use transgenesis to introduce new phenotypes into genomes) or loss-of-function mutations (which can use insertional mutagenesis to destroy endogenous genes), allows for the functional importance of genes to be determined.[19] However, the lack of transposon technology within most animal species of medical or agricultural importance (e.g. fish, cattle, mosquitos and parasitic worms) has been a major issue until recently. Evidence suggests that in vertebrates, after successfully colonizing a genome, transposons are inactivated by mutations as all of the transposon copies that have been isolated have been dead remnants of once active transposons.[19,26] Interestingly, following transposition, evidence or a "footprint", signifying that transposition has occurred, is left behind. For

Tc1/*mariner* transposons, this manifests as 2 or 3 base-pair (bp) gaps in the sequence of the DNA strand.[19,27,28]

Mariner/Tc1 elements possess some potential advantages over other gene-delivery technologies (viral or non-viral). The basis of long-term expression (throughout many generations) is formed from the mediation of stable, single-copy integration of transgenes into chromosomes by transposon vectors. While other gene-delivery methods (such as retroviruses, adenoviruses and adeno-associated viruses) may be limited by maximal-insert sizes, transposition of elements up to 14 kb have been observed.[29] Despite the frequency of transposition decreasing with an increase in insert size, if the frequency of transposition is not an important factor then transposons may hold an advantage over other methods, due to the aforementioned single-copy integration forming the basis of long-term expression.[19]

A major advantage of *mariner*/Tc1 transposons (inherent to class II transposons) is that transposition is mediated only by the transposase protein and thus expression of the transposase can be used to control the site of integration and moment of jumping.[19]

The same issues encountered with retroviral vectors have been seen with transposases. Where human trials are concerned (such as random integration into the chromosome), the Tc1 transposase Sleeping Beauty has shown to be useful in human trials in the treatment of B-cell lymphoma[30] and in pre-clinical studies concerning the reduction of age-related macular degeneration.[31] Interestingly, the Sleeping Beauty transposase no longer exists in nature but has been reconstructed from phylogenetic data, allowing fragments of inactive transposons to be recombined to once again form a functional transposon from which the Sleeping Beauty transposase can be expressed. It is now one of the most efficient transposases currently available.[26]

There is therefore a drive to determine the most efficient transposition system and to do this an understanding of the transposition mechanism employed by *mariner*/Tc1 transposases is required.

6.1.2.2. Mariner/Tc1 Element Mos1

The work presented in the remainder of this chapter focusses on the *mariner*/Tc1 element, Mos1 (first isolated from *Drosophila mauritiana*[32]). The Mos1 transposon consists of a ~1.3 kb transposon that is framed by 28 bp imperfect IRs and encodes a 345 amino acid transposase.[9] The Mos1 transposase contains two domains: an N-terminal DNA-binding domain (residues 1- 112) and a C-terminal catalytic domain (residues 126

– 345) that, *in vitro,* performs a cut-and-paste DNA transposition mechanism that is common to all class II transposases.[16,33]

6.1.2.3. Transposition Mechanism of the Mos1 Transposase

So far there has been a great deal of work performed to understand the mechanism involved in the transposition of the naturally active eukaryotic transposon Mos1. As the Mos1 transposon is a member of the *mariner*/Tc1 superfamily of transposons, the transposition mechanism proceeds via a series of nucleo-protein complexes common to this family. This mechanism involves coordinate pairing and cleavage of the transposon ends followed by integration of the cleaved ends at a new genomic location. The mechanism of transposition is shown in Figure 6.1 and described in more detail below.

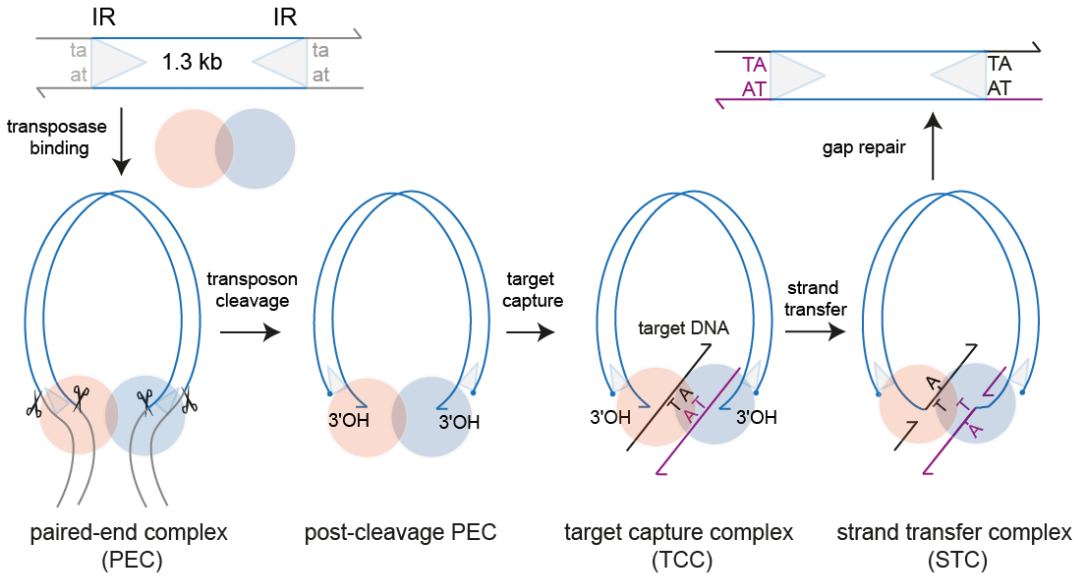

Figure 6.1: Schematic of the Mos1 Transposition pathway and the complexes formed during transposition. The Mos1 transposon (1.3 kb), flanked by TA target site duplications, contains a 28 bp IR sequence (triangle) at either end. The transposase homodimer binds to the transposon IR DNA to form the pair-end complex (PEC), in which cleavage of the first and second strands (scissors) occurs with a three bp stagger and results in a 5' phosphate (filled circle) on the non-transferred strand (NTS) 3 bases into the IR. A 3'OH (arrow) at the end of the transferred strand (TS) is also generated. The target DNA is then captured by the complex and the transposon 3' ends and integrated at a symmetrical TA target sequence, which results in a 5 nt gap. The TA sequence is then duplicated by gap repair. This figure has been reproduced from the publication of Morris *et al.*[9]

Firstly, a transposase homodimer forms and binds to the IR at one end of the transposon.[34] Next, the homodimer captures the IR at the other end of the transposon, resulting in the formation of the pair-end complex (PEC). The PEC has been found to regulate the coordinated excision of the transposon ends and cross-talk between transposase sub-units[35,36] by adopting a *trans* configuration,[22] in which the IR region is recognised by the binding domain of one sub-unit and recognised by the catalytic domain of other sub-unit (and *vice versa*). Cleavage of the Mos1 transposon occurs via two hydrolysis reactions (shown as scissors in Figure 6.1), which result in the cleavage of both DNA strands and excision of the transposon with a 3 nucleotide (nt) stagger, generating a 5' phosphate group on the non-transferred strand (NTS) and a 3'-OH group on the transferred strand (TS). This then forms the post-cleavage PEC (Figure 6.1). After this step, the Mos1 enzyme-DNA complex locates a target integration site (with sequence TA) and binds there to form the target capture complex as shown in Figure 6.1.[24] The previously excised transposon is then joined via a DNA strand transfer reaction in which the 3'-OH at each end of the transposon attacks the phosphodiester 5' at the TA dinucleotide target site forming the strand transfer complex (STC) (Figure 6.1). The product of the strand transfer contains gaps at each end of the newly inserted transposon, which are then later repaired by cellular machinery.[16]

To date, there has be a wealth of research involving the isolation and study of each of the complexes formed during the Mos1 transposition mechanism.[9,11,24,37] Structural analysis via x-ray diffraction techniques accompanied with biological assays and fluorescence spectroscopy have revealed a great amount of detail of the specifics of the mechanisms and the complexes formed at each step, as will be summarised below.

Mos1 Transposon Excision and Formation of the Mos1 Pair-End Complex

In 2006, Richardson *et al.*[37] presented a crystal structure of the catalytic domain of the Mos1 transposase and combined it with a model for the bipartite DNA-binding domain that was derived from the similar Tc3 transposase (another member of the *mariner*/Tc1 superfamily). From this, they were able to put forward one of the first crystal structures of the Mos1 PEC, enabling for a better understanding of the DNA-enzyme interactions and configurations involved in the mechanism of transposition of the Mos1 transposon.

Excision of the transposon occurs via a pair of staggered double-strand breaks at the end of the IRs in the Mos1 PEC. Proceeding via two hydrolysis reactions, the staggered cut results in a three base-pair 3'-hydroxyl overhang at the 3' termini, since

the 5' end is cleaved three bases inside the transposon, while 3' excision occurs at the end of the transposon.[38] The two cleavage events of the TS strand and the NTS strand are known to be sequential.[37] 5' cleavage of the NTS strand is known to occur primarily and does not require pairing of the ends.[22] Formation of the PEC is required before cleavage of the TS strand can occur to release the 3' ends of the transposon.[22]

Target Capture and the Mos1 Target Capture Complex

Target capture is a key step in the transposition mechanism that is important for the selection of new sites for the insertion of the excised transposon DNA. Pfliegler *et al.* showed that only the target capture complex (TCC) (the complex present after cleavage and before integration of the transposon) is capable of target capture.[24] The TA dinucleotide target sequence has been shown to be a key component for both target recognition and for the chemistry of the strand transfer reaction.[25] It was also found that the nicks in the DNA strands that are two nt apart from the TA target sequence were preferential for capture of the bent target DNA molecules.[24]

Strand Transfer and the Mos1 Strand Transfer Complex

After capture of the target DNA and formation of the Mos1 TCC has occurred, the 5' phosphodiester of the TA dinucleotide is attacked by the 3'-OH groups at each end of the transposon, joining the excised transposon to the TA target site. Figure 6.2 shows the DNA strand transfer reaction.

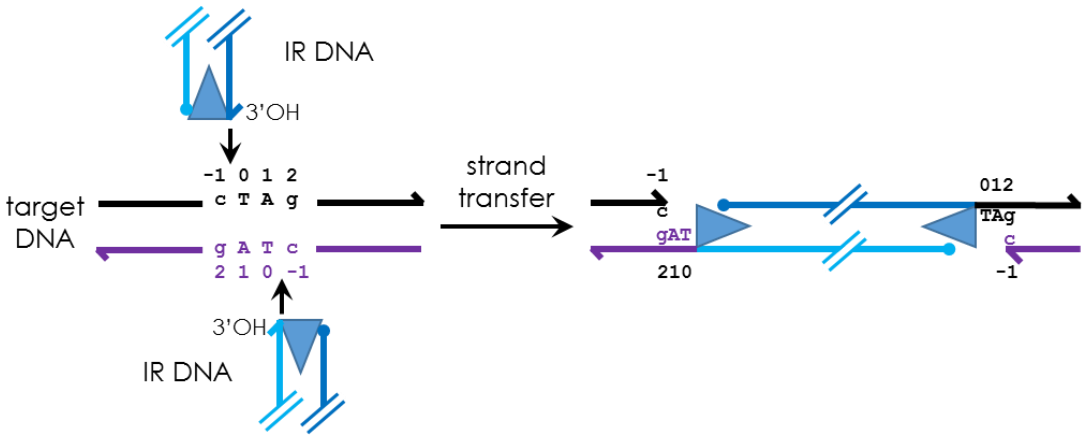

Figure 6.2: Strand transfer reaction for the insertion of the excised Mos1 transposon at the TA target site. 3'OH ends of the transposon attack the phosphodiester bonds between T_0 and C_{-1} on both strands of the target DNA, joining the target strand to the target DNA while separating the TA base-pairs and leaving a 3'OH at C_{-1}.

Crystal Structure of the Mos1 STC

After the strand transfer reaction has occurred, the DNA transposition product (containing gaps in the DNA strands at each end of the transposon) is bound to the transposase in a strand transfer complex (STC), as seen in Figure 6.1.

Using a mixture of the Mos1 transposase with DNA representing the transposon integration product, Richardson *et al.* were able to construct a DNA-enzyme complex that mimics the Mos1 STC. From this, they were able to crystallise the DNA-enzyme complex and use X-ray diffraction techniques to determine the crystal structure of the Mos1 STC.[9,10] The DNA mimicking the transposon integration product (the TS) consisted of three parts: the transposon IR, an unpaired TA dinucleotide and the target DNA. These three parts were joined together, from 5' to 3', to form one DNA strand (similar to those shown in Figure 6.5). Complementary DNA strands were composed of two parts: NTS DNA and target DNA. Annealing of DNA, to form duplexes that each mimicked one end of the transposon, resulted in a 5 nt gap left between the two components of the complementary strand. A cohesive 4 nt overhang at the 5' end of the complementary target DNA oligonucleotide was used to promote interactions between adjacent complexes in the crystal lattice (as shown in Figure 6.3(c)). The method used by Morris *et al*. to assemble the STC bypassed the need for catalysis of integration. This method had previously been shown to be successful in the preparation of *bona fide* PFV STCs.[39] The DNA-enzyme complex used to mimic the STC during transposition relates to that shown in Figure 6.1, mimicking the result of post-strand transfer but before repair of the gaps in the DNA strands, which are a result of transposon insertion, has occurred. The crystal structure determined by Morris *et al.*, via X-ray diffraction (Figure 6.3) showed the crystallographic asymmetrical unit to contain one Mos1 STC. Each Mos1 STC was composed of the transposase homodimer bound to two DNA duplexes (similar to binding two ends of the transposon) while the overhanging 5' ends of the target DNA second strands were involved in base-pairing interactions with neighbouring complexes and facilitated crystal packing. The target DNA was found to bind in a channel between the two catalytic domains while the strand transfer products are contained within the active sites of the Mos1 transposase. Due to similarities in the crystal structure of the Mos1 TCC[24] and the crystal structure determined for the Mos1 STC,[9] both of which contain a transposase dimer, it has been strongly suggested that Mos1 strand transfer is also catalysed by a transposase dimer.[9]

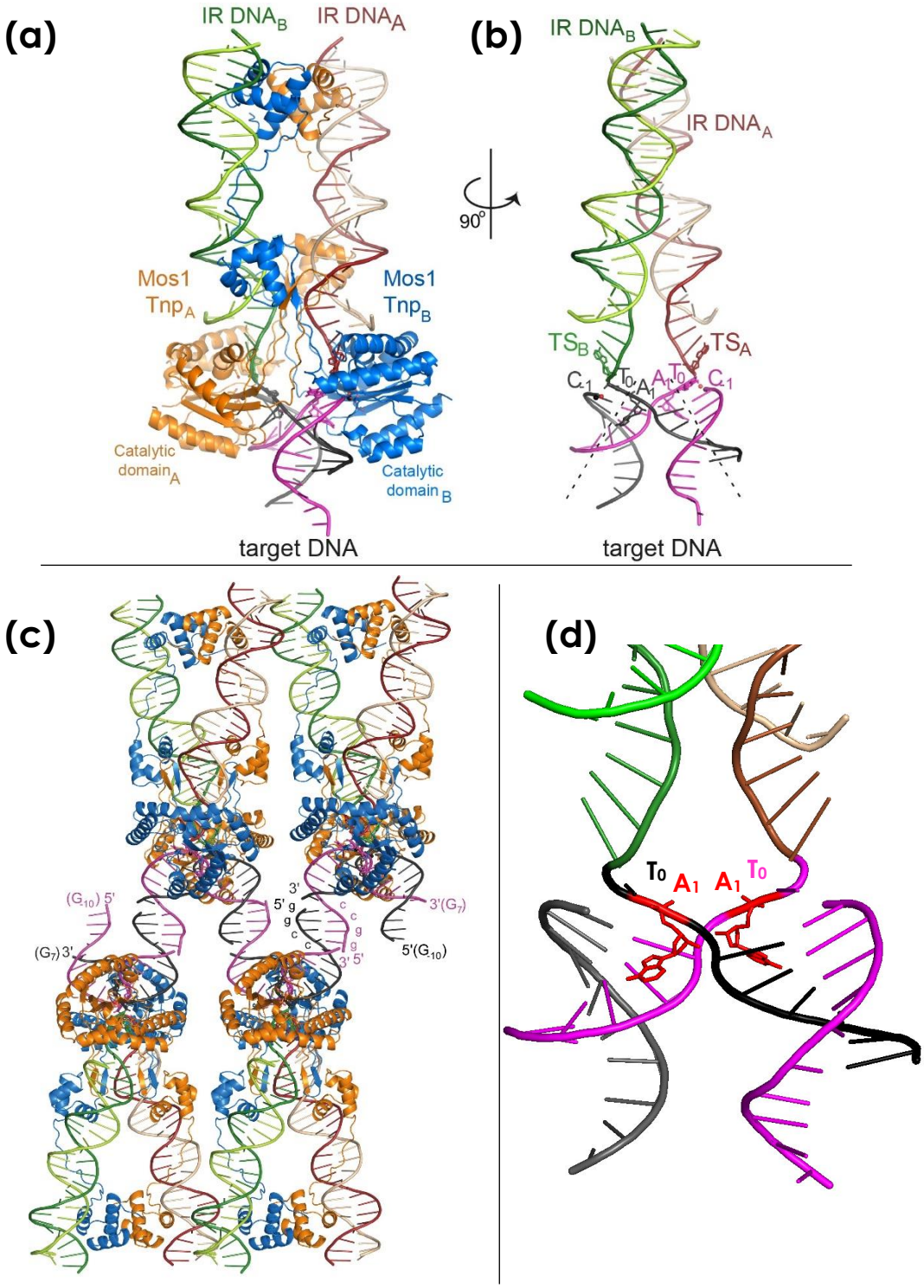

Figure 6.3: Architecture of the Mos1 STC. (a) Crystal structure of the STC showing the transposase subunits (orange and blue), IR DNA (red and green) and target DNA (magenta and black). (b) Crystal structure rotated by 90° showing only the DNA components. The ~140° bend in the target DNA is shown as dashed lines. (c) Packing arrangement and DNA interactions in the Mos1 STC crystal lattice. (d) Active site of the catalytic domain showing the flipped base at position A_1 (red). Figures (a),(b) and (c) have been reproduced from Morris *et al.*,[9] while (d) has been generated from data generously supplied by E. Morris.

The Mos1 STC has also been shown to be similar to previously determined *pre*- and *post*-TS cleavage Mos1 PECs in that the transposase subunits are arranged in a *trans*-configuration with the IR DNA within the complex (as shown by Morris *et al. via* a direct overlay of the STC crystal structure with that of the pre-TS cleavage PEC).[9] In this arrangement, the IR DNA of one strand is recognised by the DNA-binding domain of one subunit, while the other subunit recognises the catalytic domain and *vice versa* (illustrated in the crystal structure shown in Figure 6.3). This arrangement would allow the cleaved transposon ends to be brought together and facilitates the integration of the TS into the target site (TA) of the target DNA.

One of the main features identified in the Mos1 STC crystal structure was the presence of a 147° bend in the backbone of the target DNA (as shown by the dotted lines in Figure 6.3(b)) which results in a distortion to the target DNA away from the typical B-form DNA conformation. At the apex of this bend is the TA target sequence. These TA sequences are known to be relative "weak spots" for the unwinding of DNA, compared to GC sequences, due to the lower stability of base-pairing, the minimal base-to-base overlap and low twist angles inherent to pyrimidine-purine steps. The strand transfer results in nicks in both target DNA strands at the 5'-side of the thymine base at sequence position 0 (i.e. T_0) in the target sequence (as sequence positions of the bases are labelled in Figure 6.2). Interactions of the Mos1 transposase with phosphate groups of nucleotides surrounding the target sequence act to support this conformation. The nicks in the DNA strands allow for such an extreme bend in the target DNA across the target sequence by relieving steric constraints in this region.[9]

As a result of the extreme distortion to the target DNA backbone in the crystal structure of the Mos1 STC, it was found that the adenine of the TA target site (A_1) was flipped out into extra-helical positions (as shown in Figure 6.2). Base-pairing of A_1 with the complementary T_0 base is then inhibited due to a 180° rotation of the phosphate backbone atoms of G_2 and A_1, with respect to adjacent nucleotides. Compared to unbound DNA, the conformation of A_1 is now extra-helical and in a different environment. As such, the crystal structure determined by Morris *et al*. showed the presence of interactions of A_1 with key residues of the Mos1 transposase that are in close enough proximity to interact with the bound DNA, acting to stabilise the distorted conformations of DNA.

Transposase Residues Stabilise the Target DNA Distortions

Morris *et al.* determined that some key residues, that stabilise the DNA backbone distortion in the strand transfer product, are also vital for transposon integration *in vitro*.

Conservation of these key residues between members of the *mariner*/Tc1 family of transposons implies that this mechanism of strand transfer is common to all members. The key amino acid residues of the Mos1 transposase identified by Morris *et al*. were F187, W159, R186, and K190. These residues were identified by their close proximity to the strand transfer integration site (the TA target site), suggesting that interactions between these residues and the bound-DNA play an important role in the stabilisation of the Mos1 STC.

Mos1 is known to bend sharply the strand of the bound-DNA, flipping the target adenine base (A_1) into an extrahelical position via rotation of the phosphate backbone, allowing the aromatic ring of the F187 residue to occupy the space that has been vacated by the flipped A_1 base (as shown in Figure 6.4). In doing so, F187 forms a π-π stack with

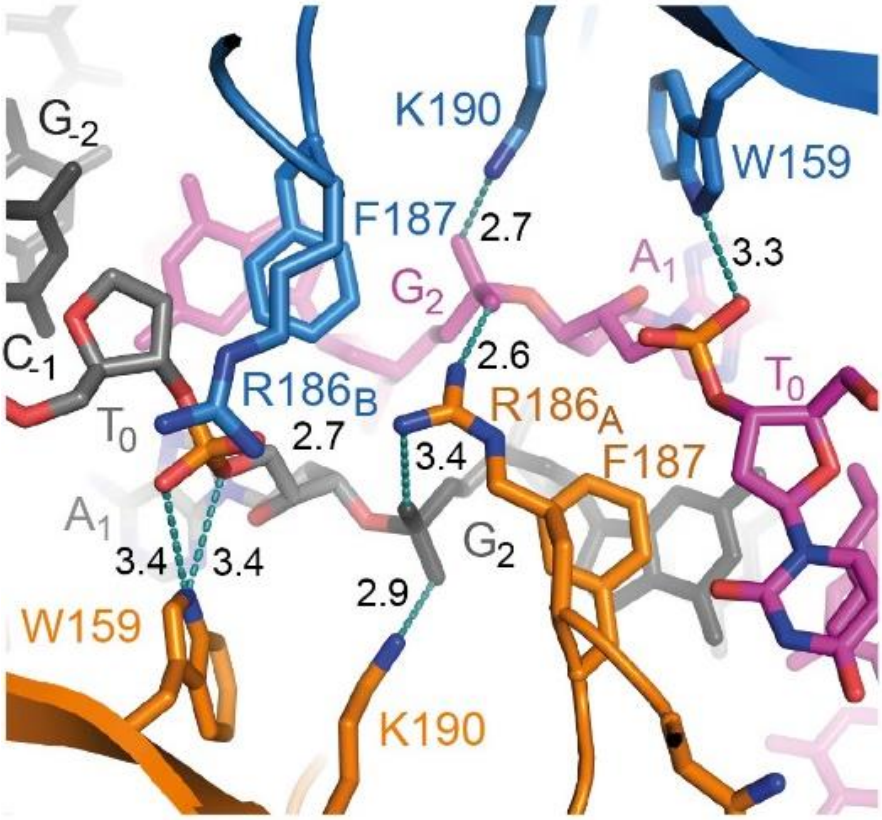

Figure 6.4: Interactions of the key residues of the Mos1 transposase with rotated backbone phosphates stabilise the target DNA. Phosphates of target DNA interact with residues of the Mos1 transposase catalytic domain. Side chains of residues R186, W159 and K190 can form H bonds (dotted lines) with phosphate oxygens in the DNA backbone associated with A_1 and G_2 (with distances shown in Å). Figure reproduced from the publication of Morris *et al.*[9]

the adjacent G_2 base and results in stabilisation of the base-flipped conformation shown in Figure 6.3.[9]

Side-chain atoms of the other key residues (W159, R186 and K190) stabilise the distortion to the DNA structure surrounding the target site by interacting with the DNA backbone, forming salt bridges with the phosphate atoms of A_1 and G_2, as shown in Figure 6.4.

The crystal structure of the Mos1 STC shows that rotation of the DNA backbone has enabled the G_2 phosphates of both target DNA strands to come into close proximity of each other and close to the guanidinium group of R186. This allows H-bonds to form with the oxygen of the G_2 phosphates on one strand while a side-chain of K190 forms a salt-bridge with the other. The W159 indole N_1H is found to interact with an A_1 phosphate oxygen and stability is further enhanced by proximity of W159 indole ring with a side chain of K190, forming a cation-π stack.

6.1.3. 2-Aminopurine as a Probe of DNA-Enzyme Interactions

As mentioned previously, to date, the fluorescent analogue of adenine, 2AP, has been effectively used as a sensitive tool to study the interactions between many DNA-enzyme systems.[1–8]

The work presented in the remainder of this chapter uses fluorescence spectroscopy to explore enzyme-DNA interactions between the Mos1 transposase and the bound DNA in the Mos1 STC complex in solution phase. Replacement of an adenine base by its fluorescent analogue, 2AP, at key locations in the DNA sequence enabled information about the DNA structure, both for the DNA alone and in the presence of the enzyme, to be determined. Steady-state fluorescence spectroscopy was initially used to investigate the response of 2AP fluorescence caused by binding of the transposase enzyme to the DNA (to form the Mos1 STC). Time-resolved fluorescence spectroscopy was then employed to understand better the dynamics of the system that the crystallographic snapshot was unable to show. By using time-resolved fluorescence spectroscopy of mutant Mos1 enzymes (where key amino acid residues of the Mos1 transposase crucial for transposon integration had been mutated to be replaced with alanine residues), the local interactions of nearby transposase residues with the flipped base (resulting from the DNA backbone distortion) in the Mos1 STC were also investigated.

6.2. Materials and Methods

6.2.1. DNA Oligonucleotides

HPLC purified oligonucleotides were purchased from ATDBio (Southampton, UK) and were diluted for use in fluorescence experiments to approximately 10 μM in calcium buffer (containing 25 mM PIPES-NaOH pH 7.5, 250 mM NaCl, 20 mM $CaCl_2$ and 1 mM DTT).

Oligonucleotide sequences were designed to resemble the IR and target DNA of one end of the transposon found in the Mos1 STC after strand transfer has occurred. Five 2AP-labelled, 3'-extended TS sequences (in relation to the oligonucleotides used for crystallisation experiments by Richardson and co-workers[9,22]) were synthesised: two were extended to a length of 42 nt (s) and three extended to a length of 46 nt (l). The shorter oligonucleotides (those with a suffix "s") were initially synthesised to mimic the Mos1 strand transfer product studied in crystallisation experiments while oligonucleotides with a 3'-extended nt sequence were later synthesised in order to include 2AP in the sequence at a position outside the enzyme-binding region but not at the end of the sequence, while also mimicking the product of Mos1 strand transfer. Each oligonucleotide contained the 28 nt IR and either 18 nt (l) or 14 nt (s) target DNA sequence, depending on the length of the oligonucleotide. For fluorescence experiments, an adenine base was replaced with 2AP (a fluorescent analogue of adenine) in each oligonucleotide (except in the case of TS_A_1) in order to probe for changes in the DNA structure in that region, as shown in Table 6.1.

Name	Sequence	Length (nt)
TS_A_1l	5' AAA CGA CAT TTC ATA CTT GTA CAC CTG ATA GCA GTG GAC GTA GGC C	46
TS_P_1l	5' AAA CGA CAT TTC ATA CTT GTA CAC CTG AT**P** GCA GTG GAC GTA GGC C	46
TS_P_{13}l	5' AAA CGA CAT TTC ATA CTT GTA CAC CTG ATA GCA GTG GAC GT**P** GGC C	46
TS_P_{-23}s	5' AAA CG**P** CAT TTC ATA CTT GTA CAC CTG ATA GCA GTG GAG CCG	42
TS_P_1s	5' AAA CGA CAT TTC ATA CTT GTA CAC CTG AT**P** GCA GTG GAG CCG	42
NTS	5' GGT GTA CAA GTA TGA AAT GTC GTT T	25
target-l	5' GGC CTA CGT CCA CTG C	16
target-s	5' GGC CTA CGT CCA	12

Table 6.1: Sequences of the 2AP-containing DNA oligonucleotides used in fluorescence experiments where "P" represents the position where 2AP has replaced an adenine base sequence. The sequences for the complementary strands (NTS and target-l or target-s) are also shown.

Four 2AP-labelled ss-oligonucleotides (TS_P_1l, TS_P_{13}l, TS_P_{-23}s and TS_P_1s) (sequences shown in Table 6.1) and four corresponding 2AP-labelled duplexes (GP_{-23}s, TP_1s, TP_1l, and TP_{13}l) (sequences shown in Figure 6.5) were studied via steady-state and time-resolved fluorescence experiments while TS_A_1l and the associated duplex (TA_1l) were used as a non-fluorescent control oligonucleotides. Duplexes were annealed by mixing TS oligonucleotides with NTS and either target-s or target-l (depending on the length of the TS oligonucleotide) with a small excess of the non-2AP containing strands to ensure that all labelled strands were annealed. Figure 6.5 shows a comparison of the structure and sequences of the unlabelled duplex with the 2AP-labelled duplexes used which were synthesised to mimic the DNA in the Mos1 STC.

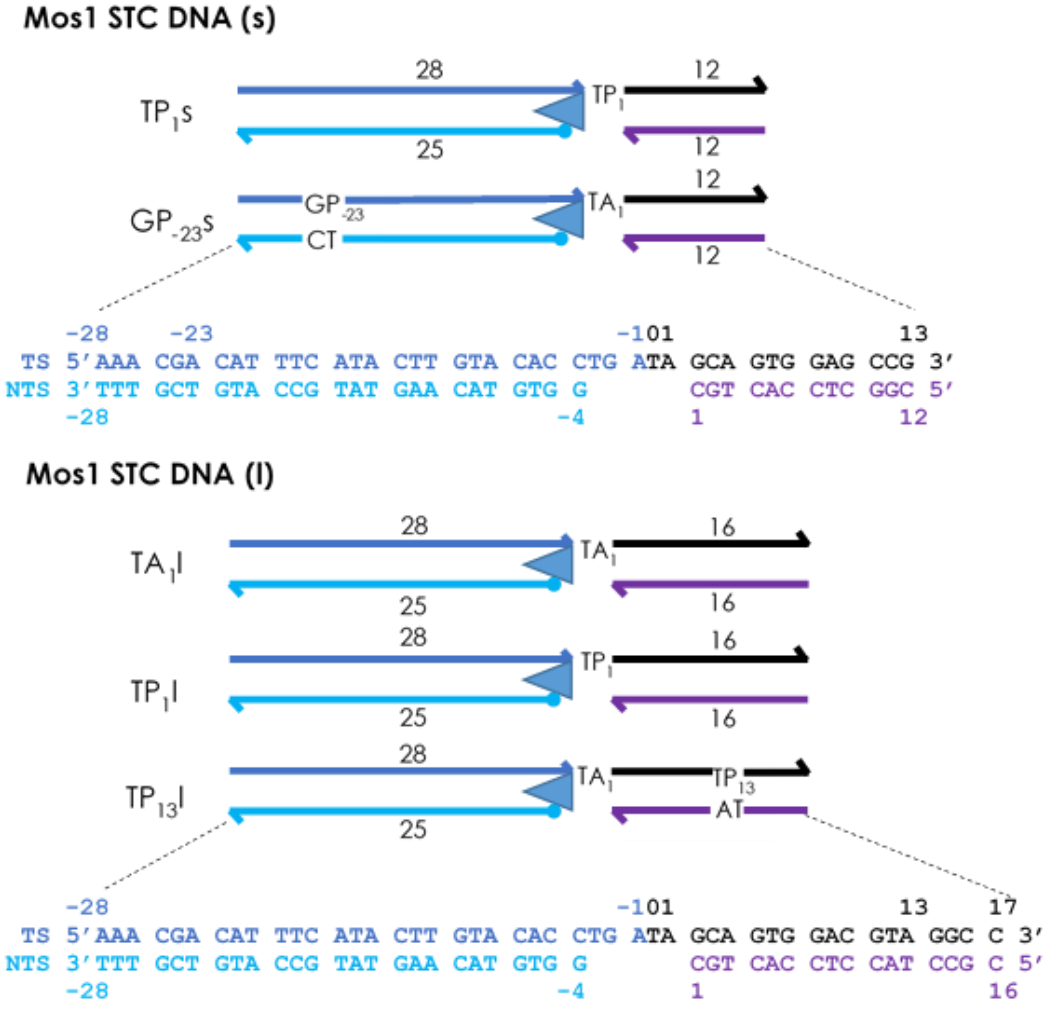

Figure 6.5: Sequence and numbering of the DNA duplexes used in the fluorescence spectroscopy experiments composed of regions of IR DNA (blue), single-stranded TA dinucleotide target sequence, and target DNA (black/purple) . Key nt positions (A_{-23}, A_1 and A_{13}) are labelled above the relative positions in the sequences to show where adenine has been substituted for 2AP (P) in samples GP_{-23}s, TP_1(s/l) and TP_{13}l respectively.

The oligomers used in this study were designed such that the duplexes formed contained 2AP in one of three different environments. Duplex TP_{13}l contains 2AP in a double-stranded DNA region that does not interact with the Mos1 transposase, and is therefore used as a control. On the other hand, the location of 2AP in the TP_1(s/l) duplexes is at the TA target site, which is a single-stranded DNA region flanked by double-stranded DNA regions. The GP_{-23}s duplex contains 2AP in a double-stranded region that is within the transposon IR, which is the region in which the Mos1 transposase binds to the transposon. The three positions that have been labelled with 2AP are illustrated in Figure 6.6.

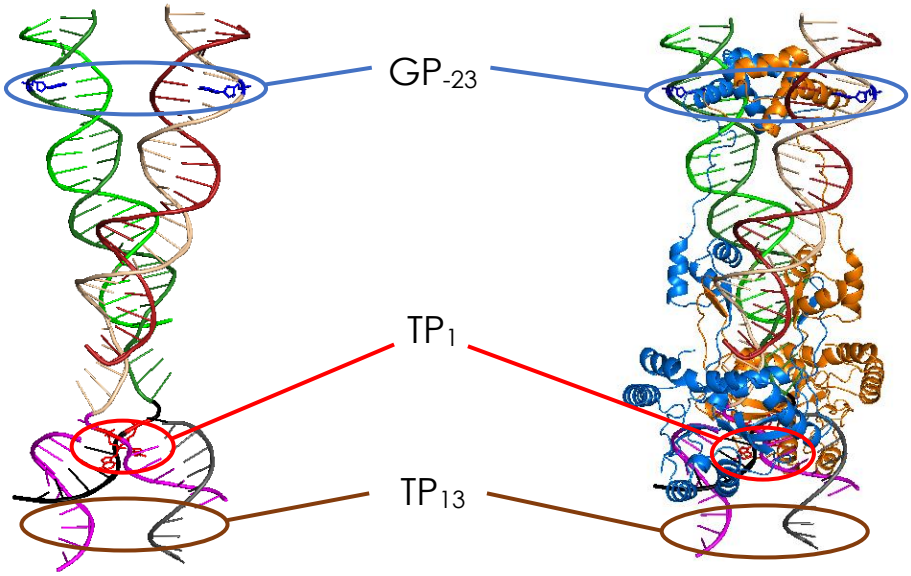

Figure 6.6: Illustration of the regions of the labelled positions GP_{-23} (blue), TP_1 (red) and TP_{13} (brown) in the DNA structure showing the DNA alone (left) and DNA with the enzyme present (right). The crystal structure shown (relating to the shorter length DNA used to crystallise the complex) (from data provided by E. Morris, University of Edinburgh) is used for illustrative purposes only and does not represent the structures of all oligonucleotides used in this work. For this reason, only the region of the TP_{13} label is shown and not the actual base.

6.2.2. Transposase Mutation, Expression and Purification

Transposase mutation, expression and purification were performed by E. Morris (University of Edinburgh) as follows.[9] Mos1 transposase mutants W159A, R186A, F187A, and K190A (discussed previously in Section 6.1.2.3) were generated from expression constructs encoding these mutations by site-directed mutagenesis (Quikchange, Stratagene) of the codon-optimised Mos1 gene,[40] according to the manufacturer's

protocol. Soluble expression of Mos1 transposase in *E. coli* was achieved by incorporating the T216A mutation into each plasmid, as described by Richardson *et al.*[10] Expression and purification of each mutant transposase was performed as described by Richardson *et al.*[10] Following this, mutant transposases were then each exchanged into buffer (containing 25 mM PIPES pH 7.5, 250 mM NaCl, 0.5 mM DTT and 50% (v/v) glycerol) and were concentrated to between 10-20 mg/mL for use in experiments.

6.2.3. Fluorescence Spectroscopy

6.2.3.1. Steady-state Fluorescence Spectroscopy

Fluorescence emission spectra were collected over a range of 340-420 nm for the shorter 2AP-labelled duplexes while a range of 325-550 nm was used for solutions of longer 2AP-containing duplexes (10 μM) in Ca buffer. Fluorescence emission spectra of the Mos1 transposase and of the duplexes bound to the Mos1 transposase were also recorded. The latter were prepared by adding Mos1 transposase (11 μM) in buffer (25 mM PIPES-NaOH pH 7.5, 250 mM NaCl, 20 mM $CaCl_2$, 1 mM DTT) to solutions of the duplexes to give a final DNA to enzyme molar ratio of 1:1.1. A circulating water bath was used to maintain a constant sample temperature of 25°C during measurements.

6.2.3.2. Time-resolved Fluorescence Spectroscopy

Time-resolved fluorescence decays were collected for samples of 2AP-containing ss-oligomers and duplexes by way of TCSPC, as described in Chapter 3 and the resulting fluorescence decay data were fit using the data fitting procedure described in Chapter 3. Decays were collected at two emission wavelengths (375 nm and 390 nm) and were analysed both individually and globally. Samples were prepared in the same way as described for steady-state fluorescence measurements. No temperature control was utilised during these measurements.

6.3. Results and Discussion

6.3.1. Steady-state Fluorescence

The steady-state fluorescence emission spectrum of the Mos1 transposase is shown in Figure 6.7, alongside that of the solvent (H_2O) and buffer, and the steady-state fluorescence emission spectra of the 2AP-labelled duplexes alone and in the presence of the Mos1 transposase are shown in Figure 6.8.

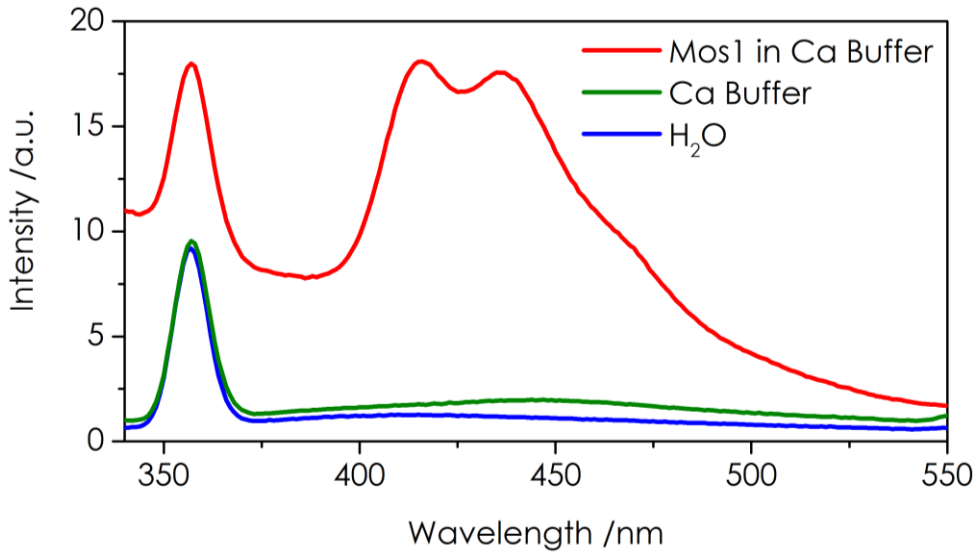

Figure 6.7: Steady-state fluorescence emission spectra of the Mos1 transposase in Ca Buffer (red), and of the solvent: H_2O only (blue) and aqueous Ca buffer (green). An excitation wavelength of 317 nm was used and slit widths were kept constant between all measurements presented in this figure.

There are two features of note seen in the emission spectra of the Mos1 transposase (shown in Figure 6.7). Firstly, the peak at 355-360 nm is identified as a Raman band (due to Raman scattering from the solvent (H_2O)) and can be seen in the recorded emission spectra for H_2O and buffer. There is also some fluorescence emission from the Mos1 transposase, in the region of 400 to 480 nm. However, this emission is weak (comparable in intensity to the Raman band) and is very probably due to an impurity. In the presence of 2AP-containing duplexes, this emission is only evident when the fluorescence emission of 2AP is very weak (as in the case of duplex $TP_{13}l$ in the presence of the Mos1 transposase (Figure 6.8 (c)).

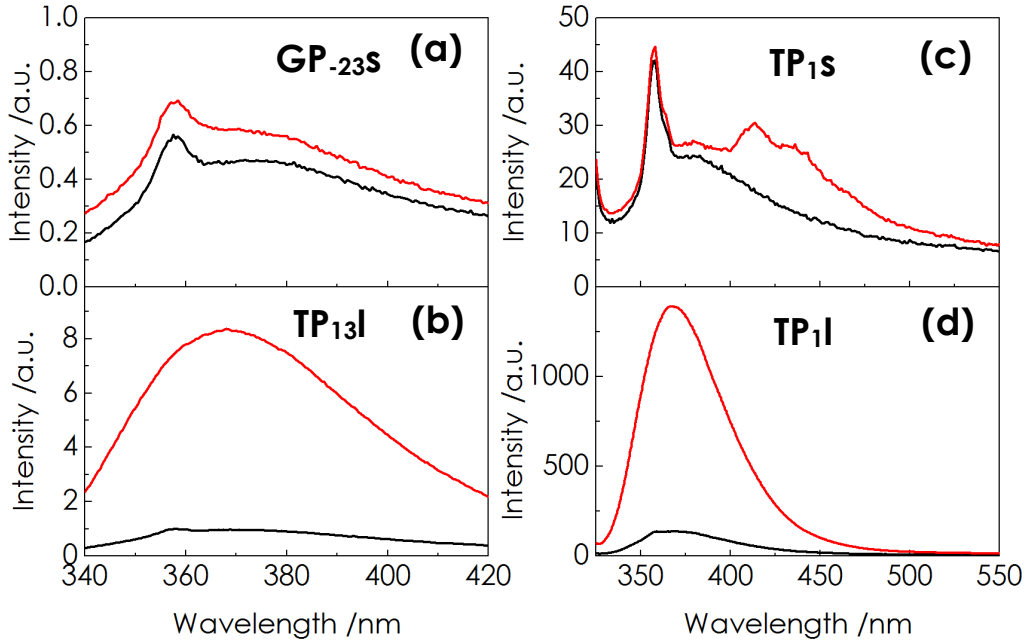

Figure 6.8: Steady-state emission spectra of 10 µM 2AP-duplexes $GP_{-23}s$ (a), TP_1s (b), $TP_{13}l$ (c) and TP_1l (d) (black) and 2AP-duplexes in the presence of the Mos1 transposase (11 µM) (red). Slit widths were kept constant for each set of duplexes with the same length (s or l) but were optimised for each set. An excitation wavelength of 317 nm was used for all measurements presented in this figure. Note the different scales used on the y-axis.

The fluorescence emission intensities of the duplexes alone increases in the order TP_1(s/l)>>GP_{-23}s>TP_{13}l (when corrected for any differences in slit widths). This trend is as is expected since the level of fluorescence quenching for 2AP in the single-stranded region (in TP_1) will be less than that for 2AP in double-stranded sections.[1]

As shown in Figure 6.8, a large increase in the fluorescence emission intensity of 2AP occurs upon binding of the Mos1 transposase when 2AP is located at position A_1, while there is negligible change to the fluorescence emission intensity upon enzyme binding when 2AP is located at position A_{13}. The fluorescence intensity ratios of the bound and free duplex, with 2AP in each position, are shown in Table 6.2.

Sample	2AP Intensity Ratio (DNA-enzyme complex/DNA duplex)
TP_1s	8.6
TP_1l	9.3
$GP_{-23}s$	1.3
$TP_{13}l$	1.1

Table 6.2: Fluorescence intensity ratio of enzyme-bound and unbound states for each of the 2AP labelled duplexes. The fluorescence intensities were measured at 370 nm.

An increase in the fluorescence emission intensity from 2AP is an indication of the formation of a local duplex conformation in which 2AP is less well-stacked, with a consequent reduction in fluorescence quenching interactions with neighbouring bases. When the Mos1 transposase binds to the duplexes where 2AP is located at the TA target site (TP_1(s/l)), there is an almost 10 fold increase in the fluorescence emission intensity, while the duplexes with 2AP outside the target site, $GP_{-23}s$ and $TP_{13}l$, show negligible increases in intensity on enzyme binding. While these observations confirm the existence of a distortion to DNA structure at the TA target site that is suggested by the crystal structure, the nature and extent of the distortion cannot be inferred from steady-state fluorescence measurements alone.

6.3.2. Time-resolved Fluorescence

In order to gain a better insight into the base-dynamics involved in the formation of the Mos1 STC time-resolved fluorescence decay curves were measured. Figure 6.9 shows the fluorescence decay curves recorded for 2AP-labelled DNA duplexes in the absence of and in the presence of the Mos1 transposase.

While the decay curves for TP_1(s/l) and $GP_{-23}s$ (Figure 6.9 (a) to (c)) show a noticeable response upon in the presence of the enzyme, the decay curve for $TP_{13}l$ shows no response (Figure 6.9 (d)). $TP_{13}l$ was used as a fluorescent control, since the position of the 2AP label is outside the region in which the enzyme binds to the duplex (which is within the TS IR DNA region, as shown in Figure 6.6) and binding of the enzyme is not expected to cause any distortion to the DNA structure in this region. However, for the other three duplexes, where the 2AP base is located within the DNA binding region (either at the TA target site (TP_1 (s/l)) or within the TS IR region), there is a distinct change in the 2AP environment on binding of the enzyme.

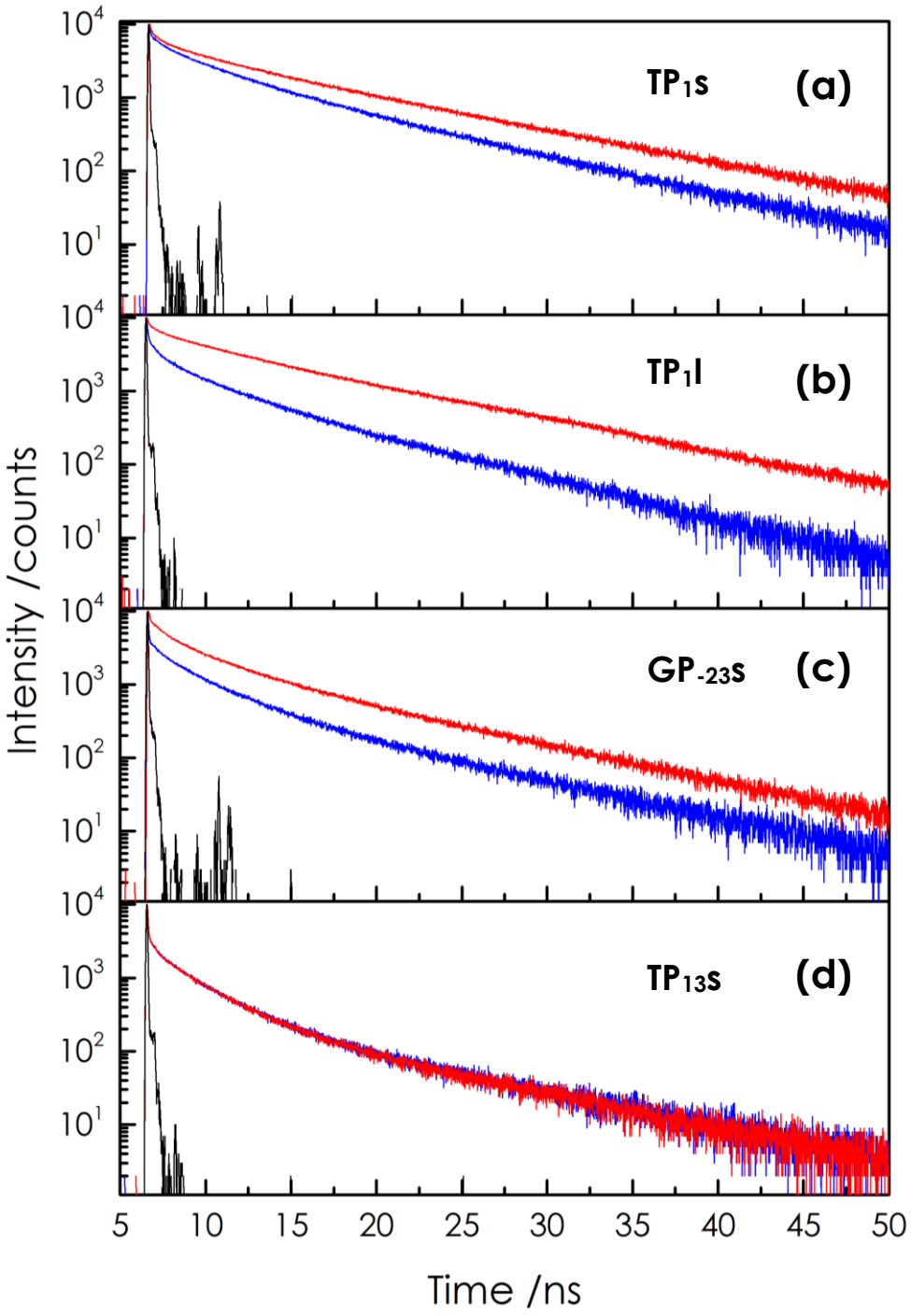

Figure 6.9: Fluorescence decay curves for 2AP labelled duplexes TP_1s (a), TP_1l (b), $GP_{-23}s$ (c) and $TP_{13}l$ (d). The decays for duplexes alone are shown in blue while those in the presence of the Mos1 transposase are shown in red. Also shown is the IRFs (black) for each set of measurements.

Data fitting was performed on the fluorescence decay curves shown in Figure 6.9 and the resulting parameters are presented in Table 6.3.

Sample	Lifetime /ns				Fractional Population				$<\tau>$ /ns
	τ_1	τ_2	τ_3	τ_4	A_1	A_2	A_3	A_4	
TP_1s	0.06	0.51	2.8	7.5	0.71	0.13	0.09	0.07	0.89
+Mos1WT	*0.09*	*0.61*	*3.7*	*9.5*	*0.38*	*0.15*	*0.16*	*0.31*	*3.67*
TP_1l	0.05	0.46	2.7	7.5	0.76	0.10	0.08	0.06	0.76
+Mos1WT	*0.08*	*0.36*	*3.2*	*9.7*	*0.38*	*0.15*	*0.16*	*0.31*	*3.56*
GP_{-23}s	0.02	0.39	2.4	7.8	0.93	0.03	0.03	0.01	0.16
+Mos1WT	*0.04*	*0.45*	*2.7*	*8.0*	*0.78*	*0.10*	*0.08*	*0.04*	*0.59*
TP_{13}l	0.03	0.39	2.5	8.7	0.90	0.04	0.05	0.01	0.25
+Mos1WT	*0.03*	*0.36*	*2.5*	*8.5*	*0.90*	*0.04*	*0.05*	*0.01*	*0.26*

Table 6.3: Fluorescence decay parameters of the 2AP-labelled duplexes alone and in the presence of the Mos1 transposase (shown in italics). Those shown are the parameters obtained from global fits of the emission at 375 nm and 390 nm. The A-factors showed minimal wavelength dependence and only those for 380 nm emission are shown. The fitted χ^2 values were <1.2, indicating a good fit of the data. Experimental uncertainties (estimated by dividing the standard deviation of values by the corresponding values): $\tau_1 \leq 5\%$, $\tau_2 \leq 3\%$, $\tau_3 \leq 1\%$, $\tau_4 \leq 1\%$, $A_1 \leq 3\%$, $A_2 \leq 2\%$, $A_3 \leq 2\%$, $A_4 \leq 1\%$.

In the absence of the Mos1 transposase, it was possible to fit the fluorescence decay of 2AP in GP_{-23}s and TP_{13}l with fluorescence decay parameters typical to 2AP in double-stranded DNA (fitting within the regions presented in Table 2.2 for ds-DNA). These decay parameters indicate a tightly stacked duplex structure where ~70-90% of the emitting 2AP population is due to the highly quenched conformation, with the shortest lifetime, τ_1, while the remainder of the population is spread across the other lifetime components. The decay parameters of the free duplexes, TP_1s and TP_1l, are very similar to each other, but differ significantly from those of GP_{-23}s and TP_{13}l. In TP_1s and TP_1l, 2AP is located in an unpaired environment and the decay parameters are similar to those seen for single-stranded oligomers. As previously mentioned in Chapters 2 and 4, the decay parameters for 2AP in single-stranded oligomers, compared to that in double-stranded oligomers, show ~20-30% lower population of τ_1 and an associated increase that is spread across the populations of the other lifetimes. For comparison, the decay parameters for the corresponding 2AP-containing single-stranded oligomers (TS_P_1s and TS_P_1l) used to anneal the duplexes are presented in Table 6.4.

Sample	Lifetime /ns				Fractional Population				< τ >
	τ_1	τ_2	τ_3	τ_4	A_1	A_2	A_3	A_4	(ns)
TS_P$_1$s	0.04	0.46	2.8	7.4	0.79	0.08	0.07	0.06	0.70
TS_P$_1$l	0.05	0.47	2.4	6.5	0.79	0.11	0.07	0.03	0.47

Table 6.4: Fluorescence decay parameters for 2AP-labelled ss-oligomers containing 2AP at position A_1. The parameters shown are obtained from global fits of the emission at 375 nm and 390 nm. The A-factors demonstrated minimal wavelength dependence and only those for 380 nm emission are shown. The fitted χ^2 values were <1.2 indicating a good fit of the data. Experimental uncertainties (estimated by dividing the standard deviation of values by the corresponding values): $\tau_1 \leq 5\%$, $\tau_2 \leq 3\%$, $\tau_3 \leq 1\%$, $\tau_4 \leq 1\%$, $A_1 \leq 3\%$, $A_2 \leq 2\%$, $A_3 \leq 2\%$, $A_4 \leq 1\%$.

From a comparison of the values of the decay parameters for duplexes TP$_1$(s/l) (in Table 6.3) with the corresponding single-stranded oligomers TS_P$_1$(s/l) (in Table 6.4), it can be seen that, even in the "duplexes", the environment of 2AP at position A_1 is more akin to single-stranded DNA despite the presence of nearby double-stranded regions. The smaller population of τ_1 (and associated increase spread over the other lifetime components) in the decay parameters reveals that, in the single-stranded region at the TA target site of the "duplexes", the bases are not as well stacked compared to the flanking duplex regions. In turn, these areas possess a higher degree of flexibility than the surrounding duplex regions, as shown by the decrease in the population of highly-stacked conformations.

6.3.2.1. Enzyme-binding Causes Distortion to the DNA Backbone at Target Site

Upon addition of the Mos1 transposase, TP$_{13}$l showed essentially no change in the decay parameters and thus it can be established that addition of the enzyme has no effect on the local environment of 2AP, which remains tightly stacked in the duplex. This confirms the validity of TP$_{13}$l as a fluorescent control sample.

On the other hand, duplexes TP$_1$(s/l) show the greatest difference upon addition of the Mos1 transposase to form the Mos1 STC. The most notable difference in the parameters is the transfer of population from the well-stacked conformation, τ_1, to the de-stacked states. The large decrease in the population of the highly stacked conformations, falling to 38%, is accompanied by an increase of ~25% in the population of τ_4, implying that the enzyme is capable of stabilising or inducing the formation of a conformation in which 2AP is extra-helical. This confirms that the base at position A_1

experiences base-flipping out of the helix in the Mos1 STC. The lengthening of the longest lifetime (τ_4) from ~7.5 ns to ~9.5 ns can be explained by the change in the environment experienced by 2AP in the extra-helical conformation. The value of 7.5 ns is comparable to that of 2AP in a solvent somewhat less polar than water (e.g. ethanol)[2] and suggests that the base does not achieve a fully extrahelical state in the absence of the enzyme. In the presence of the Mos1 transposase, the longer lifetime is consistent with flipping of the base out of the duplex into more polar, aqueous environment.

The decay parameters in Table 6.3 show that when 2AP is located at the target site and in the presence of the transposase, 31 % of 2AP is flipped out into an unquenched environment while 38% remains highly quenched. A possible reason for this is that base-flipping of 2AP at this position is a dynamic process, and in turn, samples a number of conformational states including base-flipped and base-stacked environments.

Alternatively, an explanation for 38% remaining in a highly quenched environment is the possibility that the flipped 2AP base interacts with and is stabilised by residues of the transposase. As was discussed previously and demonstrated in the crystal structure presented by Morris *et al.,* side-chain atoms of residues of the transposase stabilise the distortion to the surrounding target DNA during base-flipping of A_1, forming salt bridges or H-bonds with the backbone of A_1 or G_2.[9] It is possible that the proximity of these key residues could provide a mechanism through which 2AP fluorescence is quenched. However, the crystal structure clearly shows these key residues either occupying the gap left by the base during base-flipping (F187) or interacting with the DNA backbone, rather than the flipped-base (W159, K190 and R189). This implies that these key residues are not responsible for the quenching of 2AP fluorescence unless a dynamic system is involved (not shown in the crystal structure).

It is important to remember that the DNA-enzyme complexes used in these studies to mimic the Mos1 STC each contain a transposase homodimer bound to two duplexes of DNA, with each duplex representing one end of the transposon. This results in the presence of two 2AP bases present per complex. The crystal structure presented by Morris *et al*. shows both the target bases, A_1, in each target DNA strand to be flipped at the same time. However, as mentioned previously, the crystal structure only provides a static interpretation of a potentially dynamic system. The signal observed in time-resolved fluorescence measurements results from the excitation of both 2APs present in the complex. Therefore, the decay parameters shown in Table 6.3 reflect the average conformation of the two duplexes within the complex, whether base-flipping occurs sequentially or simultaneously. While the crystal structure suggest that both target

bases will be flipped out simultaneously, one explanation for the almost equivalent populations of 2AP that is highly quenched (well stacked) and minimally quenched (extra-helical) is that only one target base is flipped at any one time. Further investigation is required to determine the dynamics and mechanisms involved but based on the observation of the flipped-conformation in the crystal structure, it is suggested that the base-flipping distortion is the lowest energy state (and thus the most stable).

Interestingly, the response shown by $GP_{-23}s$ to the addition of the enzyme is neither a control (in which no response would be observed) nor a base-flipping response but lies somewhere between the two extremes. The reduction in the population of τ_1 (of ~14%) does not transfer solely to τ_4 and instead is spread out between τ_2, τ_3 and τ_4. This implies that while there is a perturbation to the DNA duplex structure caused by enzyme-binding in this region of the IR DNA, it is not as severe as the base-flipping distortion observed in the other duplexes where 2AP is at position A_1. The resulting fluorescence decay parameters show a close resemblance to the decay parameters for the similar single-stranded DNA oligomers (shown in Table 6.4 for TS_P_1(s/l) and in Table III.1 in Appendix III for $TS\_P_{-23}s$ and $TS\_P_{13}l$). A possible explanation for the observed results is that binding of the enzyme in this region disrupts local base-pairing interactions between the two DNA strands in the IR and results in a 2AP environment that is more single-stranded in nature in the locality of the base at position A_{-23}.

6.3.2.2. Time-resolved Fluorescence of Mutant Mos1 Transposase and the Effect on the Stability of the Distorted DNA

The distortion to the DNA backbone caused by the Mos1 transposase is stabilised by interactions with amino acid residues of the transposase.[9] Key residues W159, K190, F187 and R186 were identified by Morris *et al.* in the crystal structure and are known to be conserved between members of the *mariner*/Tc1 family of transposons.[9] The conservation of key residues involved in stabilisation of distortions to the target DNA imply that this mechanism may also occur with other transposons in the same family. The role of each of these residues has been discussed previously (in Section 6.1) and the effect of mutating these residues has been investigated by fluorescence spectroscopy in order to determine the effect on the stability of the DNA distortion caused by replacing each residue with the non-polar, aliphatic amino acid residue alanine, producing five mutant Mos1 transposases.

The fluorescence decay parameters for 2AP in the DNA-mutant enzyme complexes are shown in Table 6.5 while Figure 6.10 shows a graphical representation of the decay parameters, in which A_i is plotted versus τ_i.

Sample	Lifetime /ns				Fractional Population				< τ >
	τ_1	τ_2	τ_3	τ_4	A_1	A_2	A_3	A_4	/ns
TP_1s	0.06	0.51	2.8	7.5	0.71	0.13	0.09	0.07	0.89
+Mos1WT	0.10	0.61	3.7	9.5	0.38	0.15	0.16	0.31	3.67
+F187A	0.06	0.41	3.9	9.5	0.40	0.09	0.11	0.40	4.30
+W159A	0.08	0.57	3.3	10.0	0.40	0.16	0.16	0.28	3.42
+K190A	0.06	0.35	3.5	9.8	0.45	0.10	0.11	0.34	3.81
+R186A	0.07	0.48	3.3	9.7	0.41	0.12	0.11	0.36	3.92

Table 6.5: Fluorescence decay parameters of TP_1s duplex and complexes of TP_1s with Mos1 transposase and mutants of the Mos1 transposase. Those shown are the parameters obtained from globally fits of the emission at 375 nm and 390 nm. The A-factors showed minimal wavelength dependence and only those for 380 nm emission are shown. Experimental uncertainties (estimated by dividing the standard deviation of values by the corresponding values): $\tau_1 \leq 8\%$, $\tau_2 \leq 4\%$, $\tau_3 \leq 2\%$, $\tau_4 \leq 1\%$, $A_1 \leq 5\%$, $A_2 \leq 3\%$, $A_3 \leq 2\%$, $A_4 \leq 1\%$.

It can be seen that the complexes involving mutants W159A, K190A and R186A show a very similar response to that observed for the addition of wild-type Mos1 transposase. The decay parameters for the mutant complexes, shown in Table 6.5 and illustrated graphically in Figure 6.10, confirms that while these residues may interact with the DNA backbone, they do not majorly interact with the flipped base (A_1) nor are they solely responsible for stabilising the base-flipping that results from the DNA distortion in the target DNA region. However, in the decay parameters for the complex involving mutant F187A, a significant increase in the population of τ_4 is observed that is almost solely transferred from the populations of less well-stacked 2AP (τ_2 and τ_3) rather than from the population that is well-stacked (τ_1). This suggests that residue F187 has a specific effect on the conformational stability of the DNA, but does not act to stabilise the flipped base directly or cause it to flip. The crystal structure indicates that the structural role of residue F187 is to fill the gap left by the flipped the base in position A_1 (potentially stacking with neighbouring DNA bases), confirming the role of F187 in stabilising the base-flipping indirectly. No other significant differences in the decay parameters of the mutant complexes compared to the wild type complex could be made, which possibly results from the presence of complex dynamics in the system resulting from two 2AP bases present.

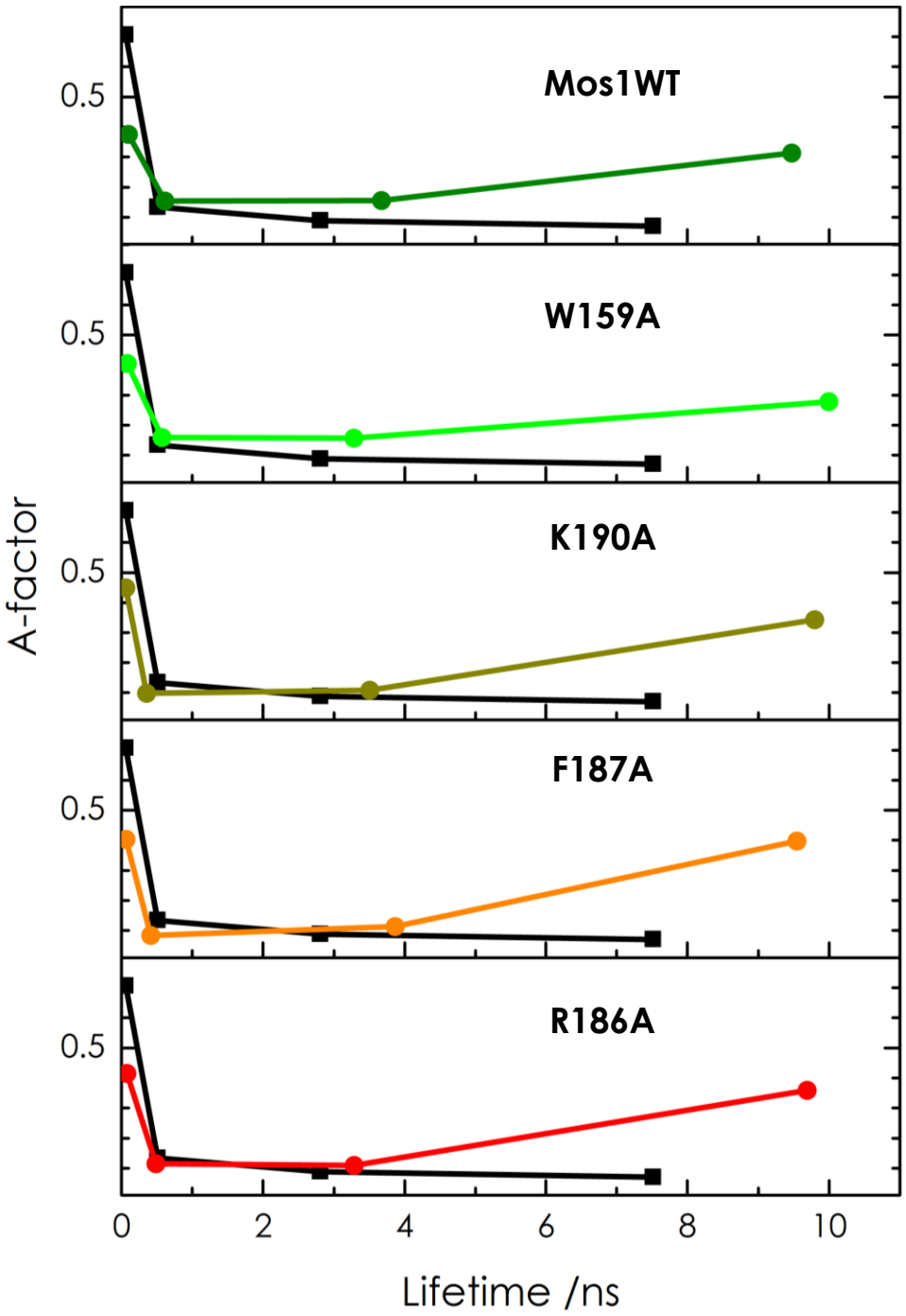

Figure 6.10: Graphical representation of the 2AP-base-flipping effect caused by the formation of the complex of TP_1s with wild-type Mos1 and with mutant Mos1 enzymes. For comparison, the TP_1s duplex (black squares) is shown in each case, while the enzyme-DNA complexes (circles) are as follows: TP_1s+Mos1WT (dark green), TP_1s+W159A (light green), TP_1s+K190A (dark yellow), TP_1s+F187A (orange) and TP_1s+R186A (red). The fitted decay parameters are shown in Table 6.5.

6.4. Conclusions

Using the crystal structure as a starting point, investigations into the dynamics and interactions at key locations within the Mos1 STC have been performed using steady-state and time-resolved fluorescence spectroscopy.

Time-resolved fluorescence studies of 2AP-labelled Mos1 STC have confirmed the presence of a base-flipping distortion at position A_1 in the DNA sequence, when the DNA is bound to the enzyme in the strand transfer complex. The transfer of the population of the lifetimes for 2AP in a highly stacked environment, (τ_1) to those that are in less well-stacked (τ_2 and τ_3) and completely de-stacked (τ_4) environments, resulting from the addition of the Mos1 transposase, is a clear indication of a base-flipping mechanism induced by enzyme binding. No such DNA distortion was detected for the base at position A_{13}. However, the base at position A_{-23} (located within the IR DNA-binding region) was found to experience a perturbation in the DNA duplex structure upon binding of the enzyme. This duplex distortion results in 2AP fluorescence lifetime parameters similar to those found in single-stranded DNA, indicating that binding of the enzyme causes an effect similar to unwinding of the DNA duplex in this region.

The local interactions of the flipped base of the TA target site with nearby key amino acid residues (known to be vital for transposition *in vitro)* were investigated using mutant Mos1 transposases, in which key residues have been replaced with alanine. The fluorescence response resulting from the addition of each mutant enzyme was compared with the fluorescence response obtained using wild-type Mos1 transposase. The resulting fluorescence decay parameters suggested that three of the investigated residues (W159 R186 and K190) do not individually interact with the flipped base to stabilise it in an extra-helical position but that their interactions are only with the nearby DNA backbone, stabilising this flipped-conformation indirectly. On the other hand, the mutation of residue F187 resulted in a transfer of population from 2AP that is stacked imperfectly (τ_2) to extra-helical 2AP (τ_4). As only one residue was mutated to an alanine in each mutant enzyme, there is insufficient evidence based on the fluorescence measurements alone to speculate on whether all of these residues are vital to stabilise the DNA distortion in the strand transfer complex. However, plasmid-based transposon cleavage assays performed by Morris *et al.* that found that residues F187, R186, and K190 are essential for target DNA integration and are not required for earlier cleavage steps, while residue W159 is required for both excision and strand transfer. This

suggests that these residues may also play another role in the mechanism of strand transfer outwith the stabilisation of the flipped target base at position A_1.

The work presented here gives an insight into the dynamics involved in the Mos1 STC and the mechanism of Mos1 transposon integration that could not be determined from the Mos1 STC crystal structures presented by Morris *et al.* As such, the findings presented here aid in providing a framework for designing Tc1/*mariner* transposases with modified target specificities.

6.5. References

1 A. C. Jones and R. K. Neely, *Q. Rev. Biophys.*, 2015, **48**, 244–279.

2 R. K. Neely, PhD Thesis, University of Edinburgh, 2005.

3 X. Wu, PhD Thesis, University of Edinburgh, 2012.

4 L. Ma, PhD Thesis, University of Edinburgh, 2012.

5 T. Lenz, E. Y. M. Bonnist, G. Pljevaljcić, R. K. Neely, D. T. F. Dryden, A. J. Scheidig, A. C. Jones and E. Weinhold, *J. Am. Chem. Soc.*, 2007, **129**, 6240–6248.

6 E. Y. M. Bonnist, K. Liebert, D. T. F. Dryden, A. Jeltsch and A. C. Jones, *Biophys. Chem.*, 2012, **160**, 28–34.

7 R. K. Neely, G. Tamulaitis, K. Chen, M. Kubala, V. Siksnys and A. C. Jones, *Nucleic Acids Res.*, 2009, **37**, 6859–6870.

8 R. K. Neely, *Nucleic Acids Res.*, 2005, **33**, 6953–6960.

9 E. R. Morris, H. Grey, G. McKenzie, A. C. Jones and J. M. Richardson, *Elife*, 2016, **5**, 1–23.

10 J. M. Richardson, L. Zhang, S. Marcos, D. J. Finnegan, M. M. Harding, P. Taylor and M. D. Walkinshaw, *Acta Crystallogr. Sect. D Biol. Crystallogr.*, 2004, **60**, 962–964.

11 J. M. Richardson, D. J. Finnegan and M. D. Walkinshaw, *Acta Crystallogr. Sect. F Struct. Biol. Cryst. Commun.*, 2007, **63**, 434–437.

12 B. McClintock, *Proc. Natl. Acad. Sci.*, 1950, **36**, 344–355.

13 V. Nanjundiah, *Resonance*, 1996, **1**, 56–62.

14 R. A. Elbarbary, B. A. Lucas and L. E. Maquat, *Science*, 2016, **351**, 1–7.

15 L. Pray, *Nat. Educ.*, 2008, **1**, 204.

16 I. V. Nesmelova and P. B. Hackett, *Adv. Drug Deliv. Rev.*, 2010, **62**, 1187–1195.

17 K. A. Majorek, S. Dunin-Horkawicz, K. Steczkiewicz, A. Muszewska, M. Nowotny, K. Ginalski and J. M. Bujnicki, *Nucleic Acids Res.*, 2014, **42**, 4160–4179.

18 S. Watkins, G. van Pouderoyen and T. K. Sixma, *Nucleic Acids Res.*, 2004, **32**, 4306–4312.

19 R. H. A. Plasterk, Z. Izsvák and Z. Ivics, *Trends Genet.*, 1999, **15**, 326–332.

20 M. Tudor, M. Lobocka, M. Goodell, J. Pettitt and K. O'Hare, *MGG Mol. Gen. Genet.*, 1992, **232**, 126–134.

21 J. C. Vos and R. H. Plasterk, *EMBO J.*, 1994, **13**, 6125–6132.

22 J. M. Richardson, S. D. Colloms, D. J. Finnegan and M. D. Walkinshaw, *Cell*, 2009, **138**, 1096–1108.

23 S. P. Montaño, Y. Z. Pigli and P. A. Rice, *Nature*, 2012, **491**, 413–417.

24 A. Pflieger, J. Jaillet, A. Petit, C. Auge-Gouillou and S. Renault, *J. Biol. Chem.*, 2014, **289**, 100–111.

25 M. Tellier, C. C. Bouuaert and R. Chalmers, *Microbiol. Spectr.*, 2015, **3**, 1–19.

26 Z. Ivics, P. B. Hackett, R. H. Plasterk and Z. Izsvák, *Cell*, 1997, **91**, 501–510.

27 D. Hartl, *Genetics*, 2001, **157**, 471–476.

28 J.-L. Bessereau, *WormBook*, 2006, 1–29.

29 D. A. Lidholm, A. R. Lohe and D. L. Hartl, *Genetics*, 1993, **134**, 859–868.

30 S. N. Maiti, H. Huls, H. Singh, M. Dawson, M. Figliola, S. Olivares, P. Rao, Y. J. Zhao, A. Multani, G. Yang, L. Zhang, D. Crossland, S. Ang, H. Torikai, B. Rabinovich, D. A. Lee, P. Kebriaei, P. Hackett, R. E. Champlin and L. J. N. Cooper, *J. Immunother.*, 2013, **36**, 112–123.

31 S. Johnen, Z. Izsvák, M. Stöcker, N. Harmening, A. K. Salz, P. Walter and G. Thumann, *Investig. Opthalmology Vis. Sci.*, 2012, **53**, 4787–4796.

32 H. M. Robertson, *J. Insect Physiol.*, 1995, **41**, 99–105.

33 D. J. Lampe, M. E. Churchill and H. M. Robertson, *EMBO J.*, 1997, **16**, 4153–4153.

34 M. G. Cuypers, M. Trubitsyna, P. Callow, V. T. Forsyth and J. M. Richardson, *Nucleic Acids Res.*, 2013, **41**, 2020–2033.

35 J. Dornan, H. Grey and J. M. Richardson, *Nucleic Acids Res.*, 2015, **43**, 2424–2432.

36 C. Claeys Bouuaert, N. Walker, D. Liu and R. Chalmers, *Nucleic Acids Res.*, 2014, **42**, 5799–5808.

37 J. M. Richardson, A. Dawson, N. O'Hagan, P. Taylor, D. J. Finnegan and M. D. Walkinshaw, *EMBO J.*, 2006, **25**, 1324–1334.

38 M. Trubitsyna, H. Grey, D. R. Houston, D. J. Finnegan and J. M. Richardson, *J. Biol. Chem.*, 2015, **290**, 13531–13540.

39 Z. Yin, M. Lapkouski, W. Yang and R. Craigie, *Protein Sci.*, 2012, **21**, 1849–1857.

40 M. Trubitsyna, E. R. Morris, D. J. Finnegan and J. M. Richardson, *Biochemistry*, 2014, **53**, 682–689.

Chapter 7: Development of Ultrafast Fluorescence Techniques

7.1. Introduction

Thus far in this thesis, the time-resolved fluorescence technique TCSPC has been utilised to study the time-resolved fluorescence properties of 2AP in DNA. However, the time resolution of TCSPC is restricted to the measurement of lifetimes of approximately tens of picoseconds due to inherent limitations of the fast electronics used for the detection of photons emitted from a sample via fluorescence. Unfortunately, some chemical processes and photophysical events occur on shorter timescales than those accessible by TCSPC. These include such processes as solvent relaxation or changes in the vibronic structure of molecules and are of great interest to understanding the nature of the molecules themselves. Due to the advancement of femtosecond pulsed lasers and the use of optical techniques that allow for the gating of the fluorescence signal, emission-based measurements of the photophysics of a molecule can now be performed on the femtosecond timescale. These measurements are typically only limited by the duration of the laser pulse, and the accuracy of the temporal delay between the excitation and "gate" pulses.

This chapter deals with the development of an ultrafast spectroscopic technique with the eventual aim of measuring the ultrafast photophysical and chemical dynamics taking place in biological molecules. Initially the goal set out was to construct a system utilising sum-frequency generation as a fluorescence gating technique to overcome the time-resolution limitations set by standard TCSPC techniques.[1–8] Following this, the system would be adapted to enable broadband detection of ultrashort fluorescence lifetimes (preferably into the UV region where fluorescence from biological molecules is typical). Many fluorescence upconversion instruments exist that utilise systems with a low repetition rate (~1 kHz), amplified femtosecond laser/optical parametric amplifier (OPA) arrangement. However, these suffer from a number of issues; the high pulse energy of such systems is largely wasted, as the sample cannot be irradiated too strongly (particularly when using UV photons and biological samples) and the low repetition rate

limits signal averaging and delay stage scan rate. An alternative is to use just an oscillator-based excitation source operating at tens of MHz. However in these systems, the low pulse energy severely limits the excitation intensity (particularly in the UV) and the inter-pulse separation is, without pulse picking or cavity dumping, usually limited to ~12 ns (thus limiting measurements to samples with fluorescence decay dynamics on the few nanosecond timescale). Also, in the absence of an optical parametric oscillator, the wavelength range accessible for excitation pulses is restricted. A compromise is to use a high pulse repetition rate (100 kHz) amplifier/OPA system. This system used in the present work allows for pulses with moderate energies to be used, which is ideal for the study of biological molecules because it prevents unnecessary damage to the biological systems that may be harmed by excessive exposure to high pulse energies, particularly in the UV region. The low level of detected signal can be compensated for by recording data over longer periods of time, reducing noise-levels through the averaging of spectra.

Unfortunately, due to technical issues experienced and due to time-constraints, efficient collection and gating of fluorescence emission from a sample could not be achieved for the upconversion system. However, correlation spectra of laser pulses could be measured, demonstrating the functionality of the set-up. Rather than abandon the system, the decision was made to carry on with the development of the system and modify the gating technique from sum-frequency generation to a newly reported transient-grating-based photoluminescence technique to enable broadband detection.[5] From the interference of two gate pulses in a medium, a transient grating (TG) is formed for the duration of the laser pulses. TGs can act like a diffraction grating and interact with the input fluorescence emission to gate the signal via diffraction. The diffracted signal will be detected for the duration that the TG is present, allowing for a time resolution that is proportional to the pulse duration rather than limited by the electronics or optics used. Unlike fluorescence upconversion, phase matching conditions are met for all wavelengths for TG, meaning that angle tuning of a crystal is no longer a requirement for efficient gating. Regrettably, the same technical issues and time-constraints were met as before, such that the TG system was characterised from control spectra recorded from laser pulses and efficient collection and gating of fluorescence emission from a sample was not achieved.

7.1.1. The Limitations of TCSPC

As previously mentioned in Chapter 2, the time resolution achievable by TCSPC techniques is limited by the response of the electronics due to a combination of several factors: the transit time spread of the MCP or PMT detector, the time jitter in the electronics and the "dead time" associated with the discharge of the time-to-amplitude converter (TAC). Historically the limitations of TCSPC systems were more severe and these systems were restricted to the measurement of fluorescence lifetimes on the many hundreds of picosecond timescales. To avoid effects such as pulse pile-up and to take into account the dead time of the electronics involved in the system, many TCSPC systems were required to be run in reverse-TAC mode. In reverse mode, the detection of an emitted photon acts as the start pulse and the reference pulse from the laser acts as a stop pulse. This mode also required an additional delay of the reference pulse to be created in order to ensure its arrival at the TAC later than the start pulse. Further details of the limitations of TCSPC are discussed at length in "Principles of Fluorescence Spectroscopy" by Lakowicz,[9] including those related to the decay time of the sample (limiting the repetition rate used) or the dead time associated with the TAC. Due to the more recent advancement of detectors and electronics with faster response times, the boundaries of TCSPC have been pushed further but still are unable to measure into the ultrafast (femtosecond (fs)) timescales required for probing events such as solvation dynamics, DNA photophysics or energy transfer, which occur on too fast a timescale.[10] Although measures are taken to avoid the collection of erroneous data, such as the control of the count rate of photons incident on the detector and control of the repetition rate of the pulsed laser, these are only sufficient to allow for the resolution of fluorescence lifetimes of ~20 ps and slower. The TCSPC set-up utilised previously in this thesis (described in Chapter 3) to study the fluorescence lifetimes of 2AP in DNA, on the sub ps – ns timescale, was shown to be have a time resolution of ~40 ps (based on the IRF presented in Figure 3.2).

As far as this author is aware, although a small selection of ultrafast fluorescence decay measurements of 2AP-containing DNA have been performed,[11–13] to date only one set of directly comparable TCSPC and ultrafast fluorescence decay measurements on 2AP-containing DNA systems (DNA hairpins) exists: the works of Godet *et al.*[14] and Gelot *et al.*[15], respectively. The TCSPC measurements reported four-component decays with lifetimes of ~100 ps, ~700 ps, ~3 ns and ~8 ns, alongside unresolvable dark states (accounting for ~80% of the 2AP population). The ultrafast fluorescence decays,

measured *via* femtosecond fluorescence downconversion, were also fit with four components of ~3 ps, ~20 ps, ~100 ps and 3 ns. While the former two ultrashort lifetimes correspond to species undetectable by TCSPC (dark states), the latter two longer lifetimes are consistent with two components measured by TCSPC. In the ultrafast decay measurements, a combination of the limited time-range (3 ns) of the ultrafast measurements and the inability to extract more than four components from the data has resulted in the longer lifetime components measured by TCSPC to be compressed into two components. It is evident that, in order to achieve a complete picture of the decay properties, a combination of both techniques should be used.

To achieve faster time resolutions, optical techniques have been employed that bypass the limited time-resolution of the detectors. In these systems, the fluorescence emission generated from the excitation of a sample using the "pump" pulse is gated using a technique that relies on a non-linear process, such as sum-frequency generation (SFG) or the optical Kerr (OK) effect. The generated gated-signal is proportional to the fluorescence emission for the period that the gate is "open", which is typically dependent on the duration of the gate pulse used. In this way, a time-resolution can be achieved that is limited by the width of the gate pulse and the accuracy of the delay between the pump and gate pulses. Further details of relevant ultrafast fluorescence spectroscopic techniques are discussed in the remainder of this introduction.

7.1.2. Fluorescence Upconversion Spectroscopy

The foremost ultrafast methods currently used are fluorescence upconversion spectroscopy[2,4,6,7] and related fluorescence downconversion spectroscopy[16,17]. The terms "upconversion" and "sum-frequency generation" are used synonymously in this chapter. Put simply, upconversion occurs when two pulses (with frequencies ω_1 and ω_2) are simultaneously focussed into a birefringent crystal and generate a pulse, ω_3, with a frequency that is the sum of the frequencies of the incident pulses, i.e.

$$\omega_3 = \omega_1 + \omega_2 \qquad \textbf{7.1}$$

The more in-depth considerations of sum-frequency generation will be considered from here on in the context of fluorescence upconversion spectroscopy, where ω_1 is the frequency of the gate pulse (ω_G), ω_2 is the frequency of the fluorescence emission from a sample (ω_F) and ω_3 is the frequency of the upconverted signal (ω_s).

The mechanism of sum-frequency generation is shown in Figure 7.1, involving the generation of an upconverted signal via a cross-correlation between the fluorescence emission from a sample and the gate pulse.

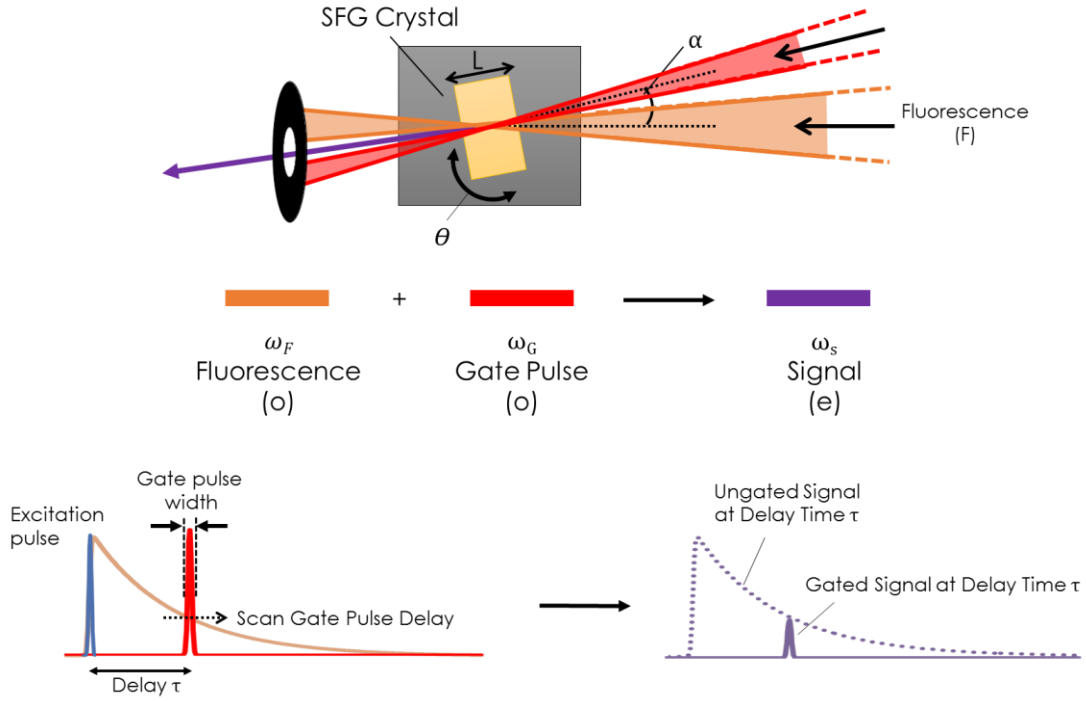

Figure 7.1: Schematic and mechanism of the upconversion gating technique.

For measurement of the fluorescence decay of a sample, the sample is electronically excited by an excitation pulse (at time t =0) and the resulting fluorescence emission (ω_F) is collected and focussed, to overlap with a gate pulse, into a nonlinear optical crystal (SFG crystal). Two examples of such nonlinear crystals used for sum-frequency generation are potassium dihydrogen phosphate (KDP)[18] or β-barium borate (BBO)[19] and are typically selected based on their lack of inversion symmetry in their crystal structures, resulting in the exhibition of birefringent properties. The angle of the SFG crystal is required to be orientated such that phase-matching conditions are met in relation to the wavelengths of the fluorescence emission and the gate pulse for efficient SFG to occur. Photons of upconverted signal are only generated during the time that the gate pulse is overlapped (spatially and temporally) with the emission signal in the crystal (opening the gate), enabling for a time resolution that is only limited by the width of the gate pulse. Use of a non-collinear angle allows the upconverted signal produced to be both spatially and spectrally separated from any remaining gate pulse or background fluorescence present, enabling for a greater signal-to-noise ratio.

For SFG there are two laws that must be observed, the conservation of energy:

$$\omega_S = \omega_G + \omega_F \quad \textbf{7.2}$$

and the conservation of momentum:

$$\overrightarrow{k_S} = \overrightarrow{k_G} + \overrightarrow{k_F} \quad \textbf{7.3}$$

where ω and $\vec{k}$ are the frequency and the wave vector, respectively. The subscripts F, G and s denote the fluorescence emission, gate pulse and sum-frequency generated signal, respectively.

For efficient conservation of momentum, the phase mismatch, Δk, must be set to zero. Δk is given as shown in Equations 7.4 and 7.5.

$$\Delta\vec{k} = \overrightarrow{k_S} - \overrightarrow{k_G} - \overrightarrow{k_F} \quad \textbf{7.4}$$

$$= \frac{n_S}{\lambda_S} - \frac{n_G}{\lambda_G} - \frac{n_F}{\lambda_F} \quad \textbf{7.5}$$

where n is the refractive index and λ is the wavelength. A favourable property of non-linear optics is the birefringence of certain crystals.[4,20] As such, the crystal angle can be altered which changes the relative refractive index of the beams allowing phase matching conditions to be met. Alternatively, the temperature of the crystal can be changed to have the same effect of altering the refractive index. Unfortunately, the minimisation of phase mismatch is highly dependent on the wavelength of the interacting photons and any change in this wavelength requires the angle (or the temperature) of the crystal to be adjusted appropriately. This typically complicates the use of SFG as a gating technique since broadband detection is not inherently possible in the set-up. However, the work of Cannizzo *et al.*[1] has demonstrated that (after calibration) the use of a computer-controlled rotational stage, to rotate the SFG crystal for a duration at a constant speed at each delay-stage position, can enable the collection of upconverted signals through a range of wavelengths (and even into the UV region). Broadband fluorescence upconversion systems have also been designed for ultrashort pulse systems, but these are not yet readily configured, particularly on high repetition rate systems.[21,22]

Another degree of freedom that should be considered is the angle between the two incident beams (F and G), labelled as "α" in Figure 7.1. Figure 7.2 shows a vector diagram of the two possible geometric cases: collinear and non-collinear.

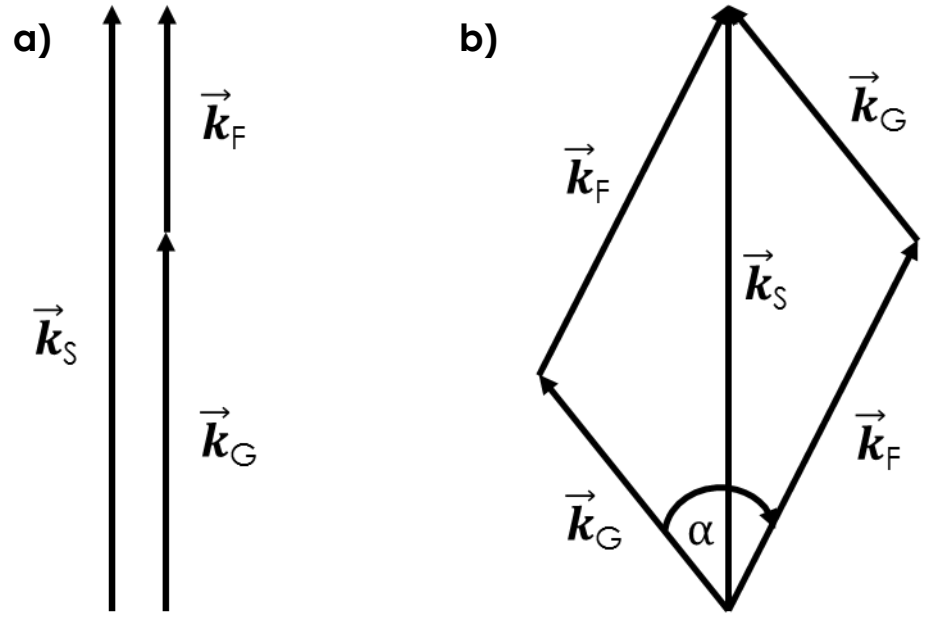

Figure 7.2: Possible geometric arrangements for sum-frequency generation: a) collinear and b) non-collinear.

If α = 0, the two beams are collinear but the photons generated *via* sum-frequency generation will spatially overlap with those of the parent beams. On the other hand, when α ≠ 0 and a non-collinear arrangement is used (as is favourable for generation of a spatially separated signal), the $\vec{k}$ components can be obtained from the cosine law, as follows:

$$\overrightarrow{k_s^2} = \overrightarrow{k_G^2} + \overrightarrow{k_F^2} - 2\overrightarrow{k_F}\,\overrightarrow{k_G}\cos(\pi - \alpha) \qquad \textbf{7.6}$$

There are two types of phase matching possible: type I and type II, and are described as follows. In type I phase matching, the polarisation of the two incident waves is in the same plane (ordinary and ordinary (o + o)) and the polarisation of the third wave is in a plane perpendicular to that of the other two (extraordinary, e):

$$\overrightarrow{k_F}\,(o) + \overrightarrow{k_G}\,(o) = \overrightarrow{k_s}\,(e) \qquad \textbf{7.7}$$

Type II phase matching is when the two incident waves are polarized perpendicular to each other (o + e) and the polarisation of the third wave can be in the plane of either of the parent waves (with the properties of the nonlinear crystal used typically determining which):

$$\overrightarrow{k_F}\,(o) + \overrightarrow{k_G}\,(e) = \overrightarrow{k_s}(e/o) \qquad \textbf{7.8}$$

The quantum efficiency, η, of upconversion is an important factor that should be considered in these experiments and optimisation of the efficiency will allow for effective

collection of signal vs noise. The quantum efficiency for phase matched (Δk = 0) SFG is reliant on a range of parameters, as shown by Equation 7.9,[2]

$$\eta(\Delta k = 0) = \frac{2\pi^2 d_{eff}^2 L^2 P_G}{Ac\varepsilon_0^3 n_F n_G n_s(\theta_m)} \quad \textbf{7.9}$$

where L is the length of the crystal (as shown in Figure 7.1), P_G is the peak power of the gate pulse, ε_0 is the free space permittivity, A is the cross-sectional area of the gate laser beam, c is the velocity of light, n_i is the refractive index of component I (F, G, or s), Θ_m is the phase matching angle and d_{eff} is the effective nonlinearity of the crystal. Equation 7.9 assumes that the peak pulse power and area of focus of the gate pulse are larger than for those associated with the fluorescence emission and thus terms associated with the fluorescence emission are not included in this equation.

Alternatively, for cases in which phase-matching conditions are not precisely met, the quantum efficiency becomes

$$\eta(\Delta k) = \eta(0)\frac{sin^2(\Delta kL)}{(\Delta kL)^2} \quad \textbf{7.10}$$

where η(0) is the efficiency for phase matched cases and Δk is the phase mismatch.

Overall, it can be seen from Equations 7.9 and 7.10 that the efficiency of upconversion, to generate a signal with peak power P_s, is directly proportional to the peak powers of the fluorescence and gate pulses, P_F and P_G, and is strongly dependent on reducing the phase mismatch, Δk, and the length of the SFG crystal, L. Assuming that major attenuation of the power and focus area of the fluorescence emission are not required, Equation 7.11 shows an approximated version of Equation 7.10 highlighting the important variables in the context of the work presented in this chapter.

$$P_s \propto P_G L^2 \frac{sin^2(\Delta kL)}{(\Delta kL)^2} \quad \textbf{7.11}$$

Clearly, the best way to optimise the efficiency of SFG is to use a crystal with a large length. However, the acceptance angle (defined as the angle where the phase mismatch is <90°), ΔΘ, is inversely proportional to the crystal length and can be calculated for collinear and non-collinear geometries as shown in Equations 7.12 and 7.13, respectively.

$$\Delta\theta = \frac{\pi}{L}\left(\frac{\delta k_s}{\delta\theta}\right)^{-1} \quad \textbf{7.12}$$

$$\Delta\theta = \frac{2.78 n_{o,F}\lambda_F}{L\left[1 - \left(n_{o,F}\lambda_s\right)/(n_s(\theta_m)\lambda_F)\right]} \quad \textbf{7.13}$$

As such, thinner crystals have larger acceptance angles than thicker crystals. Since fluorescence from a sample is collected and focussed to a point in the crystal in a broad cone, acceptance angles are typically smaller than the focussed-cone of the emission and as such, the small spot size required is not achieved. This results in only a small portion of the fluorescence emission mixing with the gate pulse to generate the upconverted signal.

Another important property that must be taken into account when considering non-linear processes is the group velocity (GV) mismatch. The group velocity, v_g, is the velocity at which a wave (in this case, of light) propagates in a medium. For processes in linear optics, pulse broadening due to GV mismatch is not observed. However, for non-linear processes such as SHG or SFG using fs-length laser pulses, GV mismatch can result in the temporal separation of pulses that were originally overlapping and is dependent on the crystal length. In order to minimise or avoid the effects of GV mismatch, it is necessary to use crystals with a shorter length. Unfortunately, with shorter crystals comes the requirement for higher pulse intensities in order to maintain a high degree of efficiency in the frequency conversion (to combat the small acceptance angle). However, when using high pulse intensities with shorter crystal lengths, optical damage of the crystal can occur and thus great care must be taken. In this way, GV mismatch can limit the achievable efficiency of the desired frequency conversion.

While fluorescence upconversion spectroscopy enables for impressive time resolution, there are limitations associated with the complexity of the instrumentation and non-linear processes involved. The ability to measure lifetimes longer than 1-2 ns is made problematic by the use of an optical delay line, which has a finite length. A nanosecond delay roughly equates to about 30 cm and alignment of multiple or long delay lines becomes difficult to maintain. Since only a small portion of the fluorescence emission is gated at each delay position (for reasons discussed previously), high efficiency of SFG is required for a good signal-to-noise ratio. The efficiency of SFG is strongly dependent on minimising the phase-mismatch (achieved via angle tuning the crystal) and even a slight change in emission wavelength necessitates reorientation of the crystal. Consequently, fluorescence upconversion is commonly used for wavelength-specific detection of fluorescence emission. Despite this, Cannizzo et al. achieved broadband detection in upconversion spectroscopy using a computer-controlled rotational stage to rotate the crystal through an angle of 28° at each delay position.[1] Unfortunately, this adds yet another layer of complexity to the already complex instrumentation and requires the need for an extra calibration step.

Fluorescence upconversion has been used widely to study the ultrafast dynamics of a wide range of molecules, including biological molecules. Although DNA bases have extremely low fluorescence quantum yields, ultrafast components in the fluorescence decays of adenine, deoxyadenosine and deoxyadenosine 5'-monophosphate (dAMP) were recorded by Gustavsson *et al.* using fluorescence upconversion spectroscopy.[23] To explain the difference measured in the ultrafast decay of adenine compared to its nucleotide and nucleoside Gustavsson et al. invoke the idea of the presence of different tautomeric forms of adenine, demonstrating the level of information that can be determined from minimally fluorescent molecules using fluorescence upconversion spectroscopy. More recently, Banyasz *et al.* investigated the electronic transitions in adenine oligomers (A_{20}) using a combination of theoretical (time-dependent-DFT) and experimental (steady-state and time-resolved fluorescence) studies and a comparison was made with dAMP.[24] It was demonstrated that the electronic processes in A_{20} are highly complex and dependent on the wavelength of excitation and emission. Fluorescence anisotropy decays measured by Banyasz *et al. via* fluorescence upconversion measurements were able to provide evidence that energy transfer occurs between bases through the involvement of exciton states. The lack of a fluorescent probe in these DNA systems (with A bases being both the energy donor and energy acceptor) resulted in only a limited study of energy transfer in these systems. However, further discussion on interbase electronic energy transfer in DNA can be found in Chapter 4 of this thesis.

7.1.3. Optical Kerr Gate

An alternative to fluorescence upconversion that allows for broadband detection is optical Kerr (OK) gate spectroscopy. Originally proposed by Duguay and Hansen in 1968,[25] OK-gate set-ups are typically arranged like standard fluorescence gating systems, where a gate pulse is used to effectively open a gate *via* an optical effect. Instead of gating the signal *via* sum-frequency generation (as in upconversion spectroscopy) a portion of the fluorescence is instead sampled using the optical Kerr effect to open a "shutter" that has been constructed from a Kerr medium (typically a crystal or glass but occasionally a gas) positioned between two orthogonal linear polarisers. A simplified schematic of an OK-gate set-up is illustrated in Figure 7.3.

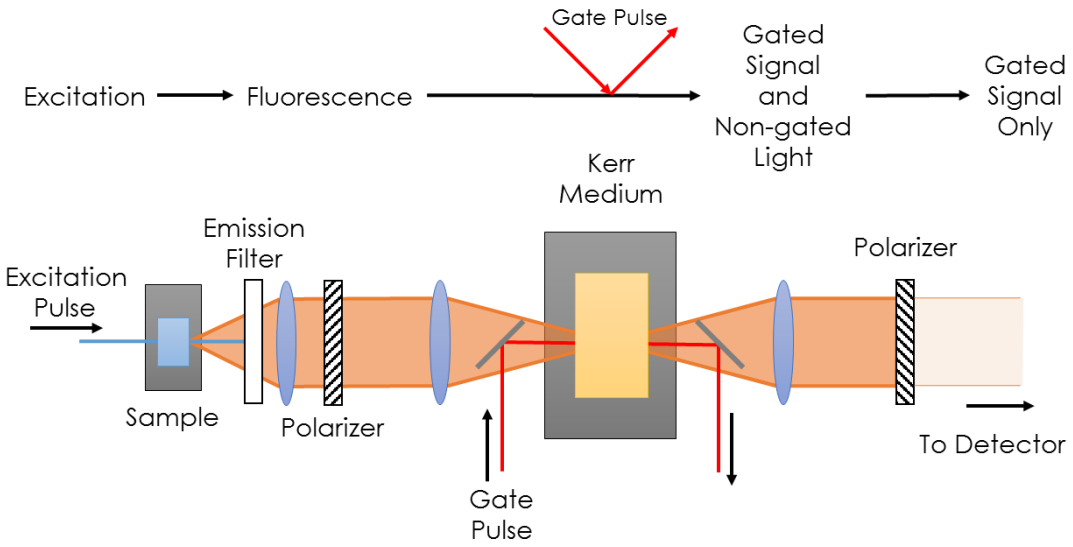

Figure 7.3: Simplified schematic of an Optical Kerr-gate set up.

Only a general overview of the OK effect will be presented here since OK-gating is not utilised as a gating technique in this work, but an intensive discussion of the physics and theory underlying the OK effect can be found in the works of Bartolini.[20]

The fluorescence emission from a sample passes through the first polariser while the second polariser is aligned perpendicular to the first in order to allow for maximum extinction of the transmitted fluorescence. When no gate pulse is present (shutter closed), the Kerr medium is transparent and isotropic and does not alter the polarisation of the transmitted light. When an intense pulse of light (the gate pulse) is present, the Kerr medium becomes anisotropic and a transient birefringence is induced in the Kerr medium. This alters the polarisation of the transmitted light for a time that is proportional to the duration of the gate pulse and allows a portion of it to pass through the second polariser. The time resolution in these systems is usually limited to the recovery time of the medium, the duration of which (~200 fs in the best cases) exceeds that of the width of the gate pulse (typically ~50-100 fs). The majority of OK-gate set-ups have used (CS_2), benzene or a glass plate as a Kerr medium, while, fused silica (quartz) and strontium titanate ($SrTiO_3$) have also been included for use as the Kerr medium more recently.[20,26–28] Although fused silica is UV-transparent (a property not held by the other media previously used), the recovery time was found to be relatively long and presented in a small shutter contrast.[2] As such, OK-gate set-ups are often hindered by low sensitivity and the extinction ratio of the thin polarisers used in the set-up as even a small leakage of background intensity can overwhelm the gated signal. The limited transmission wavelengths of the Kerr medium also typically limit detection to

the visible spectrum for the more efficient Kerr media used and thus OK-gate set-ups are not typically ideal for the study of biological molecules, where most fluorescence emission occurs with very low quantum yields and typically in the UV range. In addition, thin (low dispersion) high extinction polarisers for the UV are not readily available.

7.1.4. Transient Grating Photoluminescence Spectroscopy

In order to achieve broadband detection with higher sensitivity than in OK-gate spectroscopy, the work presented in this chapter aims to utilise a transient grating, generated in an appropriately transparent medium, to sample a portion of the emission spectrum *via* diffraction. This concept was published recently as an alternative to the other methods of femtosecond photoluminescence measurements discussed above, and holds promise to extend detection into the UV range.[5] The transient grating is generated *via* the interference pattern from two interacting femtosecond gate pulses that intersect within a medium, and where the refractive index of the medium is modulated by the OK effect.

7.1.4.1. Diffraction Grating Theory

Diffraction gratings, a common component in spectroscopy, are used to disperse light in different directions, the angle of which depends on the wavelength of the light. They are typically constructed from a series of closely spaced parallel grooves etched on a hard glassy metallic material that has been coated with a reflective material so that it acts as a mirror. Figure 7.4 shows an example of how white light incident on a reflection grating at 90° is dispersed.[29] The general equation for diffraction by a grating is:

$$m\lambda = d(sini + sin\theta) \qquad \textbf{7.14}$$

where Θ and i are the angles of reflectance and incidence, respectively (measured from the normal to the surface), d is the groove spacing, λ is the wavelength and m (= 0, 1, 2 …) is the order of diffraction.

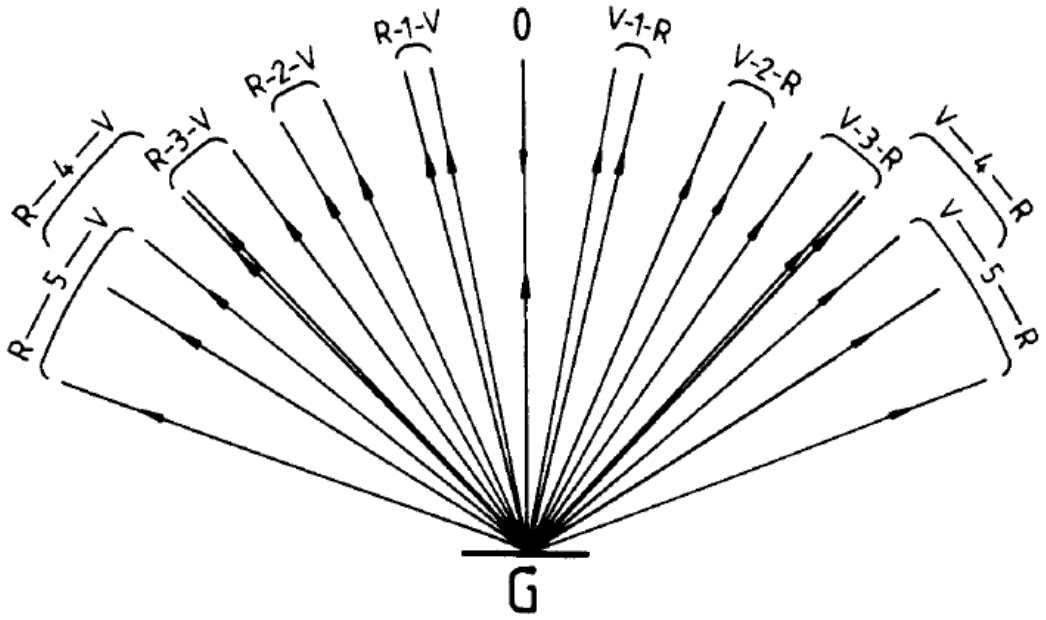

Figure 7.4: Diagram showing how white light incident normal to the surface of a reflection grating (G) is dispersed. "R" and "V" indicates the red and violet ends of the spectrum, respectively, while the central number is the order of diffraction. At larger orders of diffraction, the diffracted light from multiple orders overlaps. Figure reproduced from Modern Spectroscopy by Hollas.[29]

7.1.4.2. Transient Grating Theory

The grating used in this work is transient and only exists in the medium for the duration of the overlapping gate pulses. In this way, the diffracted signal can be sampled from the complete emission spectra, to a temporal resolution limit that is controlled by the duration of the gate-pulse (or by the GV mismatch). The principles behind the generation of a TG from the interaction of two pulses of light will now be discussed and a comprehensive discussion on the theory can be found in "Laser Induced Dynamic Gratings" by Eicheler, Günter and Pohl.[30] First, one must consider the superposition of two plane waves in a medium. Essentially, the grating formed from two pulses of light is generated for a duration that is proportional to that of the pulses. Figure 7.5 shows a schematic of two plane waves interacting in a medium and the formation of a grating from the periodic interference pattern. The interference pattern creates a spatially periodic variation of the optical properties of the medium via standing-wave creation of some mode of the medium.[30]

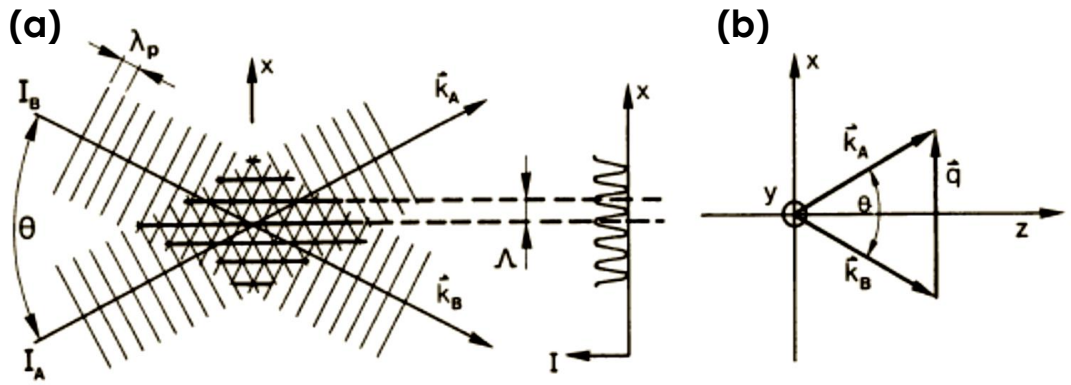

Figure 7.5: (a) Principal set-up of the production of grating by the interference of two light waves. (b) Vector diagram of the interacting light waves with wave vectors k_A and k_B to produce grating vector q. Figure reproduced from Laser-Induced Dynamic Gratings by Eichler, Günter and Pohl.[30]

Initially, two laser beams, A and B, are produced (usually by splitting one powerful beam into two using a beamsplitter) with wave vectors $\mathbf{k_A}$ and $\mathbf{k_B}$, electric amplitudes $\mathbf{A_A}$ and $\mathbf{A_B}$, and intensities I_A and I_B. Arrangement of the beams to intersect at an angle Θ (where the angle of incidence, $\Theta_i = (\Theta/2)$) in a medium with refractive index n, results in the generation of an interference pattern with grating vector, $\mathbf{q}$, which is given as:

$$\boldsymbol{q} = \pm(\vec{\boldsymbol{k}}_{\boldsymbol{A}} - \vec{\boldsymbol{k}}_{\boldsymbol{B}}) \qquad \textbf{7.15}$$

From Equation 7.14, it can be seen that the angle of dispersion is only dependent on the angle of incidence and the period of the grooves (not their shape). The spatial period of the grating generated by the interference pattern of two plane waves, Λ, (equivalent to the grating spacing d in Equation 7.14) is given as:

$$\Lambda = \frac{2\pi}{q} \qquad \textbf{7.16}$$

where $q = |\boldsymbol{q}|$. The period can also be expressed in terms of the pump wavelength, λ_p and the angle Θ

$$\Lambda = \frac{\lambda_p}{2\sin(\theta/2)} \qquad \textbf{7.17}$$

So far, in the equations presented, $\mathbf{k_A}$, $\mathbf{k_B}$, λ_p and Θ have been for measurements performed in a medium. Typically it is more reasonable to measure these parameters outside of the medium in which the TG is generated and to do this, the change in refractive index must be taken into account for each parameter; i.e. the wavelength measured outside the medium, λ_{0p} (= $n\lambda_p$), and the intersection angle measured outside the medium, $\sin\Theta_0$ (= $n \sin\Theta$). It can be seen from Equation 7.17 that the grating period

can be changed by varying Θ_0. Typically, the maximum value of Λ is limited by the diameter of the laser beam that is being used to induce the grating. Typical experimental values of Λ have ranged up to approximately 100 μm, while the smallest values of Λ (~100 nm) are achieved using an antiparallel configuration (where $\Theta = 180°$) coupled with use of light in the visible range and using a medium with a high refractive index. When anti-parallel and near-parallel configurations are used, the grating period can be simplified as:

$$\Lambda = \frac{\lambda_p}{2} = \frac{\lambda_{0p}}{2n} \quad for\ \theta = 180° \tag{7.18}$$

$$\Lambda = \frac{\lambda_p}{\theta} = \frac{\lambda_{0p}}{\theta_0} \quad for\ \theta \ll 1 \tag{7.19}$$

However, grating periods of such a small size are not used in the work performed in this thesis.

For all cases, the grating will be limited to a finite size due to the finite cross-section of the beam. The size of the grating period should be optimised relative to the wavelength range of the light to be diffracted and to obtain a sufficient order of diffraction. Three conditions should be considered for the formation of an ideal plane grating. Firstly, the minimum width of the interaction zone must be large compared to the grating period. Secondly, the overlap of the two beams in the z-direction must be large compared to the medium thickness, and thirdly, any absorption of the beam by the medium must be negligible. Each of these conditions hold significance for the femtosecond photoluminescence set-up under consideration here. The first condition limits the extent of the focus of the beam (typically used to increase the beam intensity). The second condition controls the angle at which the beams coincide, while the third condition is typically the limiting factor in the selection of the gating medium and a suitably transparent material (in the wavelength range of the beam) should be carefully selected.

When a TG is generated, the refractive index is modulated by the Kerr effect, resulting in the equal interaction of the TG with all wavelengths. The broad bandwidth of TG-based techniques can be understood when the focussing geometry is considered. A grating vector, $\vec{k}_G$, is generated from the interference of two gate k vectors (as shown in Figure 7.6).

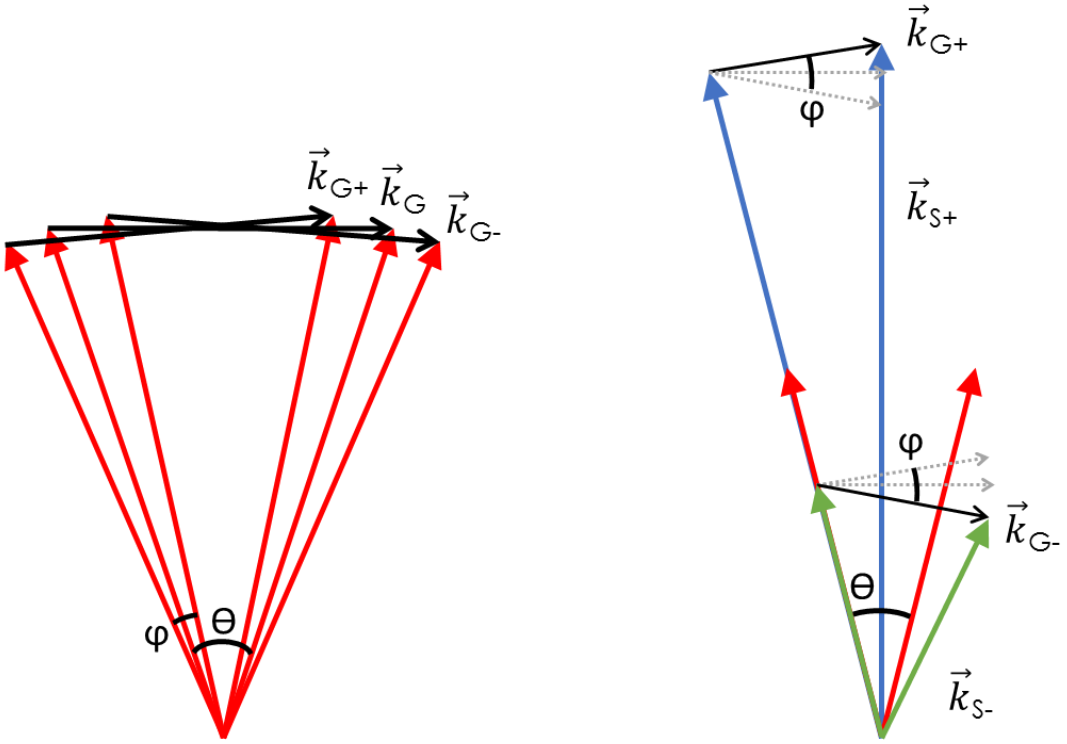

Figure 7.6: Vector diagram relating to TG. Left: Generation of grating vectors spanning $\vec{k}_{G-}$ to $\vec{k}_{G+}$ from gate vectors corresponding to gate beams focussed with an internal angle of φ, which cross at an angle of Θ. Right: phase-matched diffraction of signals spanning $\vec{k}_{S-}$ to $\vec{k}_{S+}$ using the range of grating vectors generated ($\vec{k}_{G-}$ to $\vec{k}_{G+}$)

A diffracted signal, $\vec{k}_S$, is then generated from the interaction of an input signal, $\vec{k}_F$, with the grating vector where the conservation of momentum (Equation 7.3) satisfies the Bragg condition of the grating (Figure 7.6) such that,

$$\vec{\boldsymbol{k}}_{\boldsymbol{S}} - \vec{\boldsymbol{k}}_{\boldsymbol{G}} = \boldsymbol{q}m, \qquad m = \pm 1, \pm 2, \ldots \tag{7.20}$$

The optical properties of the medium can be modified by the real part of the refractive index (birefringence and/or phase grating) or in its imaginary part (dichroic and/or amplitude grating).[30] However, for the materials used as the TG medium in this thesis, the electric fields of the gate pulses are not resonant with the material energy levels and so the TG induced is mainly due to the birefringence-phase grating (similar to the OK effect).

In the work presented in this chapter, a TG technique is developed that is based upon recent work performed by Chen *et al.*,[5] who constructed and characterised a transient-grating photoluminescence spectroscopy (TGPS) set-up, that originally took inspiration from the use of a TG in frequency resolved optical gating (FROG). FROG is a

technique that is well known for the characterisation of ultrafast laser pulses in which a laser pulse is split in two by either a mask or beamsplitter and recombined in a non-linear medium to produce a correlation profile of the original pulse.[31–33] Chen *et al.* demonstrated the effectiveness of TG-based techniques for the measurement of ultrafast photoluminescence lifetimes with 200 fs resolution (using excitation and gate pulses with a duration of 100 fs) comparable with OK-gate and upconversion spectroscopic methods, and also demonstrated broadband spectral resolution (400 nm – 860 nm) with low background detection. In the experimental set-up, the spectral range of detection was only limited to above 400 nm by the optics used (which were not optimised for use in the UV range) and limited to less than 860 nm by a short-pass filter (used to eliminate background caused by residual gate-pulse intensity). Chen *et al*. emphasise the possibility to extend the detection range into the UV and near-IR by substituting the limiting optics for those optimised for wavelengths in suitable regions (IR or UV). Importantly, the only aspect of the TG medium that limits the broadband detection range is the optical transparency of the medium used, since phase-matching conditions are met for all wavelengths, and thus parameters such as the angle or temperature of the crystal do not need to be controlled. More recently, the TGPS set-up developed by Chen *et al.* has been proven effective in a range of measurements of the ultrafast fluorescence from conjugated polymers,[34] pentacene dimers[35] and in energy transfer studies in perylene-based multichromophore arrays.[36]

In the remainder of this chapter, the development of an ultrafast fluorescence technique based on a high pulse repetition rate (100 kHz) femtosecond laser is presented. Initially a fluorescence upconversion system was constructed and characterised but, due to technical issues and time-constraints, collection and gating of fluorescence emission from a sample was not achieved. However, initial characterisation of the set-up was performed via the measurement of correlation spectra of laser pulses. Following this, the system was adapted to allow for broadband detection by changing the gating technique from sum-frequency generation to a TG-based gating technique. Since the same issues were encountered as before, only initial characterisation of the system was performed by this author. Development of the system has, however, been carried on in the time since and the advancements of the system show promise for use of the system in the future for the measurement of ultrafast time-resolved fluorescence decays from biological molecules.

7.2. Materials and Methods

7.2.1. Sample Preparation

2, 5-diphenyloxazole (PPO) and auramine O were purchased from Sigma Aldrich and coumarin 153 was purchased from LambdaChrome and all were used with no further purification. Samples were prepared to a concentration of approximately 0.1 to 1 μM in ethanol for characterisation of the set-ups.

7.2.2. The Laser System

The set-ups described in this chapter were built through sequential adaption of the same set-up and so the laser system employed to drive the experiments was identical up until a certain point in each set-up described. Specifications of each set-up will be covered in the appropriate sections.

The output of an 18 W Nd:Vanadate laser (532 nm CW) (Verdi V18, Coherent) was split using a 1:2 beamsplitter to pump a Ti:sapph oscillator (Coherent, MiraSeed) with 6 W, while the remaining 12 W was used to pump a regenerative amplifier (Coherent RegA 9050, 100 kHz). The Ti:sapph oscillator operated at 76 MHz with a pulse duration of approximately 50 fs (FWHM), 400 mW. While capable of producing pulses in the range of 700 – 1000 nm, in the current set up the Ti:sapph oscillator (and therefore amplifier) was tuned to 800 nm. The output of the Ti:sapph oscillator was passed through a pulse shaper (MIIPS Box 640, Biophotonics Solutions) and was then directed to a pulse expander (EC9150, Coherent) to stretch the pulse (reducing the peak power) before being injected into the RegA. Following amplification (typically consisting of ~15 round trips of the regenerative amplifier), the pulses (~1000mW average power, 94 kHz) were recompressed using a compressor (EC9150, Coherent) to provide pulses of duration ~50 fs. Following this point, the beam paths are distinct to the experimental set-ups and will be discussed further in the relevant sections.

7.2.3. Frequency Noise and Detection Rate

Since the techniques discussed here are performed in the ultrafast time domain, the effect of noise in the time domain will have a much greater impact on the measurements compared to those performed on slower timescales. It should be understood that the minimisation of fluctuations stemming from the laser or from the sample is paramount to improving the signal-to-noise ratio. However, in the ultrafast timescale that is observed, residual noise will still likely persist after all feasible

minimisation has been performed. Frequency noise (or $1/f$ noise) is a known issue in experimental measurements and, as the name implies, the level of noise is inversely proportional to the frequency.[37] It follows then that contributions from low-frequency noise from fluctuations of the laser and sample can be avoided by using a high detection rate. Similar to ultrafast TA measurements, the ultrafast systems discussed here use phase-sensitive detection in which the signal is modulated at a high frequency. To achieve this, a mechanical chopper is inserted into the beam path (of either the excitation or the gate pulses), providing a reference frequency for a lock-in amplifier. Typically, the upper frequency limit in this scenario is shot-to-shot detection, in which a single gated pulse intensity is recorded per triggered acquisition. However, in the systems described later in this thesis, one of the beams in the multiple beam experiments is chopped at a frequency that is only a fraction of the laser repetition-rate, resulting in a series of alternating "on" (gated) and "off" (non-gated) signals. The use of a lock-in amplifier multiplies the input signal with a sine wave at the reference frequency, while the modulation of the signal via the use of a chopper essentially turns the signal into a binary response consisting of "on" and "off" signals.

Since high wavelength resolution was not a requirement for the initial systems developed, it was possible to use a combination of a photodiode (PD) or photomultiplier tube (PMT) with a lock-in amplifier, accompanied by a chopper wheel (set at a reference frequency of 150 Hz), to further reduce contributions from frequency noise and to enhance the signal-to-noise ratio.

7.3. Time-Resolved Fluorescence Upconversion Spectroscopy

7.3.1. The Experimental Set-up

The optical components of the experimental set-up of the fluorescence upconversion system, following the generation of the regeneratively amplified femtosecond laser pulses, are shown in Figure 7.7 and described as follows.

The output from the compressor was split by a 50:50 beamsplitter and half of the output was used to pump an optical parameter amplifier (OPA) (OPA 9450, Coherent)) while the remaining half was used as the gate pulse for SFG. The gate pulse was focussed onto the Type I BBO crystal (Castech Inc.) used for sum frequency generation ("BBO (SFG)") at a non-collinear angle, relative to the fluorescence emission, after passing through a variable optical delay line (Newport, UTS150PP with ESP 300 controller) and

a λ/2 waveplate. The gate beam was focussed using a 750 mm lens and directed to pass through the BBO (SFG) at the focal point.

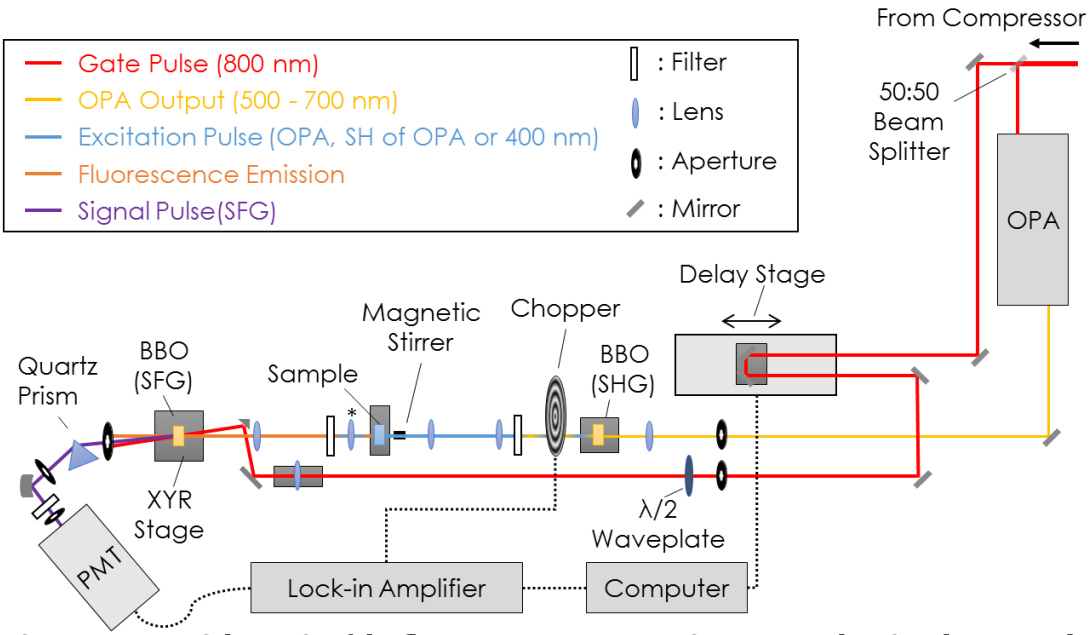

Figure 7.7: Schematic of the fluorescence upconversion system showing the gate pulse (red), the OPA output (yellow), excitation pulse (blue), the fluorescence emission (orange) and the upconverted signal pulse (purple). In this set-up, the delay stage features in the beam path of the gate pulse.

Excitation pulses were generated from the OPA, which could be tuned to produce pulses between 500 nm and 700 nm, or alternatively, pulses of 400 nm could be obtained from the residual second harmonic that is generated within the OPA. Excitation pulses in the UV range (250 nm – 350 nm) could be obtained by generation of the second harmonic of the OPA output via a BBO crystal (Castech Inc.) ("BBO (SHG)"), angle-tuned for generation of the second harmonic of a specific wavelength. The excitation pulses were modulated with a light chopper (Thorlabs), while a lock-in amplifier (EG&G 186a) was referenced to the same frequency. Excitation pulses were passed through a shortpass filter to remove excess OPA output and attenuated to prevent photobleaching or damage to the sample, before being focussed onto the sample. The sample was held within a 2 mm quartz cuvette and was continuously stirred by way of a magnetic stirrer.

Fluorescence emission from the sample was collected and focussed via refractive optics and residual excitation light was removed using a longpass filter. The BBO (SFG) was mounted on an XYR stage for easy optimisation of the focal length and angle-tuning of the crystal. Residual gating pulses and fluorescence emission were removed from the SFG signal by way of an aperture and short pass filter and were further dispersed using

a quartz prism. The upconversion signal was directed and focussed onto a photomultiplier tube (PMT) (1P28) using a UV-enhanced curved mirror. The experiment was controlled using an in-house written MatLab GUI, written in parts by Dr D. A. Smith (University of Edinburgh) and Dr B. E. Robotham (University of Melbourne). For characterisation of the set-up, a cross-correlation of the 800 nm gating pulse and 400 nm second harmonic was achieved by removing the sample and the BBO (SHG) crystal (which was not required when 400 nm second harmonic pulses were obtained from the OPA) to allow for the sum-frequency signal to be generated. Temporal overlap of the pulses ("time zero") was achieved by synchronising the pulses using the variable optical delay line in the path of the gating pulse. Due to the long path-length of the pulses within the OPA, only delay of the gating pulse was required.

Measurements of time-resolved decays were attempted but not achieved. However, cross-correlation profiles between laser pulses were recorded by measuring the intensity of SFG, as the optical delay time of the gate pulse is varied (using the computer controlled optical delay line). The integration time for signal collection could range from 0.03 – 30 seconds at each optical delay position and was controlled using the MatLab GUI. The voltage of the PMT was controlled using the PMT control box and was typically set at ~600 V. Scans were recorded and averaged in order to reduce the signal-to-noise ratio.

Optimisation of the upconverted signal was achieved by iteratively rotating the BBO (SFG) crystal manually and performing a scan of the delay stage. Initially the generated signal was too weak to be seen by eye and so the signal was only detected by the PMT. Once time-zero had been located and set, the optimisation of the angle of the crystal could be performed by eye and from the fluorescence resulting from a piece of white card in the beam path.

7.3.2. Characterisation of the System

As mentioned previously, efficient collection and gating of fluorescence emission from a sample was not possible at this time and, as such, the capabilities of the set-up to measure fluorescence decays on the ultrafast timescale could not be tested. Initially time-zero was located by obtaining a cross-correlation between the excitation pulse (400 nm second harmonic) and the gate pulse (800nm fundamental) and optimising the system under these conditions. The parameters optimised were the phase of the lock-in amplifier, the angle of the BBO crystal, the voltage level of the PMT, the position of the BBO in the focus of the beams and the spatial overlap of the beams at the crystal.

Figure 7.8 shows the obtained upconverted signal generated in a Type I BBO crystal from the cross-correlation between the gate pulse (fundamental, 800 nm) and the second harmonic (400 nm). These measurements were performed without the presence of a sample in the sample holder and by removing any filters in the excitation beam path that would normally filter out the 400 nm excitation pulses.

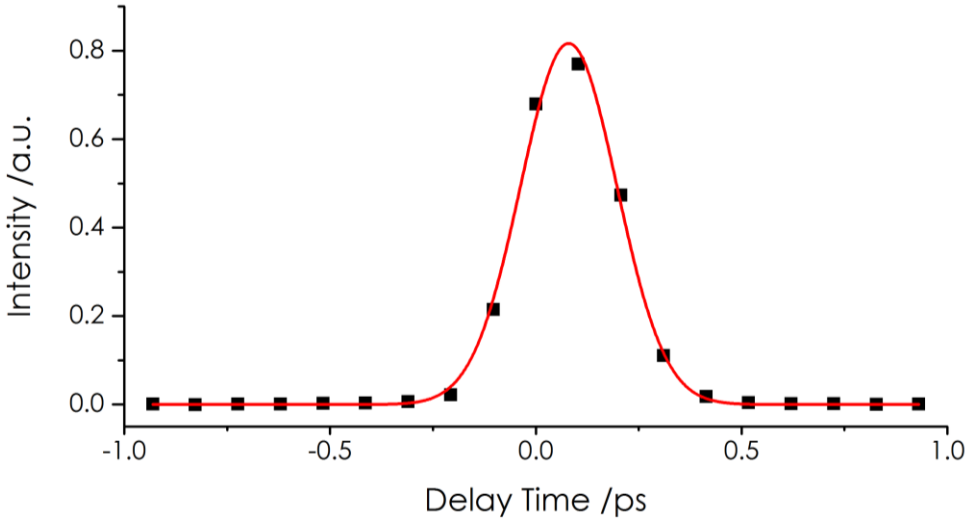

Figure 7.8: Cross-correlation between the second harmonic (400 nm) and the gate pulse (fundamental, 800 nm) in a Type I BBO crystal. A Gaussian fit of the data (red line) gives a FWHM of 275 fs.

From a Gaussian fit of the cross-correlation (using data fitting functions in Origin 2015, OriginLab), the FWHM was measured to be 275 fs, suggesting that the time resolution of the upconversion set-up could be as short as ~150 fs (estimated by the half width at half maximum (HWHM)). However, this is only a preliminary estimate and further evidence is required for a better estimate of the time-resolution. Enhancement of the resolution achievable by the set-up could possibly be achieved through use of a pulse-compressor, optimisation of the optics used in the set-up, or by using deconvolution in the fitting of recorded data.

Following this step, to attempt to measure the fluorescence decay from a sample, the excitation source was swapped to the OPA output which was subsequently frequency doubled to produce pulses of 300 nm. A sample (PPO in ethanol) held in a fused silica cuvette (2 mm path length) was inserted in the sample holder and a filter was placed into the beam path after the sample to remove excess excitation intensity. The lenses for collection and focussing of the fluorescence emission had already been optimised previously. PPO in ethanol was chosen as a fluorescent sample due to its high fluorescence quantum yield (0.89 ± 0.03),[38] the similarity of fluorescence profile (λ_{exc} =

310 nm, λ_{em} = 370 nm) to 2AP, and the proximity of the fluorescence emission to the 400 nm second harmonic pulses used for characterisation of the set-up. Following repeated scans of the delay stage, no detectable signal could be located from the gating of the fluorescence emission from PPO and the resulting spectra only showed background noise (not shown). The downside of using PPO is that it has a fluorescence lifetime 1.4 ns in ethanol.[39] When comparing this to the timescale window observable in the current set up (~1 ns across the entire delay stage), the suitability of PPO as a fluorescent sample to test the system is brought into question. If the high quantum yield of PPO is spread across the entire 1.5 ns, then the upconverted signal will be very low from mixing with a ~100 fs gate pulse.

Unfortunately, due to time constraints, no more time could be spent on trying to achieve collection and gating of fluorescence emission from a sample in the upconversion system. Initially the reasons for the lack of detectable signal were thought to either be due to the way in which the fluorescence was collected and focussed onto the crystal (using refractive optics) or due to the low peak pulse energies of the laser system (due to the high rep-rate), resulting in a very low signal-to-noise ratio. As the upconversion system was later made functional, further discussion of the solution to the issues will be covered in Section 7.5, in which the subsequent development of the system is discussed and the ability for the fluorescence upconversion system to measure ultrafast fluorescence lifetimes is demonstrated.

Since an upconverted signal could be generated via cross-correlation of laser pulses, the decision was made to postpone the use of a fluorescent sample and proceed with the development of the system to enable broadband detection using a transient grating-based gating technique.

7.4. Transient Grating Photoluminescence Spectroscopy

7.4.1. Experimental Set-up

Figure 7.9 shows the experimental set-up used for TGPS constructed by this author, while a side view and a top view of the optics used for gating of the signal are shown in Figure 7.10.

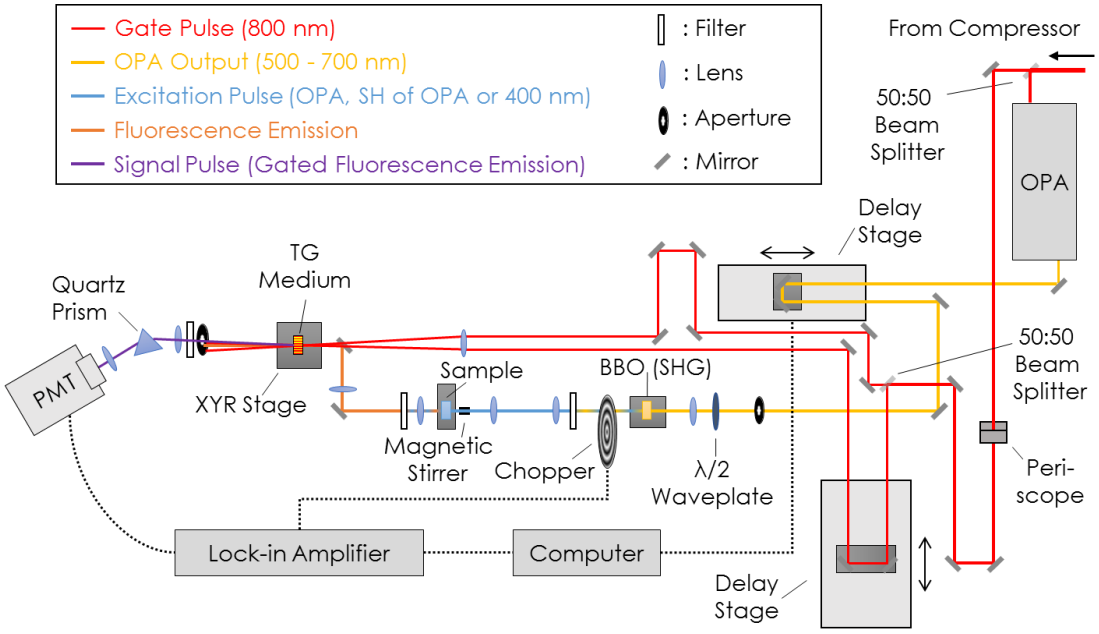

Figure 7.9: Schematic of the system used for TGPS showing the gate pulses (red), OPA output (yellow), excitation pulse (blue), fluorescence emission (orange) and the signal pulse (purple).

In this set-up, the output from the compressor is split by a 50:50 beam splitter to direct half of the output to the OPA while the remainder is raised by 25 mm using a periscope arrangement of IR-enhanced mirrors. The raised beam is then split by a second 50:50 beamsplitter to produce the two gating pulses, which eventually recombine at the TG medium (at an angle of 5°) to generate the transient grating. A manually driven optical delay stage (Thorlabs) is used to achieve temporal overlap of the two gating pulses and the position of this delay stage is kept fixed throughout the experiment. A lens is used to focus the two gate beams into the gating medium while also being used to lower the height of the beams to overlap spatially with the focussed fluorescence emission at the TG medium (as shown in Figure 7.10). A boxcar geometry was used for the spatial overlap of the fluorescence emission and gating pulses to ensure spatial separation of the diffracted signal from ungated emission and residual gate beams. Excitation pulses were generated as described for the upconversion experiment, using an OPA for visible range pulses (500 – 700 nm) or an OPA and a BBO crystal for UV region pulses (250 nm – 350 nm). A variable optical delay line (Newport, UTS150PP with ESP 300 controller) was placed in the beam path of the excitation pulse and a λ/2 waveplate was used to control the polarisation of the OPA output to match that of the gate pulses. After being filtered to remove excess OPA output, the excitation pulses were directed *via*

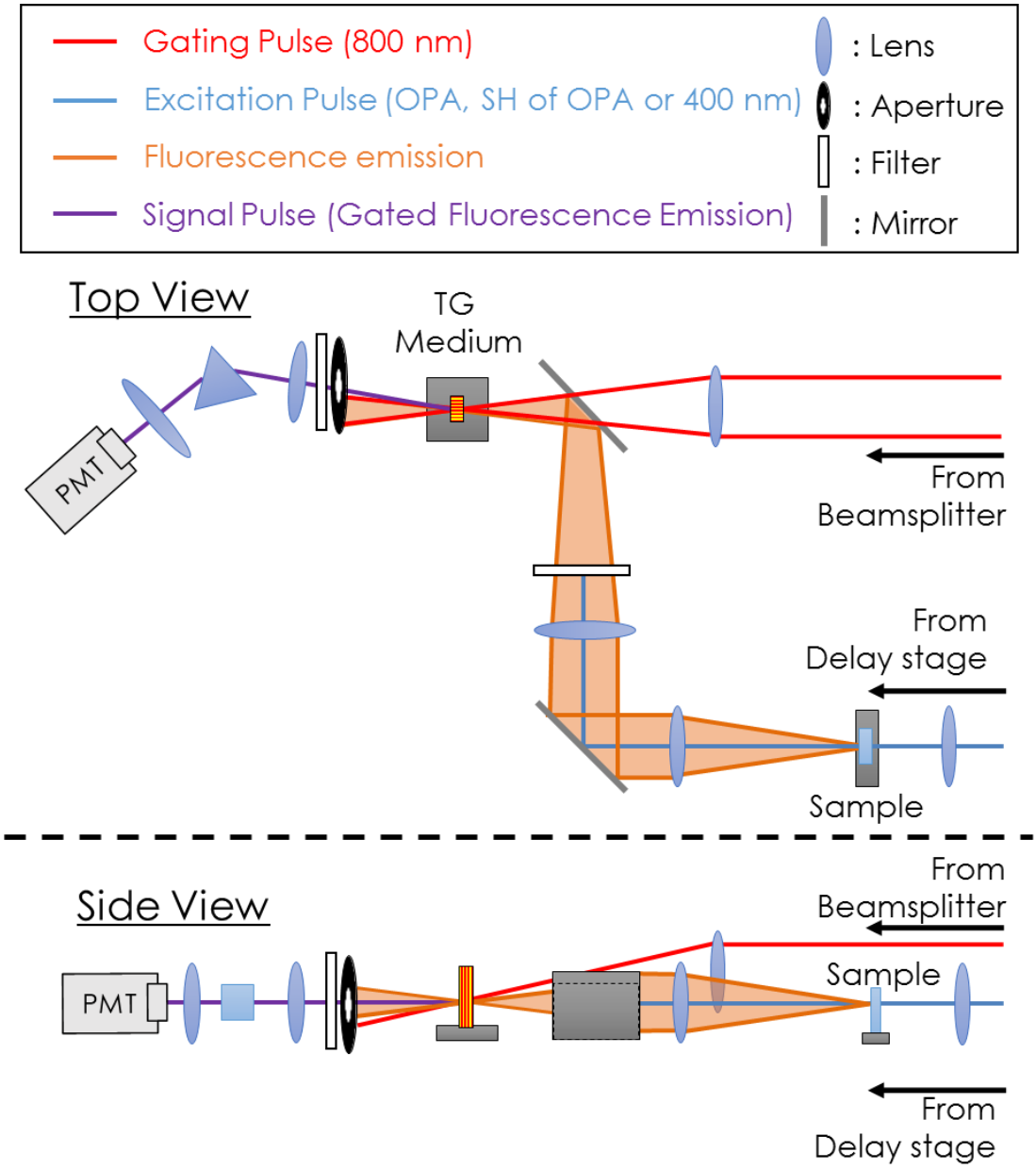

Figure 7.10: Schematic (not to scale) of the transient-grating set up showing the view from above (top) and from the side (below).

a light chopper to focus on the sample, which was held in a 2 mm quartz cuvette. Fluorescence emission from the sample was collected using a lens and passed through a filter to remove excess excitation light. The emission was directed to and focussed into the TG medium to overlap with the gating pulses. Residual gate beams and any ungated fluorescence emission were removed using an aperture and a filter, placed after the TG medium, and a quartz prism was used to redirect the gated signal *via* a focussing lens onto the photomultiplier tube (PMT, 1P28).

The experiment was initially controlled by way of the same in-house written MatLab GUI as was used for the upconversion set-up. Temporal overlap of the two gating pulses with the fluorescence emission at the TG medium was achieved using a combination of fixed and variable optical delay lines. Fixed optical delay lines provided rough adjustment to the time delay of the pulses while the computer-controlled variable optical delay lines enabled the fine adjustment of the arrival time of the pulses.

7.4.2. Characterisation of the System

Characterisation of the TG set up was achieved by measuring the signal obtained from gating a pulse of 400 nm, obtained from the residual second harmonic from an OPA, at different delay positions. For these measurements, removal of the BBO (SHG) crystal and any filters that block light of this wavelength was required and no sample was contained in the sample holder.

For generation of the TG in the grating medium, both gate pulses were required to arrive at the grating medium at the same time. Following measurement of the length of the beam paths taken for each gate pulse, the length of the path was first made roughly equal using a fixed delay line (arrangement of mirrors) and then precise temporal synchronisation of the two gate pulses was achieved using a manual delay stage. An autocorrelation method was used to achieve the temporal overlap of the gate pulses, in which a BBO crystal was placed in the position of the TG medium. By altering the manual delay stage, the observation of a "flash" of light on a white card between the two red (800 nm) beams signified the SHG of 400 nm light and the achievement of temporal overlap of the gate pulses. Control of the delay position was made *via* adjustment of a micrometer by hand and once temporal overlap was achieved, the position of the manual delay stage was kept constant throughout the experiment.

The diversity of the TG set-up constructed was demonstrated using the Type I BBO crystal (previously used for the upconversion system) as the TG medium. In the initial stages of the development of the TG system, the BBO crystal was used to synchronise the gate pulses with the excitation pulses. However, it was also found that, when using the BBO in place of the TG medium, it was simultaneously possible to generate the TG, diffracting the 400 nm excitation pulses, and to generate the sum-frequency of 800 nm and 400 nm pulses as well as from the two 800 nm gate pulses (producing 400 nm second harmonic). Figure 7.11 shows the pattern of the signals observed simultaneously on a white card positioned after the TG medium (a BBO crystal).

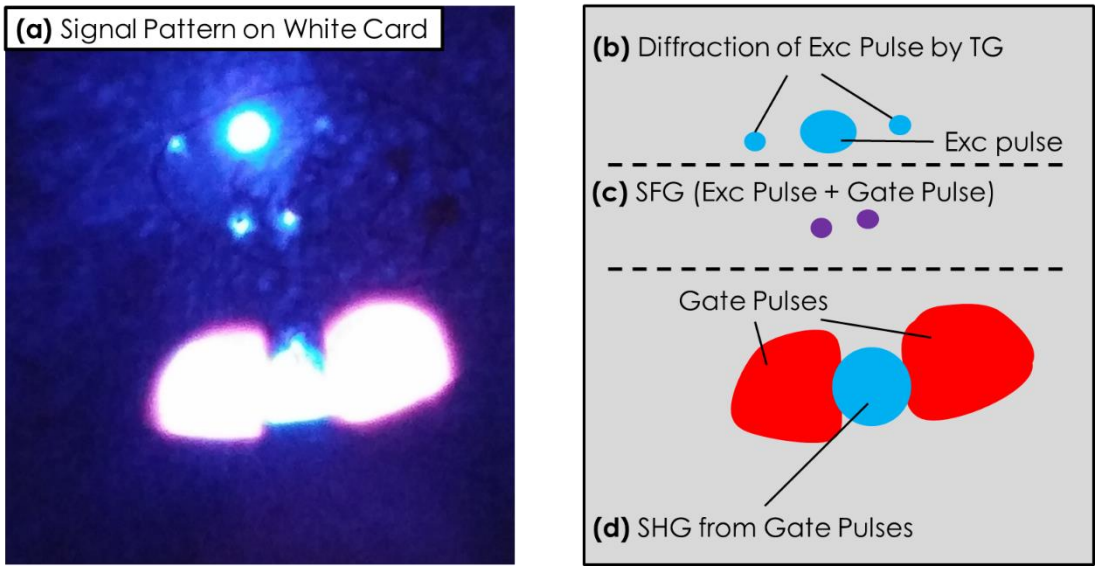

Figure 7.11: Left: (a) Original photo (taken using the camera on a mobile phone (Apple iPhone 4)) of the pattern on a white card placed after the TG medium (a BBO crystal). Right: representation clarifying the patterns observed. (b) diffraction of 400 nm excitation pulse *via* the TG generated from two 800 nm gate pulses in the BBO crystal, (c) sum-frequency generation (of ~266 nm pulses) from mixing excitation (400 nm) and gate (800 nm) pulses, and (d) second harmonic generation (of 400 nm pulses) resulting from the mixing of two 800 nm gate pulses.

Despite the variety of processes present, the presence of the multiple processes observed is not deemed beneficial since these processes will compete for the limited power of each pulse and therefore lower the efficiency of each process. The parameters (such as the angle of the crystal or the overlap of the gate pulses that generate the TG) could be used to determine which process is more favourable. However, the pattern shown in Figure 7.11 was achieved using the second harmonic of the fundamental (400 nm) (i.e. a laser pulse) and it is not clear whether the conditions for gating fluorescence emission from a sample would produce the same outcome of multiple ongoing processes in the crystal. Theoretically, this is a possible outcome but the extremely lower power of the fluorescence emission relative to that of the excitation pulse and the large temporal spread of the fluorescence emission, compared to that of an ultrashort laser pulse, makes this doubtful. It was concluded that, for this reason, use of a BBO crystal is not a suitable choice for the TG medium. On the other hand, the ability for easy conversion of the set-up to a fluorescence upconversion system has been demonstrated (and later exploited).

A variety of other materials were considered and tested for use as the TG medium, and a comparison of the relevant properties of these are shown in Table 7.1.

Medium	Refractive Index at 800 nm	Thickness /mm	Transmission range /nm
BK7 Glass	1.51	1.2	>350
Fused-silica	1.45	1.2	> 200
$SrTiO_3$	2.34	0.3	> 400

Table 7.1: Table of possible media for use in TG experiment and comparison of relevant properties of refractive index, thickness of medium and useable transmission range.

While the transmission range is a very important factor in the selection of the material used as the TG medium, with BK7 glass and fused silica allowing for a greater range of detection (into the near UV range), the refractive index is also of paramount importance. A large refractive index will result in the diffraction of light occurring at a greater angle than for a smaller refractive index. In turn, this will allow for an increased the signal-to-noise ratio, which is highly advantageous in ultrafast fluorescence set-ups such as these. $SrTiO_3$ possesses a markedly higher refractive index than the other two materials considered here for the TG medium and has commonly been used previously as a medium in OK-gate experiments, due to its high non-linearly properties and reasonably low nonlinear response time (~200 fs).[40] Since a TG is formed from the periodic OK effect in a medium from the interference of two laser pulses, the initial characterisation of this set up was chosen to be performed using $SrTiO_3$ as the TG medium. Other TG-media were considered but in light of the time-constraints of this project, no other media were bought or characterised.

Figure 7.12 shows the resulting average of three scans of the signal obtained from the diffraction of a 400 nm laser pulse from the TG formed in $SrTiO_3$ from the interference of two 800 nm gate pulses.

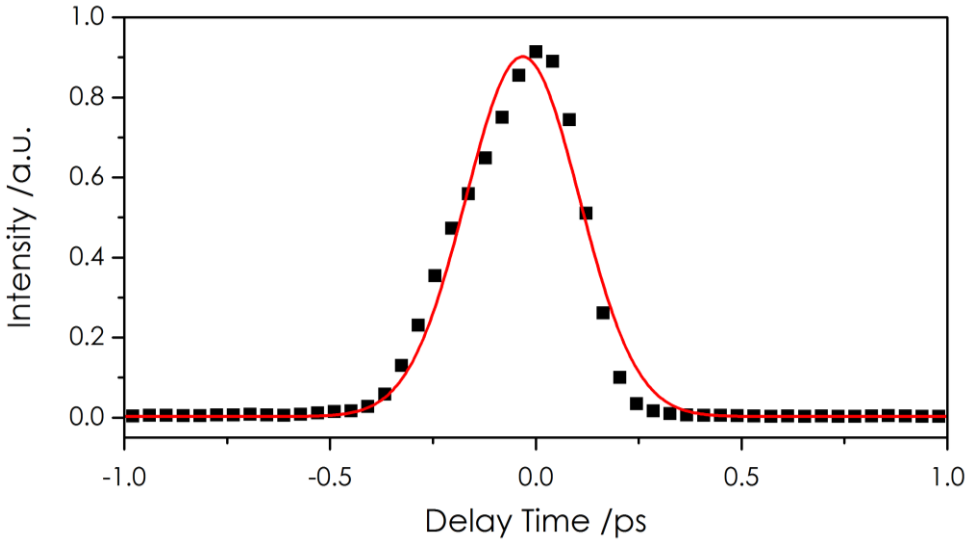

Figure 7.12: Profile of a 400 nm pulse diffracted by a TG generated from two 800 nm gate pulses in $SrTiO_3$. Data is averaged over three scans, using an integration time of 0.3s at each delay position. A Gaussian fit of the data (red line) has a FWHM of 325 fs.

The resulting FWHM of the 400 nm pulse diffracted by the TG is in good agreement with the pulse profile obtained from the upconversion system (shown in Figure 7.8). In Figure 7.12, a slight shoulder is observed on the earlier (negative delay) side of the profile of the pulse. This shoulder suggests that the alignment of the two gate pulses at the time could have been further optimised or is indicative of the non-homogeneity of the beam through all optics (possibly due to damage or dust on a mirror, lens or crystal).

At this stage in the development, the detection of diffracted signal was not wavelength selective, but through use of appropriate short pass filters and apertures, only light of ~400 nm reached the detector (also confirmed by use of an optical-fibre mounted spectrometer (Ocean Optics Maya2000 Pro)).

7.4.2.1. Broadband detection

Characterisation of the broadband detection capabilities of the TG set up were demonstrated by removing the PMT detector and replacing it with an optical-fibre mounted spectrometer (Ocean Optics Maya2000 Pro). The chopper wheel used previously was also removed, as the lock-in amp was not included in the development of broadband detection using a spectrometer (with the idea being to include this again at a later stage). The previously developed Matlab GUI (as used for upconversion experiments) was replaced with another home-written Matlab GUI, which had originally been written for the collection of ultrafast transient absorption spectra.[41,42] The TA GUI was modified by Peng Zeng (The University of Melbourne) to allow it to be used for TG

experiments. The adapted-TA GUI allowed for the collection of spectra across a range of wavelengths (350 nm to 900 nm) simultaneously at each delay position.

Due to not being able to efficiently collect and gate the fluorescence emission from a sample, the decision was made to move on and test the capabilities of the system using pulses of light that could be easily obtained in the current set up. The pulses that were used were the residual second harmonic from the OPA (400 nm), the output from the OPA (tuned to 600 nm), and a "white light" pulse (obtained from the OPA by blocking the second harmonic beam inside the OPA that is normally involved in selection and amplification of the wavelength of the OPA output).

Initially two pulses with narrow spectral bandwidths (400 nm and 600 nm) were used to test the system. The intensity landscape of the signal generated via diffraction of 400 nm pulses, by the TG generated in $SrTiO_3$ from the interaction of two 800 nm gate pulses, is shown in Figure 7.13. Evidence of spatial chirp of the pulse can be seen in the slightly skewed shape of the pulse resulting in a spread of the arrival time of the pulse.

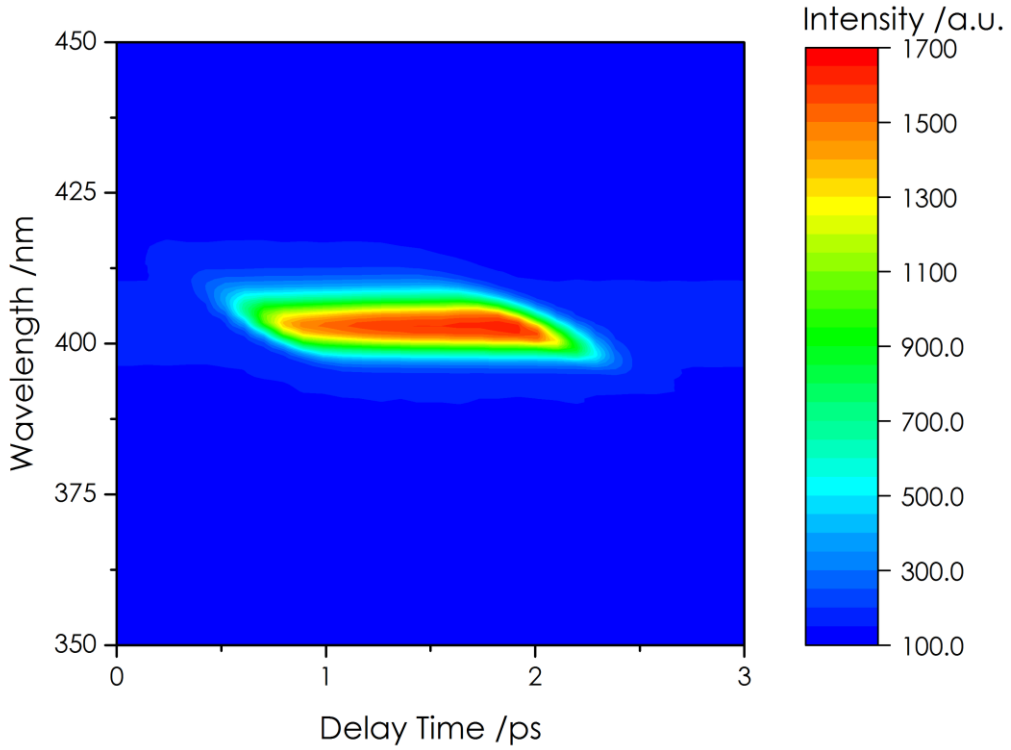

Figure 7.13: 3D landscape plot of the signal generated from diffraction of a 400 nm pulse by a TG generated in $SrTiO_3$ medium.

Figure 7.14 contains two plots extracted from Figure 7.13, showing the maximum values of intensity by wavelength (top) and by delay time (bottom) for the signal generated *via* diffraction of 400 nm pulses. From the extracted spectra, the pulse duration was measured to be ~1.54 ps (FWHM) and the spectral bandwidth was measured to have a FWHM of ~8 nm centred at 402 nm.

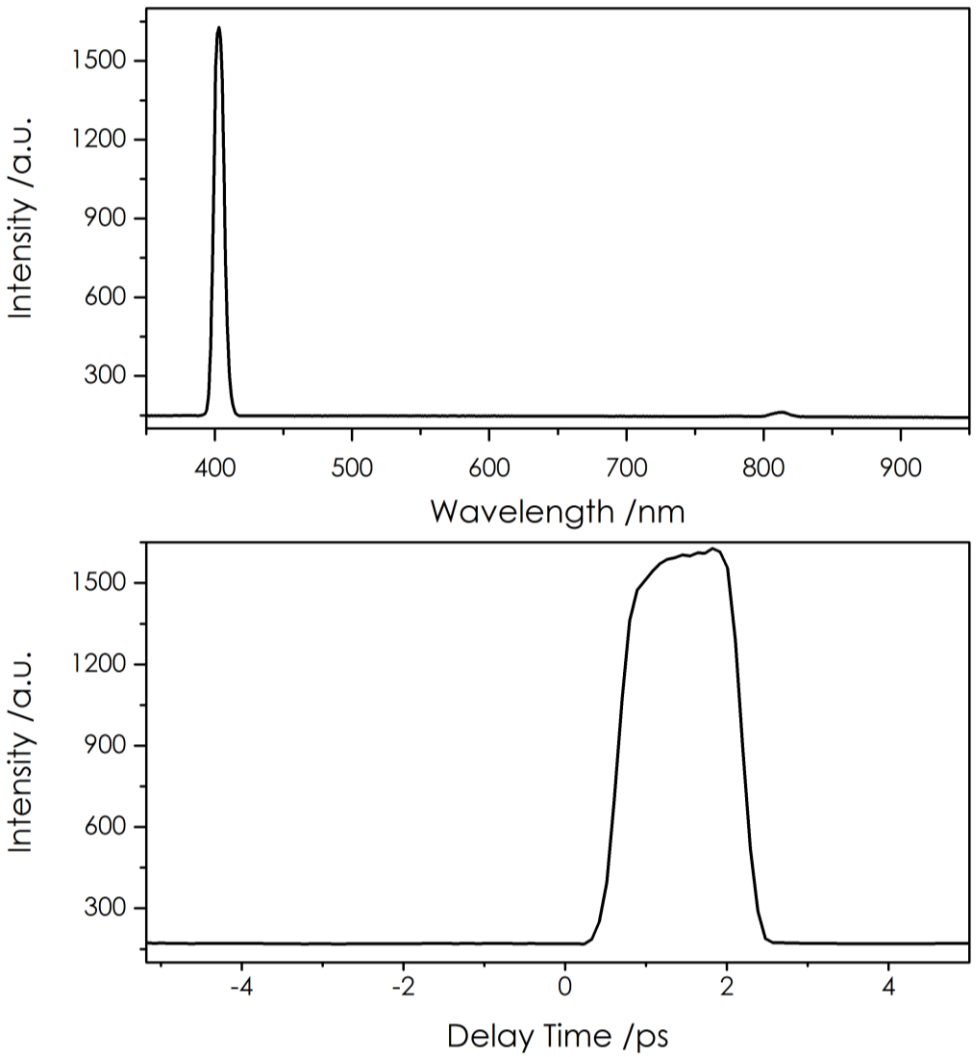

Figure 7.14: Spectra extracted from Figure 7.13. Top: Maximum values of diffracted signal intensity vs wavelength across the entire recorded spectrum range. Bottom: Maximum values of diffracted signal intensity vs delay time.

Evident from Figure 7.14 is that a considerably longer duration of the 400 nm excitation pulse was measured *via* TG than previously measured by fluorescence upconversion (Figure 7.8). This longer pulse duration is most likely a result of the lack of UV-optimised optics present in the set-up, alongside the transmission range of $SrTiO_3$

falling off sharply at wavelengths below 400 nm. As such, it is likely that unfavourable interactions of the 400 nm pulses will occur with the TG medium used here ($SrTiO_3$).

Similar to the diffracted 400 nm signal, Figure 7.15 shows the collected signal resulting from diffraction of 600 nm pulses by a TG generated in $SrTiO_3$ without realignment of the TG medium (although realignment of the beam path was required to optimise and direct the 600 nm beam through the path previously taken by the 400 nm beam).

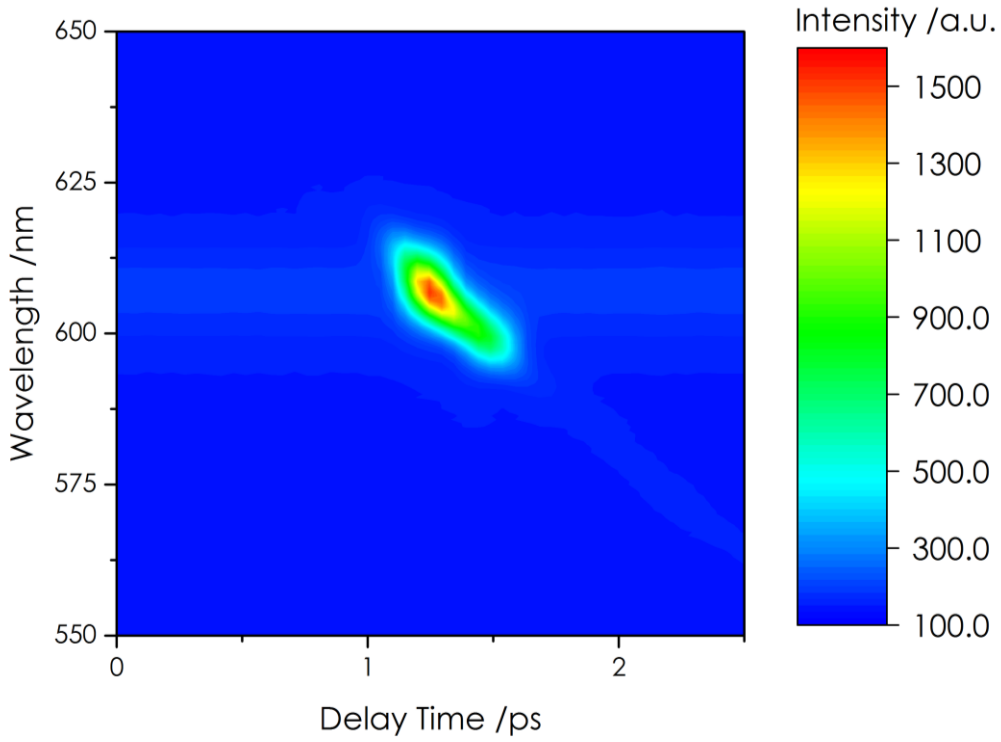

Figure 7.15: 3D landscape plot of the signal generated from a 600 nm pulse diffracted by the TG generated in $SrTiO_3$ medium.

The spectra extracted from Figure 7.15 are shown in Figure 7.16 for the maximum intensity values of the diffracted signal by wavelength (top) and by delay time (bottom). By fitting the data obtained with a Gaussian (not shown), the 600 nm pulse was found to have a duration of ~300 fs and a bandwidth of ~13 nm centred at 606 nm. Compared to the 400 nm pulse, the 600 nm pulse (generated from the OPA) has a much shorter duration, but a slightly wider bandwidth. An explanation for the shorter duration of the 600 nm pulse could be that the optics used in the set-up are better optimised for pulses at this longer wavelength (lower frequency) than those at 400 nm, creating less GV dispersion.

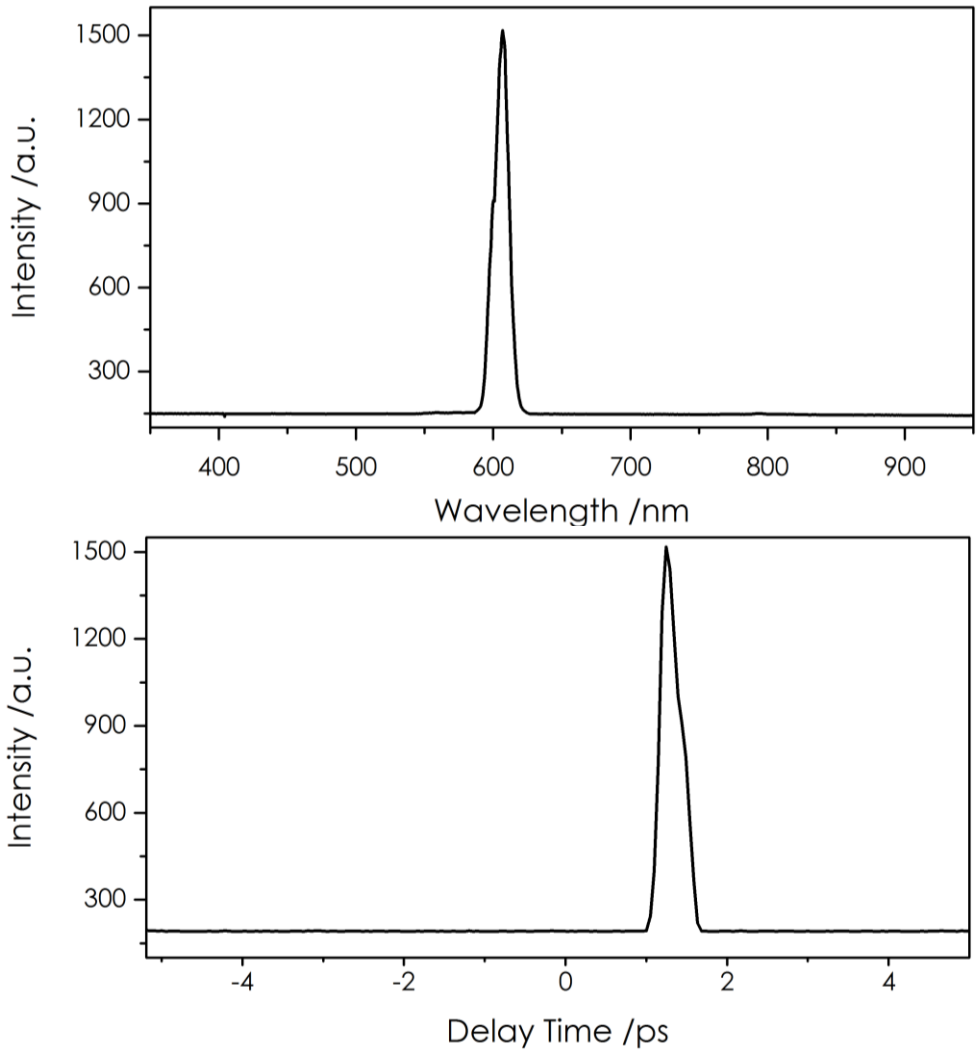

Figure 7.16: Spectra extracted from Figure 7.15. Top: Maximum values of diffracted signal intensity vs wavelength for the entire recorded spectral range. Bottom: Maximum values of diffracted signal intensity vs delay time.

The real test of broadband detection using the generated TG is to diffract and detect polychromatic light without the need for realignment or for repeat measurements. To do this, a pulse of "white light" was obtained from the OPA and was directed down the beam path normally used for excitation pulses.

Figure 7.17 shows the signal generated and collected from gating the white light continuum (generated from within the OPA) using the TG generated in $SrTiO_3$ and Figure 7.18 contains the extracted spectra showing the maximum values of signal intensity by wavelength (top) and by delay time (bottom).

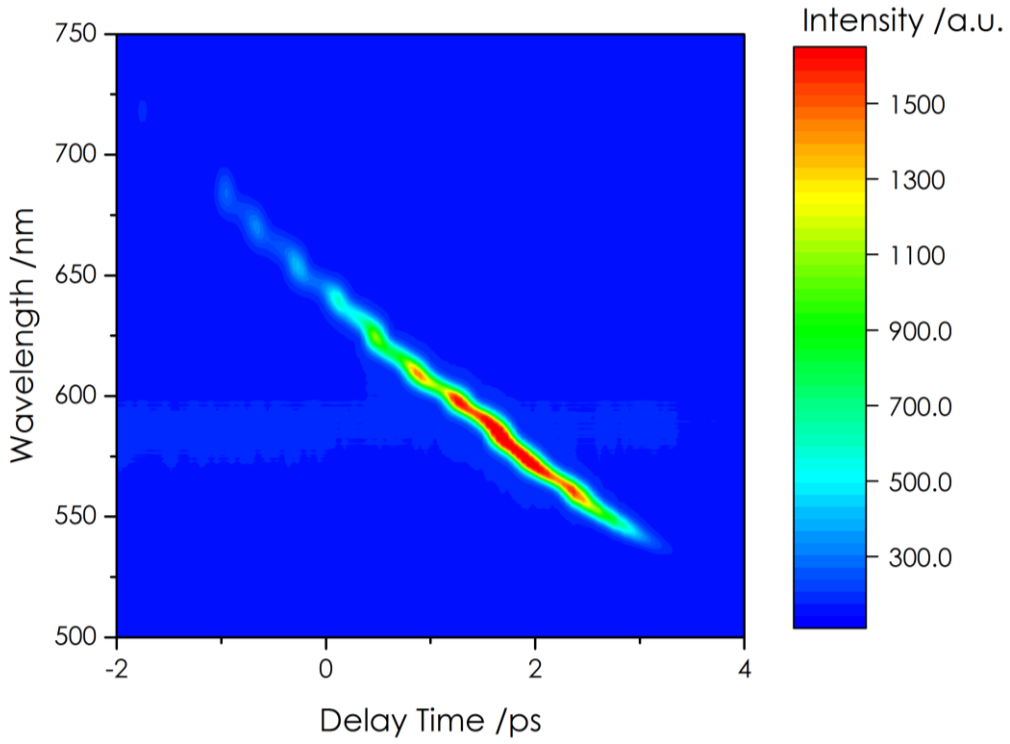

Figure 7.17: Contour landscape plot of the intensity of the signal generated from the diffraction of a white light pulse diffracted by a TG generated in $SrTiO_3$.

The spectral chirp of the white light pulse is readily apparent in Figure 7.17, with light of 550 nm arriving ~3 ps later than that of 650 nm. This factor is expected for such a long wavelength range as is present in the white light pulse and should be accounted for at later stages if broadband detection using TG is to be used for samples with fluorescence emission over a large range of wavelengths. The extracted spectra shown in Figure 7.18 reveal the duration of the white light pulse to be ~2 ps FWHM and with a bandwidth of ~68 nm centred at 586 nm. It should be noted that the white light pulse generated in the OPA is not commonly directed out of the OPA and used in this way. Typically, its function is for the generation and amplification of light at 500 nm – 700 nm within the OPA and only monochromatic light is output from the OPA. As such, the wavelength range demonstrated in Figure 7.18 has not been optimised for the entire wavelength range but was likely previously optimised for the generation of 600 nm output from the OPA (as it can be seen that the intensity at ~600 nm is the most intense).

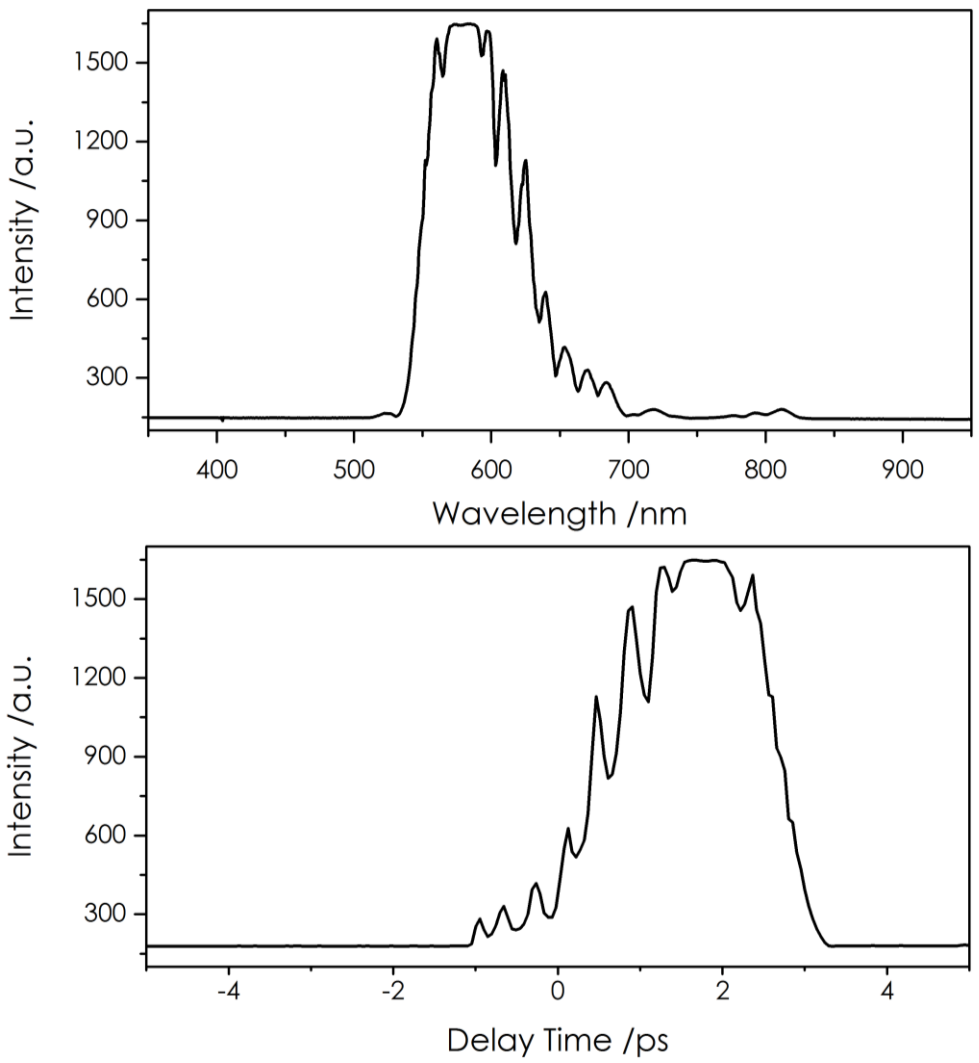

Figure 7.18: Spectra exctracted from Figure 7.17. Top: Maximum values of the diffracted signal intensity vs wavelength. Bottom: Maximum values of the diffracted signal intensity vs delay time.

Following this point in the development of the ultrafast TG system, attempts were once again made to diffract and detect the fluorescence emission from a sample. Unfortunately, these attempts did not meet with success before the time available for this part of this project expired.

7.5. Subsequent Development

Due to time constraints, the work performed by this author to develop the high repetition rate ultrafast fluorescence set-up ended before the complete development of the system was achieved. Despite this, in the time since, further development of the ultrafast set-up was performed and achieved by Peng Zeng (University of Melbourne). In summary, the TG set-up was reverted to use SFG as the gating technique and efficient collection and gating of fluorescence emission from a sample was achieved. This allowed for ultrafast fluorescence decays of laser dyes coumarin 153 and auramine O (in ethanol) (with fluorescence quantum yields of 0.4[43] and 0.03,[44] respectively) to be measured alongside a cross-correlation spectrum of the second harmonic pulse (400 nm) with the gate pulse (800 nm). These data were generously collected and passed on by Zeng and analysis of the data was performed by this author.

Modification of the set-up from TG to upconversion was easily achieved by substituting the TG medium for the previously used BBO (SFG) crystal and by removing the beamsplitter that was used to create the two gate pulses in the TG set-up. Minor adjustments of other components were also made to optimise the alignment of the pulses. Since the upconverted signal is wavelength specific (due to the requirement of angle-tuning the crystal in order to minimise phase-mismatch), the detection system was reverted to a PMT with a lock-in amplifier. A monochromator (Jobin Yvon, H10) was also embedded in the path of the upconverted signal before the PMT in order to enhance selection of the detection wavelength over any scattered light or background signals present. The experimental set-up of this fluorescence upconversion system is shown in Figure 7.19.

In a comparison with the layout of the previously built upconversion set-up (shown in Figure 7.7), elements that were introduced for the TG set-up remain. For example, the redirection of the fluorescence emission following collection by a lens, the paths of the beams (gate, excitation and fluorescence emission), and the presence of the optical delay stage in path of the excitation beam are consistent.

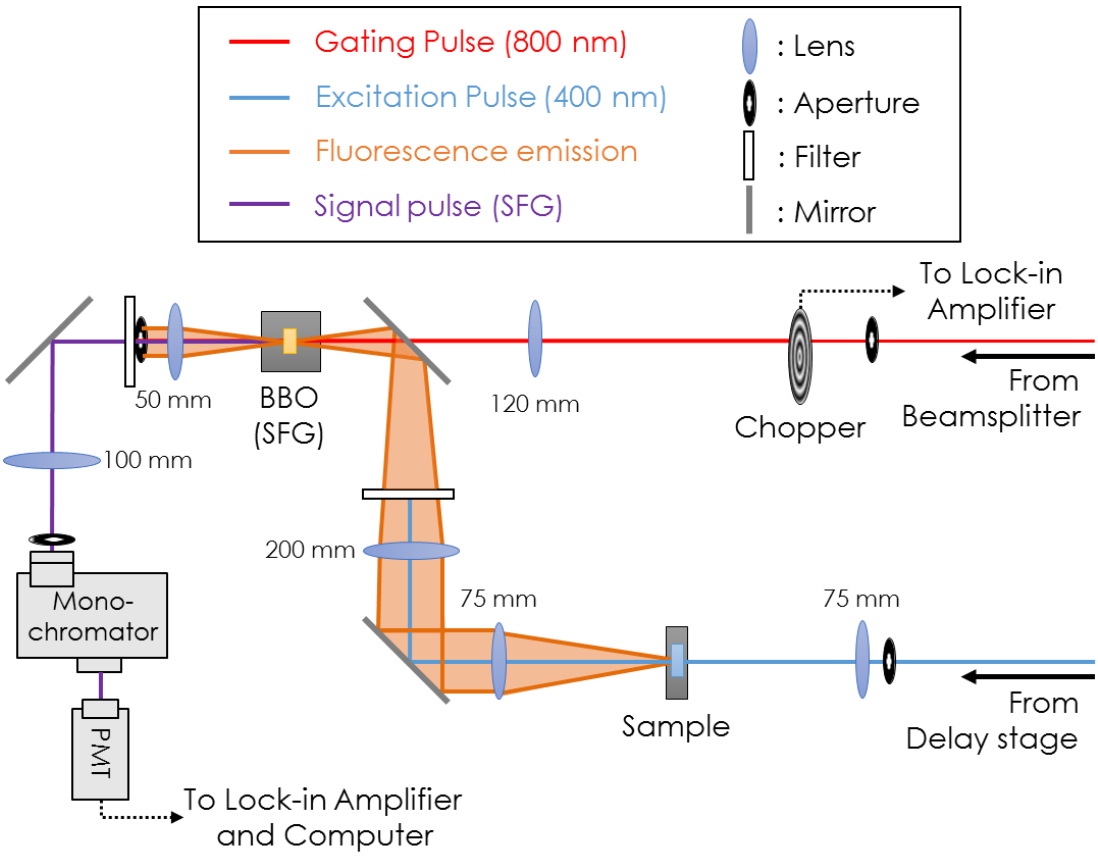

Figure 7.19: Experimental set up of the upconversion system following adaptation from the TG set-up. In this layout, the amplifier fundamental output (800 nm) is used as the gating pulse and the excitation pulse is the residual second harmonic (400 nm) from the OPA. The optical variable delay line (delay stage) (not shown) is embedded in the path of the excitation pulse.

In the time between the development of the TG system and this newer upconversion system, the femtosecond pulsed laser used to drive the set-ups was realigned to generate pulses that were more homogeneous. This is thought to have played a large role in allowing the upconversion system to function well enough to gate fluorescence emission from a sample. Another component that was altered was the lens used to collect the fluorescence emission. In the newer upconversion set-up, this lens now has a longer focal length (75 mm) compared to the previously used lens (25 mm focal length).

The functionality of the upconversion system has initially been demonstrated and is shown in Figure 7.20, in which the cross-correlation of the 400 nm pulse with the gate pulse, and the signals obtained from the sum-frequency mixing of the emission from coumarin 153 and auramine O (both in ethanol) with the 800 nm gate pulse are shown.

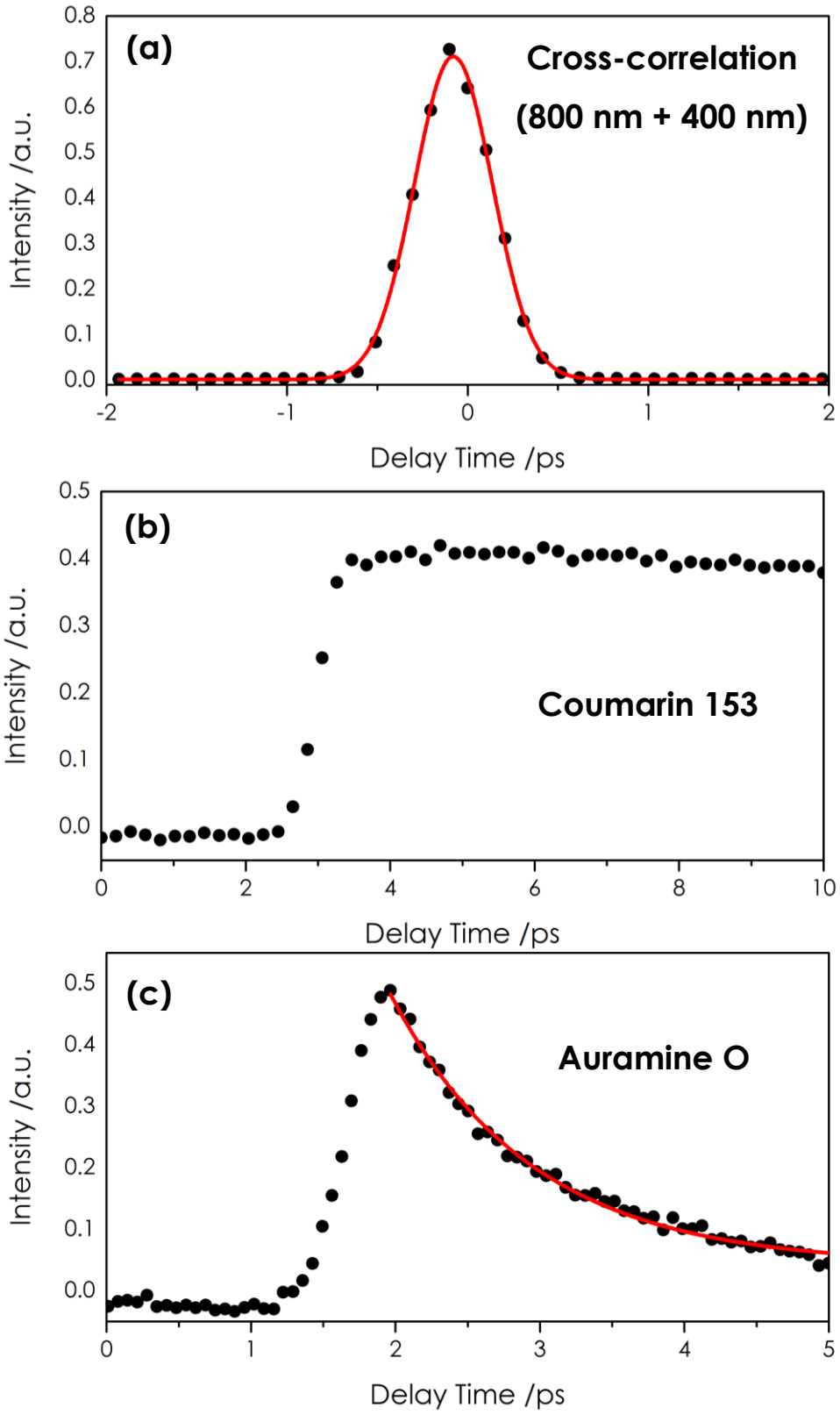

Figure 7.20: Upconverted signals generated via SFG in a Type I BBO crystal using an 800nm gate pulse. All data sets were recorded using a 1 s integration time and were averaged over 3 scans. Data sets (black circles) were fit using Origin software (red line). (a) Cross-correlation of the gate pulse and excitation pulse (400 nm) (FWHM ~500 fs). (b) and (c) coumarin 153 and auramine O, respectively, in ethanol. Excitation and emission wavelengths were 400 nm, and 500 nm, respectively.

From the cross-correlation spectra shown in Figure 7.20(a), the FWHM of the Gaussian fit of the data was found to be ~500 fs. Compared to estimates of the pulse width in this work (~300 fs), the pulse duration was measured to be slightly longer but is within expectations. Further optimisation of this system is still required, and is in progress.

The decay of the upconverted signal obtained from auramine O, gated by 800 nm pulses and averaged over 3 scans, has been fit with a single exponential (using Origin software) of ~980 fs (± 40 fs), with the rising edge of the upconverted signal of ~245 fs (± 20 fs) (fit not shown). These fits of auramine were performed without reconvolution and so are tail-fits of the data, as shown in Figure 7.20. The initial estimate of the lifetime of the fluorescence decay measured here for auramine O in ethanol is comparable with that found in the literature: ~1 ps in aqueous solvent[45] and an average lifetime of 1.5 ps in ethanol.[46]

While a fit of the rising edge of the upconverted signal of coumarin 153 gave a lifetime of ~370 fs (±40 fs) (comparable to the pulse width of the excitation pulse), a satisfactory fit of the decay curve could not be achieved. The reported lifetime of coumarin 153 in the literature is 4.68 ns,[47] which is significantly greater than the 1 ns window that is experimentally observable in the current set up, thus demonstrating the limitation of the ultrafast fluorescence technique described here.

However, although the initial results contain a high level of uncertainty, the upconversion system shows a good level of signal-to-noise ratio. This is an important factor in any technique and has been demonstrated here in the measurement of the fluorescence decay of auramine O, which only has a quantum yield of 0.03 and the ratio could be greater enhanced through averaging of a higher number of collected spectra. It is clear however, that further optimisation of the system is required before measurements that are more precise can be obtained.

7.6. Conclusions

This chapter has presented the development of an ultrafast fluorescence-based technique that will one day allow for the measurement of ultrafast photophysical processes in biomolecules using a high repetition rate (100 kHz) regenaratively amplified/OPA system to provide pulses with moderate energies. The employment of such a laser system is ideal for the study of biological systems, which are highly susceptible to damage from high pulse energies, particularly in the UV region.

For the initially constructed fluorescence upconversion set-up, characterisation of the apparatus was achieved from a cross-correlation between the gate pulse and the excitation pulse, providing an initial demonstration of the capabilities of the system. A resolution of ~150 fs was estimated from the HWHM of the cross-correlation spectra recorded, which could possibly be further reduced upon additional optimisation of the system and using a deconvolution method for fitting of the data. Unfortunately, the capabilities of the system could not be determined in relation to the ultrafast gating of fluorescence emission from a sample at that stage in the development. In hindsight, it is believed that this was due to in efficient collection of the fluorescence emission partly due to the non-optimised refractive optics used and due to a degree of inhomogeneity in the laser pulses used.

In order to enable broadband detection, the set-up was modified to use a TG generated in a medium ($SrTiO_3$) to gate the signal. Initial characterisation of the system was carried out in a similar way to that performed for the upconversion set-up, with estimates of the resolution achievable in good agreement to before. Broadband detection capabilities were ultimately demonstrated through the diffraction of 'white light' laser pulses that had been obtained from the OPA, with a detection range of approximately 500 – 700 nm demonstrated. An abundance of ways exist in which the TGPS set-up could be further developed. The main component in this set-up is the TG medium, in which the transient grating is generated. Only a small selection of the possible media have been explored. One such medium under consideration for future direction of this set-up is yttrium aluminium garnet (YAG) which, although typically used in pump lasers in the form of a Nd-doped crystal, has recently shown promise for use in femtosecond spectroscopy in the generation of a white light continuum.[48] YAG has a refractive index of ~1.82 (at 800 nm) and has a transmission range of 0.21 to 5.5 μm, making it a suitable alternative to the $SrTiO_3$ used here. Use of YAG as the TG medium would enable the

broadband detection to extend into the UV region, a requirement for the study of biomolecules.

In the current state of the set-up, at the time of writing this thesis and following the subsequent development covered in Section 7.5, the system has been reverted to use fluorescence upconversion as the gating technique and fluorescence emission decays have been recorded, providing an initial demonstration of the capability of the system. While the fluorescence upconversion does not allow for simple broadband detection (as angle-tuning of the sum-frequency crystal is required to meet phase-matching conditions), the gating of fluorescence emission from a sample has now been demonstrated. The resulting decay curves presented here following the excitation of coumarin 153 and auramine O by pulses of 400 nm only provide an initial demonstration of the capabilities of the system and there is a wealth of possible ways to further enhance and optimise the system. It should be noted that the current upconversion set-up has not been optimised for detection in the UV, and thus would require optimisation of the optics and detector to enable this. This author firmly believes that since efficient collection of fluorescence emission from a sample has now been demonstrated, modification of the gating technique to a TG-based method would be a more simplistic way to enable broadband detection than the computer-driven rotational stages employed by Cannizzo *et al.*[1]

Overall, the set-up developed shows great promise for measurements of ultrafast fluorescence decays in the future, with the hope of one day using this set-up to measure the ultrafast fluorescence decay of 2AP in DNA not measurable by the TCSPC system utilised previously in this thesis.

7.7. References

1 A. Cannizzo, O. C. Bräm, G. Zgrablic, A. Tortschanoff, A. A. Oskouei, F. van Mourik and M. Chergui, *Opt. Lett.*, 2007, **32**, 3555–3557.

2 J. Xu and J. R. Knutson, in *Methods in enzymology*, Elsevier Inc., 1st edn., 2008, vol. 450, pp. 159–183.

3 H. R. Schanz, PhD Thesis, Humbolt University of Berlin, 2002.

4 J. Shah, *IEEE J. Quantum Electron.*, 1988, **24**, 276–288.

5 K. Chen, J. K. Gallaher, A. J. Barker and J. M. Hodgkiss, *J. Phys. Chem. Lett.*, 2014, **5**, 1732–1737.

6 S. Haacke, R. a. Taylor, I. Bar-Joseph, M. J. S. P. Brasil, M. Hartig and B. Deveaud, *J. Opt. Soc. Am. B*, 1998, **15**, 1410–1417.

7 H. Mahr and M. D. Hirsch, *Opt. Commun.*, 1975, **13**, 96–99.

8 O. Bräm, A. Cannizzo, A. A. Oskouei, A. Tortschanoff, F. van Mourik and M. Chergui, in *Ultrafast Phenomena XVI*, Springer Berlin Heidelberg, 2009, pp. 346–348.

9 J. R. Lakowicz, in *Principles of Fluorescence Spectroscopy*, Springer US, Boston, MA, 1999, pp. 95–140.

10 W. Becker, *Advanced Time-Correlated Single Photon Counting Techniques*, Springer Berlin Heidelberg, Berlin, Heidelberg, 2005, vol. 81.

11 P. Manoj, C. K. Min, C. T. Aravindakumar and T. Joo, *Chem. Phys.*, 2008, **352**, 333–338.

12 H.-N. Nguyen, L. Zhao, C. W. Gray, D. M. Gray and T. Xia, *Biochemistry*, 2011, **50**, 8989–9001.

13 T. Fiebig, C. Wan and A. H. Zewail, *Chemphyschem*, 2002, **3**, 781–788.

14 J. Godet, N. Ramalanjaona, K. K. Sharma, L. Richert, H. de Rocquigny, J.-L. Darlix, G. Duportail and Y. Mely, *Nucleic Acids Res.*, 2011, **39**, 6633–6645.

15 T. Gelot, P. Tourón-Touceda, O. Crégut, J. Léonard and S. Haacke, *J. Phys. Chem. A*, 2012, **116**, 2819–2825.

16 A. Christ, PhD Thesis, University of Paderborn, 2013.

17 P. T. Touceda, T. Gelot, O. Crégut, J. Léonard and S. Haacke, *Tech. Dig. OSA 2012*, 2012, 6–7.

18 D. Eimerl, *Ferroelectrics*, 1987, **72**, 95–139.

19 G. Ghosh, *J. Appl. Phys.*, 1995, **78**, 6752–6760.

20 P. Bartolini, M. Vilfan, I. Drevenšek Olenik, M. Čopič, R. Eramo, Y.-L. Li, C. Manzo, L.

Marucci, R. J. D. Miller, C. J. Milne, D. Paparo and A. Taschin, *Time-Resolved Spectroscopy in Complex Liquids*, Springer US, Boston, MA, 2008.

21 M. Sajadi, M. Quick and N. P. Ernsting, *Appl. Phys. Lett.*, 2013, **103**, 83–86.

22 X. X. Zhang, C. Würth, L. Zhao, U. Resch-Genger, N. P. Ernsting and M. Sajadi, *Rev. Sci. Instrum.*, 2011, **82**, 63108-1–63108-8.

23 T. Gustavsson, A. Sharonov, D. Onidas and D. Markovitsi, *Chem. Phys. Lett.*, 2002, **356**, 49–54.

24 A. Banyasz, T. Gustavsson, D. Onidas, P. Changenet-Barret, D. Markovitsi and R. Improta, *Chem. - A Eur. J.*, 2013, **19**, 3762–3774.

25 M. A. Duguay and J. W. Hansen, *Appl. Phys. Lett.*, 1968, **13**, 178–180.

26 B. Schmidt, S. Laimgruber and P. Gilch, in *2003 European Quantum Electronics Conference. EQEC 2003 (IEEE Cat No.03TH8665)*, IEEE, 2003, vol. 814, p. 177.

27 S. Arzhantsev and M. Maroncelli, *Appl. Spectrosc.*, 2005, **59**, 206–220.

28 K. Appavoo and M. Y. Sfeir, *Rev. Sci. Instrum.*, 2014, **85**, 55114-1–55114-14.

29 J. M. Hollas, *Modern spectroscopy*, John Wiley & Sons, Fourth Edi., 2004.

30 H. J. Eichler, P. Günter and D. W. Pohl, *Laser-induced dynamic gratings*, 1986.

31 M. Li, J. P. Nibarger, C. Guo and G. N. Gibson, *Appl. Opt.*, 1999, **38**, 5250–5253.

32 J. N. Sweetser, D. N. Fittinghoff and R. Trebino, *Opt. Lett.*, 1997, **22**, 519–521.

33 R. Trebino, *Frequency-Resolved Optical Gating: The Measurement of Ultrashort Laser Pulses*, Springer US, Boston, MA, 2000.

34 J. K. Gallaher, K. Chen, G. S. Huff, S. K. K. Prasad, K. C. Gordon and J. M. Hodgkiss, *J. Phys. Chem. Lett.*, 2016, **7**, 3307–3312.

35 S. Lukman, A. J. Musser, K. Chen, S. Athanasopoulos, C. K. Yong, Z. Zeng, Q. Ye, C. Chi, J. M. Hodgkiss, J. Wu, R. H. Friend and N. C. Greenham, *Adv. Funct. Mater.*, 2015, **25**, 5452–5461.

36 J. E. A. Webb, K. Chen, S. K. K. Prasad, J. P. Wojciechowski, A. Falber, P. Thordarson and J. M. Hodgkiss, *Phys. Chem. Chem. Phys.*, 2016, **18**, 1712–1719.

37 P. Bak, C. Tang and K. Wiesenfeld, *Phys. Rev. Lett.*, 1987, **59**, 381–384.

38 J. R. Small, J. J. Hutchings and E. W. Small, in *Proc. SPIE*, ed. E. R. Menzel, 1989, 26–35.

39 J. Léonard, T. Gelot, K. Torgasin and S. Haacke, *J. Phys. Conf. Ser.*, 2011, **277**, 12017-1–12017-5.

40 L.-H. Yan, S. Jia, J.-H. Si, S. Matsuo, F. Chen and X. Hou, *Chinese Phys. Lett.*, 2012, **29**, 74207-1–74207-4.

41 B. E. Robotham, PhD Thesis, University of Melbourne, 2013.

42 S. K. Sugunan, B. Robotham, R. P. Sloan, J. Szmytkowski, K. P. Ghiggino, M. F. Paige and R. P. Steer, *J. Phys. Chem. A*, 2011, **115**, 12217–12227.

43 K. H. Drexhage, *J. Res. Natl. Bur. Stand. Sect. A Phys. Chem.*, 1976, **80A**, 421–428.

44 P. Gautam and A. Harriman, *J. Chem. Soc. Faraday Trans.*, 1994, **90**, 697–701.

45 N. H. Mudliar, B. Sadhu, A. M. Pettiwala and P. K. Singh, *J. Phys. Chem. B*, 2016, **120**, 10496–10507.

46 M. J. van der Meer, H. Zhang and M. Glasbeek, *J. Chem. Phys.*, 2000, **112**, 2878–2887.

47 M. Maroncelli and G. R. Fleming, *J. Chem. Phys.*, 1987, **86**, 6221–6239.

48 M. Bradler, P. Baum and E. Riedle, *Appl. Phys. B Lasers Opt.*, 2009, **97**, 561–574.

Chapter 8: Conclusions

The overall goal of the work presented in this thesis has been to use 2-aminopurine as a fluorescent probe of DNA, thus enabling the use of fluorescence-based techniques in the exploration of photophysical processes that occur in DNA molecules, with an emphasis on the integral role played by base dynamics in these processes. This chapter summarises the most significant findings and provides suggestions towards the possible future direction of this work.

The fluorescence decay parameters measured for 2AP-containing oligonucleotides and 2AP-containing dinucleotides in a frozen glassy matrix at 77 K, were compared with those measured in fluid solutions at room temperature and the effect of base dynamics on interbase quenching of 2AP fluorescence has been explored. The decay parameters obtained from 2AP-containing oligonucleotides have allowed for the interbase interactions of 2AP with all nearby bases to be examined and are in good agreement with results previously reported by Neely and Jones.[1] Whereas the decay parameters for oligonucleotides in room-temperature solutions characteristically require four lifetime components for an adequate description, those of the same oligonucleotides frozen at 77 K only require three components, with the elimination of the shortest decay component, τ_1. This confirms that base dynamics are required for rapid interbase quenching of 2AP fluorescence via charge transfer. In cases where no G base is present in close proximity to 2AP, further elimination of τ_2 occurs and, as such, only two components are required to describe the fluorescence decay. The predominant decay time of the longest component, τ_4, is characteristic of unquenched 2AP. The persistence of τ_3 in all cases demonstrates the presence of quenching mechanisms on the nanosecond timescale that do not rely on base dynamics. This contradicts the three-state model presented by Somsen *et al.*,[2] in which τ_3 was attributed to some thermally activated conformational change. As a repercussion of the elimination of τ_1 and τ_2 at 77 K, there are two possible scenarios explaining this observation. The first scenario is that the short decay components relate to the excitation of equilibrium ground-state structures that require geometric relaxation on the excited-state potential energy surface for rapid charge-transfer to occur. The second scenario is that these short decay components relate to ground-state conformations that are non-equilibrium states and that conformational motions are required in order to access these conformations. As such, the investigation

of these two possible scenarios is an area for future study. A substantial difference is observed between the values of fluorescence quantum yields determined from decay parameters and those determined from steady-state intensities and this is indicative of the presence of dark (non-emitting) states. In turn, this means that a significant fraction (~50%) of the conformational population is not observed via fluorescence detection using TCSPC. For observation and measurement of these dark states, ultrafast fluorescence techniques are required to access the femtosecond timescale on which it is likely that these decay processes occur.

The mechanism of interbase electronic energy transfer in 2AP-containing dinucleotides has been investigated through a combination of steady-state and time-resolved fluorescence measurements and has provided insight into the nature of the conformational states of DNA bases involved in energy transfer, a level of insight which has not been possible from steady-state fluorescence measurements alone. While steady-state fluorescence measurements have been used for the quantitative determination of energy transfer efficiencies (by Nordlund *et al*,[3] for example) , the work presented in this thesis has shown that the measured efficiencies greatly underestimate the true transfer efficiencies, as a consequence of assuming that the fluorescence quantum yield of 2AP in oligonucleotides is independent of the excitation pathway. If this were true, then energy transfer would homogeneously excite all conformational states of 2AP in the dinucleotides. However, time-resolved fluorescence measurements enabled the determination of decay parameters that solely result from the population of species via energy transfer and provided direct evidence that energy transfer preferentially excites 2AP in highly stacked conformations of DNA bases, resulting in a lower quantum yield than for direct excitation. Energy transfer efficiencies determined directly from decay parameters and those calculated from steady-state fluorescence measurements, which have been corrected for the difference in fluorescence quantum yields, were in good agreement. It was found that, at room temperature, energy transfer with the highest efficiency, around 25%, occurs from A, with efficiencies of around 10% from the other bases. This supported the conclusion from Nordlund's[3] work that A is the most efficient donor, but showed that the transfer efficiencies estimated by Nordlund *et al.* for the other bases were greatly underestimated. In the future, time-resolved studies should be extended to 2AP-containing single-stranded oligonucleotides, such as those studied previously by Nordlund *et al.*, in order to determine the correct energy transfer efficiencies. Further extension of the time-resolved studies to energy transfer in duplexes would be a logical next step, to determine the effect of base-pairing on the

mechanism of energy transfer, as formation of the duplex is known to promote base-stacking interactions and DNA is more commonly found as a duplex *in vivo*. Initially, however, the next step should be to perform studies on 2AP-containing trinucleotides, thus building upon the simple system of the dinucleotides from a bottom-up approach. As discussed previously for inter-base electron transfer in DNA, the study of inter-base electronic energy transfer in DNA would greatly benefit from the employment of ultrafast fluorescence measurements, allowing for the determination of the extent of involvement of dark states and permit the detection of a rise-time on the 2AP fluorescence decay curve.

The suitability of 2AP as a sensitive probe of DNA-enzyme interactions has been exploited in a study of the Mos1 strand transfer complex (STC), and has built upon the averaged, static representation of the STC obtained from its crystal structure, to elucidate the dynamics of the complex and the importance of specific amino acid residues in the interaction of the Mos1 enzyme with its target.[4] Through incorporation of a 2AP base at key locations in the DNA sequence, the occurrence of dynamic base-flipping of a specific adenine nucleotide (A_1) in the DNA target sequence of the Mos1 STC was identified. Since the Mos1 STC complex is composed of a transposase homodimer bound to two DNA duplexes (mimicking the ends of the transposon), in the studies presented, formation of the complex results in the presence of two 2AP bases per complex. This brings into question whether the base-flipping observed at positions A_1 in each duplex occurs simultaneously or sequentially. The measured decay parameters relate to an averaging of the conformations present and it is not possible to resolve the cooperativity of the dynamics involved (if any). If future studies were able to incorporate only one 2AP-containing duplex into the complex (with the possibility of incorporating a second suitably distinct fluorescent probe into the other duplex), further insight into the mechanism involved in the Mos1 STC could be obtained. The interactions of key residues of the Mos1 transposase with the target site DNA were explored through site-selective mutation of these residues. The decay parameters for 2AP located at the target site in the mutated Mos1 STCs, showed no major differences compared to those for the wild-type STC. However, the presence of minor differences in the decay parameters are indicative of an indirect interaction that affects the stability of the distorted base conformation and are consistent with the interaction of the key residues with the DNA backbone, as observed in the crystal structure. Time-resolved fluorescence measurements were performed for complexes in which only one key residue had been mutated. If, however, the interactions that stabilise the DNA distortion are complex and involve multiple key

residues, this will not have been reflected in the studies performed and is an area for future investigation.

Progress towards the development of an ultrafast fluorescence technique that is suited to the study of biological molecules has been presented. Although completion of the set-up was not achieved due to time-constraints and technical issues experienced, development is continuing at the University of Melbourne and shows great promise for the future. The laser system employed utilises a high repetition rate (100 kHz) regeneratively amplified/OPA system to provide pulse energies with moderate energies. These conditions are advantageous for the study of biomolecules, which may be damaged by the use of high pulse energies or suffer from degradation during lengthy signal collection times inherent to laser systems with low pulse energies and repetition rates in the MHz range. An initial demonstration of the gating capabilities of the set-up was achieved using fluorescence upconversion as the gating technique, obtaining signals from cross-correlations between gate pulses (800 nm) and laser pulses (400 nm). Subsequently, the set-up was modified to enable broadband detection through use of a transient-grating-based gating technique. The true broadband capabilities have been demonstrated through the diffraction of pulses of a white light continuum (ranging from 500 – 700 nm) using a transient grating generated in $SrTiO_3$. Extension of the broadband detection range into the UV region need only require optimisation of the optics and for the selection of a suitable TG medium. One such medium is yttrium aluminium garnet (YAG) which has appropriate optical properties and a suitable transmission range of 0.21 to 5.5 μm. Subsequent development of the system, following the exodus of this author, has occurred and efficient collection of fluorescence emission from a sample has been achieved, such that measurement of ultrafast fluorescence decays is now possible and has been demonstrated. This set-up shows great promise for its future use in the measurement of ultrafast fluorescence decays of biomolecules, with a hope that the dark states of 2AP in DNA, as discussed previously in this thesis, will one day be detected and measured in this system.

Overall, the work presented here has provided valuable insight into photophysical processes occurring in DNA and it is clear that conformational dynamics play an essential part in these processes and in the functionality of DNA. A detailed understanding of the full extent of the influence of base dynamics on the structure, stability and biological function of DNA is yet to be achieved and remains a thoroughly fascinating area of study with many possible avenues still to be explored.

8.1. References

1 R. K. Neely and A. C. Jones, *J. Am. Chem. Soc.*, 2006, **128**, 15952–15953.

2 O. J. G. Somsen, L. B. Keukens, M. N. De Keijzer, A. van Hoek and H. van Amerongen, *Chemphyschem*, 2005, **6**, 1622–1627.

3 T. M. Nordlund, *Photochem. Photobiol.*, 2007, **83**, 625–636.

4 E. R. Morris, H. Grey, G. McKenzie, A. C. Jones and J. M. Richardson, *Elife*, 2016, **5**, 1–23.

Appendix I

Fluorescence Decays of 2AP-containing Oligonucleotides and Corresponding Duplexes

The fluorescence decay curves recorded for 2AP-containing oligonucleotides ss2, ss3 and ss4 and for 2AP-containing duplexes ds2, ds3 and ds4 are shown below for measurements performed at room temperature (Figure I.1) and at 77 K (Figure I.2).

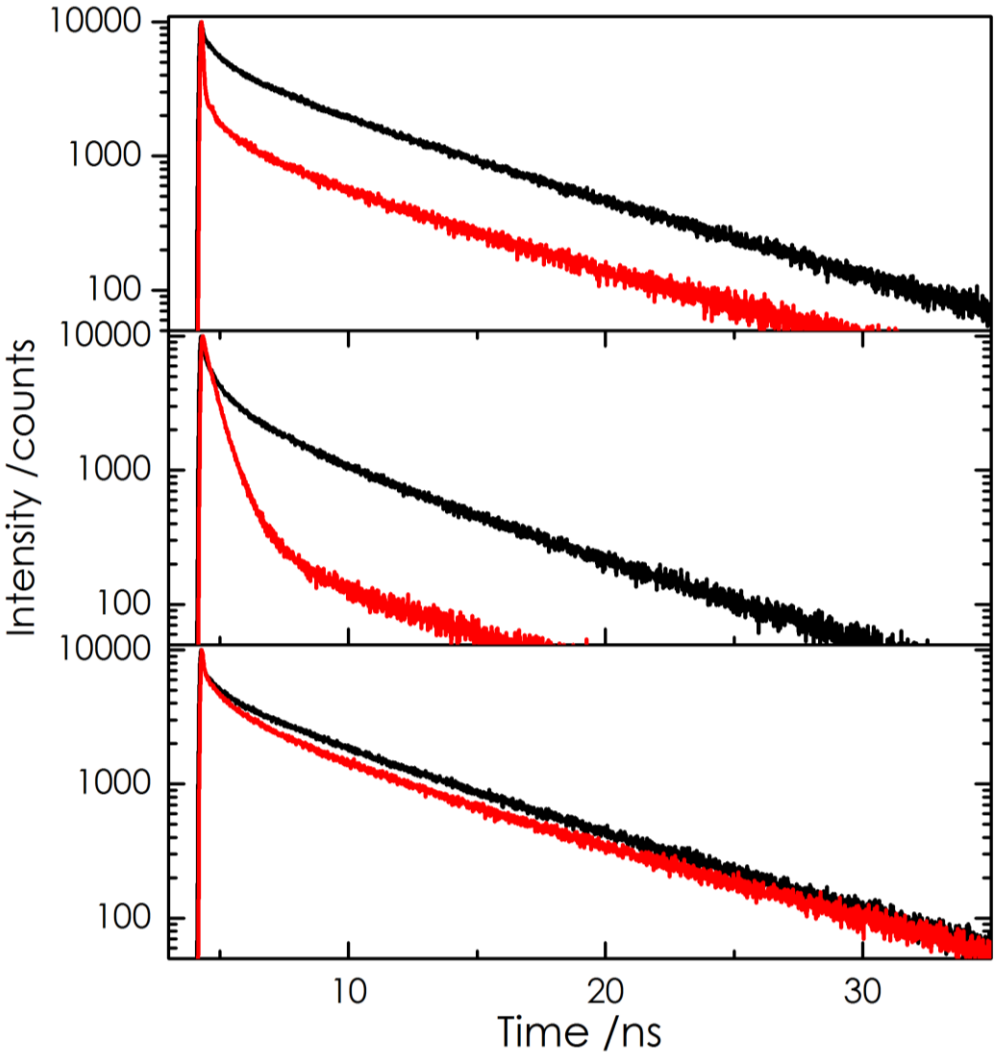

Figure I.1: Fluorescence decay curves for ss2-4 (black, top to bottom, respectively) and ds2-4 (red, top to bottom, respectively) in aqueous LiCl at room temperature. Excitation and emission wavelengths were 310 nm and 380 nm, respectively.

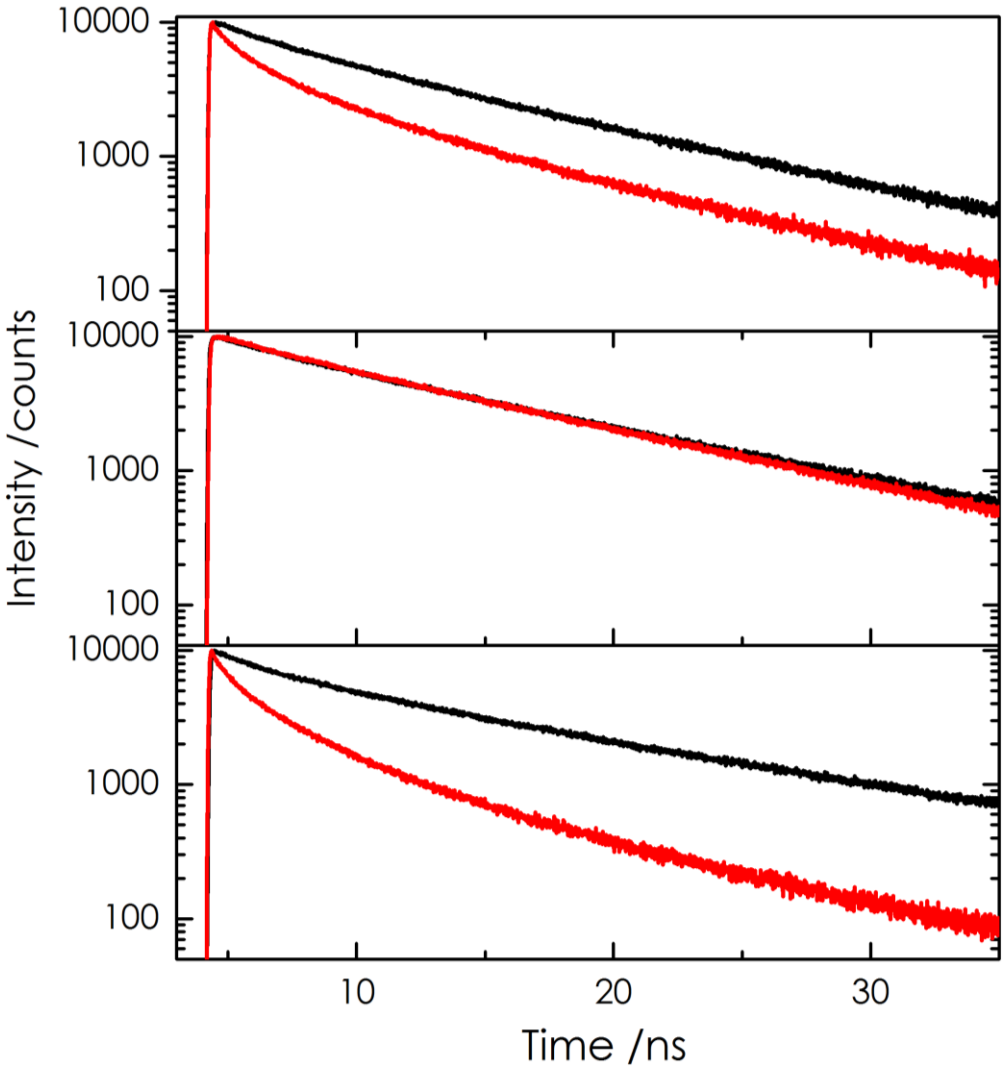

Figure I.2: Fluorescence decay curves for ss2-4 (black, top to bottom, respectively) and ds2-4 (red, top to bottom, respectively) in aqueous LiCl at 77K. Excitation and emission wavelengths were 310 nm and 380 nm, respectively.

The Effect of Freezing on the Decay Curves of 2AP-containing Oligonucleotides

Figure I.3 shows the effect of freezing on the decay curves of ss2, ss3, ds2 and ds3, while the effect of freezing on those for ss4 and ds4 are shown in Figure I.4.

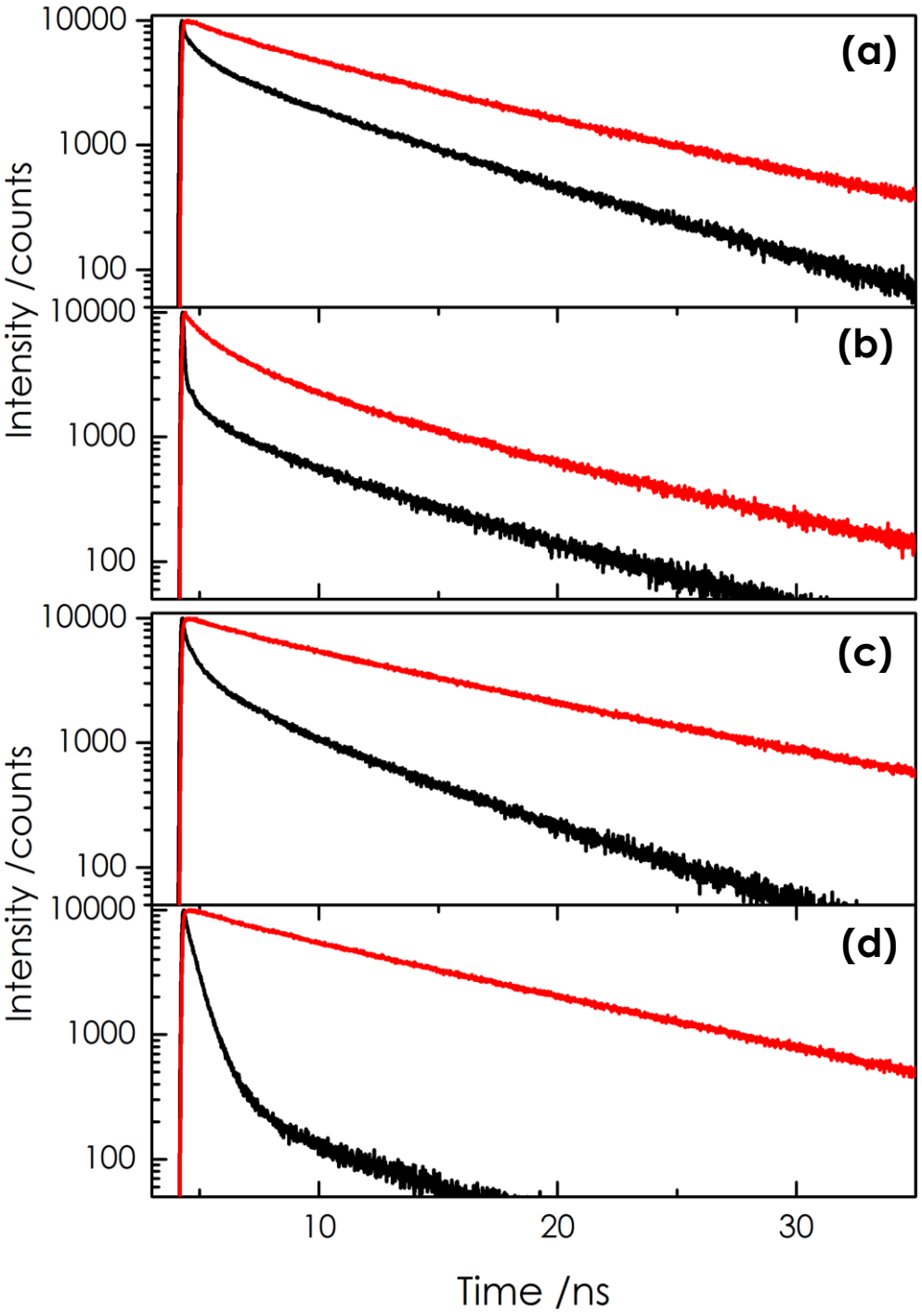

Figure I.3: Fluorescence decay curves recorded at room temperature (black) and at 77 K (red) for ss2 (a) ds2 (b), ss3 (c) and ds3 (d) in aqueous 6M LiCl. Excitation and emission wavelength were 310 nm and 380 nm respectively.

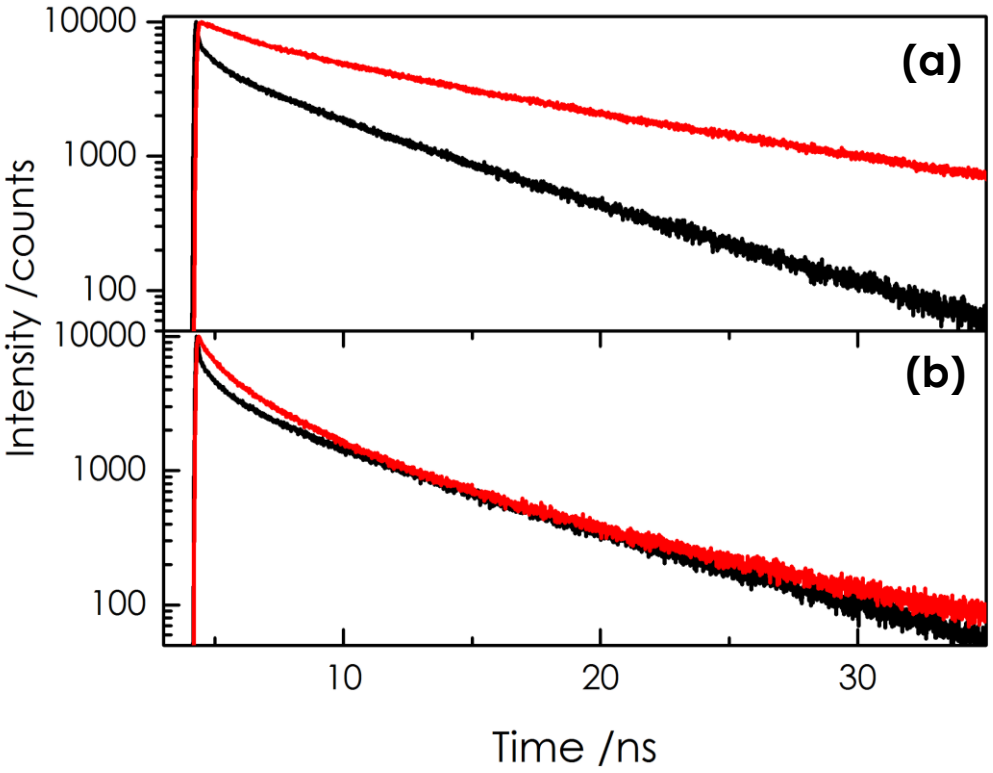

Figure I.4: Fluorescence decay curves recorded at room temperature (black) and at 77 K (red) for ss4 (a) and ds4 (b) in aqueous 6M LiCl. Excitation and emission wavelength were 310 nm and 380 nm respectively.

Normalised Steady-state Spectra of 2AP-containing Dinucleotides at Room Temperature

Figures I.5 and I.6 show the steady-state excitation and emission spectra for 2AP-containing dinucleotides at room temperature in a aqueous tris buffer and aqueous LiCl solution normalised to the characteristic peaks of 2AP (~305 nm for excitation and ~370 nm for emission).

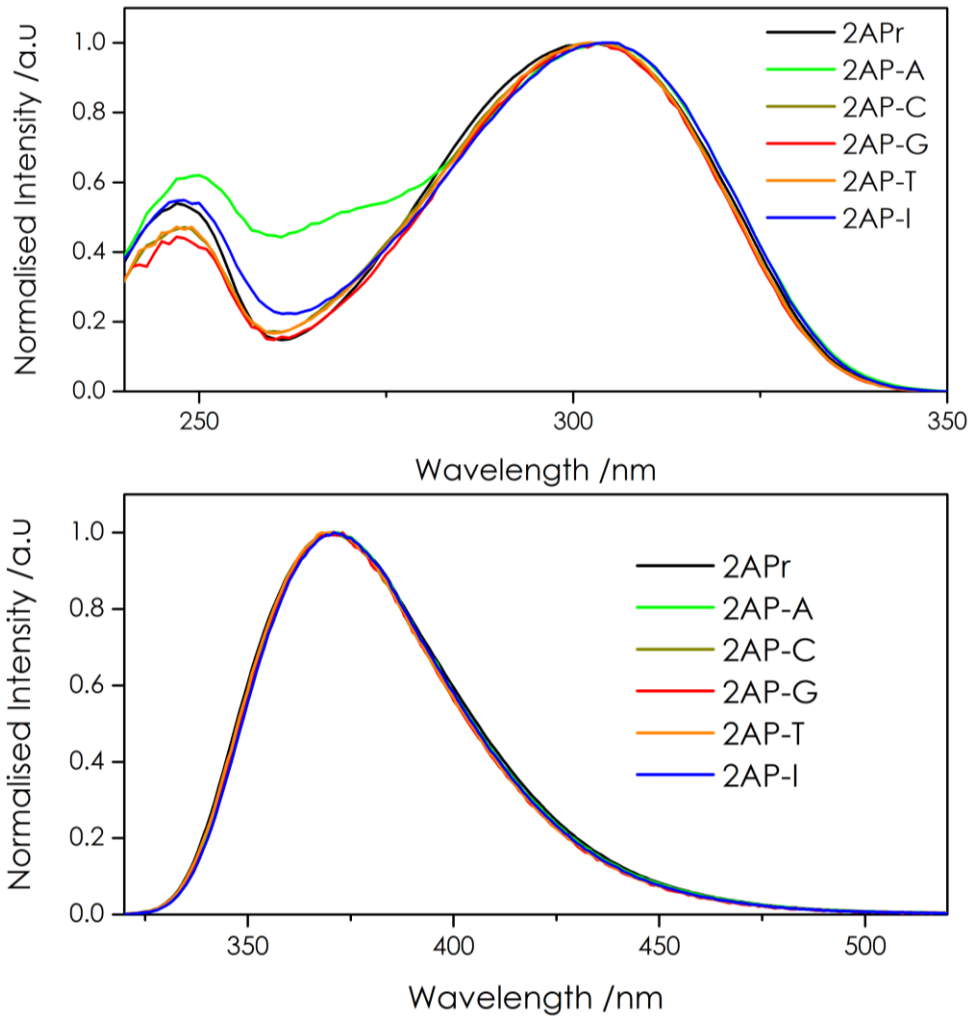

Figure I.5: Normalised steady-state spectra for dinucleotides in aqueous tris buffer recorded at room temperature. Excitation spectra (top) were recorded monitoring an emission wavelength of 370 nm and emission spectra (bottom) were excited at 305 nm. Excitation spectra have been normalised to the excitation peak of 2AP at ~305 nm and the area of increased intensity at ~260 nm (most apparent for 2AP-A) can be attributed to energy transfer (as discussed in Chapter 5). Emission spectra have been normalised to the emission peak of 2AP at 370 nm.

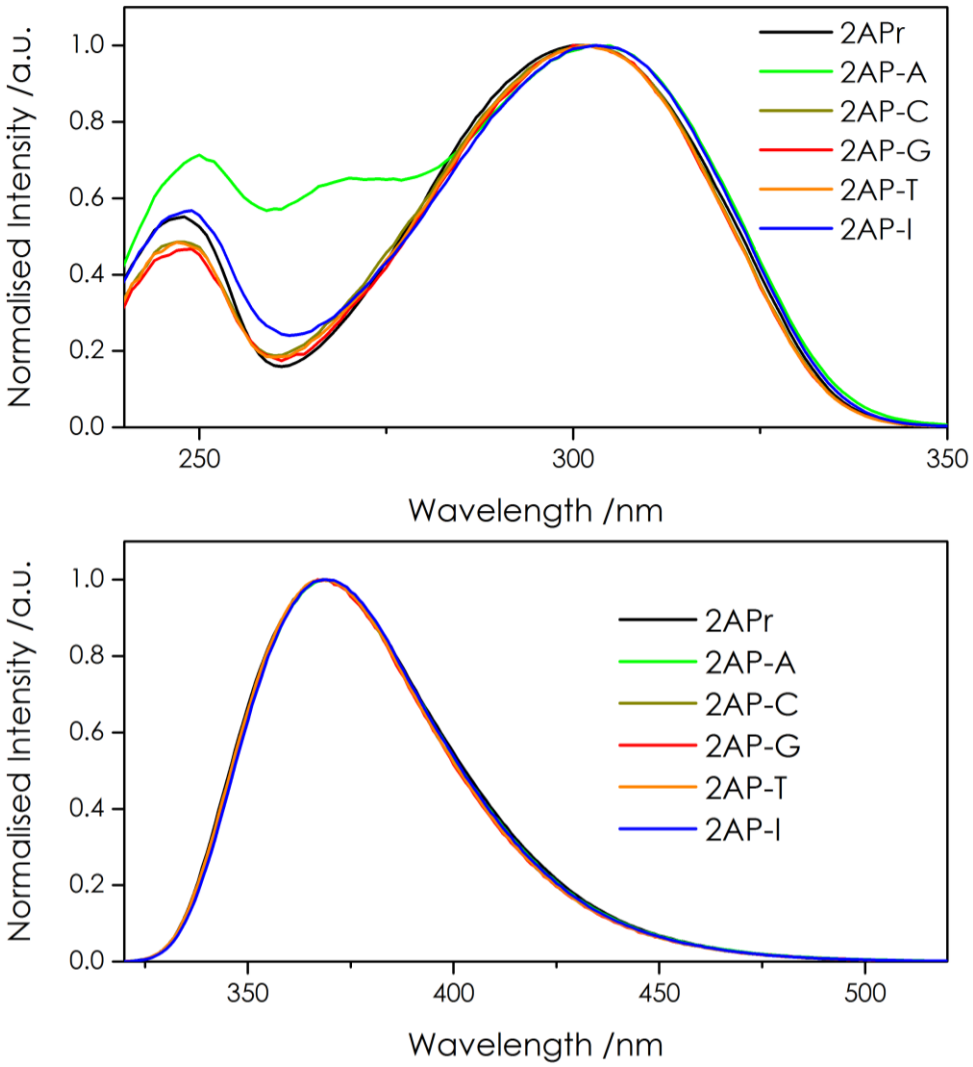

Figure I.6: Normalised steady-state spectra for dinucleotides in aqueous LiCl solution recorded at room temperature. Excitation spectra (top) were recorded monitoring an emission wavelength of 370 nm and emission spectra (bottom) were excited at 305 nm. Excitation spectra have been normalised to the excitation peak of 2AP at ~305 nm and the area of increased intensity at ~260 nm (most apparent for 2AP-A) can be attributed to energy transfer (as discussed in Chapter 5). Emission spectra have been normalised to the emission peak of 2AP at 370 nm.

Normalised Steady-state Spectra of 2AP-containing Dinucleotides at 77 K

Figure I.7 shows the steady-state excitation and emission spectra for 2AP-containing dinucleotides frozen at 77 K in a LiCl matrix normalised to the characteristic peaks of 2AP (~305 nm for excitation and ~355 nm for emission).

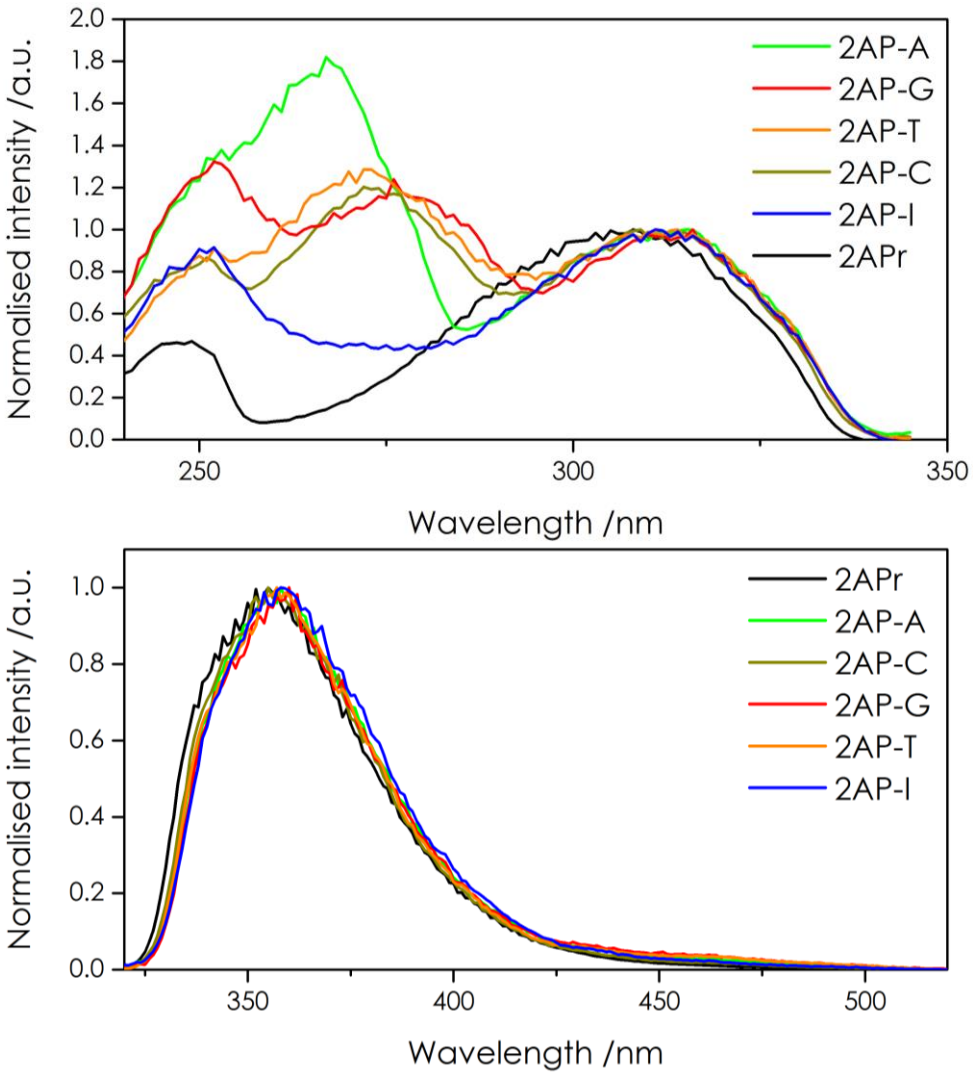

Figure I.7: Normalised steady-state spectra for dinucleotides recorded at 77 K. Excitation spectra (top) were recorded monitoring an emission wavelength of 355 nm and emission spectra (bottom) were excited at 305 nm. Excitation spectra have been normalised to the excitation peak of 2AP at ~305 nm and shorter wavelength excitation peaks can be attributed to energy transfer (as discussed in Chapter 5). The order of the samples in the legend of the excitation spectra reflects the order of the intensities at ~260 nm. Emission spectra have been normalised to the emission maximum of 2AP at ~355 nm.

Steady-state Fluorescence of 6 M Aqueous Lithium Chloride

The steady-state excitation and emission spectra for 6 M LiCl solution at room temperature and frozen at 77 K are shown in Figure I.8.

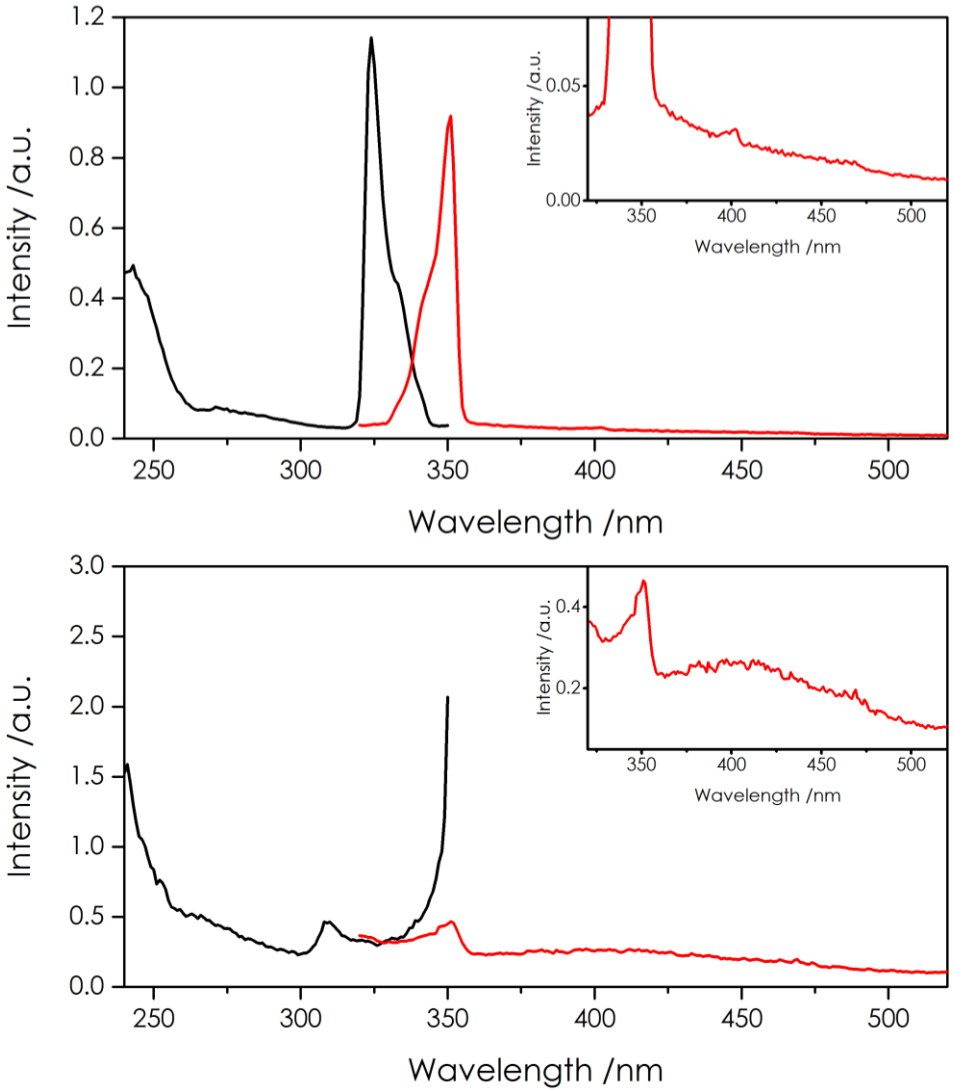

Figure I.8: Steady-state fluorescence of aqueous LiCl at (a) room temperature and (b) 77 K. Excitation spectra (when observing 370 nm at room temperature and 355 nm at 77K) are shown in black and emission spectra (when excited at 305 nm) are shown in red. The inset shows a close up of the fluorescence emission intensity in the region at which the dinucleotides where recorded.

Decay Parameters for the Three-components Fits of the Fluorescence Decay of 2AP-A and 2AP-I

Table I.1 and Table I.2 show the decay parameters for the three-component fits for 2AP-A and 2AP-I in aqueous buffer and aqueous LiCl solution, respectively.

X	τ_i /ns				A_i				<τ> / ns
	τ_1	τ_2	τ_3	τ_4	A_1	A_2	A_3	A_4	
A	-	0.31	1.65	8.95	-	0.54	0.34	0.12	1.77
I	-	0.41	2.69	8.11	-	0.35	0.55	0.10	2.42

Table I.1: Fluorescence lifetimes, τ_i, and corresponding fractional amplitudes, A_i, of the three-component fits of the fluorescence decay of 2AP-A and 2AP-I in aqueous buffer solution at room temperature using an excitation wavelength of 310 nm. Decay parameters were determined from globally fitting the decays collected at 360 nm, 380 nm and 400 nm; the A factors showed minimal wavelength-dependence, and A factors are quoted for 380-nm emission. Experimental uncertainties (estimated by dividing the standard deviation of values by the corresponding values): $\tau_2 \leq 10\%$, $\tau_3 \leq 1\%$, $\tau_4 \leq 1\%$, $A_2 \leq 2\%$, $A_3 \leq 3\%$, $A_4 \leq 2\%$.

X	τ_i /ns				A_i				<τ> / ns
	τ_1	τ_2	τ_3	τ_4	A_1	A_2	A_3	A_4	
A	-	0.70	2.83	7.65	-	0.57	0.24	0.19	2.52
I	-	0.86	3.07	6.00	-	0.33	0.41	0.27	2.68

Table I.2: Fluorescence lifetimes, τ_i, and corresponding fractional amplitudes, A_i, of the three-component fits of the fluorescence decay of 2AP-A and 2AP-I in aqueous LiCl solution at room temperature using an excitation wavelength of 310 nm. Decay parameters were determined from globally fitting the decays collected at 360 nm, 380 nm and 400 nm; the A factors showed minimal wavelength-dependence, and A factors are quoted for 380-nm emission. Experimental uncertainties (estimated by dividing the standard deviation of values by the corresponding values): $\tau_2 \leq 10\%$, $\tau_3 \leq 1\%$, $\tau_4 \leq 1\%$, $A_2 \leq 2\%$, $A_3 \leq 3\%$, $A_4 \leq 2\%$.

Appendix II

Parameters Used to Calculate Energy Transfer Efficiencies in 2AP-containing Dinucleotides

Tables II.1 and II.2 show the experimentally determined parameters used in conjunction with Equation 5.2 for calculation of energy transfer efficiencies, η_{SS}, for energy transfer from X to 2AP, in 2AP-containing dinucleotides (2AP-X), dissolved in aqueous tris buffer and 6 M aqueous LiCl solution, respectively.

Sample	Absorbance ratio $\left(\frac{A_a(\lambda_{ex})}{A_d(\lambda_{ex})}\right)$	Fluorescence ratio $\left(\frac{F(\lambda_{ex})}{F_a(\lambda_{ex})}\right)$	$\frac{1}{Q_{rel}}$	η_{SS} /%
2APr	1.000	1.00	1.00	-
2AP-G	0.070	0.08	13.60	0.4
2AP-T	0.111	0.15	8.20	2.2
2AP-C	0.122	0.20	5.94	2.3
2AP-A	0.072	0.55	5.63	15.0
2AP-I	0.117	0.41	3.95	7.4

Table II.1: Experimentally determined parameters used in conjunction with Equation 5.2 to calculate the energy transfer efficiencies, η_{SS}, presented in Table 5.5 for 2AP-containing dinucleotides in aqueous tris buffer. Where A_a and A_d are the absorbance values of the energy acceptor and donor, respectively; F_a and F are the fluorescence intensity of directly excited energy acceptor or the 2AP-containing dinucleotide, respectively, at λ_{ex}; and Q is the ratio of the quantum yield of 2APr and that for 2AP in the dinucleotide.

Sample	Absorbance ratio $\left(\frac{A_a(\lambda_{ex})}{A_d(\lambda_{ex})}\right)$	Fluorescence ratio $\left(\frac{F(\lambda_{ex})}{F_a(\lambda_{ex})}\right)$	$\frac{1}{Q_{rel}}$	η_{SS} /%
2APr	1.000	1.00	1.00	-
2AP-G	0.075	0.14	8.11	1.1
2AP-T	0.121	0.25	4.59	1.8
2AP-C	0.125	0.35	3.36	2.3
2AP-A	0.075	0.93	3.79	18.9
2AP-I	0.117	0.64	2.48	7.0

Table II.2: Experimentally determined parameters used in conjunction with Equation 5.2 to calculate the energy transfer efficiencies, η_{SS}, for 2AP-containing dinucleotides in 6M aqueous LiCl solution. Where A_a and A_d are the absorbance values of the energy acceptor and donor, respectively; F_a and F are the fluorescence intensity of directly excited energy acceptor or the 2AP-containing dinucleotide, respectively, at λ_{ex}; and Q is the ratio of the quantum yield of 2APr and that for 2AP in the dinucleotide.

Comparison of the Fluorescence Decay parameters for 2AP-C Following Excitation at 260 nm or 310 nm

Tables II.3 and II.4 show the decay parameters for 2AP-C following excitation at 310 nm (direct) and 260 nm (indirect) in aqueous tris buffer and 6 M aqueous LiCl solution, respectively.

X	Excitation pathway	τ_i /ns				A_i				<τ> / ns
		τ_1	τ_2	τ_3	τ_4	A_1	A_2	A_3	A_4	
C	Indirect	0.11	-	1.9	9.5	0.26	-	0.16	0.58	5.86
	Direct	0.09	0.47	2.4	9.0	0.46	0.10	0.41	0.03	1.34

Table II.3: Fluorescence lifetimes, τ_i, and corresponding fractional amplitudes, A_i, of the three-component fits of the fluorescence decay of 2AP-C in aqueous buffer solution at room temperature, for indirect excitation (λ_{exc} = 260 nm) or direct excitation (λ_{exc} = 310 nm). Decay parameters were determined from globally fitting the decays collected at 360 nm, 380 nm and 400 nm; the A factors showed minimal wavelength-dependence, and A factors are quoted for 380-nm emission. The average lifetimes, <τ>, are also given. Experimental uncertainties (estimated by dividing the standard deviation of values by the corresponding values): $\tau_1 \leq 10\%$, $\tau_2 \leq 5\%$, $\tau_3 \leq 1\%$, $\tau_4 \leq 1\%$, $A_1 \leq 1\%$, $A_2 \leq 2\%$, $A_3 \leq 3\%$, $A_4 \leq 2\%$.

X	Excitation pathway	τ_i /ns				A_i				<τ> / ns
		τ_1	τ_2	τ_3	τ_4	A_1	A_2	A_3	A_4	
C	Indirect	0.08	0.75	4.0	9.0	0.38	0.17	0.21	0.24	3.14
	Direct	0.12	0.82	3.8	7.5	0.27	0.14	0.50	0.09	2.72

Table II.4: Fluorescence lifetimes, τ_i, and corresponding fractional amplitudes, A_i, of the three-component fits of the fluorescence decay of 2AP-C in aqueous LiCl solution at room temperature, for indirect excitation (λ_{exc} = 260 nm) or direct excitation (λ_{exc} = 310 nm). Decay parameters were determined from globally fitting the decays collected at 360 nm, 380 nm and 400 nm; the A factors showed minimal wavelength-dependence, and A factors are quoted for 380-nm emission. The average lifetimes, <τ>, are also given. Experimental uncertainties (estimated by dividing the standard deviation of values by the corresponding values): $\tau_1 \leq 10\%$, $\tau_2 \leq 5\%$, $\tau_3 \leq 1\%$, $\tau_4 \leq 1\%$, $A_1 \leq 1\%$, $A_2 \leq 2\%$, $A_3 \leq 3\%$, $A_4 \leq 2\%$.

Comparison of the Fluorescence Decay Parameters for 2AP-containing Dinucleotides in 6 M Aqueous LiCl Solution Following Excitation at 260 nm or 310 nm

The fluorescence decay parameters measured for the dinucleotides in aqueous LiCl solution following excitation at 260 nm (indirect) are presented in Table II.5, in comparison with those following excitation at 310 nm (direct). The results for 2AP-C are omitted from the table but can be found above, in Table II.4.

X	Excitation pathway	τ_i /ns				A_i				<τ> / ns
		τ_1	τ_2	τ_3	τ_4	A_1	A_2	A_3	A_4	
G	Indirect	0.06	0.57	2.9	7.9	0.76	0.11	0.09	0.04	0.69
	Direct	0.07	0.67	3.1	7.7	0.53	0.11	0.23	0.13	1.82
T	Indirect	0.06	0.61	3.5	7.5	0.68	0.12	0.17	0.03	0.94
	Direct	0.06	0.68	3.6	6.4	0.43	0.10	0.38	0.09	2.04
A	Indirect	0.33	0.90	3.0	8.2	0.24	0.63	0.10	0.04	1.27
	Direct	0.08	0.76	3.0	7.7	0.14	0.50	0.20	0.16	2.22
I	Indirect	0.07	0.91	3.3	8.4	0.15	0.47	0.28	0.10	2.20
	Direct	0.03	0.90	3.1	6.0	0.15	0.28	0.35	0.22	2.66

Table II.5: Fluorescence lifetimes, τ_i, and corresponding fractional amplitudes, Ai, for 2AP-X (X= A, G, T or I) in 6 M aqueous LiCl at room temperature, for indirect excitation (λ_{exc} = 260 nm) or direct excitation (λ_{exc} = 310 nm). Lifetimes were obtained from global fitting of decays recorded at three emission wavelengths (360nm, 380 nm and 400 nm). The fractional amplitudes show little variation with emission wavelength and those for 380 nm emission are given. The average lifetimes, <τ>, are also given. The fluorescence decay parameters for 2AP-C are not shown in this table but can be found in Table II.4. Experimental uncertainties (estimated by dividing the standard deviation of values by the corresponding values): $\tau_1 \leq 5\%$, $\tau_2 \leq 2\%$, $\tau_3 \leq 1\%$, $\tau_4 \leq 1\%$, $A_1 \leq 2\%$, $A_2 \leq 3\%$, $A_3 \leq 3\%$, $A_4 \leq 2\%$.

Appendix III

Decay parameters of 2AP-containing Single-stranded Oligomers

Table III.1 shows the decay parameters measured for single-stranded oligomers TS_P$_{-23}$ and TS_P$_{13}$l.

Sample	τ_i /ns				A_i				< τ >
	τ_1	τ_2	τ_3	τ_4	A_1	A_2	A_3	A_4	(ns)
TS_P$_{-23}$s	0.03	0.44	2.7	7.4	0.79	0.08	0.07	0.06	0.69
TS_P$_{13}$l	0.04	0.29	1.6	5.9	0.87	0.09	0.03	0.01	0.17

Table III.1: Fluorescence decay parameters for 2AP-labelled ss-oligomers, TS_P$_{-23}$s and TS_P$_{13}$l, which contain 2AP at positions A$_{-23}$ and A$_{13}$, respectively (corresponding to the labelled positions shown in Figure 5.5). The parameters shown are obtained from global fits of the emission at 375 nm and 390 nm. The A-factors demonstrated minimal wavelength dependence and only those for 380 nm emission are shown. The fitted χ^2 values were <1.2 indicating a good fit of the data.

Appendix IV

Publications

A bend, flip and trap mechanism for transposon integration

E. R. Morris, H. Grey, G. McKenzie, A. C. Jones and J. M. Richardson, *Elife*, 2016, **5**, 1–23.

DOI: 10.7554/eLife.15537

URL: http://dx.doi.org/10.7554/eLife.15537

Lectures, Courses and Training

University of Edinburgh:

Laser Safety Course

Safety Risk Assessment Lecture

General Safety Lecture

Managing your PhD (Chemistry)

Introduction to Computational chemistry (Scottish Universities Physics Alliance)

Gaussian Workshop

School of Chemistry Colloquia

1st Year Report Writing Workshop

EaStChem PhD Thesis Workshop

IAD PhD Viva Workshop

How to Beat Writers Block Workshop

University of Melbourne:

Safety Exam

Induction and Safety Program

Laser Safety and Radiation Training

Demonstrating Induction

MATLAB Fundamentals

PhD Completion Seminars

Conferences and Meetings

UoE Physical chemistry section Meetings, Firbush Point, Killin

RACI PhysChem 2013, Hobart, Tasmania, December 2013

FLIM workshop, Swinburne University, Melbourne, Australia, April 2014

MATLAB Tour 2014 Conference, Melbourne, Australia, August 2014

Joseph Black Conference 2015, University of Edinburgh, United Kingdom, May 2015

MAF 14, 14th Conference on Methods and Applications of Fluorescence, Wurzburg, Germany, September 2015